
Watching Nanoparticles Form: In Situ and Single-Particle X-ray Studies of Nucleation and Growth

Dissertation
zur Erlangung des Doktorgrades
an der Fakultät für Mathematik, Informatik und Naturwissenschaften
Fachbereich Physik
der Universität Hamburg

vorgelegt von
Sani Yusuf Harouna-Mayer

Hamburg 2026

Gutachter/innen der Dissertation:

Prof. Dr. Dorota Koziej
Prof. Dr. Gabriel Bester

Zusammensetzung der Prüfungskommission:

Prof. Dr. Dorota Koziej
Prof. Dr. Gabriel Bester
Prof. Dr. Wolfgang J. Parak
Dr. Irene Fernandez-Cuesta
Dr. Kartik Ayyer

Vorsitzender der Prüfungskommission:

Prof. Dr. Wolfgang J. Parak

Datum der Disputation:

01.04.2026

Vorsitzender des Fach-Promotionsausschusses PHYSIK:

Prof. Dr. Johannes Haller

Leiter des Fachbereichs PHYSIK:

Prof. Dr. Markus Drescher

Dekan der Fakultät MIN:

Prof. Dr.-Ing. Norbert Ritter

Abstract

All solid materials are formed through nucleation. During this process, atomic or molecular building blocks assemble to form nuclei in solution or at interfaces, which may subsequently grow into nanoparticles. The size, structure, composition, and morphology of nanoparticles – and thus their functional properties – are established during these nucleation and growth stages. Consequently, a mechanistic understanding of nanoparticle formation is a fundamental prerequisite for the rational design of nanoparticles with targeted functionality. Despite its central importance, nucleation and growth in solution are insufficiently understood, particularly for complex or poorly explored material classes, which continues to limit predictive control over nanoparticle synthesis.

Metal nitrides are a challenging and comparatively understudied material. In contrast to many metal oxides, their formation mechanisms in solution remain largely unclear, primarily due to the demanding synthesis conditions that typically involve high temperatures and/or pressures. In addition, metal nitrides are often unstable under ambient or operando conditions and tend to transform into the thermodynamically favored oxide or metallic phase. These factors complicate both their synthesis and characterization and have so far limited systematic investigations of their nucleation and growth pathways.

In this thesis, the formation of different metal oxide and metal nitride nanoparticles in solution is investigated using complementary X-ray techniques. Wide-angle X-ray scattering (WAXS) techniques resolve the atomic arrangement and crystallographic structure of a nanoparticle, while small-angle X-ray scattering (SAXS) is sensitive to the nanoparticle size, shape, and assembly. X-ray absorption spectroscopy (XAS) probes the electronic structure and the local environment around the absorbing atom. A central contribution of this thesis is the development of a versatile reactor that enables *in situ* WAXS, SAXS, and XAS measurements under identical reaction conditions at synchrotron sources, providing a comprehensive picture of the electronic and structural evolution during nanoparticle nucleation and growth.

This is here demonstrated for the reaction of iron acetylacetonate to iron oxide (Fe_3O_4) nanoparticles, where *in situ* WAXS in combination with XAS reveal the presence of an intermediate iron acetate cluster prior to crystallization, providing direct insight into multi-step nucleation and growth pathways. Additional *in situ* attenuated total reflection infrared spectroscopy of the iron oxide synthesis in the same reactor shows the thermal decomposition of the acetylacetonate to acetate, which coordinates to the intermediate iron species.

Building on this methodology, a low-temperature synthesis route for copper palladium nitride (Cu_3PdN) nanoparticles is introduced, and comprehensively studied using *in situ* WAXS and XAS to elucidate the reaction mechanism. The resulting Cu_3PdN nanoparticles are phase-pure, stable at ambient condition, and most interestingly exhibit strong cation-site disorder within the crystal structure. The nanoparticles are further evaluated as electrocatalysts for the hydrogen evolution reaction, demonstrating good catalytic activity and excellent stability. At extended reaction times, *in situ* WAXS reveals the reduction of the nitride nanoparticles into bimetallic copper palladium (Cu_3Pd). Such phase impurities are clearly present yet unnoticed in most previously reported colloidal Cu_3PdN nanoparticles.

Finally, this thesis extends beyond ensemble-averaged measurements by introducing single-particle SAXS (SP-SAXS) at X-ray free-electron lasers as a powerful approach to resolve structural heterogeneity within nanoparticle populations. While conventional synchrotron-based X-ray measurements inherently average over the illuminated sample volume and may obscure transient, dilute, or low-contrast species, SP-SAXS overcomes this limitation by analyzing scattering snapshots from individual particles. Applied to the synthesis of cobalt oxide (CoO) nanoparticle assemblies, SP-SAXS reveals the formation of amorphous organometallic spherical precipitates that subsequently contract during crystallization into cavernous nanoparticle assemblies, explaining the emergence of hierarchical CoO structures rather than isolated nanocrystals.

Overall, this thesis advances synthetic, analytical, and experimental methodologies and provides new mechanistic insights into the nucleation and growth of metal oxide and metal nitride nanoparticles.

Zusammenfassung

Alle festen Materialien entstehen durch Nukleation. Während dieses Prozesses entstehen in Lösung oder an Grenzflächen aus atomaren oder molekularen Bausteinen Keime, die anschließend zu Nanopartikeln heranwachsen können. Größe, Struktur, Zusammensetzung und Morphologie der Nanopartikel – und damit ihre funktionellen Eigenschaften – werden während dieser Nukleations- und Wachstumsphasen festgelegt. Ein mechanistisches Verständnis der Nanopartikelbildung ist daher eine grundlegende Voraussetzung für das rationale Design von Nanopartikeln mit gezielt einstellbarer Funktionalität. Trotz ihrer Wichtigkeit sind Nukleation und Wachstum in Lösung bislang nur unzureichend verstanden, insbesondere für komplexe oder wenig erforschte Materialklassen, was die Vorhersagbarkeit der Nanopartikelsynthese einschränkt.

Metallnitride stellen eine besonders anspruchsvolle und vergleichsweise wenig untersuchte Materialklasse dar. Im Gegensatz zu vielen Metalloxiden sind ihre Bildungsmechanismen in Lösung weitgehend ungeklärt, was vor allem auf die anspruchsvollen Synthesebedingungen zurückzuführen ist, die typischerweise hohe Temperaturen und/oder Drücke erfordern. Darüber hinaus sind Metallnitride unter Umgebungs- oder Operando-Bedingungen häufig instabil und neigen dazu, in die thermodynamisch bevorzugte Oxid- oder Metallphase überzugehen. Diese Faktoren erschweren sowohl ihre Synthese als auch ihre Charakterisierung und haben bislang systematische Untersuchungen ihrer Nukleations- und Wachstumspfade stark beeinträchtigt.

In dieser Arbeit wird die Bildung verschiedener Metalloxid- und Metallnitrid-Nanopartikel in Lösung mithilfe komplementärer Röntgenmethoden untersucht. Weitwinkel-Röntgenstreuung (WAXS) liefert Informationen über die atomare Anordnung und die kristallographische Struktur der Nanopartikel, während Kleinwinkel-Röntgenstreuung (SAXS) sensitiv für Größe, Form und Assemblierung der Partikel ist. Die Röntgenabsorptionsspektroskopie (XAS) ermöglicht Einblicke in die elektronische Struktur sowie die lokale chemische Umgebung des absorbierenden Atoms. Ein zentraler Beitrag dieser Arbeit ist die Entwicklung eines vielseitigen Reaktors, der *in situ*-WAXS-, SAXS- und XAS-Messungen unter identischen Reaktionsbedingungen an Synchrotronquellen erlaubt und damit ein umfassendes Bild der elektronischen und strukturellen Entwicklung während der Keimbildung und des Wachstums von Nanopartikeln liefert.

Dies wird exemplarisch an der Reaktion von Eisenacetylacetonat zu Eisenoxid-Nanopartikeln (Fe_3O_4) gezeigt. *In situ*-WAXS-Messungen in Kombination mit XAS weisen auf die Bildung eines intermediären Eisenacetat-Clusters vor der Kristallisation hin und liefern damit direkte Einblicke in nicht-klassische Nukleations- und Wachstumsmechanismen. Ergänzende *in situ*-Messungen der abgeschwächten Totalreflexions-Infrarotspektroskopie der gleichen Synthese im selben Reaktor zeigen die thermische Zersetzung des Acetylacetonat-Liganden zu Acetat, das an die intermediären Eisenspezies koordiniert.

Aufbauend auf dieser Methodik wird ein Niedrigtemperatur-Syntheseweg für Kupfer-Palladium-Nitrid-Nanopartikel Cu_3PdN vorgestellt und mittels *in situ*-WAXS und XAS umfassend untersucht, um den zugrunde liegenden Reaktionsmechanismus aufzuklären. Die resultierenden (Cu_3PdN)-Nanopartikel sind phasenrein, unter Umgebungsbedingungen stabil und weisen be-

merkwürdigerweise eine ausgeprägte Unordnung der Kationenplätze innerhalb der Kristallstruktur auf. Darüber hinaus werden die Nanopartikel als Katalysatoren für die elektrochemische Wasserspaltung untersucht und zeigen eine gute katalytische Aktivität bei gleichzeitig hoher Stabilität. Bei verlängerten Reaktionszeiten zeigt *in situ*-WAXS die Reduktion der Nitrid-Nanopartikel zu bimetallischem Kupfer-Palladium (Cu_3Pd). Solche Phasenverunreinigungen sind in den meisten veröffentlichten kolloidalen Cu_3PdN -Nanopartikeln vorhanden, blieben jedoch weitgehend unbemerkt.

Abschließend geht diese Arbeit über ensemble-gemittelte Messungen hinaus und etabliert die Einzelpartikel-SAXS (SP-SAXS) an Röntgen-Freie-Elektronen-Lasern als leistungsfähigen Ansatz zur Auflösung struktureller Heterogenität innerhalb von Nanopartikelpopulationen. Während konventionelle, synchrotronbasierte Röntgenmethoden zwangsläufig über das bestrahlte Probenvolumen mitteln und dadurch transiente, niedrig konzentrierte, oder kontrastarme Spezies unentdeckt bleiben können, überwindet SP-SAXS diese Einschränkung durch die Analyse von Streuschnappschüssen einzelner Partikel. Angewandt auf die Synthese von Kobaltoxid-Nanopartikel-Assemblierungen zeigt SP-SAXS die Bildung amorpher, organometallischer sphärischer Aggregaten, die sich während der Kristallisation zusammenziehen und dabei hohle Nanopartikel-Assemblierungen ausbilden. Dies erklärt die Entstehung hierarchischer CoO -Strukturen anstelle isolierter Nanokristalle. Allumfassend erweitert diese Arbeit synthetische, analytische, und experimentelle Methodiken und liefert neue mechanistische Einblicke in die Nukleation und das Wachstum von Metalloxid und Metallnitrid-Nanopartikeln.

Contents

Abstract	i
Zusammenfassung	iii
1 Introduction	1
2 Nucleation and Growth of Nanoparticles in Solution	4
2.1 Classical and nonclassical nucleation theory	4
2.2 Nucleation and growth of transition metal oxides and nitrides in solution . .	6
3 Fundamentals of X-ray-based Methods	8
3.1 Following nanoparticle formation with X-ray methods	8
3.2 X-ray generation	9
3.2.1 Laboratory X-ray sources	9
3.2.2 Synchrotron radiation	9
3.2.3 X-ray free electron laser	10
3.3 X-ray scattering	10
3.3.1 Wide-angle X-ray scattering	12
3.3.2 Small-angle X-ray scattering	16
3.4 X-ray absorption	19
3.4.1 Extended X-ray absorption fine structure	20
3.4.2 X-ray absorption near edge structure	21
3.4.3 High energy resolution fluorescence detected X-ray absorption spec-	
troscopy	22
4 Modular <i>In Situ</i> Reactor for X-ray Scattering, Spectroscopy, and ATR-IR Studies of Solvothermal Nanoparticle Synthesis	24
4.1 Abstract	24
4.2 Introduction	24
4.3 Reactor design	27
4.4 Performance of the reactor	30
4.5 Conclusion	36
4.6 Experimental section	37
S4 Supporting information	39
5 <i>In Situ</i> X-ray Study on Cation-Site Disordered Cu₃PdN Nanoparticles for Hydrogen Evolution Electrocatalysis	51
5.1 Abstract	51
5.2 Introduction	52
5.3 Results and Discussion	53
5.4 Conclusion	60
5.5 Experimental Section	62

S5	Supporting information	65
6	Single-Particle X-ray Scattering Reveals a High Local Supersaturation of Precursors as the Origin of CoO Nanoassembly Formation	89
6.1	Abstract	89
6.2	Introduction	90
6.3	Results	91
6.4	Conclusion	95
S6	Supporting information	97
7	Conclusions	106
	Appendix	109
A1	<i>In situ</i> X-ray Scattering Study on Sn:Fe _x O _y	109
A2	Synthesis of - the Role of Acetylacetonate on Phase-purity	116
A3	X-ray and Electron Diffraction of CoO Nanoassemblies and Intermediate Phases	121
A4	Fabrication of Nanotextured TiO ₂ Thin-films	128
	Bibliography	130
	List of Abbreviations	154
	List of Figures	156
	List of Tables	158
	List of Publications	160
	Curriculum Vitae	162
	Acknowledgements	163
	Eidesstattliche Versicherung	164

1 Introduction

Over the past three decades, intense interest in nanoscience and nanotechnology has driven rapid advances in the synthesis and characterization of materials at the nanoscale.^{1,2} Materials are referred to as nanomaterials when they exhibit characteristic length scales of approximately 1–100 nm in at least one dimension. The distinctive properties of these materials – and their technological potential – originate from their high surface-to-volume ratio and from their unique electronic structures that lie intermediate between those of molecules and crystalline solids.³

The properties of nanoparticles are governed by their size, shape, composition, and crystallographic phase. Liquid-phase synthesis, in which nanomaterials form from a precursor solution, offers a versatile route to tailor these properties through controlled variation of synthesis parameters, such as temperature, and precursor type and concentration. Traditionally, such optimization has relied largely on empirical trial-and-error approaches. However, understanding the underlying formation mechanism in solution enables predictive control and provides the basis for the rational design of functional nanomaterials.^{1,4}

Nucleation marks the onset of nanoparticle formation, during which primary building blocks phase-separate to form nuclei that may subsequently grow into nanoparticles. Since the foundational treatment of nucleation 150 years ago⁵, the process has remained an active topic of research and debate.^{6–10} One of the reasons is that nucleation pathways depend strongly on the specific chemical system and reaction conditions, making it difficult to generalize.¹¹ Moreover, nucleation and growth span extremely broad temporal and spatial scales, which continue to pose significant analytical and theoretical challenges for their experimental investigation and quantitative description.^{12,13}

X-ray methods have proven to be vital tools for investigating nucleation and growth in solution, as they provide complementary information on different stages of nanoparticle formation.¹⁴ When applied at high-flux synchrotron sources, they allow real-time observation of nanoparticle formation inside a chemical reactor. In this way, *in situ* X-ray methods enable elucidation of nanoparticle formation mechanisms in solution, which is a key prerequisite for rationally controlling syntheses and designing functional and complex nanoparticles.

In this thesis, the formation of different metal oxide and nitride nanoparticles in solution is investigated using complementary X-ray methods. In contrast to metal oxide nanoparticles, the nucleation and growth pathways of metal nitride nanoparticles are poorly understood, largely due to the challenging and comparatively unexplored synthesis routes for these materials.

Here, new synthesis routes for metal nitride nanoparticles are presented and comprehensively investigated using *in situ* X-ray techniques. In addition, a versatile reactor for *in situ* X-ray characterization is presented and applied to study the new metal nitride syntheses as well as established metal oxide synthesis routes, providing new mechanistic insight into the underlying nucleation and growth pathways. Furthermore, a novel single-particle X-ray approach for studying individual nanoparticles within heterogeneous ensembles is introduced. Altogether, this thesis advances mechanistic understanding and expands the synthetic and analytical

toolbox for investigating nanoparticle formation.

Structure of the thesis

After this general introduction, Chapter 2 discusses the fundamental concepts of nucleation and growth theories, followed by a brief review of reported formation mechanisms of various metal oxide and nitride nanoparticles.

Chapter 3 introduces the X-ray scattering and X-ray absorption spectroscopy techniques employed throughout this thesis. It begins with a summary of the applied X-ray techniques and illustrates how they can be used to probe different stages of nanoparticle formation, highlighting their respective strengths and limitations (Section 3.1). Subsequently, X-ray generation from different types of sources is summarized (Section 3.2). Finally, the fundamental principles of X-ray scattering and X-ray absorption spectroscopy methods are discussed (Sections 3.3 and 3.4).

In Chapter 4, a modular reactor for complementary *in situ* X-ray scattering and X-ray absorption spectroscopy is introduced. Its performance is demonstrated using iron oxide nanoparticle synthesis, where an intermediate pre-nucleation cluster is identified. The content of this Chapter has been published in Reference 15.

In this context, Chapter A1 in the appendix of this thesis presents *in situ* X-ray scattering studies of the same iron oxide synthesis with the addition of small amounts of a tin precursor, yielding tin-doped iron oxide nanoparticles and revealing how tin incorporation alters the iron oxide crystal structure.

In Chapter 5, a novel synthesis route of phase-pure copper palladium nitride nanoparticles is presented, and cation-site disorder within the crystal structure is revealed. The reaction mechanism is comprehensively analyzed using *in situ* X-ray scattering and X-ray absorption spectroscopy in the reactor introduced in Chapter 4. The as-synthesized copper palladium nitride nanoparticles are further evaluated as electrocatalysts for the hydrogen evolution reaction, demonstrating good catalytic activity and excellent stability. The content of this chapter has been published in Reference 16.

Building on these findings, Chapter A2 addresses the synthesis of copper nitride nanoparticles, showing that phase purity can be achieved by introducing acetylacetonate ligands.

In Chapter 6, a novel technique, referred to as single-particle small-angle X-ray scattering (SP-SAXS), is applied to study CoO nanoassemblies at different reaction times. This SP-SAXS study provides the missing mechanistic link to explain the formation of nanoassemblies rather than individual nanoparticles. SP-SAXS makes use of ultrashort and ultraintense X-ray free electron pulses (Section 3.2.3), enabling the analysis of individual particles. In contrast, conventional X-ray scattering methods average over the entire illuminated sample volume, which can obscure the presence of low-contrast particle populations. This limitation is overcome by SP-SAXS. The content of this Chapter has been published in Reference 17.

Furthermore, Chapter A3 discusses conventional X-ray diffraction and electron microscopy data of CoO at different reaction times, which reveal the formation of side reaction products.

Finally, in Chapter A4, the fabrication of nanotextured titanium oxide on a sapphire substrate is discussed.

The thesis concludes with a summary of the main results and an outlook on future developments of analytical X-ray methods for studying nanoparticle formation at synchrotron and

free-electron laser facilities (Chapter 7).

All results presented in this thesis were obtained in collaboration with fellow scientists. The specific contributions of the author to each study are described at the beginning of the respective chapter.

Comment on the use of the term *we* in this thesis: in chapters explaining the theoretical background, *we* refers to both the reader and the author of the thesis and is used to guide the reader through the text. In chapters presenting experimental results, *we* denotes all authors involved in the respective study.

2 Nucleation and Growth of Nanoparticles in Solution

2.1 Classical and nonclassical nucleation theory

The physical and chemical properties of nanoparticles can be tailored through careful control of the reaction pathways during their formation. Hence, understanding these pathways is crucial for the rational design of functional nanoparticles. Despite numerous efforts to develop a universal model for nanoparticle formation, a "one-fits-all" approach is not feasible.¹⁴ These formation pathway models are generally classified into two main theories: classical and nonclassical nucleation.^{1,18}

Classical nucleation theory describes how monomers – atoms, ions, or molecules – driven by increasing supersaturation directly aggregate to form a nucleus, which may eventually grow into a nanoparticle. This process is schematically illustrated by the well-known LaMer model in Figure 2.1. A stable nucleus is quantified in terms of the Gibbs free energy, ΔG , as function of the spherical nucleus radius, r (equation 2.1). The total free energy is the sum of the surface free energy, $\Delta G_{\text{surface}}$, and the crystal or bulk free energy, ΔG_{bulk} . The competing terms, $\Delta G_{\text{surface}} \propto r^2$ and $\Delta G_{\text{bulk}} \propto -r^3$, give rise to a critical nucleus size r_c , beyond which the nucleus becomes stable. For small radii ($r < r_c$) the surface free energy dominates, causing the nucleus to dissolve. However, once the radius exceeds r_c , the nucleus overcomes the critical thermodynamic energy barrier $\Delta G_c = \Delta G(r_c)$ and the nucleus grows.¹¹

$$\Delta G(r) = \Delta G_{\text{surface}}(r) + \Delta G_{\text{bulk}}(r) \quad (2.1)$$

In nonclassical nucleation models, nucleation kinetics is altered by the presence of intermediate structures, also referred to as pre-nucleation clusters.²⁰ Those metastable intermediates evoke local minima in the energy landscape along the nucleation pathway, which can effectively lower the energy barrier for nucleation so it can take place at a level of supersaturation lower than predicted in classical nucleation.¹ The next section reviews classical and nonclassical nucleation and growth pathways in solution-based synthesis of selected transition metal oxides and nitrides.

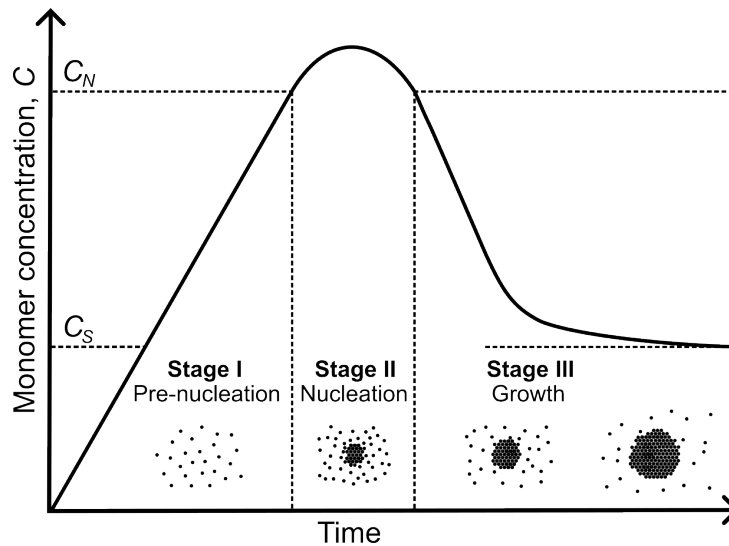


Figure 2.1: LaMer diagram. Stage I: The concentration of monomers increases as they are formed or added to the reaction system reaching a level of supersaturation above the saturation concentration, C_S . **Stage II:** Once the supersaturation reaches a critical concentration level for nucleation, C_N , the monomers aggregate to form nuclei. As monomers are consumed in the nucleation process and nuclei growth, the concentration increase slows down and eventually decreases, dropping below C_N , thus ending the nucleation stage. **Stage III:** The nuclei grow through the diffusion of monomers, and as time progresses, the concentration of monomers converges to C_S . This figure is inspired by reference 19.

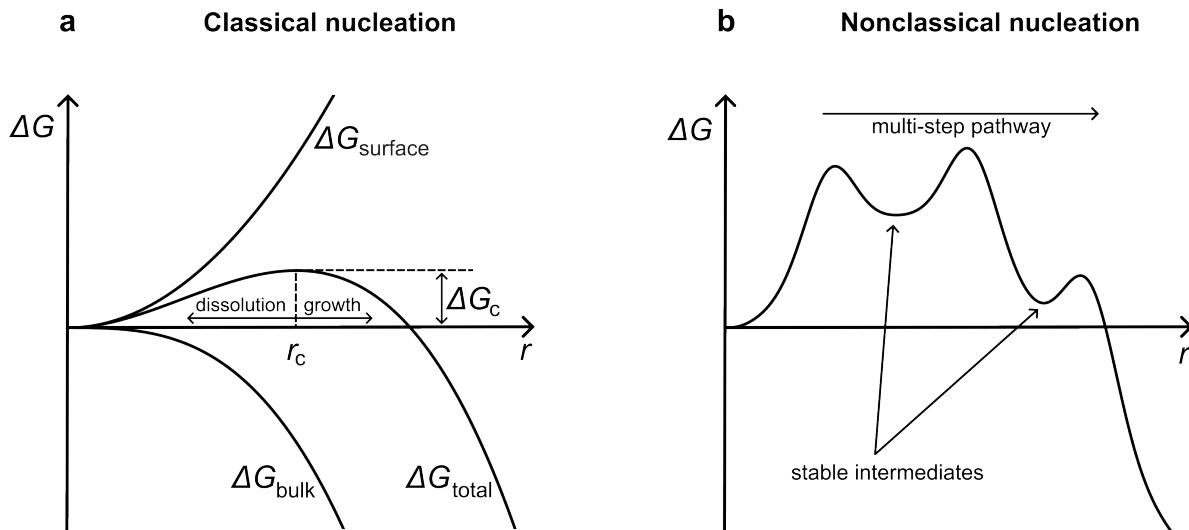


Figure 2.2: Plot of the Gibbs free energy for the classical and the nonclassical nucleation pathways. In the classical model, **a**, the Gibbs free energy exhibits a maximum at the critical radius r_c , below which nuclei are unstable and tend to dissolve. Nuclei exceeding r_c are stable and tend to grow. In contrast, the nonclassical model, **b**, involves one or more thermodynamically stable intermediates along a multi-step nucleation pathway. This figure is inspired by references 21–23.

2.2 Nucleation and growth of transition metal oxides and nitrides in solution

The synthetic procedure plays a crucial role in determining the composition, crystal structure, size, and morphology of nanoparticles. For example, iron oxide can be synthesized from iron chloride precursors in aqueous solution, typically yielding nanoparticles with broad size distributions and nonuniform morphologies.²⁴ Increasing the pH or the precursor concentration leads to the formation of larger nanoparticles,²⁵ while decreasing the pH leads to the formation of iron oxyhydroxide instead of iron oxides.²⁶

As exemplified by iron oxide, empirical correlations between synthesis parameters and the properties of the resulting products have been established for numerous transition metal oxides (TMOs), enabling a comparatively high degree of synthetic control for oxide nanoparticles. In contrast, transition metal nitrides (TMNs) remain far less explored due to their challenging synthesis. Consequently, mechanistic understanding and predictive control over nitride nanoparticle formation are still limited. This section first reviews reported formation pathways of TMOs, followed by a discussion of TMN synthetic methods and their underlying mechanisms, and relates these pathways to classical and nonclassical nucleation concepts.

In general, one way to achieve monodisperse nanoparticles is by separating a short burst nucleation phase, followed by slow growth, as described in the classical LaMer model (Figure 2.1).²⁷ This can be achieved, for example, through "hot-injection" methods,²⁸ where the monomer species is rapidly added to a solvent at elevated temperatures, causing a sudden increase in supersaturation. This process has been demonstrated for various TMOs, where the formation mechanism follows the classical nucleation pathway.²⁸ In the case of iron oxides, the hot-injection method further allows control over size and morphology through the addition of co-solvents in different concentrations.²⁹ Similarly, in a semi-classical description of the formation of monodisperse iron oxide nanoparticles, the thermal decomposition of the initial iron species during rapid heating results in the formation of an intermediate structure that, in fact, acts as a monomer in the LaMer model description, forming monodisperse iron oxide nanoparticles after a burst nucleation.³⁰ In some cases, despite the increasing complexity of the system, the LaMer model is still applicable, such as in the case of cobalt ferrite.^{29,31}

However, in most systems, nonclassical nucleation and growth models become essential to fully understand the nucleation and growth processes, particularly when more complex morphologies and structures are involved. Numerical simulations suggest that, under low supersaturation conditions, a two-step nucleation via an amorphous-to-crystalline transition is energetically favored over direct crystallization, as described in classical nucleation theory.¹ This nonclassical nucleation pathway has been observed in various iron oxide synthesis.³²⁻³⁵ Also, in many systems, iron oxo clusters are shown to form as intermediate structures prior to nucleation.^{11,24,36-38} Though, identifying the exact structure of these intermediate species is challenging, as they exist only transiently, and often can not be isolated. Nonetheless, understanding these intermediates, is crucial for tailoring the final product. For example, it has been shown that the addition of a co-polymer causes the initial iron species to form a complex with the polymer, which subsequently reacts to form a nanoparticle. The co-polymer then attaches to specific surface sites on the nanoparticle, leading to the formation of iron oxide rose-like structures.^{39,40} In another example, acetylacetonate ligation of the intermediate iron species prevents reduction, resulting in the controlled formation of twin-structured nanoparticles.²⁴

Compared to TMOs, solution-based synthesis routes for transition metal nitrides (TMNs) are much less explored, primarily due to the challenging synthesis conditions that often require high temperatures and pressures. As a result, analyzing the nucleation and growth processes for TMNs is more difficult, and reports on their formation mechanisms are scarce. However, similar to TMOs, reaction mechanisms for TMNs have been identified that follow the classical or nonclassical models.^{41,42}

Most TMN fabrication methods rely on sputtering or solid-state reactions. For instance, various TMNs can be synthesized by solid-state reactions of TMOs at very high temperatures and pressures in a nitrogen or ammonia atmosphere.⁴³⁻⁴⁵ In solution-based synthesis, some studies report the *in situ* formation of intermediate oxide phases during the heating of the reaction mixture, which then undergo nitridation at higher temperatures.^{46,47} The formation of an intermediate sulfide phase prior to nitride formation has also been observed.⁴⁸ Similar to TMOs, some studies report the formation of an amorphous intermediate before the crystalline TMN nanoparticle forms.⁴⁹⁻⁵² These synthesis methods typically require very high temperatures of ≥ 800 °C. The reaction temperature can be drastically reduced by forming highly reactive intermediates. For example, in the case of copper nitride, an *in situ* formed copper azide reacts to form copper nitride at a reaction temperature as low as 200 °C.^{51,53} Additionally, low-temperature solvothermal nitride synthesis can be achieved using primary amines, which decompose under ammonia elimination, acting as the nitrogen source.^{41,54,55} In general, size and morphology control for TMNs, as it is the case for TMOs, can be achieved by adjusting the reaction temperature and time, thereby regulating the nucleation and growth processes, as demonstrated for nickel nitride⁴¹ and copper nitride⁵⁶.

In summary, the reaction mechanisms behind TMO as well as TMN nanoparticle formation vary significantly, but they can generally be explained by classical or nonclassical nucleation and growth models. Understanding these formation pathways is crucial for tailoring their physical and chemical properties, although these mechanisms are often poorly understood or only partially elucidated. *In situ* studies provide valuable experimental insights into the nucleation and growth phenomena of TMOs and TMNs. X-ray-based methods, in particular, have proven to be vital tools, providing valuable information about the electronic and structural evolution at the atomic and nanoscale.^{14,35,57} The next chapter discusses the fundamentals of X-ray-based methods that enable monitoring the formation of nanoparticles in solution.

3 Fundamentals of X-ray-based Methods

The experimental work presented in this thesis relies on several X-ray scattering and absorption techniques. This chapter provides an overview of the underlying X-ray theory and introduces the methods used throughout the thesis. Parts of this chapter are paraphrased from textbooks by Als-Nielsen & McMorrow⁵⁸, Willmott⁵⁹, Mobilio, Boscherini, & Meneghini⁶⁰, Egami & Billinge⁶¹, Billinge & Jensen⁶², Newville⁶³, and Glatzel & Juhin⁶⁴.

3.1 Following nanoparticle formation with X-ray methods

The different X-ray methods discussed in this chapter provide complementary information on the various aspects of nanoparticle nucleation and growth in solution. Figure 3.1 schematically summarizes the X-ray techniques used in this thesis and indicates the stages of nanoparticle formation at which they are applied. Table 3.1 lists the individual methods, their primary structural sensitivity, and references the sections of this chapter in which their theoretical foundations are introduced.

In summary, X-ray absorption near edge structure (XANES) probes the electronic structure of a material and provides information on the formal oxidation state and local coordination environment around the absorbing atom. Extended X-ray absorption fine structure (EXAFS) yields insight into the short-range atomic arrangement surrounding the absorbing atom. Both XANES and EXAFS are element-specific techniques and can be applied to very dilute systems and small structures, making them particularly well suited for studying early stages of nanoparticle formation, including precursor conversion, cluster formation, and nucleation.^{57,65} The pair distribution function (PDF) obtained from total scattering (TS) data resolves the local atomic structure without requiring long-range order and can therefore capture pre-nucleation species as well as nucleation and growth processes, covering a broad range of formation stages.⁶⁶ In contrast, powder X-ray diffraction (PXRD) is sensitive to crystalline order and thus becomes applicable from the onset of crystallization onward, providing information on crystal

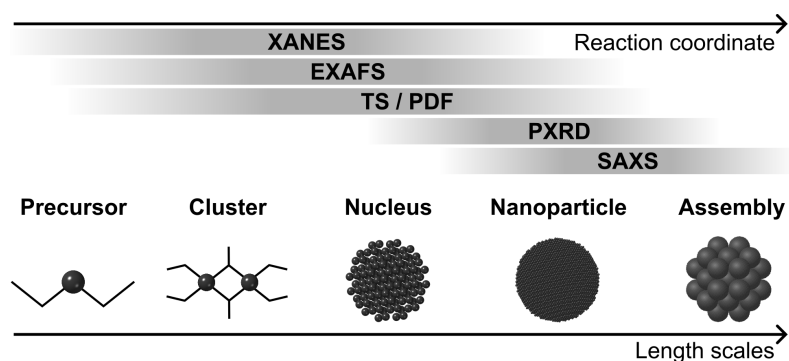


Figure 3.1: Schematic overview of X-ray methods and sensitivity along the nanoparticle formation pathway.

structure as well as crystallite size, shape, and growth. Small-angle X-ray scattering (SAXS) is sensitive to the mesoscale structure, and allows to observe the evolution of particle size, shape, and assembly of particles.⁶⁷

All of these X-ray techniques can be applied *in situ* at high-intensity synchrotron sources, enabling real-time monitoring of nanoparticle formation pathways on relevant time scales.^{14,35} However, they inherently average over the illuminated sample volume and may obscure low-contrast or minority particle populations. In this context, single-particle small-angle X-ray scattering (SP-SAXS) at X-ray free-electron lasers overcomes this limitation by enabling the quantitative structural analysis of heterogeneous nanoparticle ensembles.

Table 3.1: Summary of X-ray methods, their accessibility, structural sensitivity, and reference to corresponding section.

Method	Accessibility	Size / Shape amorphous	Size / Shape crystalline	Structure amorphous	Structure crystalline	Electronic structure	Section
PXRD	Lab. source / Synchrotron	No	Yes	No	Yes	No	3.3.1
TS / PDF	Lab. source / Synchrotron	No	Yes	Yes	Yes	No	3.3.1
SAXS	Lab. source / Synchrotron	Yes	Yes	No	No	No	3.3.2
SP-SAXS	X-ray free electron laser	Yes	Yes	No	No	No	3.3.2
EXAFS	Lab. source / Synchrotron	No	No	Yes	Yes	Yes	3.4.1
XANES	Lab. source / Synchrotron	No	No	Local	Local	Yes	3.4.2

3.2 X-ray generation

This thesis makes use of X-rays generated from different types of sources, namely laboratory tubes, synchrotrons, and X-ray free electron lasers (XFELs), which are briefly summarized in this section. In general, X-rays are produced when high-energy electrons are rapidly decelerated or forced to change direction in electromagnetic fields.

3.2.1 Laboratory X-ray sources

In laboratory X-ray sources (X-ray tubes), electrons are accelerated onto a metal target, where they produce radiation through two mechanisms. First, a broad bremsstrahlung spectrum arises from the deceleration of electrons in the target, where its maximum photon energy is given by the applied acceleration voltage. Superimposed on the bremsstrahlung are sharp characteristic lines. These lines originate when an incident electron ejects an inner-shell electron from a target atom and the resulting vacancy is filled by an electron from a higher shell, emitting fluorescence (Figure 3.10). For experiments requiring a monochromatic beam, the intense $K\alpha$ line is commonly selected, as it is several orders of magnitude stronger than the bremsstrahlung.

3.2.2 Synchrotron radiation

Synchrotrons consist of an evacuated storage ring in which high-energy electrons circulate at relativistic velocities. Synchrotron radiation is produced by bending magnets needed to keep electrons in the storage ring orbit or insertion devices such as undulators. The insertion devices contain arrays of alternating magnets that force electrons to follow oscillating trajectories. In

undulators, the electrons undergo small-amplitude oscillations causing the coherent addition of radiation from each oscillation.

3.2.3 X-ray free electron laser

Synchrotron radiation of undulator insertion devices is highly intense, well collimated, and exhibits a partially monochromatic spectrum. Although the radiation emitted by a single electron along an undulator is coherent, there is no fixed phase relationship between different electrons in the synchrotron electron bunches. As a result, the overall emission is only partially coherent, and synchrotrons do not generate ultrashort pulses. In contrast, XFELs produce nearly fully coherent, ultrashort X-ray pulses through the self-amplified spontaneous emission (SASE) process: emitted X-rays from an electron in the undulators causes the electrons in the electron bunches to modulate into microbunches on the scale of the X-ray wavelength. These microbunches then emit in phase, leading to exponential amplification of the radiation as the electrons move downstream.

The quality of an X-ray beam is described by its brilliance:

$$\text{Brilliance} \left[\frac{\text{photons / seconds}}{(\text{mm}^2 \text{ source area}) (\text{mrad}^2) (0.1\% \text{ BW})} \right]. \quad (3.1)$$

It is defined as the photon flux normalized by the source size, the beam divergence or collimation, and the spectral bandwidth (BW). Laboratory X-ray sources have a relatively low photon flux and very low brilliance owing to its emittance in every direction, which typically restricts the investigation of nanoparticle formation to *ex situ* measurements of quenched reaction aliquots. In contrast, synchrotron sources provide a brilliance that is several orders of magnitude higher, enabling *in situ* observation of nanoparticle formation. X-ray free-electron lasers (XFELs) deliver yet another several orders of magnitude increase in brilliance compared to synchrotrons.

3.3 X-ray scattering

X-ray scattering measures the angular distribution of scattered intensity and thereby provides structural information about the scattering object. At the most fundamental level, the scattering process can be described classically: the electromagnetic field of an incident X-ray wave induces sinusoidal oscillations of the electrons in a material. These accelerated electrons then emit secondary radiation, giving rise to the scattered X-ray wave. A monochromatic X-ray beam can also be described in terms of photons, each carrying an energy $\hbar\omega$ and momentum $\hbar\mathbf{k}$, where \hbar is the reduced Planck constant, ω is the X-ray frequency, and \mathbf{k} the wavevector. A scattering event is described by the wavevector transfer or scattering vector $\mathbf{q} = \mathbf{k} - \mathbf{k}'$, where \mathbf{k} is the incident, and \mathbf{k}' is the scattered X-ray wavevector (Figure 3.2). In elastic scattering, also referred to as Thomson scattering, the energy is preserved and the magnitude of the incident and scattered X-rays is the same $|\mathbf{k}| = |\mathbf{k}'| = 2\pi/\lambda$, where λ is the X-ray wavelength. The magnitude of the scat-

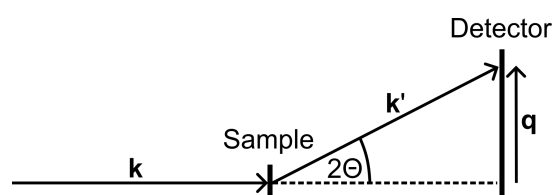


Figure 3.2: Schematic of an X-ray scattering experiment in transmission.

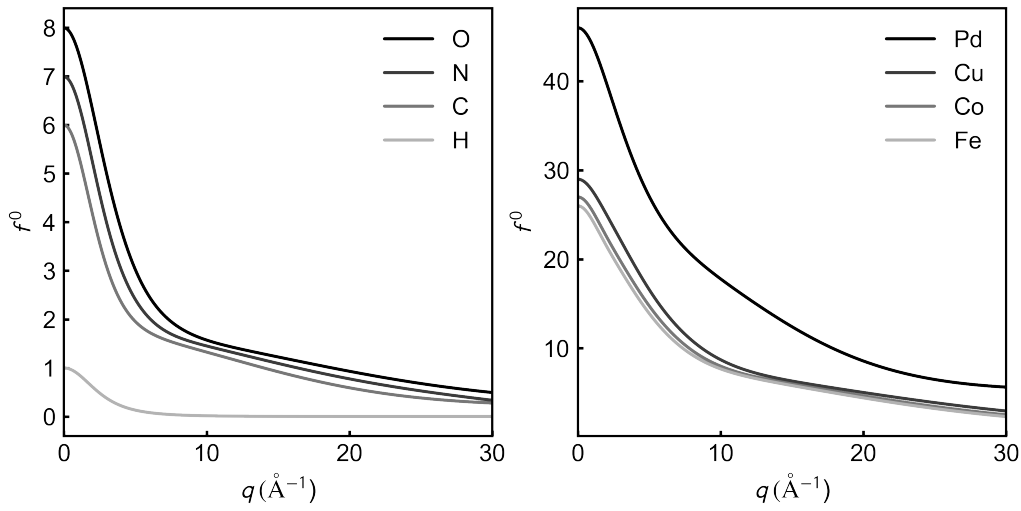


Figure 3.3: Atomic form factors of selected elements. Data is generated from databases.⁶⁸

tering vector is $|\mathbf{q}| = q = \frac{4\pi}{\lambda} \sin \Theta$, where 2Θ is the angle between \mathbf{k} and \mathbf{k}' .

The scattering amplitude of an atom is described by the atomic form factor $f^0(\mathbf{q})$. A volume element $d\mathbf{r}$ at position \mathbf{r} contributes an amount $-r_0 \rho(\mathbf{r})d\mathbf{r}$ to the scattered field, with a phase factor of $e^{i\mathbf{q}\mathbf{r}}$, which accounts for the phase shift of the scattering contributions from different volume elements at \mathbf{r} :

$$\Psi(\mathbf{q}) = -r_0 f^0(\mathbf{q}) = -r_0 \int \rho(\mathbf{r}) e^{i\mathbf{q}\mathbf{r}} d\mathbf{r}, \quad (3.2)$$

where r_0 is the Thomson scattering length, and $\rho(\mathbf{r})$ the electron density. f^0 increases with the atomic number Z . At $\mathbf{q} \rightarrow 0$ all volume elements scatter in phase and $f^0(\mathbf{q} = 0) = Z$. As \mathbf{q} increases, the different volume elements start to scatter out of phase and f^0 eventually approaches 0: $f^0(\mathbf{q} \rightarrow \infty) = 0$, as shown in Figure 3.3.

Electrons in atoms, molecules, or bulk materials are bound and have discrete energy levels. At incident X-ray energies close to the electron binding energies, the scattering amplitude exhibits resonant behavior. This effect is described by energy-dependent, or dispersion corrections to f^0 : The real part f' modifies the scattering amplitude, while the imaginary part $i f''$ accounts for X-ray absorption. The complete atomic scattering length is therefore

$$f(\mathbf{q}, \hbar\omega) = f(\mathbf{q}) + f'(\hbar\omega) + i f''(\hbar\omega). \quad (3.3)$$

The resonant, energy-dependent interactions captured by $f(\mathbf{q}, \hbar\omega)$ give rise to X-ray absorption spectroscopies, which are discussed later in chapter 3.4. For the X-ray scattering techniques, namely wide-angle X-ray scattering and small-angle X-ray scattering, discussed in the following sections, only elastic scattering is considered, as described by f^0 . Furthermore, multiple scattering and thermal motion of the atomic nuclei are neglected, as described by the *kinematic* and *Debye–Waller* approximations.

3.3.1 Wide-angle X-ray scattering

The scattering amplitude of an ensemble of atoms is given by summing over the atomic form factors of all atoms j with the corresponding phase factor:

$$\Psi(\mathbf{q}) = \sum_{\nu}^{\text{all atoms}} f_{\nu}^0(\mathbf{q}) e^{i\mathbf{q}\mathbf{r}_{\nu}} \quad (3.4)$$

Here the overall prefactor $-r_0$ is omitted. The measured intensity in an X-ray scattering experiment, $I(\mathbf{q})$, is the absolute square of the scattering amplitude $\Psi(\mathbf{q})$:

$$I(\mathbf{q}) = |\Psi(\mathbf{q})|^2 = \sum_{\nu} \sum_{\mu} f_{\nu}^0(\mathbf{q}) f_{\mu}^0(\mathbf{q}) e^{i\mathbf{q}\mathbf{r}_{\nu\mu}}, \quad (3.5)$$

where $\mathbf{r}_{\nu\mu} = \mathbf{r}_{\nu} - \mathbf{r}_{\mu}$.

If the sample is isotropic, the scattering is only depended on $q = |\mathbf{q}|$, and the orientational average of the phase factor yields $\sin(qr_{\nu\mu})/qr_{\nu\mu}$. Thus Equation 3.5 becomes

$$I(\mathbf{q}) = \sum_n \sum_{\nu} f_n^0(q) f_{\mu}^0(q) \frac{\sin(qr_{\nu\mu})}{qr_{\nu\mu}}, \quad (3.6)$$

which is known as the Debye scattering equation.

Powder X-ray diffraction

Scattering from crystalline materials, that is materials which exhibit long range periodic order, leads to constructive and destructive interference of the scattered X-rays. Constructive interference produces high-intensity peaks, known as Bragg reflections, which form the basis of structure analysis in X-ray diffraction (XRD). When diffraction is measured on a powder sample, the scattering is isotropic, and the technique is referred to as powder X-ray diffraction (PXRD). In elementary treatments, the condition for constructive interference for scattering on a crystal lattice is described by Bragg's law (Figure 3.4):

$$m * \lambda = 2d_{hkl} \sin \Theta, \quad (3.7)$$

where m is an integer, Θ is the incident (Bragg) angle, and d_{hkl} is the spacing between a set of crystal lattice planes indexed by Miller indices h , k , and l . A crystal is defined by its unit cell and lattice. The set of lattice vectors

$$\mathbf{R}_n = n_1 \mathbf{a}_1 + n_2 \mathbf{a}_2 + n_3 \mathbf{a}_3, \quad (3.8)$$

where \mathbf{a}_i are the translation vectors and n_i are integers, specifies the position of every lattice point. The vectors \mathbf{r}_j define the positions of the atoms within the unit cell. Thus, the position of any atom in a crystal is given by $\mathbf{R}_n + \mathbf{r}_j$. This allows to simplify the scattering amplitude (Equation 3.4) of a crystal, which factorizes into a unit cell term and a lattice sum:

$$\begin{aligned}
\Psi^{\text{crystal}}(\mathbf{q}) &= \sum_{\mathbf{r}_j + \mathbf{R}_n} f_j^0(\mathbf{q}) e^{i(\mathbf{r}_j + \mathbf{R}_n) \cdot \mathbf{q}} \\
&= \sum_j^{\text{unit cell}} f_j^0(\mathbf{q}) e^{i\mathbf{q}\mathbf{r}_j} \sum_n^{\text{lattice sites}} e^{i\mathbf{q}\mathbf{R}_n}
\end{aligned} \tag{3.9}$$

The phase factor in the lattice sum is of order unity unless the scattering vector satisfies

$$\mathbf{q}\mathbf{R}_n = 2\pi * \text{integer}, \tag{3.10}$$

in which case all terms interfere constructively and the lattice sum becomes of order N , the number of unit cells. Since a crystal contains an extremely large number of unit cells, the scattering amplitude vanishes if the scattering condition of Equation 3.10 is not fulfilled. To find a unique solution for the scattering condition, we introduce the reciprocal lattice, defined by reciprocal lattice vectors

$$\mathbf{a}_1^* = 2\pi \frac{\mathbf{a}_2 \times \mathbf{a}_3}{\mathbf{a}_1 \cdot (\mathbf{a}_2 \times \mathbf{a}_3)}, \tag{3.11}$$

$$\mathbf{a}_2^* = 2\pi \frac{\mathbf{a}_3 \times \mathbf{a}_1}{\mathbf{a}_1 \cdot (\mathbf{a}_2 \times \mathbf{a}_3)}, \tag{3.12}$$

$$\mathbf{a}_3^* = 2\pi \frac{\mathbf{a}_1 \times \mathbf{a}_2}{\mathbf{a}_1 \cdot (\mathbf{a}_2 \times \mathbf{a}_3)}. \tag{3.13}$$

Any site in the reciprocal lattice is given by

$$\mathbf{G} = h\mathbf{a}_1^* + k\mathbf{a}_2^* + l\mathbf{a}_3^*, \tag{3.14}$$

where h, k, l are integers, which are the Miller indices as in Equation 3.7. The product of the lattice vector in reciprocal (\mathbf{G}) and in real space (\mathbf{R}_n) is

$$\mathbf{G}\mathbf{R}_n = 2\pi * (hn_1 + kn_2 + ln_3) = 2\pi * \text{integer}, \tag{3.15}$$

which gives the solution to scattering condition in Equation 3.10. This shows that the scattering amplitude is non-vanishing if and only if \mathbf{q} coincides with the reciprocal lattice vector. This is known as the Laue condition:

$$\mathbf{G} = \mathbf{q}. \tag{3.16}$$

The Ewald sphere construction provides a geometric visualization of the Laue condition, as shown in Figure 3.4. The Ewald sphere is drawn with radius $|\mathbf{k}|$ and is centered at the origin of the incident wavevector \mathbf{k} . The origin of the reciprocal lattice, (000), is placed at the tip of \mathbf{k} . If a reciprocal lattice point \mathbf{G} lies on the surface of the Ewald sphere, the Laue condition is satisfied and diffraction occurs. The measured intensity $I(\mathbf{q})$ corresponds to the intersection of the Ewald sphere with the reciprocal lattice, projected onto the detector.

Figure 3.5 compares simulated PXRD patterns of bulk Cu with those of 5 and 2 nm Cu nanopar-

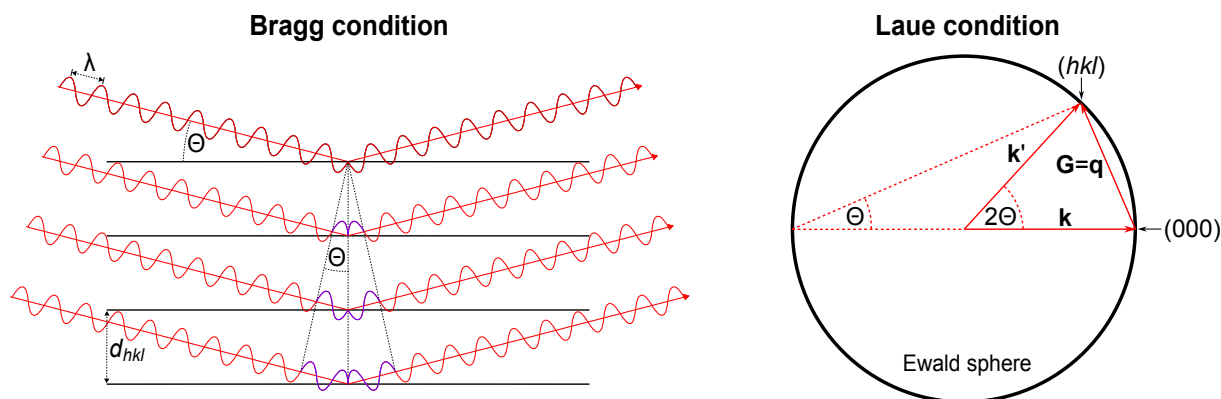


Figure 3.4: Schematic representation of the Bragg and Laue condition. Left: The Bragg condition describes constructive interference when the path-length difference between waves scattered by successive lattice planes equals $m \cdot \lambda / 2$, as highlighted in purple. Right: The Laue condition is illustrated using the Ewald sphere construction. Diffraction occurs when a reciprocal-lattice vector \mathbf{G} lies on the surface of the Ewald sphere and thus coincides with the scattering vector \mathbf{q} .

ticles. As the crystallite size decreases, the Bragg reflections broaden markedly due to the reduced number of coherently scattering lattice planes. This illustrates how nanoscale dimensions or structural imperfections, such as finite domain sizes, defects, or thermal disorder, redistribute intensity from sharp Bragg reflections into a diffuse scattering background. While conventional PXRD primarily captures the long-range periodic component of the structure, the diffuse component contains additional information that becomes increasingly relevant for nanomaterials.

The pair distribution function of total X-ray scattering

In PXRD, only the Bragg intensities are analyzed, which limits the method to crystalline materials exhibiting long-range periodic order. In contrast, total scattering (TS) includes both Bragg and diffuse scattering and therefore provides access to short-range structural information. This makes total scattering particularly valuable for materials that lack long-range periodicity, such as liquids, cluster, amorphous, nanostructured, complex, or disordered materials. From Equations 3.2 and 3.4 it is clear that the scattering amplitude is the Fourier transform of the electron density and thus directly encodes the atomic positions in a material. Although the measured scattering intensity corresponds to the absolute square of the amplitude (Equation 3.5), which removes the absolute phase information and preserves only phase differences between scattering from different atoms, the atomic structure can still be recovered by applying a specialized Fourier transform to the total scattering (TS) data. This yields the pair distribution function (PDF), which is effectively a histogram of interatomic distances and enables real-space structural analysis.

To understand the PDF, we introduce the radial distribution function (RDF), which is closely related to the PDF. It is defined as

$$R(r) = 4\pi r^2 \rho(r), \quad (3.17)$$

where, $\rho(r)$ is the atomic number density, and $4\pi r^2$ is the spherical shell at a radius r to an origin. Thus, the RDF measures the probability of finding an atom at distance r from the origin. Alternatively, the RDF can be written explicitly as a sum over all interatomic separations,

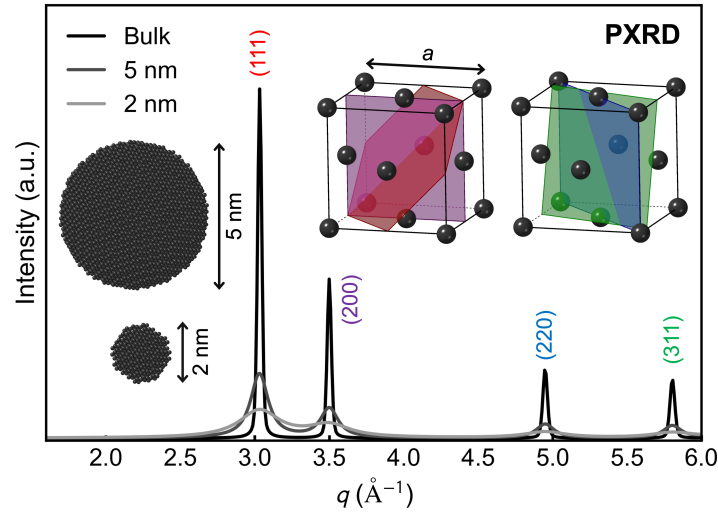


Figure 3.5: PXRD simulations of bulk Cu and Cu nanoparticles. Scattering from nanoparticles results in a broadening of the Bragg reflections (hkl). Cu exhibits the face-centered cubic (fcc) structure. Its unit cell contains atoms at fractional coordinates $(0,0,0)$, $(0, \frac{a}{2}, \frac{a}{2})$, $(\frac{a}{2}, 0, \frac{a}{2})$, and $(\frac{a}{2}, \frac{a}{2}, 0)$, where a is the cubic lattice constant. Inserting these positions in the unit cell term of the scattering amplitude (Equation 3.9) gives $A^{\text{crystal}}(\mathbf{q}) = 1 + e^{i\pi(h+k)} + e^{i\pi(h+l)} + e^{i\pi(k+l)}$. This expression vanishes unless h, k, l are either all even or all odd. The first "allowed" reflections are indexed, and the associated lattice planes are shown in the unit cell representations. The patterns are simulated using GSASII.⁶⁹

weighted by the atomic form factors:

$$R(r) = \frac{1}{N} \sum_{\nu} \sum_{\mu \neq \nu} \frac{f_{\nu}(q) f_{\mu}(q)}{\langle f^2 \rangle^2} \delta(r - r_{\nu\mu}), \quad (3.18)$$

where $r_{\nu\mu} = |\mathbf{r}_{\nu} - \mathbf{r}_{\mu}|$ is the distance between the ν^{th} and μ^{th} atom, $\langle \dots \rangle$ denotes the compositional average, and δ is the Dirac function.

Specifically, we analyze TS data by means of the reduced PDF, $G(r)$, which is related to the RDF through

$$G(r) = \frac{R(r)}{r} - 4\pi \rho(r) \gamma(r), \quad (3.19)$$

where $\gamma(r)$ is the characteristic shape function of the scattering object. Although the RDF is more intuitively to interpret, the reduced PDF, $G(r)$ (hereafter referred to simply as the PDF), is commonly used for several reasons. It does not require assumptions about particle size and shape contained in $\gamma(r)$, provides a direct measure of structural coherence, exhibits uncertainties constant to r , and oscillates around 0, making it more reliable for modeling and visualization. Most importantly, the PDF is obtained directly from the measured intensity. It is calculated by Fourier transforming of the total scattering structure function $S(q)$, defined as

$$S(q) = \frac{I(q) - \langle f(q)^2 \rangle + \langle f(q) \rangle^2}{\langle f(q) \rangle^2}. \quad (3.20)$$

In practice, the measured intensity needs to be corrected for incoherent contributions such as inelastic (Compton) scattering, multiple scattering or fluorescence. In Equation 3.20, $I(q)$

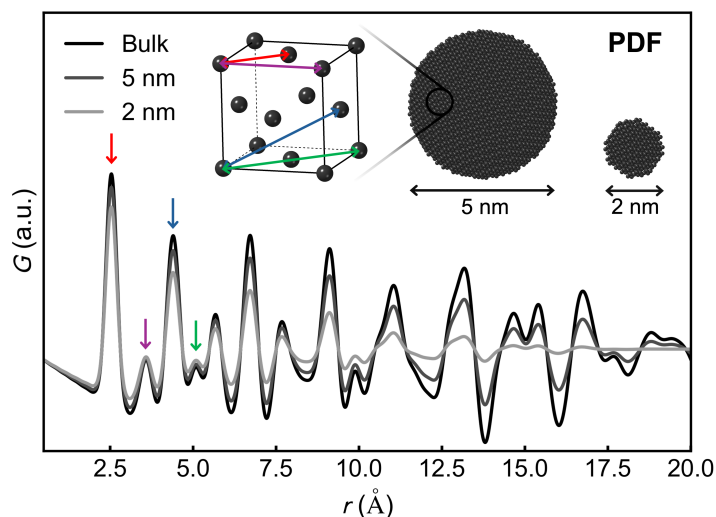


Figure 3.6: PDF simulations of bulk Cu and Cu nanoparticles. The first four interatomic distances in the fcc Cu unit cell are indicated and correspond to the highlighted peaks in the simulated PDFs. Compared to bulk Cu, the finite size of 5 and 2 nm nanoparticles leads to a progressive damping of the PDF peak amplitudes at larger r , reflecting the limited extent of structural coherence. The patterns are simulated using DiffPy-CMI.⁷¹

represents the coherent scattering fraction, which can be readily corrected using established *ad hoc* approaches.⁷⁰ The term $\langle f(q)^2 \rangle + \langle f(q) \rangle^2$ is known as the monotonic Laue scattering. It arises from imperfect cancellation of intensity under destructive interference when scatterers of different strengths are present, and it vanishes for single-species systems. Including this term ensures the correct normalization of the total scattering structure function so that the average $\langle S(q) \rangle$ approaches unity.

The PDF, $G(r)$, is calculated by the sine Fourier transform over the experimentally accessible q -values. Figure 3.6 shows simulated PDF patterns of bulk Cu and Cu nanoparticles.

$$G(r) = \frac{2}{\pi} \int_{q_{\min}}^{q_{\max}} q(S(q) - 1) \sin(qr) dq. \quad (3.21)$$

Ideally, the PDF is calculated over a very large q -range which improves the real-space resolution. The limited q -range introduces Fourier ripples with a period of $2\pi/q_{\max}$, which may render small structural features indistinguishable. For this reason, TS data is typically acquired at very high X-ray energies and with short sample-to-detector distances since $q \propto \sin \Theta / \lambda$. In practice, TS measurements commonly reach q_{\max} -values of $\sim 15\text{-}30 \text{ \AA}^{-1}$, whereas PXRD data usually extends to $\sim 6\text{-}12 \text{ \AA}^{-1}$.

The second term in Equation 3.19 originates from scattering at small q -values, corresponding to structural correlations on length scales much larger than interatomic distances.⁷² It therefore contains information about particle size and morphology, as discussed in the next section.

3.3.2 Small-angle X-ray scattering

To understand scattering at small q -values, we rearrange Equation 3.5 by assuming for simplicity monotonic and isotropic scattering:

$$I(q) = f^2(q) \sum_{\nu} \sum_{\mu} e^{iqr_{\nu\mu}} = Nf^2(q) + f^2(q) \sum_{\nu} \sum_{\mu \neq \nu} e^{iqr_{\nu\mu}}, \quad (3.22)$$

where N is the total number of atoms. We now replace the sum over $\mu \neq \nu$ by an integral of the atomic number density ρ_{ν} over the volume of the atomic arrangement V . In addition, as X-ray scattering ultimately arises from deviations in electron density from its average, we add and subtract the average density ρ_{at} . The expression for the scattered intensity then becomes

$$I(q) = \underbrace{Nf^2(q) + f^2(q) \sum_{\nu} \int_V [\rho_{\nu}(r_{\nu\mu}) - \rho_{\text{at}}] e^{iqr_{\nu\mu}} dV_{\mu}}_{I^{\text{SRO}}(q)} + \underbrace{f^2(q) \rho_{\text{at}} \sum_{\nu} \int_V e^{iqr_{\nu\mu}} dV_{\mu}}_{I^{\text{SAXS}}(q)}. \quad (3.23)$$

where $\rho_{\nu}(r_{\nu\mu})dV_{\mu}$ is the number of atoms or molecules in the volume element dV_{μ} at a distance $r_{\nu\mu}$ from the reference atom at r_{ν} . For non-crystalline materials, $\rho_{\nu}(r_{\nu\mu}) \rightarrow \rho_{\text{at}}$ beyond a few interatomic spacings, hence the first term in Equation 3.23 is sensitive to short range order (SRO). In contrast, the limit $q \rightarrow 0$ corresponds to long real-space distances, and since $q \propto \sin \Theta$, this limit occurs at small scattering angles. This is the small-angle X-ray scattering (SAXS) regime, which provides information about the size and morphology rather than atomic-level positions.

As in Equation 3.22, the remaining sum over ν can be replaced by an integral, giving

$$I^{\text{SAXS}}(q) = f^2(q) \int_V \rho_{\text{at}} e^{iqr_{\nu}} dV_{\nu} f^2(q) \int_V \rho_{\text{at}} e^{-iqr_{\mu}} dV_{\mu}, \quad (3.24)$$

which becomes

$$I^{\text{SAXS}}(q) = \left| \int_V \rho_{\text{sl}}(r) e^{iqr} dV_{\nu} \right|^2. \quad (3.25)$$

where we have introduced $\rho_{\text{sl}} = f\rho_{\text{at}}$ which when multiplied by r_0 gives the scattering length density.

When the scattering length density of the particle $\rho_{\text{sl,p}}$ and the solvent $\rho_{\text{sl,0}}$ is uniform, the scattering from a single particle is

$$I^{\text{SAXS}}(q) = (\rho_{\text{sl,p}} - \rho_{\text{sl,0}})^2 \left| \int_V e^{iqr} dV_{\nu} \right|^2. \quad (3.26)$$

By introducing the single particle form factor

$$F(q) = \frac{1}{V_P} \int_{V_P} e^{iqr} dV_P. \quad (3.27)$$

Equation 3.26 become

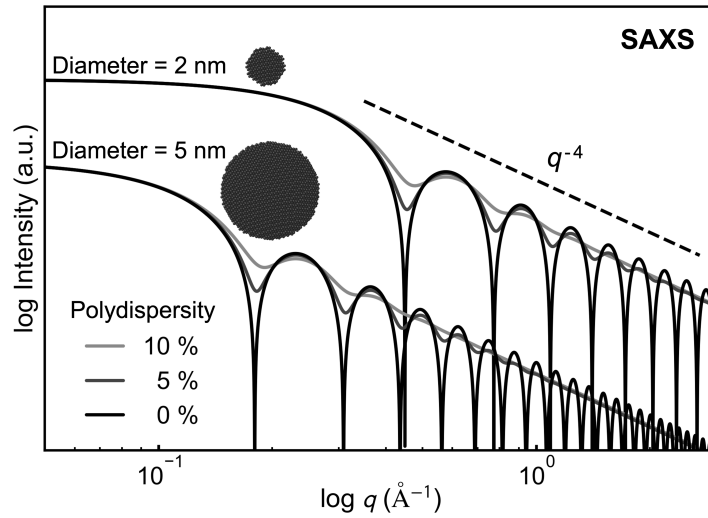


Figure 3.7: SAXS simulations of 2 and 5 nm spherical nanoparticles. The polydispersity indicates the standard deviation of a Gaussian size distribution expressed as a percentage of the mean diameter. The patterns are calculated based on Equation 3.28 and 3.29.

$$I^{\text{SAXS}}(q) = \Delta\rho^2 V_P^2 |F(q)|^2. \quad (3.28)$$

The form factor depends on the size and shape of the particle through the integral over its volume V_P , and can only be analytically evaluated in a few cases. For example, the form factor of a sphere with radius R is

$$\begin{aligned} F(q) &= \frac{1}{V_p} \int_0^R \int_0^{2\pi} \int_0^\pi e^{iqr \cos \theta} r^2 \sin \theta \, d\theta d\phi dr \\ &= \frac{1}{V_p} \int_0^R 4\pi \frac{\sin(qr)}{qr} r^2 dr = 3 \left[\frac{\sin(qR) - qR \cos(qR)}{Q^3 R^3} \right]. \end{aligned} \quad (3.29)$$

Figure 3.7 shows simulated SAXS patterns of monodisperse and polydisperse spherical nanoparticles. The spherical form factor exhibits oscillations, from which the particle size can be determined. With increasing polydispersity, these oscillations become progressively smeared out, and the scattering approaches the characteristic q^{-4} decay.

Single-particle small-angle X-ray scattering

In single-particle small-angle X-ray scattering (SP-SAXS) millions of scattering snapshots of individual particles, delivered in a dilute aerosol, are acquired and averaged into classes. Each class yields the SAXS pattern of a distinct particle population. Hence the classification disentangles the scattering contributions from different particle contributions enabling the precise, quantitative structural analysis of heterogeneous particle populations. Conceptually, SP-SAXS is closely related to established techniques such as single-particle imaging (SPI)⁷³, coherent diffractive imaging (CDI)⁷⁴, and serial femtosecond crystallography (SFX)⁷⁵. Technical details are given in the corresponding chapter 6.3.

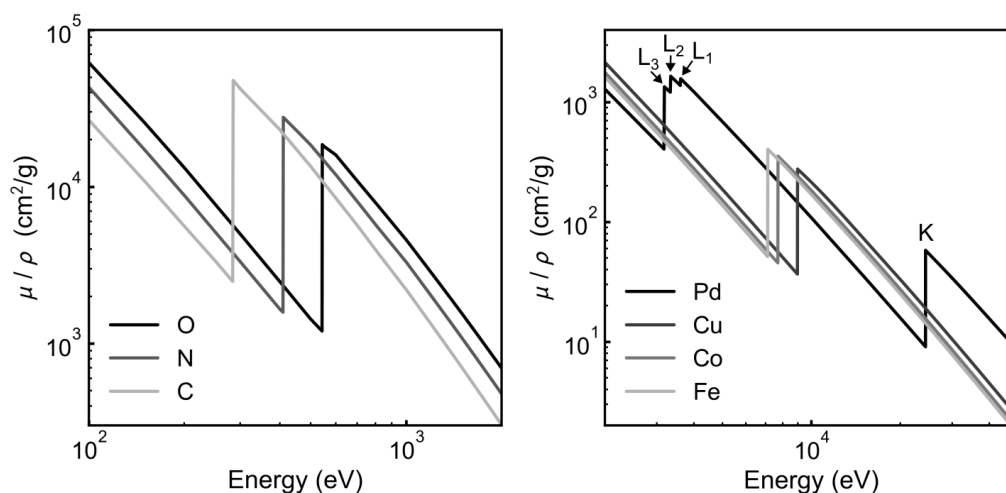


Figure 3.8: Absorption coefficient of selected elements. The absorption coefficient μ is normalized by the atom's density ρ . For Pd, the absorption edges are labeled. The data are taken from databases.^{76,77}

3.4 X-ray absorption

X-ray absorption spectroscopy (XAS) measures how the X-ray absorption of a system changes as a function of the incident photon energy. The underlying process is the photoelectric effect, in which an X-ray photon expels a core-level electron creating a core-hole in the absorbing atom. This hole is then filled by a higher level electron, either under the emission of a fluorescence photon or Auger electron. Quantitatively, the absorption is described by the absorption coefficient μ via Lambert–Beer's law:

$$I = I_0 \cdot e^{-\mu d}, \quad (3.30)$$

where I and I_0 are the transmitted and incident intensities, and d is the thickness of the sample.

The absorption coefficient μ is proportional to the imaginary part of the atomic form factor f'' (Equation 3.3) and varies approximately with the inverse third power of the photon energy. This trend is interrupted by sharp, step-like increases in absorption that occur when the photon energy reaches the binding energy of a core electron, as shown in Figure 3.8. These discontinuities are known as absorption edges. The edges are labeled with capital letters (K, L, M, ...) according to the principal quantum number ($n = 1, 2, 3, \dots$) of the initial electronic state. Except of the K-edges, all edges exhibit energetically closely lying sub-edges associated with nondegenerate quantum states which are indexed (1, 2, 3, ...) to denote different possibilities of coupling the nonzero orbital- and spin- angular-momentum components of the electronic states. Thus, the K-edge corresponds to excitation of an 1s electron, while the L₁, L₂, and L₃ edges arise from excitation of the 2s, 2p_{1/2}, and 2p_{3/2} electrons, respectively.

The absorption edge is divided into two regions, each governed by different electronic transitions (Figure 3.9). In the region around the absorption edge, one obtains the X-ray absorption near edge structure (XANES) which arises mainly from excitations into unoccupied bound states. XANES typically extends from few eV below the edge jump to a few tens of eV above it. At higher photon energies, the absorption edge often exhibits a series of oscillations. This extended X-ray absorption fine structure (EXAFS) is due to excitations into the continuum.

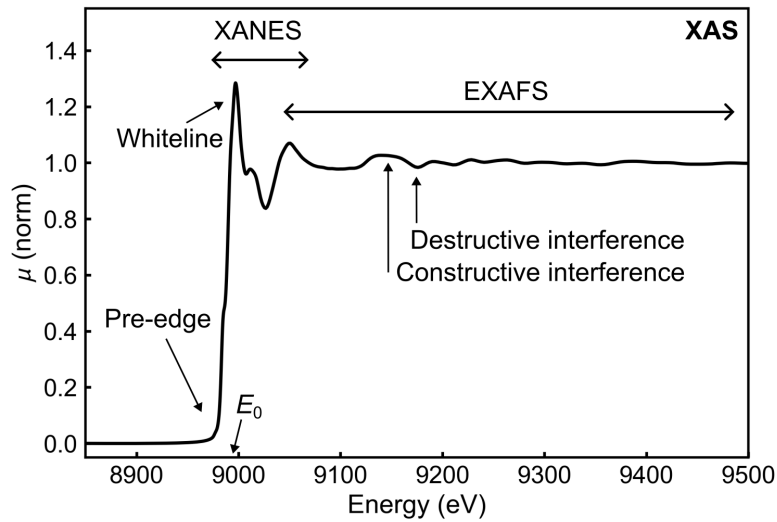


Figure 3.9: X-ray absorption spectrum of copper(II) oxide. The edge position E_0 is defined by the maximum slope of the rising edge. The region around the edge corresponds to the XANES regime and arises predominantly from excitations into unoccupied bound states. The intense feature in the XANES region is referred to as the whiteline, a term originating from detection on photographic strips in early experiments. The spectral region below the edge is known as the pre-edge. At higher photon energies, the EXAFS region is observed, characterized by oscillations resulting from interference of the photoelectron excited into the continuum. Data is taken from databases.⁷⁸

3.4.1 Extended X-ray absorption fine structure

The dominant process giving rise to EXAFS is the outgoing photoelectron, which can be described as a spherical wave emitted from the absorbing atom and scattered by the neighboring atoms. The EXAFS oscillations arise from the interference between the outgoing and backscattered photoelectron waves. Depending on the photoelectron energy, this interference is constructive or destructive, leading to oscillations in the absorption coefficient μ as a function of incident photon energy. In the EXAFS region, μ is composed of a smooth background and an oscillatory part. The normalized oscillatory path is defined as:

$$\chi(E) = \frac{\mu(E) - \mu_0(E)}{\Delta\mu_0}, \quad (3.31)$$

where μ_0 is a smooth background function representing the absorption of an isolated atom, and $\Delta\mu_0$ is the normalization factor approximated by the magnitude of the jump in absorption at the edge position E_0 .

The frequencies of the normalized EXAFS oscillations are related to the distances between the absorbing atom and its neighbors. The amplitudes of the normalized EXAFS oscillations contain information on the number and kind of neighbor atoms.

The EXAFS signal is analyzed using the EXAFS equation:

$$\chi(k) = \sum_j \frac{N_j f_j(k) e^{-2k^2\sigma_j^2}}{kR_j^2} \sin[2kR_j + \delta_j(k)], \quad (3.32)$$

where the energy E is converted to the photoelectron wavevector k .

$$k = \sqrt{\frac{2m(E - E_0)}{\hbar^2}} \quad (3.33)$$

The EXAFS equation sums over scattering contributions of the neighboring atoms j . N is the number of neighboring atoms at distance R , and σ^2 is the disorder in the neighbor distance. N , R , and σ^2 can be determined knowing the scattering amplitude $f(k)$ and the phase-shift $\delta(k)$. Furthermore, since these scattering factors depend on the atomic number, EXAFS is also sensitive to the atomic species of the neighboring atom.

The EXAFS signal can be modeled based on a structural model to determine the local atomic environment around the absorbing atom. This can be done either directly in k -space or real space by modeling the Fourier transform of $\chi(k)$.

3.4.2 X-ray absorption near edge structure

XANES is strongly sensitive to the formal oxidation state and coordination chemistry of the absorbing atom. In contrast to EXAFS, there is not a simple analytical expression that describes the XANES signal. Nevertheless, in a fingerprint approach phases can be identified by comparing a measured spectrum to reference spectra. More qualitatively, XANES features can be interpreted in terms of electronic transitions associated with photoexcitation upon X-ray absorption. The transition probability P_{gn} for an electron to be excited from the initial ground state $|g\rangle$ to an excited state $|n\rangle$ is evaluated by transition matrix elements, called Fermi's golden rule.

$$P_{gn} \propto |\langle g|\hat{O}|n\rangle|^2 \quad (3.34)$$

where \hat{O} is the transition operator in the Dirac formalism. XANES spectra can be interpreted within a theoretical framework by modeling the absorption intensity using Fermi's golden rule. Fermi's golden rule gives rise to electric dipole and quadrupole transitions that significantly contribute to the XANES, whereas the dipole transition dominates the XANES signal. Whether or not a transition has zero probability can often be evaluated using simple symmetry considerations of the electronic states. These considerations give selection rules to determine "allowed" and "forbidden" transitions. The symmetry of an orbital is described by its parity $(-1)^l$, where l is the angular quantum number. A positive parity means the orbital is inversion symmetric. Hence, s- and d-orbitals have a positive parity, while p- and f-orbitals have a negative parity and are antisymmetric. Dipole transition operator itself is antisymmetric which dictates that the initial and excited states must have opposite symmetries for the transition being allowed. For example, an sp^3 -orbital is incompatible with an inversion-symmetric state. In general, the selection rule of a electric dipole transition states that the difference of the angular quantum number of the initial and excited state is one ($\Delta l = \pm 1$), while an electric quadrupole transition is allowed for $\Delta l = 0, \pm 2$. Hence, in the case of a excitation of a 1s electron (K-edge), only orbitals with p-orbital angular momentum can be reached from electric dipole transitions, while d-orbitals are reached for electric quadrupole transitions.

This framework provides the basis for interpreting XANES spectra. For example, the K-edge in 3d transition metal ions is a few tens of eV above the Fermi level and arises from intense electric dipole $1s \rightarrow p$ transitions. The excited photoelectron has low kinetic energy and thus a large mean free path, which results in strong multiple scattering from neighboring atoms

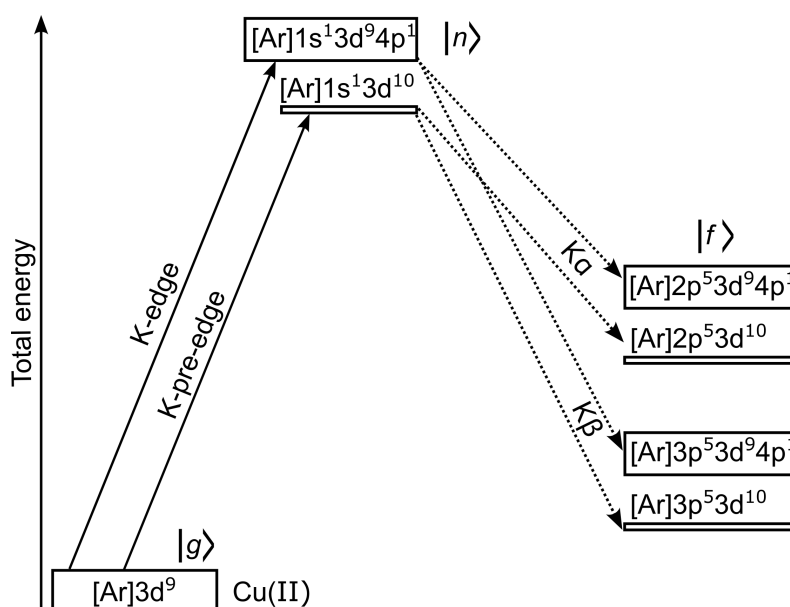


Figure 3.10: Total energy diagram illustrating electronic transitions of Cu(II). Solid arrows indicate absorption transitions from the ground state $|g\rangle$ to excited states $|n\rangle$. Dotted arrows indicate the subsequent fluorescence decay from the excited states to the final states $|f\rangle$.

at high coordination shells. Hence, the XANES signal is sensitive to both the electronic and atomic structure, making the interpretation highly challenging.⁶⁴ The position of the K-edge is primarily governed by the ionization potential and thus reflects the effective charge density at the absorbing atom. An increased charge density typically leads to a lower ionization potential and a corresponding shift of the absorption edge to lower photon energies. In general, this sensitivity is complex and the charge density is influenced from kind, distance, and number of ligands. Weak spectral features are often observed below the main absorption edge. For 3d transition metals, these so-called pre-edge features originate predominantly from quadrupole-allowed $1s \rightarrow 3d$ transitions, which accounts for their low intensity. Additionally, pre-edge features can arise from nonlocal electric dipole transitions from orbital mixing with p-orbitals from the ligand atoms, or from on-site electric dipole transitions due to local p-d mixing.

Figure 3.10 illustrates the electronic transitions of Cu(II). The Cu K-edge absorption is dominated by electric-dipole-allowed $1s \rightarrow 4p$ transitions, which give rise to the intense edge feature. A weaker pre-edge feature originates from the quadrupole-allowed $1s \rightarrow 3d$ transition. In contrast, Cu(0) and Cu(I) do not exhibit pronounced pre-edge features at the K-edge, as their 3d orbitals are fully occupied. Following core-level excitation, the system can relax radiatively when the 1s core-hole is filled by a 2p or 3p electron, resulting in the emission of a $K\alpha$ or $K\beta$ fluorescence photon, respectively.

3.4.3 High energy resolution fluorescence detected X-ray absorption spectroscopy

The extremely short lifetime of a core-hole leads to a Lorentzian spectral broadening as dictated by Heisenberg's uncertainty principle. As a consequence, the energy resolution of conventional XAS is fundamentally limited by core-hole lifetime broadening. This limitation can be overcome by probing the absorption process via a selected fluorescence emission line. The measured fluorescence intensity provides a good approximation of the absorption

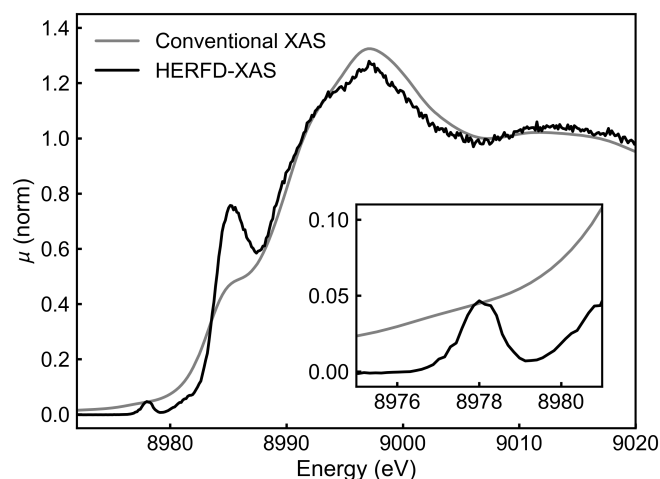


Figure 3.11: Conventional compared to HERFD X-ray absorption spectra of copper(II) oxide. The HERFD spectrum exhibits a significantly improved energy resolution which enables to properly resolve pre-edge, rising edge, and white-line features. The inset shows a zoom on the pre-edge. Data is taken from databases.^{78,79}

coefficient, while yielding a significantly enhanced energy resolution. This improvement arises because the secondary hole created during the radiative relaxation process ($|n\rangle \rightarrow |f\rangle$ in Figure 3.10) typically has a much longer lifetime than the initial core hole. This approach is known as high-energy resolution fluorescence detected X-ray absorption spectroscopy (HERFD-XAS). Figure 3.11 compares conventional and HERFD-XANES spectra.

4 Modular *In Situ* Reactor for X-ray Scattering, Spectroscopy, and ATR-IR Studies of Solvothermal Nanoparticle Synthesis

The content of this chapter was published in Journal of Synchrotron Radiation 33, 1, (2026) by Sani Y. Harouna-Mayer, Melike Gumus Akcaalan, Jagadesh Kopula Kesavan, Tjark R. L. Groene, Lars Klemeyer, Sarah-Alexandra Hussak, Lukas Grote, Davide Derelli, Francesco Caddeo, Cecilia Zito, Paul Stütze, Dorota Speer, Ann-Christin Dippel, Blanka Detlefs, Yannik Appiarius, Axel Jacobi von Wangelin, Dorota Koziej.

My contribution to this work comprises: analysis of PXRD and TS, X-ray transmission calculations, and review of reactors for in situ SAXS, WAXS, and XAS measurements.

4.1 Abstract

Understanding the chemical processes that occur during the solvothermal synthesis of functional nanomaterials is essential for their rational design and optimization for specific applications. However, these processes remain poorly understood, primarily due to the limitations of conventional *ex situ* characterization techniques and the technical challenges associated with *in situ* studies, particularly the design and implementation of suitable reactors. Here, we present a versatile reactor suitable for *in situ* X-ray scattering, X-ray spectroscopy and infrared spectroscopy studies performed during solvothermal synthesis under autoclave-like, inert conditions. The reactor enables precise control of the temperature between $-20\text{ }^{\circ}\text{C}$ and $200\text{ }^{\circ}\text{C}$, pressures up to 8 bar, magnetic stirring, and injection of gas or liquids. The reactor's capabilities are demonstrated by comprehensively studying the solvothermal synthesis of magnetite nanoparticles from iron acetylacetonate in benzyl alcohol through *in situ* X-ray scattering and spectroscopy, and ATR-IR spectroscopy.

4.2 Introduction

Solvothermal synthesis is a versatile, fast, energy-efficient and scalable method for producing a wide range of materials in which chemical reactions between precursor(s) and solvent take place in a closed reaction vessel at elevated temperatures and pressures. Although it is widely used for synthesizing materials or composites, *e.g.* for electronic devices and energy conversion, the underlying reaction mechanisms that govern key properties such as crystallinity, particle size and morphology are often poorly understood.⁸⁰⁻⁸² In conventional laboratory experiments, the understanding of these mechanisms is typically limited to *ex situ*

analysis of the final products or quenching the reaction at different reaction times. However, a deeper insight into these processes is crucial for the rational design of materials with tailor-made properties.^{83–85}

For this reason, solvothermal synthesis can be studied *in situ*, by using high flux X-ray radiation from synchrotron light sources, allowing real-time monitoring of the reaction and providing a comprehensive insight into the chemical steps involved.^{14,86} This approach requires specialized reaction vessels equipped with heating capabilities and additional features tailored to the specific reaction and technique being used. X-ray methods are particularly effective for *in situ* investigation of solvothermal synthesis as they provide valuable information about nucleation, growth and formation of intermediate states. For example, X-ray absorption spectroscopies (XAS) probe the electronic structure and the chemical environment of the absorbing atom.⁵⁷ Wide-angle X-ray scattering (WAXS) methods, such as powder X-ray diffraction (PXRD) and total scattering (TS), provide insights into the atomic structure while small-angle X-ray scattering (SAXS) enables to study particle size, polydispersity, morphology, and assembly.^{87,88} A single technique can mostly not capture the full complexity of the reaction mechanisms across multiple length and time scales. It is rather the simultaneous application of different techniques in a multimodal or complementary approach that enables a more comprehensive understanding - *e.g.* by linking electronic, atomic, and morphological evolution throughout the reaction.^{89–91} However, each X-ray technique imposes distinct and often conflicting demands on the reactor design and specifications.

In order to meet these demands, several key challenges must be addressed when designing a tailor-made reactor for *in situ* X-ray studies:

(i) Window material. The material must be X-ray transparent at the required energies, chemically inert, and stable at elevated temperatures and pressures. It should also exhibit a low or easily subtractable background signal. Various materials are used depending on the technique and required reaction conditions:

- Polyimide is flexible, highly X-ray transparent and chemically inert, making it a common choice for both XAS and scattering experiments conducted under moderate conditions.^{92–94}
- Polyether ether ketone (PEEK) offers excellent X-ray transparency along with high chemical and mechanical stability and is thus suitable for use at elevated temperatures and pressures. While it performs well in XAS setups, its semicrystalline structure produces strong background signals, making it less suitable for scattering experiments.^{93,95,96}
- Fused silica is also chemically inert and can withstand high temperatures and pressures, but it offers somewhat lower mechanical stability and a slightly reduced X-ray transparency compared to PEEK. Though, it has a low background signal for accurate background subtraction in scattering data. It is the commonly preferred window material for PXRD and TS experiments.^{67,97,98}
- Sapphire is suitable for the extreme temperatures and pressures of PXRD experiments. Its single crystal reflections can be avoided by masking the detector or angular adjustments. However, sapphire is not favorable for TS experiments due to its strong diffuse scattering signal.^{67,99,100}
- Beryllium is used in some experimental setups for its exceptional X-ray transparency and mechanical stability. However, its high toxicity necessitates strict safety protocols.^{95,101,102}

(ii) Geometry of the reactor and (iii) precise control over reaction parameters such as temperature, pressure, and (possibly) injection of reagents or gases to the chemical reactions

inside the reactor. It is highly desirable to mimic the laboratory setups of preparative-scale chemical reactions, as variations in temperature or pressure profiles and sample volume can significantly influence the reaction mechanism and outcome. At the same time, the reactor must meet the space constraints of the beamline to allow *in situ* analytical experiments. Most *in situ* setups for X-ray scattering use capillaries, where small sample volumes are heated with hot air blowers or resistive heaters.^{67,99,100} This approach requires little space and allows rapid heating and good control over the reaction parameters. It can also be extended with gas or liquid injection devices. However, such setup usually does not allow stirring of the reaction solution and the small volumes are usually not sufficient for post-synthesis analysis. Other setups use large reaction reservoirs from which small aliquots of the solution are circulated through a capillary for measurement, thereby mitigating beam damage.^{97,103} Bulky setups adapting commercial microwave reactors for the technical requirements of *in situ* measurements have also been reported.^{104,105} (*iv*) Safety of the beamline environment, especially when working at extreme conditions or with hazardous or toxic materials such as Be.¹⁰²

Table 4.1 summarizes selected literature reports on reactors enabling *in situ* analysis by XAS, WAXS, and SAXS.

In an effort to address the aforementioned diverse requirements of a modular and versatile reactor, we developed a tailor-made setup for complementary experiments at synchrotron facilities. The reactor is compatible with a wide range of X-ray techniques, including XAS, PXRD, TS, and SAXS, and supports solvothermal synthesis under inert, autoclave-like conditions. By exchanging the reactor inlet, the setup can be tailored for XAS experiments using a PEEK inlet or for scattering using glass inlets with various wall thicknesses - balancing background contribution and pressure resistance up to 8 bar. The system allows magnetic stirring and precise control of the heating ramp rate and reaction temperatures up to 200 °C or cooling to -20 °C via Peltier elements. Additional inlet modifications also support gas or liquid injection and integration of a fiber optic attenuated total reflection (ATR) probe for simultaneous ATR infrared spectroscopy (ATR-IR) measurements. The reactor achieves sub-minute time resolution for *in situ* XAS and ATR-IR, and one-second resolution for X-ray scattering experiments. This reactor has already been employed in several studies investigating the solvothermal synthesis of alloy⁹⁸, metal oxide⁹¹, metal sulfide^{96,106}, and metal nitride¹⁶ nanoparticles. In these studies, we leveraged the reactor's modular design and versatility across different X-ray techniques - exploiting, for instance, its low-background configuration for precise tracking of precursor conversion⁹⁸, its autoclave-like properties for spatially resolved synthesis at liquid-liquid interfaces at elevated pressure and temperature¹⁰⁶, and its air-tight conditions for sensitive materials¹⁶. Table S4.1 summarizes all the previous reactor designs. Here, we further demonstrate the reactor's versatility by investigating as model system the partial reduction reaction of iron(III) acetylacetonate to Fe₃O₄ magnetite nanoparticles in benzyl alcohol at 180 °C¹⁰⁷, using *in situ* PXRD, TS, XAS, and ATR-IR. Moreover, we also added cooling and injection capability to the cell, broadening its application range.

Table 4.1: Overview of reactors suitable for *in situ* XAS, WAXS and SAXS measurements during solvothermal synthesis. The sample volume is categorized as small (*e.g.* capillary-based setups), medium (*e.g.* reactors with inlets), or large (*e.g.* flow reactors with external reservoirs). The classification reflects the typical sample quantity accessible for reaction monitoring or postmortem analysis. The “+” in the temperature column indicates the temperature employed in the respective study, rather than the maximum operational temperature, which was not specified in the respective report.

Ref.	Methods	T _{max}	p _{max}	Window material	Wall thickness (mm)	Sample volume	Stirring?
108	WAXS	230	28	Steel	2.0	Medium	Yes
95	XAS	200	250	PEEK, Be	1.0, 0.5	Medium	Yes
101	XAS	600	14	Be	0.75	Small	No
99	WAXS, SAXS	1000	138	Al ₂ O ₃ , SiO ₂ , Polyimide	–	Small	No
109	XAS	400	3.5	Polyimide	0.3–1.2	–	No
		300	40	SiO ₂			
100	WAXS, SAXS	450	400	Al ₂ O ₃ SiO ₂	0.06–0.8	Small	No
110	WAXS	450+	20	SiO ₂	0.01	Small	No
111	WAXS	225	207	Be	–	Medium	No
112	WAXS, SAXS, XAS	48	–	Glassy carbon	–	–	No
93	WAXS, XAS	180+	–	PEEK	0.5	Medium	No
103	SAXS	–	–	SiO ₂	0.01	Large	Yes
113	WAXS, XAS	180	–	SiO ₂ , Al	1.0–1.5, 0.1	Medium	No
114	WAXS, XAS, IR	350	–	PTFE	–	Large	Yes
115	WAXS	1000	35	SiO ₂	>0.1	Small	No
116	WAXS	700+	–	SiO ₂	–	–	No
97	WAXS	700+	–	SiO ₂	0.05	Large	Yes
117	WAXS, SAXS, XAS	327	40	SiO ₂	0.2	Small	No
118	WAXS	500+	–	SiO ₂	0.02	Small	No
119	XAS	1200	2000	Glassy carbon, Be	–	Large	No
This work	WAXS, SAXS, XAS, ATR-IR	200	8	SiO ₂ , PEEK	0.2–0.5	Medium	Yes

4.3 Reactor design

The reactor setup features a compact and user-friendly design optimized for safe operation. The assembled cross-sectional illustration of the reactor, including all dimensions, is shown in Figure 4.1(a). For a comprehensive understanding of the system’s operating principle, it is beneficial to focus on the main elements individually. The detailed representation of the assembly is given in Figure 4.1(b). The reactor can be divided into three main components, *i.e.* the housing, the inlet, and the insulators.

The back and front center pieces were carved out of the aluminum housing in a conical shape to achieve an opening angle of 45° enabling data acquisition in transmission geometry – e.g., for high- q total scattering (TS) data – or in reflection geometry, e.g., high-energy resolution fluorescence detected X-ray absorption spectroscopy (HERFD-XAS). Figure S4.1 shows a schematic of the reactor including the X-ray beam path for transmission geometry, e.g. for scattering experiments, and for reflection geometry, e.g. for HERFD-XAS experiments. The opening angle of 45° corresponds to a maximum instrumentally accessible q -value of $q_{\text{max,inst}} = 38 \text{ \AA}^{-1}$ for an X-ray energy of 100 keV. $q_{\text{max,inst}}$ values depend on the X-ray energy as well as the instrumental set-up including the opening angle of the reactor or sample environment, and the detector size and position. The corresponding $q_{\text{max,inst}}$ values for different X-ray energies and sample-to-detector distances are summarized in Table S4.2. Heating elements are vital for the thermal performance of the reactor setup, as they influence the heating of the aluminum housing, the inlet, and the reaction solution. These factors determine the heating rate, final temperature, and temperature stability. They surround the inlet and are driven with a 24 V-50 W power supply (EA-PS 5040, Elektro-Automatik) in parallel connection. The generated dielectric heating is distributed across the area that surrounds the inlet, evenly via the thermal conductivity of the aluminum. The temperature is measured by a PT1000 model sensor (Honeywell) positioned close to the inlet and connected to an LS335 temperature controller. The measured temperature is instantly read from the temperature controller to a computer and monitored via a Python script.

The inlet works as a custom-made container for the reaction solution accommodation. It is used with a cap and a perfluoro elastomer (FFKM) O-ring to provide an air-tight environment. The inlet design offers two material options: polyether ether ketone (PEEK, Bieglo) and glass. The material is selected according to the measurement technique, and the X-ray window wall thickness can be adapted to the reaction requirements. PEEK is a favorable material for spectroscopy measurements due to its high X-ray transparency. Glass material is preferred for scattering experiments due to its low background signal although its utilization presents challenges regarding mechanical stability. In careful tests, we observed that determination of the optimum glass thickness as a balance between satisfactory data collection and structural integrity at high-pressure conditions is quite challenging. To this end, we designed glass and PEEK inlets with 0.2, 0.3, and 0.5 mm wall thicknesses. The results demonstrate that 0.2 mm thickness of the PEEK inlet and 0.3 mm thickness of the glass inlet gave the most satisfactory data for the spectroscopy and scattering experiments at relatively high pressures, respectively. Figure 4.1(c) shows the various inlet and cap configurations for specific X-ray techniques and experimental requirements, with total and scan zone volumes, which are as follows:

(i) Glass inlet for scattering experiments under air-tight, autoclave-like conditions at elevated temperatures and pressures with a wall thickness of 0.3 mm.

(ii) Thin-walled (0.05 mm) glass vial embedded in a copper body for weak background scattering contributions. The corresponding PEEK cap features a spring, which prevents the fragile thin-walled glass vial from breaking upon closure and provides a modest degree of sealing, though not fully airtight as in the standard glass inlet (i).

(iii) PEEK inlet for XAS measurements with a wall thickness of 0.2 mm.

(iv) A modified hollow-screwed PEEK cap that enables the pressure sensor to measure pressure from a close position to the solution.

(v) A modified hollow Brass cap allowing the injection of reagents during the experiment through a septum.

(vi) A modified hollow Brass cap for a fiber-optical ATR-IR probe implementation, enabling multimodal ATR-IR measurements.

Further details about the reactor tailored for cooling, photographs of the caps designated for pressure and IR measurements is given in the supporting information. A PEEK inlet can be used for X-ray scattering; however, due to its polycrystalline nature, it introduces high residual background scattering. This trade-off is acceptable for strongly scattering crystalline samples, where the sample scattering intensity is sufficient to outweigh the residual background from PEEK.⁹³

The insulation and the sealing elements complete the air-tight environment, working as the supportive components. A tightly fastened aluminum component, mounted on top of the aluminum housing, assures complete sealing of the reactor. Top, bottom, and side PEEK insulators enhance the heat retention within the system by minimizing thermal exchange between the aluminum and surrounding air as much as possible. Properties such as high thermal stability, low thermal expansion coefficient, dimensional stability, and low thermal conductivity, which make PEEK a perfect thermal insulator, support all the thermal requirements of the closed system.

To ensure a homogeneous colloidal dispersion, a micro stirrer (Variomag Thermo Scientific™), is installed on the aluminum bottom plate directly beneath the aluminum housing. A micro-magnetic stirring bar is located within the inlet, providing homogeneous mixing of the solution during the *in situ* measurements. This ensures a constant concentration of the scatterers across the cell and high data quality.

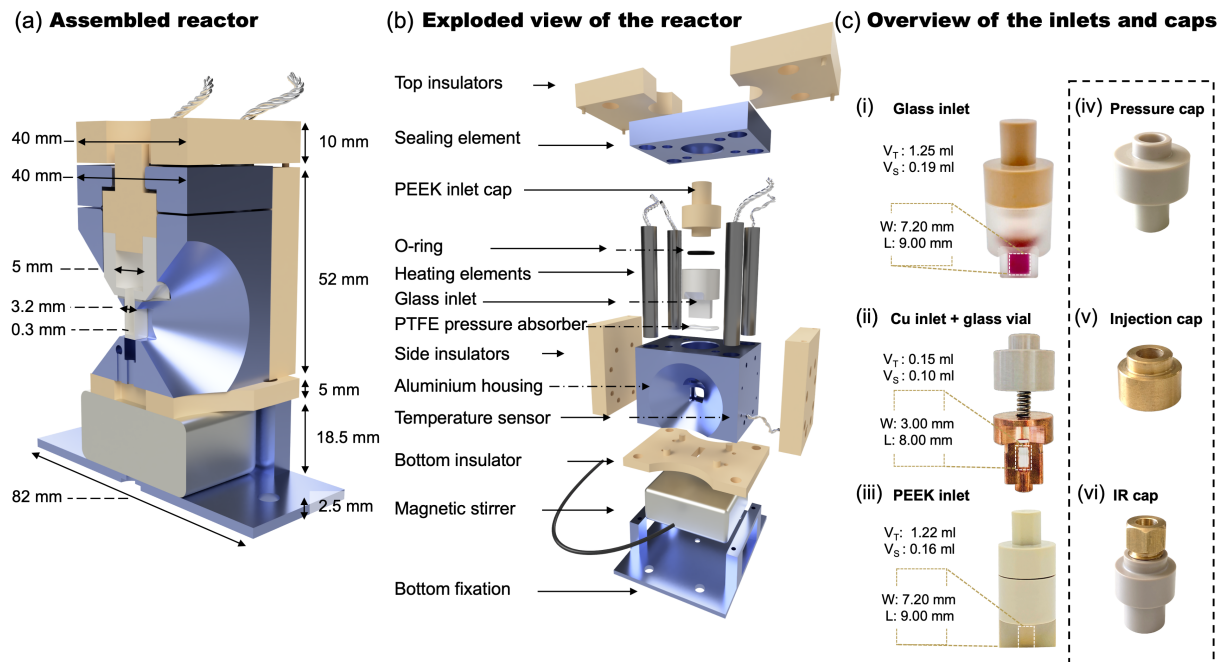


Figure 4.1: Design of the reactor. (a) Cross-sectional rendering of the assembled reactor. (b) Exploded schematic showing individual components. (c) Photograph of the interchangeable inlet modules for different experimental configurations, V_T and V_S indicate total volume and scanning area volume, respectively. W and L state the width and length of the scanning area.

4.4 Performance of the reactor

We demonstrate the performance and versatility of the reactor through a series of characterization and reaction studies. First, we evaluate its thermal response, pressure stability, and X-ray transparency (Figure 4.2). We then estimate the signal-to-noise ratio of PXRD pattern of nanoparticle dispersions at different particle concentrations (Figure 4.3). Finally, we investigate the model system, the solvothermal synthesis of magnetite nanoparticles, in detail using a combination of complementary *in situ* techniques: PXRD and PDF analysis of TS data (Figure 4.4), ATR-IR (Figure 4.5), and HERFD-XAS (Figure 4.6). By combining all analytical data from these methods, we propose a reaction mechanism of the nanoparticle formation and postulate intermediate states during the transformation of iron(III) acetylacetonate, $\text{Fe}(\text{acac})_3$, to magnetite, Fe_3O_4 , in benzyl alcohol¹⁰⁷. These results highlight the reactor's capability to integrate multiple methods, providing a comprehensive understanding of complex reaction pathways.

Figure 4.2(b) shows photographs of the glass inlet during the Fe_3O_4 nanoparticle synthesis. The color change of the reaction solution from reddish $\text{Fe}(\text{acac})_3$ in benzyl alcohol (BnOH) to black Fe_3O_4 is clearly visible during the heating ramp to 180 °C. Figure 2(c) depicts an IR image of the reactor window, illustrating uniform heat distribution in the BnOH-filled inlet at 180 °C. We further measure the temperature and pressure profiles during heating: the BnOH-filled inlet reaches 3.8 bar at 180 °C, while the water-filled inlet reaches 7.9 bar at 150 °C - both without breaking the glass inlet with a 0.3 mm wall thickness, as shown in Figure 2(d). To assess the suitability of the glass inlet for X-ray experiments, we calculate its X-ray transmission both empty and filled with the common solvents water, ethanol, and BnOH. The results indicate reasonable transmission for X-ray energies above 20 keV, as shown in Figure 4.2(e). For comparison, Figure S4.6 shows the X-ray transmission of glass and PEEK inlets with different wall thicknesses, providing guidelines for selecting suitable inlets. Details on the transmission calculations are given in the experimental section.

The glass inlet configuration offers good pressure stability and airtightness, enabling solvothermal synthesis under autoclave-like conditions for *in situ* scattering experiments. However, the relatively thick inlet walls give rise to a substantial scattering background. One major challenge of *in situ* scattering studies is the strong background signal, as scattering arises from all components in the beam path. To isolate the signal of the chemical species of interest, contributions from the solvent, reactor walls, and beamline environment must be carefully subtracted. In most PXRD experiments, background subtraction is relatively straightforward due to the strong diffraction signal of crystalline phases. However, for weakly scattering systems such as nanoparticles or dilute dispersions or solutions, background subtraction becomes significantly more demanding. This is especially true for total scattering experiments, where often non-periodic structures or small nanoparticles are being investigated and data is collected at high scattering vectors (typically $q_{\text{max}} > 15 \text{ \AA}^{-1}$), where scattering is weak and noisy. Moreover, standard baseline correction methods are not applicable in TS experiments, as both Bragg and diffuse scattering must be preserved, making accurate and precise background subtraction essential. Figure 3(a) illustrates this by comparing PXRD patterns of commercial copper(II) oxide (CuO) nanoparticles (7.4 nm diameter) at concentrations of 0.2, 0.05, and 0.02 mmol mL⁻¹ in ethanol, highlighting the dominant background relative to the nanoparticle signal. Additionally, we estimate the signal-to-noise ratio (SNR) for each concentration (Figure 3(b-e)), demonstrating that the reactor with glass inlets can still provide reasonable PXRD data even at very low particle concentrations.

We further test the reactor by studying the solvothermal synthesis of Fe_3O_4 from $\text{Fe}(\text{acac})_3$ in

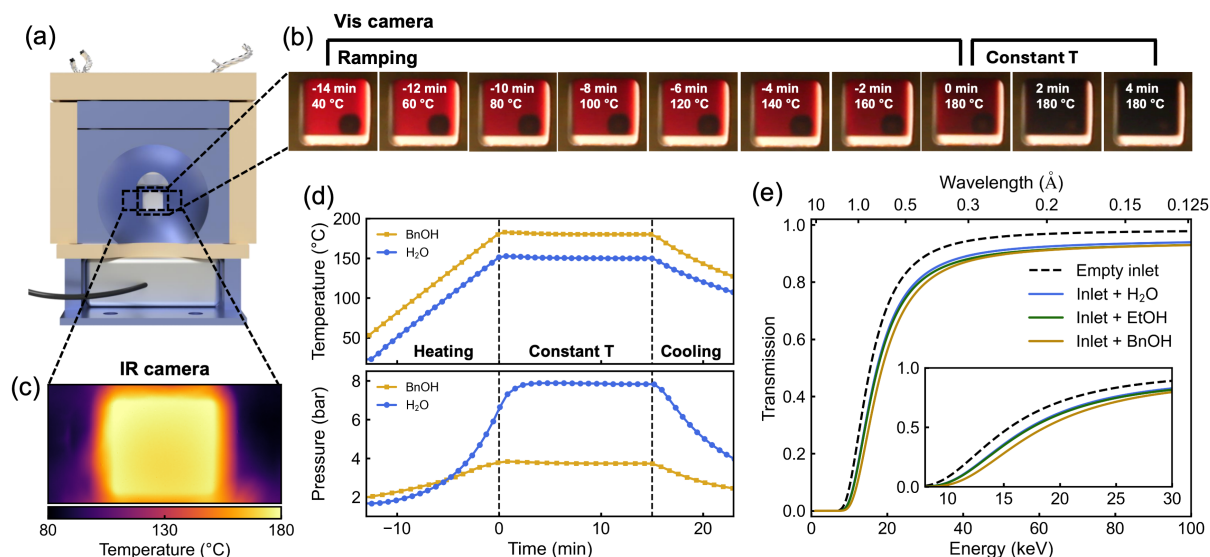


Figure 4.2: Thermal, pressure and transmission characteristics of the glass inlet with 0.3 mm wall thickness. (a) Front view rendered image of the reactor (b) Photographs showing the solution color change during Fe_3O_4 formation from $\text{Fe}(\text{acac})_3$ in BnOH upon heating. (c) IR image showing uniform heat distribution of the BnOH-filled inlet at 180 °C. (d) Temperature and pressure profiles during the heating of water and BnOH to 150 °C and 180 °C, respectively. (e) Simulated X-ray transmission of the inlet, empty and filled with the solvents water, ethanol (EtOH) and BnOH as a function of the X-ray energy.

BnOH at 180 °C.¹⁰⁷ This reaction is fast, scalable, and allows tailoring the size, morphology, and even synthesis of heterostructures.^{120–122} The organic reaction pathways during the synthesis of metal-oxides in benzyl alcohol, including Fe_3O_4 , are well-known and have been assessed in previous studies via gas chromatography-mass spectrometry (GC-MS) and nuclear magnetic resonance (NMR) analysis of the final reaction mixture. In particular, it has been proposed that benzyl acetate and 4-phenyl-2-butanone form via the reaction of benzyl alcohol with $\text{Fe}(\text{acac})_3$. Furthermore, during the reaction, one third of Fe(III) species are reduced to Fe(II) by dehydrogenative oxidation of 4-phenyl-2-butanone into 4-phenyl-3-buten-2-one. The complete organic transformation pathway is reported in literature.¹²³ However, *in situ* studies providing mechanistic insights that focus on the metal center, *e.g.* formation of intermediate complexes and monitoring the nucleation and growth of the nanoparticles, are scarce.¹²⁴

Based on our *in situ* scattering data, we propose a reaction mechanism, schematically illustrated in Figure 4.4(a). Initially, $\text{Fe}(\text{acac})_3$ is dissolved in BnOH with the Fe(III) center octahedrally coordinated by three acetylacetonate ligands, each coordinating through both oxygen atoms. Upon reaching 180 °C, an intermediate ferric acetate complex, $[\text{Fe}_3(\mu_3\text{-O})(\text{AcOR})_6(\text{ROH})_3]^+$, forms. In this complex, three Fe(III) centers are linked to a central coplanar μ_3 -oxo ligand. Acetate groups (AcOR) bridge pairs of Fe(III) centers and are further coordinated by water or alcohol molecules (ROH), maintaining an octahedral coordination. Here, R denotes either a hydrogen atom or a benzyl group. The iron complex with coordinated acetate and water is well known in literature.¹²⁵ With continued heating, the intermediate transforms into crystalline Fe_3O_4 nanoparticles.

Figure 4.4(b,c) show the temperature profiles and heatmaps of the obtained *in situ* PXRD patterns and PDFs, respectively. The reaction solution is ramped at 10 °C min^{-1} , with the time point of 0 min defined as the moment when the reaction temperature of 180 °C is reached. Both datasets clearly reflect the sequential transformation through the three structural stages

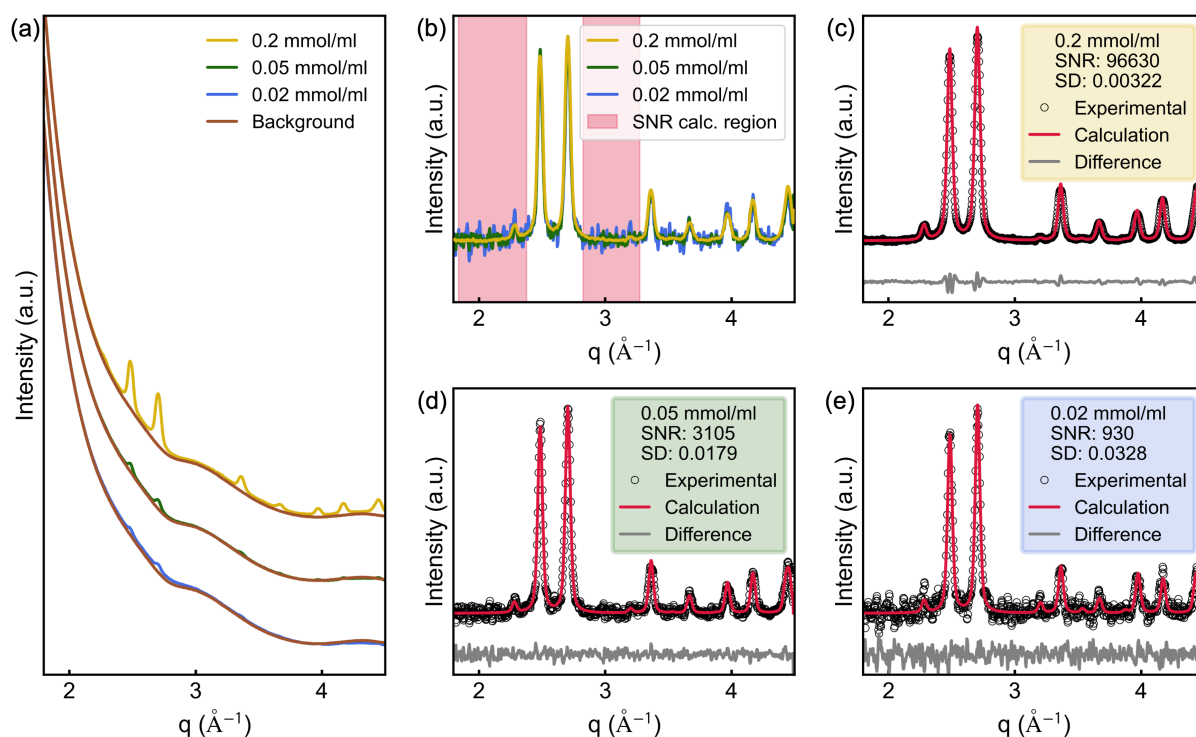


Figure 4.3: PXRD of CuO nanoparticles (7.4 nL diameter) dispersed in ethanol at concentrations of 0.2, 0.05, and 0.02 mmol mL⁻¹ and signal-to-noise ratio (SNR) estimations. (a) PXRD of the CuO dispersions compared to the background pattern which is the ethanol filled inlet. (b) Overlay of background-subtracted and normalized PXRD patterns for CuO dispersions showing increasing noise with decreasing concentration. (c-e) Rietveld refinements for each concentration. To estimate the SNR, we first normalize each pattern to 1 at the most intense Bragg peak ($\sim 2.7 \text{ \AA}^{-1}$). The SNR is then calculated as the inverse square of the standard deviation (SD) of the difference between the experimental data and the Rietveld fit. To avoid influence from imperfections in the fit, regions containing strong Bragg reflections are excluded from the SD calculation as highlighted in (a).

depicted in Figure 4.4(a). To illustrate the reaction kinetics, we calculate a Pearson correlation map of the *in situ* PXRD data. The resulting map (Figure S4.7) visualizes the degree of similarity between the PXRD patterns at the different reaction times. The structural changes indicated by the two nodes along the diagonal in the Pearson correlation map points at two transitions: one shortly after 0 min and a second around 25 min. Figure 4.4(d,e) show representative PXRD and PDF patterns for the three reaction stages: the initial molecular complex (bottom), the intermediate (middle), and the final Fe_3O_4 product (top). Rietveld refinement of the PXRD pattern of the final product confirms the phase purity of Fe_3O_4 . The non-crystalline nature of the initial and intermediate states excludes conventional PXRD refinement; however, their structures can be analyzed via PDF. The initial state is modeled using the structure of $\text{Fe}(\text{acac})_3$ while the intermediate state at 5 min reaction time is best described using a three-phase refinement with $\text{Fe}(\text{acac})_3$, $[\text{Fe}_3(\mu_3\text{-O})(\text{AcOR})_6(\text{ROH})_3]^+$, and Fe_3O_4 in a 1.00:0.92:0.70 scale ratio. Based on the reported $\text{Fe}(\text{acac})_3$ decomposition mechanism in benzyl alcohol forming benzyl acetate,¹²³ we propose the actual intermediate is a ferric acetate complex coordinated with benzyl acetate and benzyl alcohol ligands. However, for the PDF refinement, we employ the literature-reported structure $[\text{Fe}_3(\mu_3\text{-O})(\text{AcO})_6(\text{H}_2\text{O})_3]^+$, which contains acetate and water ligands.¹²⁵ We note that PDF analysis cannot unambiguously distinguish between acetate and benzyl acetate ligands, or between coordinated water and benzyl alcohol, due to the prevalence of short-range interatomic correlations involving Fe and the surrounding BnOH solvent. Nevertheless, the excellent agreement between the modeled and experimental PDFs (Figure 4(e)) strongly supports the structural assignment of the intermediate as a ferric acetate complex. The refined parameter of the Rietveld and PDF refinements are given in Table S5.3 and S5.4, respectively.

To assess the time resolution achievable with the reactor setup, Figure S4.8 compares PXRD and PDF data averaged over varying exposure times. These tests demonstrate that high-quality data can be obtained with exposures as short as 5 s during the early, low-scattering stages of the reaction, and down to 1 s for the strongly scattering crystalline final product. Overall, these results highlight the capability of the reactor to provide high-quality PXRD and PDF data at low time resolution despite significant background scattering from the glass components.

The PDF refinement of the intermediate state assumes the thermal decomposition of acetylacetonate ligands into acetate. To track the formation of organic by-products in the liquid phase during the reaction, we perform *in situ* ATR-Fourier transformed infrared (FTIR) spectroscopy using the reactor equipped with an ATR-IR fiber probe. *In situ* ATR-FTIR difference spectra collected during the reaction and reference spectra for comparison are displayed in Figure 4.5. Already during the heating process, we observe a decrease in absorption in the frequency region around 1000 cm^{-1} , which we assign to the $\nu(\text{C-O})$ stretching vibration of BnOH. Furthermore, we observe a decrease in absorption around 1600 cm^{-1} , which we attribute to the bending vibration $\delta(\text{H-O-H})$ of residual water present in the sample at ambient conditions. As the temperature increases, this water evaporates and transitions into the gas phase, leaving the liquid phase and thus causing the observed signal loss. With further heating, a broadening and increase in absorption around 1225 cm^{-1} , which we assign to the emergence of $\nu(\text{C-O})$ vibrations characteristic of an acetate functional group. We correlate this increase with the formation of benzyl acetate, supported by additional vibrational modes around 1739 cm^{-1} ($\nu(\text{C=O})$), 1026 cm^{-1} and the symmetric and asymmetric bending vibrations ($\delta(\text{CH}_3)$) at 1361 and 1380 cm^{-1} , respectively. These observations are consistent with the reported formation of acetates during acetylacetonate decomposition.¹²⁴ In addition to vibrational modes attributed to benzyl acetate formation, we also identify a vibrational mode at 1717 cm^{-1} ($\nu(\text{C=O})$), due to the contribution of acetone in the reaction mixture, which is formed alongside benzyl acetate.

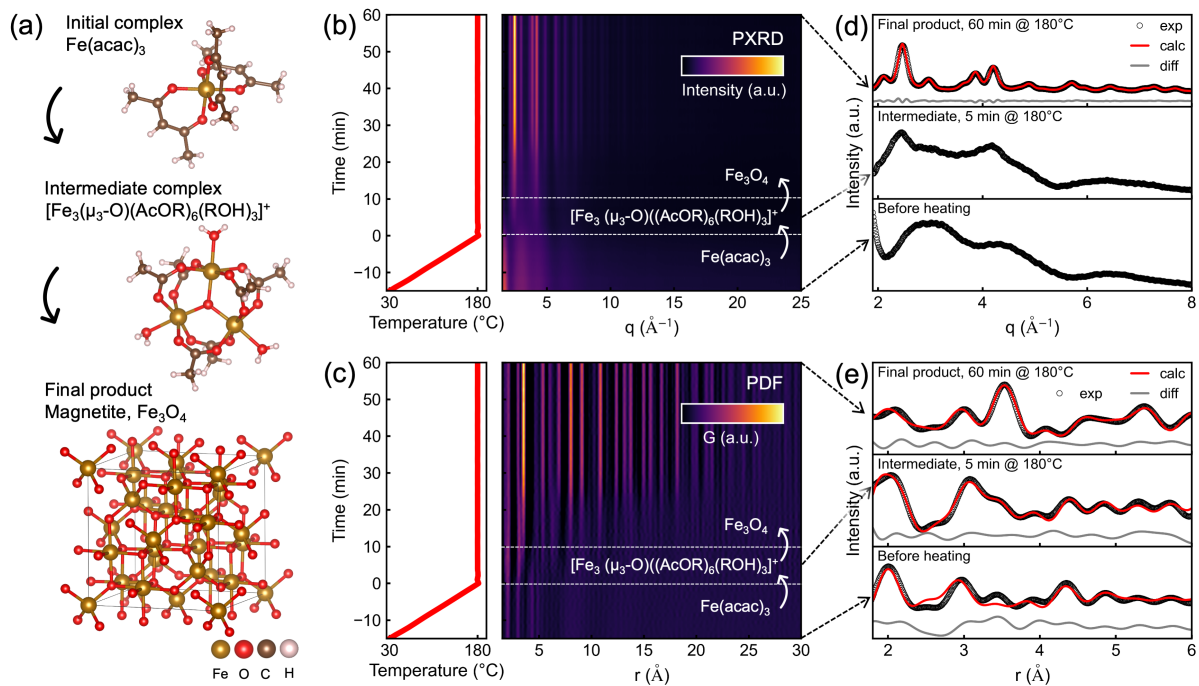


Figure 4.4: *In situ* PXRD and PDF analysis of the reaction to Fe_3O_4 . (a) Schematic of the reaction mechanism as determined by PXRD and PDF refinements. The initial complex $\text{Fe}(\text{acac})_3$ forms $[\text{Fe}_3(\mu_3\text{-O})(\text{AcOR})_6(\text{ROH})_3]^+$ after reaching the reaction temperature of 180°C which further reacts to the final product Fe_3O_4 . (b,c) Temperature profile and heatmap of PXRD and PDF data, respectively. (d,e) PXRD Rietveld and PDF refinements of the initial complex before heating, $\text{Fe}(\text{acac})_3$, the intermediate complex, $[\text{Fe}_3(\mu_3\text{-O})(\text{AcOR})_6(\text{ROH})_3]^+$, at 5 min after reaching the reaction temperature of 180°C and Fe_3O_4 . Since Rietveld refinement requires a crystalline structure only the refinement of Fe_3O_4 is shown for PXRD.

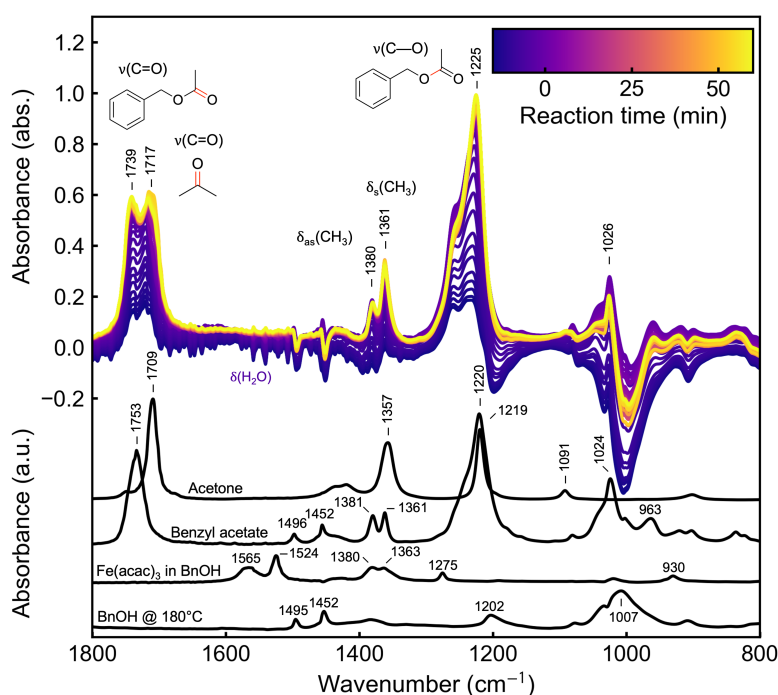


Figure 4.5: *In situ* ATR-FTIR analysis of the reaction of $\text{Fe}(\text{acac})_3$ to Fe_3O_4 in BnOH , compared to reference spectra of acetone and benzyl acetate, $\text{Fe}(\text{acac})_3$ dissolved in BnOH at room temperature, and BnOH at 180°C .

The assigned vibrational modes are listed in Table S4.5. For comparison, additional reference spectra are shown in Figure S4.9. These ATR-FTIR findings for the synthesis of Fe_3O_4 support the formation of a ferric acetate complex as an intermediate. They also demonstrate the capabilities of our reactor to acquire ATR-FTIR spectra with a spectral resolution of 4 cm^{-1} and a temporal resolution of less than 1 min during solvothermal synthesis.

Finally, we investigate the Fe_3O_4 solvothermal synthesis using XAS with the PEEK inlet configuration. Figure 4.6(a) presents Fe K-edge high-energy resolution fluorescence detected X-ray absorption near-edge structure (HERFD-XANES) spectra, showing a shift of the absorption edge to lower energy - indicating a partial reduction of Fe^{3+} in the initial and intermediate complexes to a mixed-valence $\text{Fe}^{2+}/\text{Fe}^{3+}$ state in Fe_3O_4 . Concurrently, the whiteline double peak observed in the initial state transitions into a single, broader feature in the final product, while the pre-edge intensity increases, indicating changes in Fe coordination symmetry and oxidation state. These spectral features closely resemble previously reported XANES spectra of $\text{Fe}(\text{acac})_3$ ^{126,127} and Fe_3O_4 ^{128,129}, supporting the identification of the initial complex as $\text{Fe}(\text{acac})_3$ and confirming the formation of Fe_3O_4 as the final product.

To analyze these changes quantitatively, we perform multivariate curve resolution by alternating least squares (MCR-ALS)¹³⁰ of the *in situ* HERFD-XANES dataset, which extracts three distinct Fe species, consistent with the PDF findings. Figure 4.6(b) shows the evolution of the three species during the reaction. Figure 4.6(c) shows the MCR-ALS recovered spectra. In Figure 4.6(d) we present results from FEFF simulations¹³¹ based on the structures determined from the PDF analysis. Since Fe_3O_4 comprises octahedral and tetrahedral sites in a 2:1 ratio, the simulation of Fe_3O_4 shows the linear combination of FEFF simulations with the octahedral and tetrahedral Fe as the absorbing atom in a 2:1 ratio. Since Fe_3O_4 contains Fe atoms in both octahedral and tetrahedral coordination sites in a 2:1 ratio, the simulation of Fe_3O_4 was performed as a linear combination of FEFF simulated spectra calculated with Fe in

octahedral and tetrahedral sites as the absorbing atom, weighted accordingly at a 2:1 ratio. The simulations match well with the MCR-ALS recovered spectra. Figure S4.10 shows the FEFF simulated XANES spectra together with density of states (DOS) calculation of the Fe, O, and C s, p, and d states.

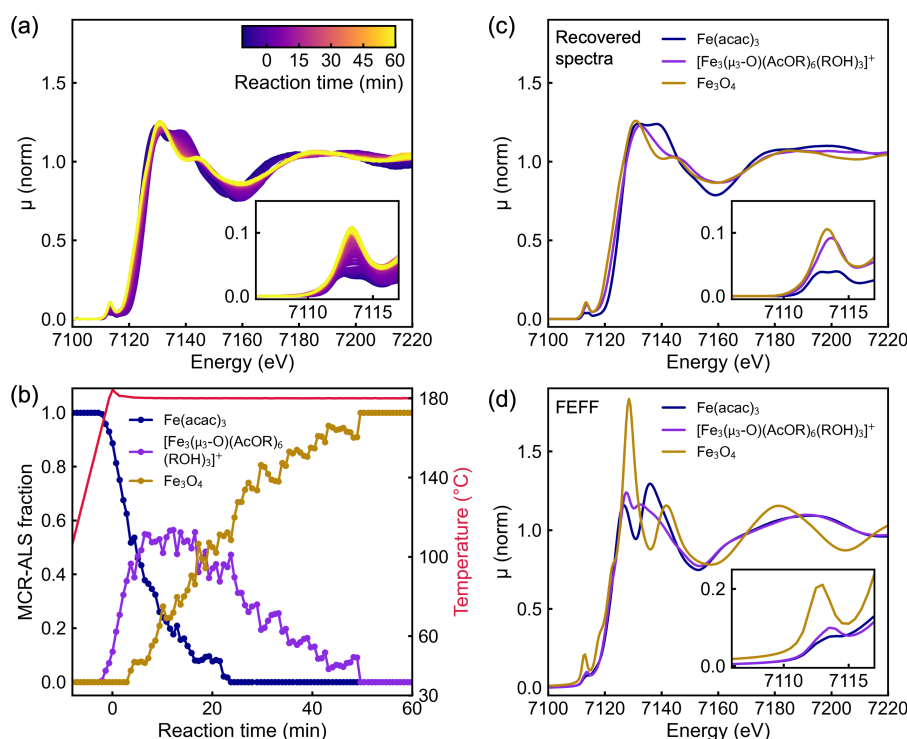


Figure 4.6: *In situ* Fe K-edge HERFD-XANES analysis of the reaction to Fe_3O_4 . (a) *In situ* HERFD-XANES data. (b) Concentration profiles of three distinct Fe species extracted via MCR-ALS. (c) MCR-ALS recovered spectra. (d) FEFF simulations based on structures determined from *in situ* PDF analysis, confirming the initial species as $\text{Fe}(\text{acac})_3$, the intermediate as $[\text{Fe}_3(\mu_3\text{-O})(\text{AcOR})_6(\text{OH})_3]^+$, and Fe_3O_4 as the final product.

Overall, these results showcase the excellent performance of the reactor for *in situ* analyses such as high-resolution XAS and WAXS, as well as ATR-FTIR measurements, and demonstrate its capability to provide detailed electronic and structural insight during solvothermal synthesis.

4.5 Conclusion

We present a versatile reactor system optimized for *in situ* X-ray scattering and X-ray absorption spectroscopy analysis of solvothermal reactions. The reactor supports techniques such as XAS, WAXS, and SAXS under inert, autoclave-like conditions. Its modular design features exchangeable inlets tailored to specific experimental requirements: PEEK for X-ray spectroscopy, and glass inlets for X-ray scattering. Additional configurations enable gas or liquid injection and integration of an ATR-IR fiber probe for simultaneous ATR-FTIR measurements. The reactor enables precise temperature control ($-20\text{ }^\circ\text{C}$ to $200\text{ }^\circ\text{C}$) with cartridge heaters or Peltier elements and magnetic stirring. The compact geometry is compatible with synchrotron beamline constraints and supports data acquisition in both transmission and reflection geometries. We demonstrate the reactor's performance by investigating the synthesis of Fe_3O_4 nanoparticles from $\text{Fe}(\text{acac})_3$ in benzyl alcohol as shown in Figure 4.7. By linking findings from *in situ* PXRD,

PDF of TS, HERFD-XANES, and ATR-FTIR, we comprehensively study the reaction pathways and reveal ferric acetate as an intermediate structure. This study underlines the potential of our reactor platform to provide mechanistic insights into solvothermal reactions and nanoparticle formation processes in real time, paving the way for rational synthesis design.

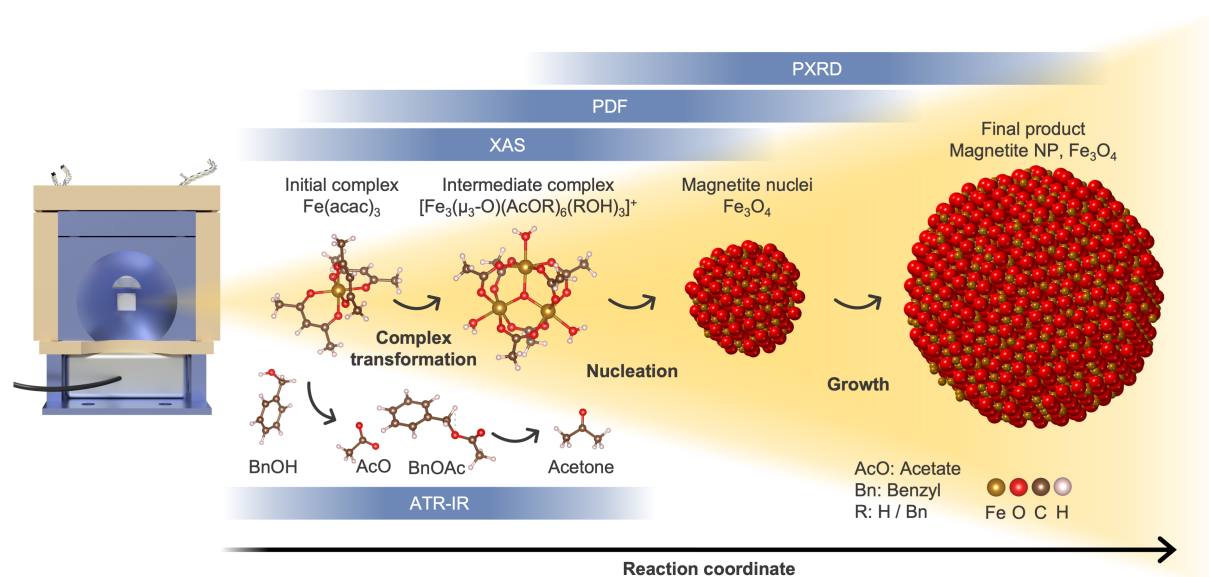


Figure 4.7: Schematic overview of the reaction pathway leading to magnetite (Fe_3O_4) nanoparticles (NPs). The mechanism is elucidated using a combination of *in situ* techniques made possible by the versatile reactor setup. ATR-IR spectroscopy monitors the evolution of organic species throughout the reaction. XAS and PDF analyses reveal the conversion of the initial iron(III) acetylacetonate complex to the intermediate ferric acetate complex, followed by the formation of the magnetite phase. PXRD measurements track the emergence of the magnetite crystal structure and nanoparticle growth.

4.6 Experimental section

Chemicals

All chemicals were purchased from commercial sources and used without further purification: $\text{Fe}(\text{acac})_3$ (Sigma Aldrich, 99.9 %), benzyl alcohol (Sigma Aldrich, 99.8 %), copper(II) oxide (Sigma Aldrich, 99.999 %), ethanol (VWR chemicals, >99.9 %). $\text{Fe}(\text{acac})_3$ and benzyl alcohol were stored and handled in the glove box under inert atmosphere (Ar 6.0 purity, $c(\text{H}_2\text{O}) < 0.1$ ppm, $c(\text{O}_2) < 0.1$ ppm).

Synthesis

In a typical synthesis, a stock solution is prepared in the glove box by adding $\text{Fe}(\text{acac})_3$ (353.2 mg, 1.0 mmol) to 5 mL of benzyl alcohol and stirring until the iron salt was completely dissolved. Subsequently, a quantity of 80 μL was transferred to the inlet of the reactor. After assembling the reactor, it was taken out of the glovebox and heated to 180 $^\circ\text{C}$ with a heating rate of 10 $^\circ\text{C min}^{-1}$ under vigorous stirring. After the desired reaction time at 180 $^\circ\text{C}$ the reactor was cooled to room temperature.

X-ray transmission calculations

X-ray transmission was calculated by first determining the X-ray absorption coefficients of the respective materials using the Xraydb Python library^{76,77} and applying Lambert's law to compute the transmission.

Attenuated Total Reflection Fourier Transformed Infrared (ATR-FTIR) Spectroscopy

A ThermoFisher Nicolet iS20 equipped with a liquid N₂-cooled MCT detector, combined with a 6.3 mm high-temperature diamond ATR-probe (art photonics, Berlin, Germany), was used for *in situ* ATR-IR measurements. Difference spectra were acquired using 32 scans and a spectral resolution of 4 cm⁻¹, resulting in a time resolution of 48 s. To minimize thermal effects on the absorbance, a background of benzyl alcohol preheated to 180 °C was used for the *in situ* analytical experiments. Spectra of reference compounds were acquired in absolute mode with a background of fiber in air.

In situ High-Energy Resolution Fluorescence Detected X-ray Absorption Near Edge Structure (HERFD-XANES)

The *in situ* HERFD-XAS was measured in the PEEK inlet with 0.2 mm wall thickness. The data was acquired at the ID26 beamline¹³² at the European Synchrotron Radiation Facility (ESRF) in Grenoble, France. HERFD-XAS measurements were performed by measuring the intensity of the Fe K α main line using a Ge(440) crystal in Rowland geometry¹³³ while scanning the incident energy across the range of 7.10 to 7.22 keV with a step size of 0.1 eV. An Si(111) monochromator was used, and the overall energy resolution was \sim 1.4 eV. To minimize radiation damage, the incident X-ray beam spot is moved onto the reaction cell after each scan, as shown in Figure S4.12 and S4.13. Each HERFD-XAS spectrum was collected over 35 s.

The HERFD-XAS datasets were processed utilizing a custom Python script. The absorption edge position was determined, and the edge jump was normalized using the LARCH-XAFS software module.¹³⁴ Spectroscopic data underwent smoothing via a Savitzky-Golay filter and additional processing with the NumPy and SciPy libraries. A comparison between the raw and processed data is depicted in Figure S4.14.

In situ Pair Distribution Function (PDF) analysis of In Situ Total Scattering (TS) and Powder X-ray Diffraction (PXRD)

In situ TS and PXRD was measured in the glass inlet with 0.3 mm wall thickness. The data were acquired at beamline P21.1 at PETRA III at Deutsches Elektronen-Synchrotron DESY, Hamburg, Germany.¹³⁵ Two-dimensional scattering patterns were recorded every 1 s at an X-ray energy of 101.39 keV ($\lambda = 0.1222 \text{ \AA}^{-1}$) using an X-ray area detector (PerkinElmer XRD1621, Varex Imaging Corp.) with 2048x2048 pixels and a pixel size of 200x200 μm . A LaB₆ powder standard packed into the fused silica inlet of the *in situ* reactor was used to calibrate the sample-to-detector distance: 0.390 m for *in situ* TS measurements of Fe₃O₄ synthesis and 1.541 m for *ex situ* PXRD of CuO. For the TS data, q_{damp} and q_{broad} values were calibrated as 0.0494 \AA^{-1} and 0.0374 \AA^{-1} , respectively. PDF data were processed with $q_{\text{min}} = 1.1 \text{ \AA}^{-1}$, $q_{\text{max}} = 14.2 \text{ \AA}^{-1}$, $q_{\text{max,inst}} = 24.0 \text{ \AA}^{-1}$, and $\Gamma_{\text{poly}} = 0.9$. Azimuthal integration and calibration were carried out using pyFAI¹³⁶, and PDF refinements were performed using diffpy-CMI⁷¹. Rietveld refinements were conducted with GSAS-II⁶⁹. A detailed description of the data processing and PDF analysis procedures is available in the literature.¹⁶

Acknowledgements

S. Y. Harouna-Mayer and M. G. Akcaalan contributed equally to this work. This research was supported by the European Research Council (LINCHPIN project, grant no. 818941), the Deutsche Forschungsgemeinschaft (DFG) through the Cluster of Excellence “Advanced Imaging of Matter” (EXC 2056, project ID 390715994) and by the Bundesministerium für Bildung und Forschung (BMBF) via the project 05K22GU7 (LUCENT II), and the project 05K2020-2019-06104

XStereoVision (grant no. 05K20GUA). The authors acknowledge DESY (Hamburg, Germany), a member of the Helmholtz Association, and ESRF (Grenoble, France) for the provision of experimental facilities. Parts of this research were carried out at PETRA III using beamline P21.1¹³⁵ and at ESRF using beamline ID26 under proposal MA5366⁷⁹. The authors also thank the beamline staff for the support with the experiments: at ID26, Dr. Pieter Glatzel; at P21.1, Dr. Martin v. Zimmermann, Dr. Fernando Igoa, Dr. Jiayu Liu, Philipp Glaeveccke, and Olof Gutowski. Further, the authors thank Stefan Fleig and the workshop team at the University of Hamburg for machining the custom reactor components.

Data availability

All data presented in this report and three-dimensional step-files of the *in situ* reactor are available at: DOI: 10.25592/uhhfdm.17624. A self-written Python script for operating the LS335 temperature controller is available at <https://gitlab.rzz.uni-hamburg.de/koziej-lab/in-situ-cell>.

S4 Supporting information

The overview of present and previously reported reactor designs, along with a comparison of their heating performance, durability, and cost, is shown in Table S4.1. The heating rate is one of the most critical parameters for achieving controlled reaction conditions. The PEEK and all-glass inlets show almost identical heating profiles and only slight differences in cooling profiles. For scattering applications using a glass vial embedded in a PEEK holder, as employed in reference 98, heat transfer to the solvent is somewhat reduced due to the insulating air gap between the two materials.

The PEEK and all-glass inlets have the same volume of 1.25 ± 0.03 mL 1.25(3) mL. The volume deviation is primarily determined by the precision of the machining. The reaction solution is continuously stirred, further ensuring the homogeneity of both the precursor solution and the temperature.

Regarding durability, the metal housing provides comparable mechanical stability across all designs, while the glass components are inherently more fragile than PEEK. However, the all-glass inlet, owing to its greater wall thickness, is considerably more robust than the thin-walled glass vials used in other setups, while remaining suitable for scattering experiments.

The primary cost of an inlet arises from material expenses, with PEEK being more expensive (6 Euro/inlet) than borosilicate glass (10 cents/inlet). Nevertheless, the overall contribution of to the total cost remains modest due to the limited material quantity used and its reusability. All components of the cell were machined within a few working days. The machining of the inlets takes up to 2 hours, where most of the time is needed for setting up the machine.

Overall, our reactor meets the requirements for a versatile, durable, and cost-efficient *in situ* design, providing stable thermal performance and flexible inlet options for a wide range of synchrotron-based experiments.

Table S4.1: Comparison of present and previous reactor designs.

Reference	Materials	Heating element number / position relating to the heating condition	Durability
1 Staniuk et al. ⁹³	PEEK inlet in Brass housing	Two heating elements connected to the housing from the bottom	High
2 Grote et al. ⁹¹	PEEK inlet in Brass housing	Two heating elements connected to the housing from the bottom	High
3 Derelli et al. ⁹⁸	Glass vial + PEEK inlet in Brass housing	Two heating elements embedded in the housing	Low
4 Klemeyer et al. ^{96,106}	Glass vial + PEEK inlet in Aluminum housing	Four heating elements embedded in the housing	Medium
5 Harouna-Mayer et al. ¹⁶	Glass vial + PEEK inlet in Aluminum housing	Four heating elements embedded in the housing	Medium
6 Present work	- PEEK inlet - Glass inlet - Glass vial + Copper inlet in Aluminum housing	Four heating elements embedded in the housing	- High - Medium - Medium/Low

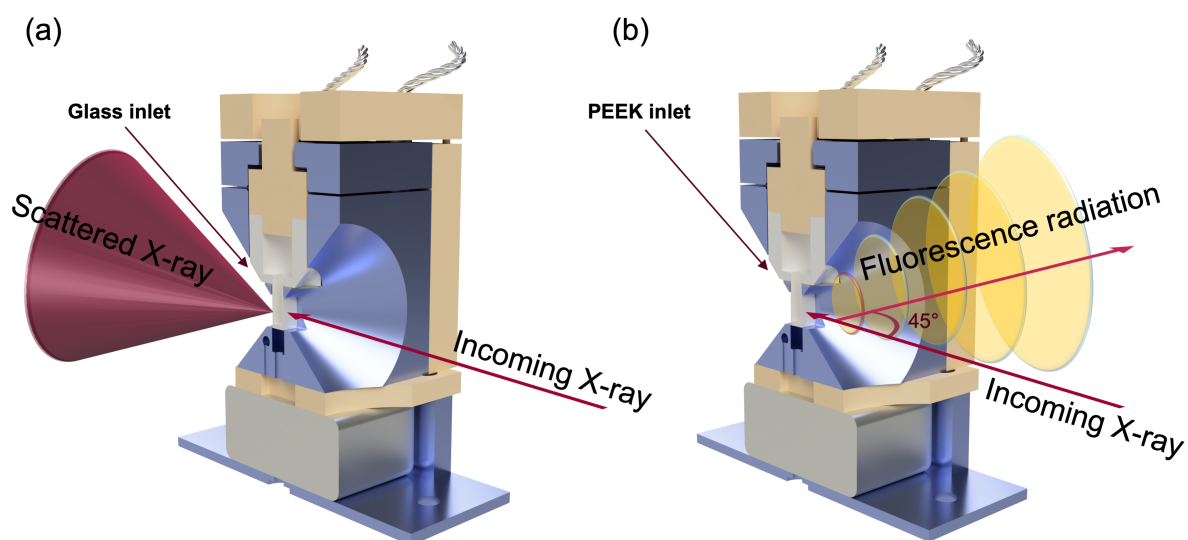
**Figure S4.1:** Cross section of the reactor including the X-ray beam path. (a) Transmission geometry used for scattering experiments. (b) Reflection geometry used for HERFD-XAS measurements.

Table S4.2: Instrumentally achievable maximum q -values ($q_{\max, \text{inst}}$) at different X-ray energies and sample-to-detector distances (SDDs), assuming a quadratic 2D area detector with a height (DH) of 500 mm and the primary X-ray beam centered on the detector. Only the detector region with full azimuthal coverage is considered, i.e., the corners are excluded. $q_{\max, \text{inst}}$ is defined by the maximum scattering angle $2\Theta_{\max, \text{inst}}$ as $q_{\max, \text{inst}} = 4\pi/\lambda \sin(2\Theta_{\max, \text{inst}}/2)$, where λ is the X-ray wavelength. At low SDD and large DH, $2\Theta_{\max, \text{inst}}$ equals the reactor opening angle (45° in our case); otherwise, it is determined by the SDD and DH: $2\Theta = \arctan(\text{DH}/2/\text{SDD})$. We calculate $q_{\max, \text{inst}}$ values for X-ray energies of 5, 10, 20, 50, and 100 keV, and for SDDs of 250, 500, 1500, and 3000 mm. At an SDD of 250 mm, $2\Theta_{\max, \text{inst}}$ equals 45° based on the above considerations. For shorter SDDs, $q_{\max, \text{inst}}$ would be limited by the reactor opening angle.

Energy (keV)	λ (Å)	SDD (mm)	$2\Theta_{\max, \text{inst}}$ (°)	$q_{\max, \text{inst}}$ (Å ⁻¹)
5	2.480	250	45.0	1.9
		500	26.9	1.2
		1500	9.5	0.4
		3000	4.8	0.2
10	1.240	250	45.0	3.9
		500	26.9	2.3
		1500	9.5	0.8
		3000	4.8	0.4
20	0.620	250	45.0	7.8
		500	26.9	4.7
		1500	9.5	1.7
		3000	4.8	0.8
50	0.248	250	45.0	19.4
		500	26.9	11.6
		1500	9.5	4.2
		3000	4.8	2.1
100	0.124	250	45.0	38.8
		500	26.9	23.3
		1500	9.5	8.4
		3000	4.8	4.2

The reactor was adapted to the cooling application and used with an injection cap for reactions operating at sub-zero temperatures and under inert conditions. For the updated version, the essential modification was to incorporate the Peltier element (Adaptive-ETC-128-14-06-E) into the design to cool the system temperature down to -20°C . The cooling places further requirements, like cooling the hot side of the Peltier element to avoid overheating and achieve better performance. This requirement is met by placing water-cooled copper blocks next to the Peltier elements by taking advantage of copper's excellent thermal conductivity. The water cooling that cycles inside the copper blocks was provided with a chiller (Hei-Chill series-Heidolph) set at 5°C . As in the previous design, the reactor temperature was monitored using a sensor mounted on the brass body, whereas the temperature of the Peltier element was controlled by a thermoelectric cooler (TEC) (Meerstetter Engineering TEC-1167) through a side-mounted sensor embedded in the copper block.

In terms of thermal insulation, polypropylene (PP) insulators are positioned on the front, back, and top sides of the brass housing to decrease the thermal leakage from the system to the air.

As for the inlet preference, both glass and PEEK inlets can be used in the reactor. An N_2 connection, which is embedded in the housing, blows vertically through the inlet's X-ray window. Thereby, possible frost that can negatively affect the measurement is prevented by

displacing the air moisture from the window surface. Figure S2 presents the configuration where the Peltier cooling-incorporated reactor is used with the glass inlet equipped with a brass injection cap.

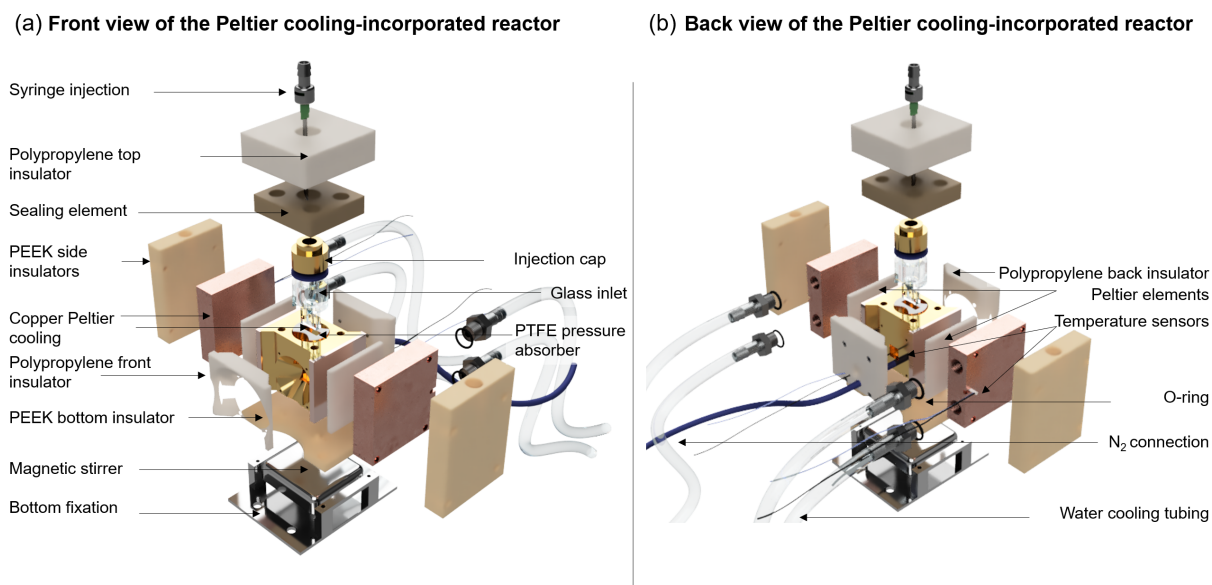


Figure S4.2: The rendered image of the Peltier cooling-incorporated reactor. (a) Exploded front view. (b) Exploded back view.

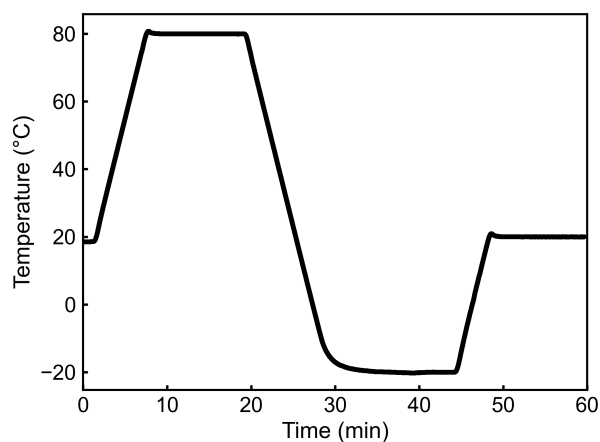


Figure S4.3: Temperature profile of the reactor equipped with Peltier cooling, showing the heating ramp to 80 °C followed by active cooling to -20 °C.

As mentioned earlier, the IR-adapted cap can be used with an ATR-IR fiber cable, allowing the cable tip to contact the solution directly and get adequate data. The IR cap consists of two components, a hollow brass screw fastener and a hollow PEEK component. The fiber cable passes through the hollow brass fastener and is screwed to the hollow PEEK cap, and these pieces are sealed into the inlet via an O-ring. Similarly, the pressure sensor is also threaded into a hollow PEEK cap, allowing the sensor to measure the pressure close to the solution interface. The pressure sensor head is wrapped in polytetrafluoroethylene (PTFE) tape first to avoid any loose connection that can affect the pressure measurement. Then, it is screwed to the cap and sealed through an O-ring to the inlet.

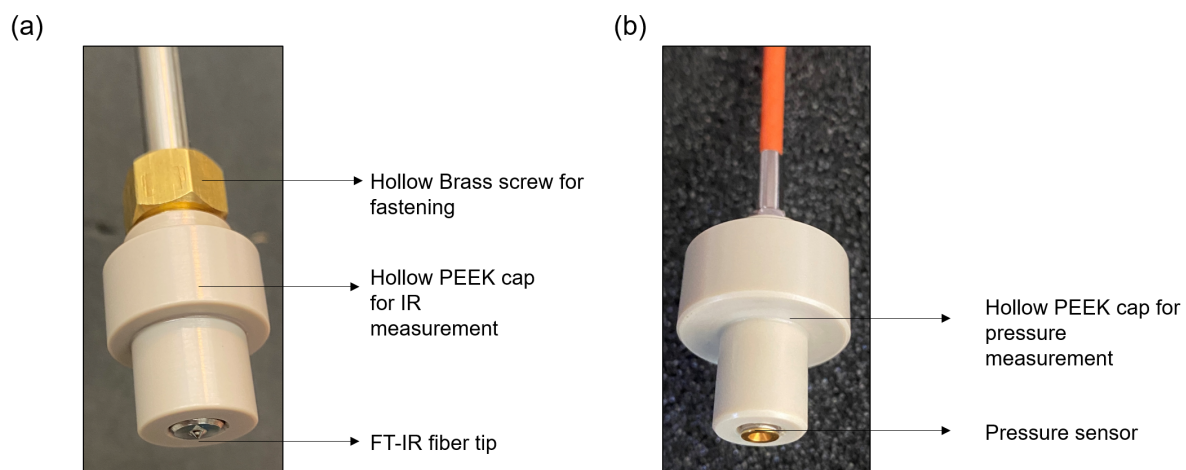


Figure S4.4: (a) The picture of Brass + PEEK cap equipped with an optical ATR-FTIR fiber probe. (b) The picture of a PEEK cap with a pressure sensor.

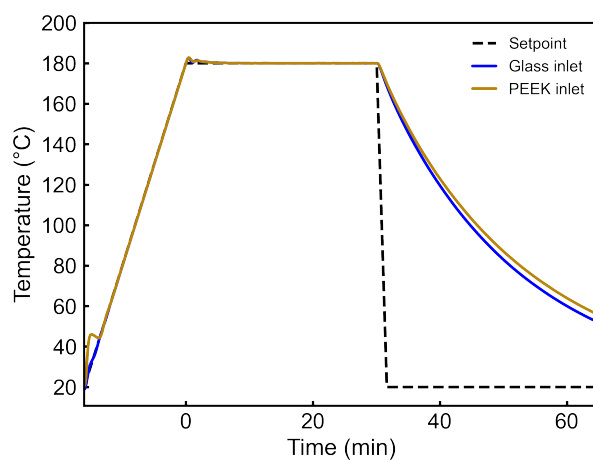


Figure S4.5: Measured temperature profiles of the reactor during heating of BnOH to 180 °C in (a) a glass and (b) a PEEK inlet. The setpoint represents the programmed heating profile of the controller, which regulates the heating.

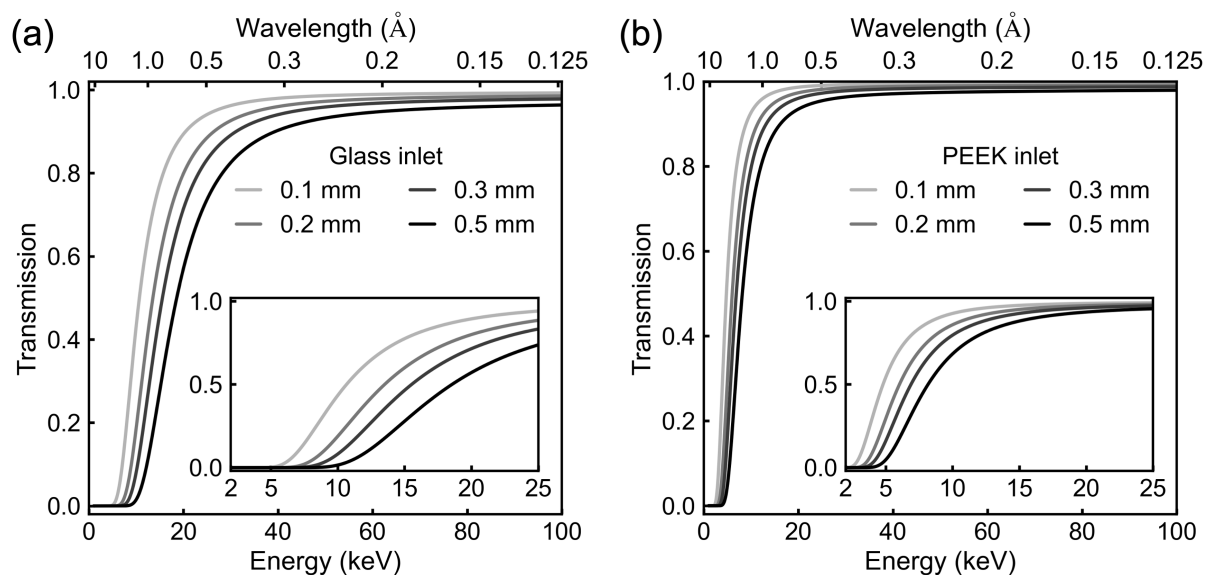


Figure S4.6: X-ray transmission of (a) the glass and (b) PEEK inlet at wall thicknesses between 0.1 and 0.5 mm. The inset shows a zoom between 2 and 25 keV X-ray energy.

Table S4.3: Refined structural parameters from Rietveld analysis of the final stage of the reaction.

R_{wp} (%)	4.34
a (Å)	8.449
Size (nm)	4.3
$Fe^{3+} U_{iSO}$ (Å ²)	0.0130
$Fe^{2+} U_{iSO}$ (Å ²)	0.0096
$O^{2-} U_{iSO}$ (Å ²)	0.0066

Table S4.4: Refined structural parameters from PDF analysis for the initial, intermediate, and final stage of the reaction.

	Reaction stage	Initial stage	Intermediate stage	Final stage
	Reaction time	-15 min	5 min	75 min
	R_w (%)	43.9	19.0	19.8
$\text{Fe}(\text{acac})_3$	Relative scale	1.000	1.000	0.000
	δ_2 (\AA^2)	1.591	1.591	-
	Fe U_{iso} (\AA^2)	9.530×10^{-4}	2.077×10^{-4}	-
	O U_{iso} (\AA^2)	1.506×10^{-2}	1.000×10^{-1}	-
	C ₁ U_{iso} (\AA^2)	3.354×10^{-2}	9.211×10^{-3}	-
	C ₂ U_{iso} (\AA^2)	1.000×10^{-1}	2.165×10^{-2}	-
	C ₃ U_{iso} (\AA^2)	1.966×10^{-3}	9.961×10^{-2}	-
$[\text{Fe}_3\text{O}(\text{AcO})_6(\text{H}_2\text{O})_3]^+$	Relative scale	0.000	0.922	0.000
	δ_2 (\AA^2)	-	3.369	-
	Fe U_{iso} (\AA^2)	-	1.365×10^{-2}	-
	O U_{iso} (\AA^2)	-	1.000×10^{-1}	-
	C U_{iso} (\AA^2)	-	3.399×10^{-2}	-
Fe_3O_4	Relative scale	0.000	0.703	1.000
	a (\AA)	-	8.859	8.437
	δ_2 (\AA^2)	-	2.370	0.823
	Fe U_{11} (\AA^2)	-	1.783×10^{-1}	8.782×10^{-3}
	Fe U_{12} (\AA^2)	-	5.192×10^{-4}	1.645×10^{-3}
	Fe U_{iso} (\AA^2)	-	6.333×10^{-3}	2.466×10^{-3}
	O U_{11} (\AA^2)	-	2.610×10^{-1}	1.622×10^{-2}
	O U_{12} (\AA^2)	-	2.626×10^{-2}	1.413×10^{-2}

Table S4.5: Assigned vibrational modes observed in the *in situ* ATR-FTIR spectra.

Peak position (cm^{-1})	Vibrational mode	Assigned to
1739	$\nu(\text{C}=\text{O})$	Benzyl acetate
1717	$\nu(\text{C}=\text{O})$	Acetone
1380	$\delta_{\text{as}}(\text{CH}_3)$	Methyl
1361	$\delta_{\text{s}}(\text{CH}_3)$	Methyl
1225	$\nu(\text{C}-\text{O})$	Benzyl acetate

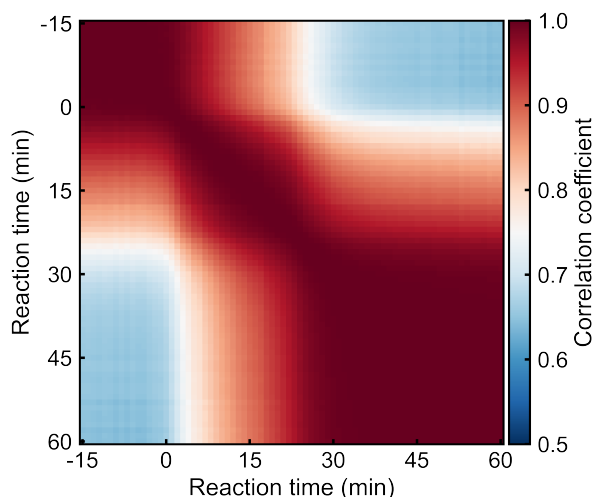


Figure S4.7: Pearson correlation map of the *in situ* PXRD data. Pearson correlation mapping quantifies the similarity between diffraction patterns collected at different time points, providing a visual representation of structural evolution during the reaction. Correlation coefficient values close to 1 (red) indicate high similarity, whereas low correlations (blue) indicate strong differences. The maps clearly reveal three distinct reaction stages corresponding to the precursor complex, the intermediate phase, and the final Fe_3O_4 product. The first transition occurs shortly after 0 min, and the second around 25 min as indicated by the nodes along the diagonal. The Pearson correlation map was calculated for PXRD pattern between q_{min} of 1.9 \AA^{-1} and q_{max} of 25.0 \AA^{-1} .

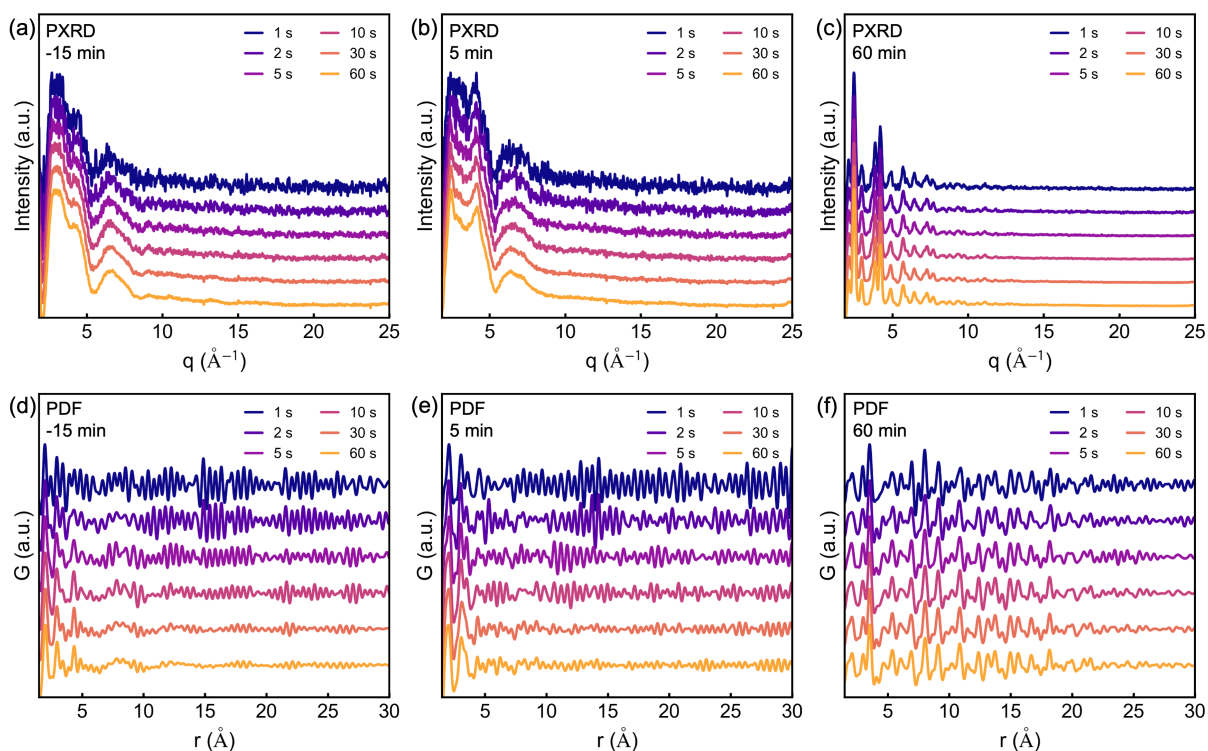


Figure S4.8: PXRD and PDF data collected at -15, 5, and 60 minutes reaction time. Data are averaged over 1 to 60 individual patterns, each acquired with a 1 s exposure time.

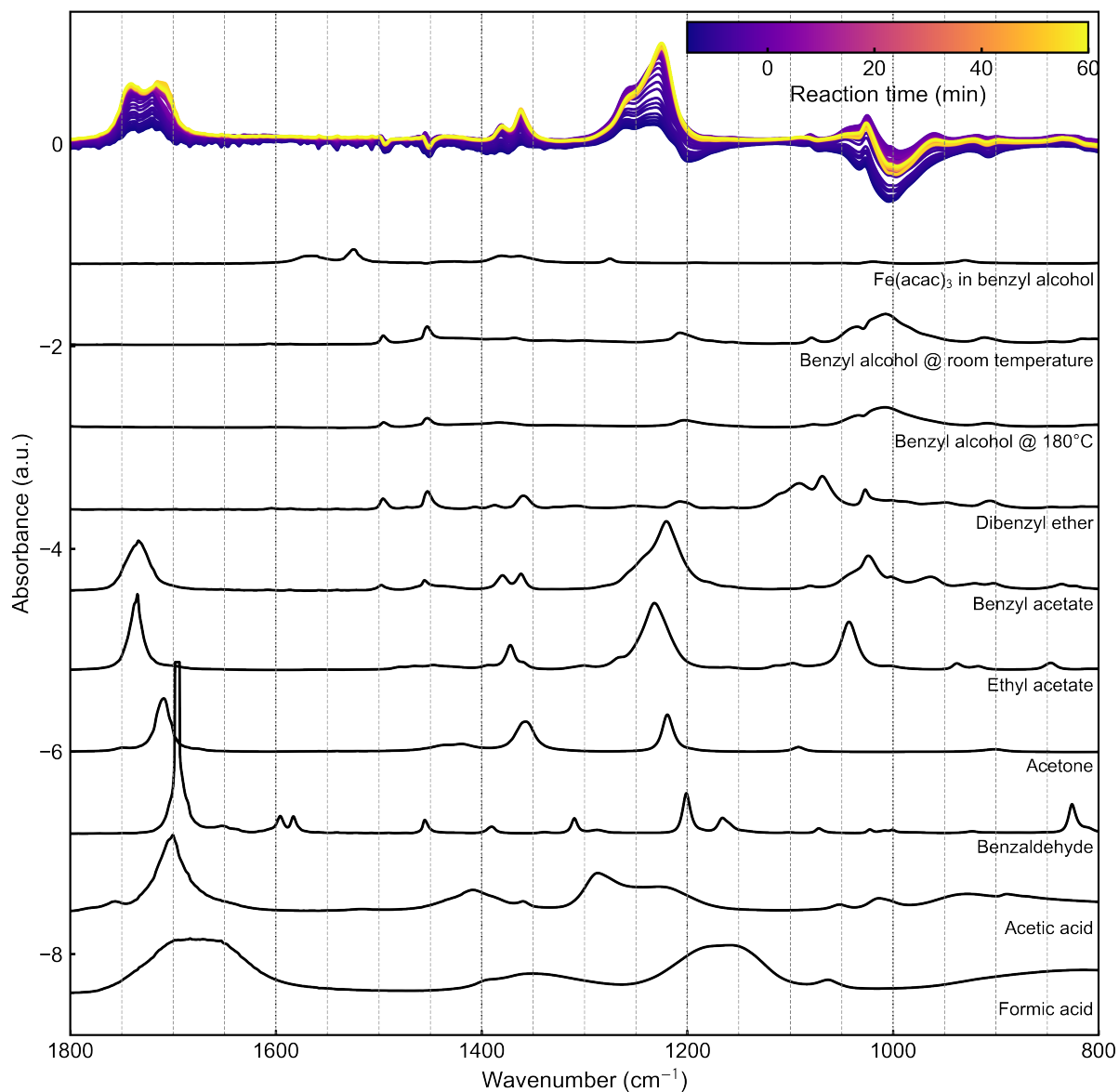


Figure S4.9: *in situ* ATR-FTIR analysis of the reaction of Fe(acac)₃ to Fe₃O₄ in BnOH, compared to reference spectra of Fe(acac)₃ dissolved in BnOH, BnOH at room temperature, and at 180 °C, dibenzyl ether, benzyl acetate, ethyl acetate, acetone, benzaldehyde, acetic acid, and formic acid.

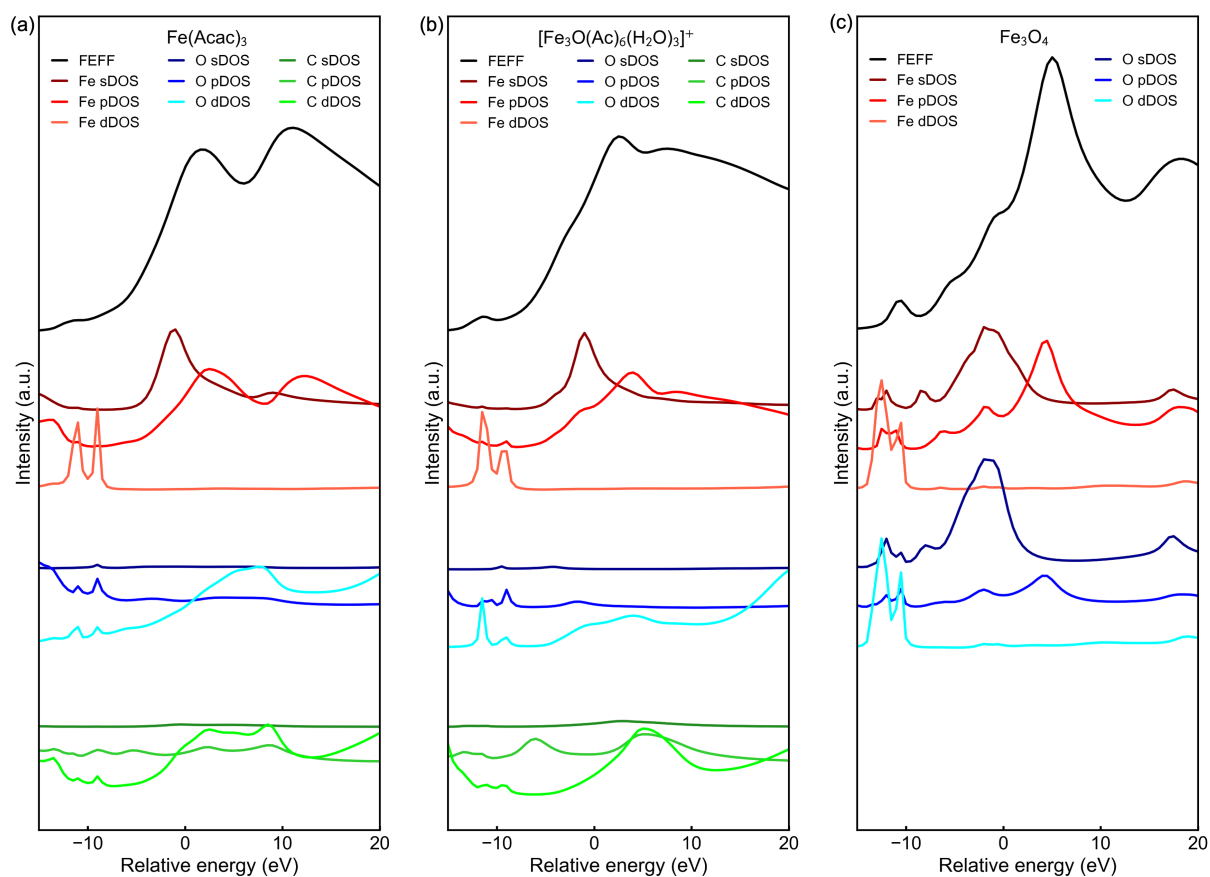


Figure S4.10: FEFF simulated XANES spectra and their corresponding density of states (DOS) of s, p and d states of (a) $\text{Fe}(\text{acac})_3$, (b) $[\text{Fe}_3\text{O}(\mu_3\text{-O})(\text{AcO})_6(\text{H}_2\text{O})_3]^+$, and (c) Fe_3O_4 .

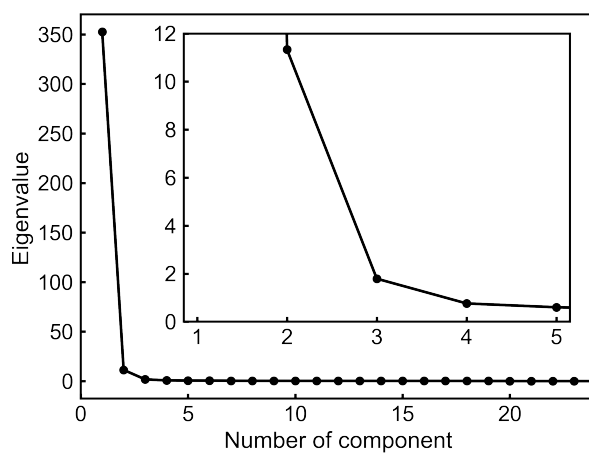


Figure S4.11: Eigenvalue profile of MCR-ALS analysis.

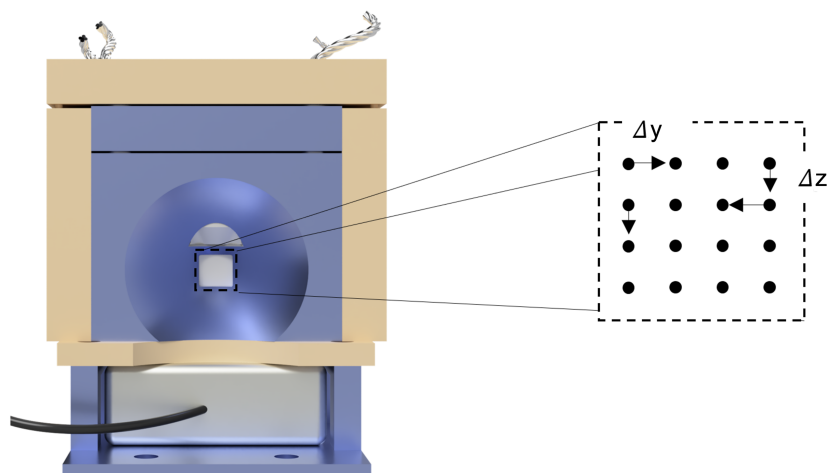


Figure S4.12: Schematic of the scanning pattern across the X-ray window used for XAS measurements to minimize beam damage. Repeated exposure of the same sample area is avoided by collecting spectra at different sample positions along a defined trajectory with step sizes Δy and Δz along the horizontal and vertical axes of the sample window.

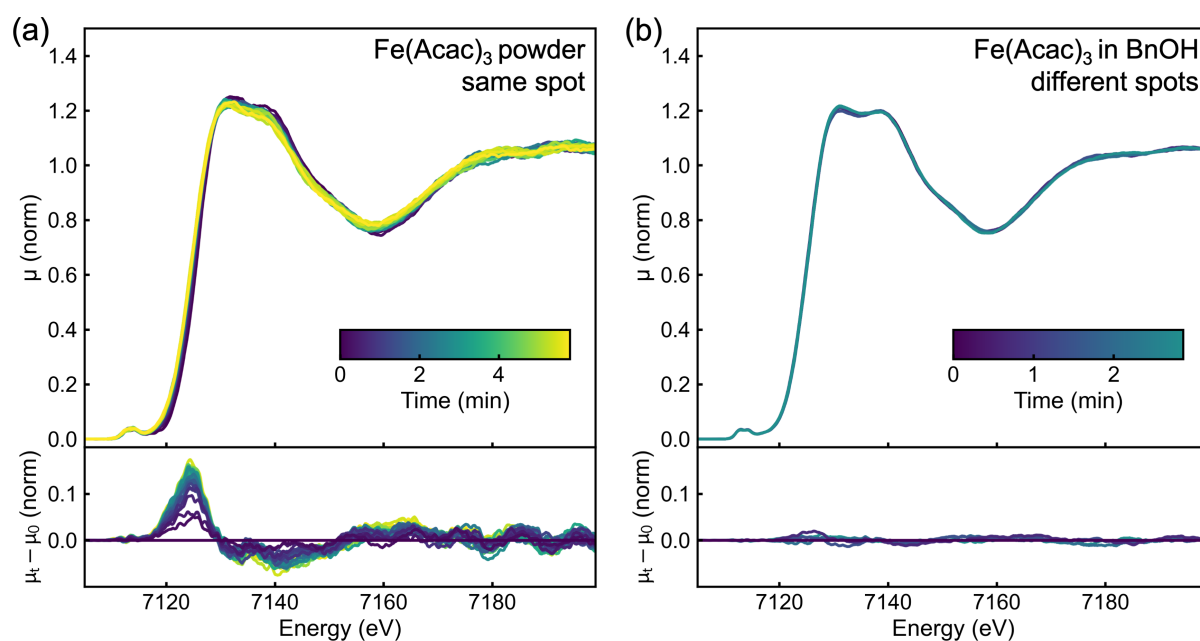


Figure S4.13: Beam damage study on $\text{Fe}(\text{acac})_3$. (a) Fe K-edge HERFD-XANES spectra of $\text{Fe}(\text{acac})_3$ powder recorded at room temperature over 30 consecutive scans (12 s each) at the same sample position on the sample. (b) Fe K-edge HERFD-XANES data of $\text{Fe}(\text{acac})_3$ in benzyl alcohol (BnOH) recorded at room temperature over 5 consecutive scans (42 s each) at different sample positions. The upper panels in (a) and (b) show the HERFD-XANES spectra while the lower panels show the difference of the spectra at the respective time μ_t and the first spectra at 0 min μ_0 . The spectra recorded at the same sample spot (a) show beam damage evident by the shift of the absorption edge and the decrease of the white-line intensity. The spectra recorded at different sample spots (b) show no strong spectral changes. This demonstrates that scanning across different sample positions, as illustrated in Figure S12, effectively enables avoiding beam damage. These scanning conditions were used for the *in situ* Fe K-edge HERFD-XANES measurements.

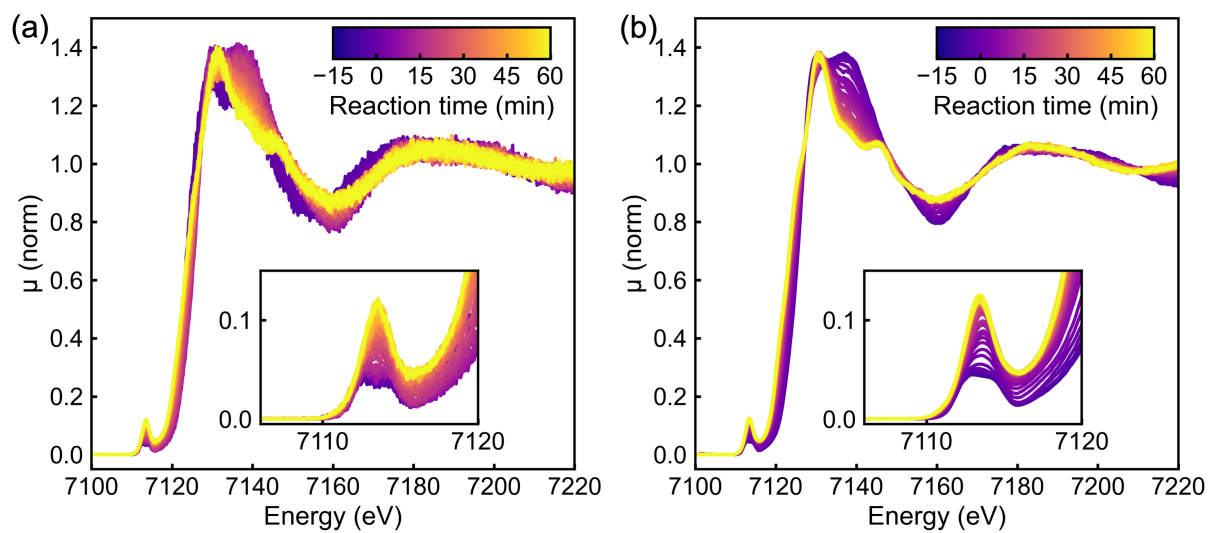


Figure S4.14: *In situ* Fe K-edge HERFD-XANES data before (a) and after (b) processing as discussed in the experimental section.

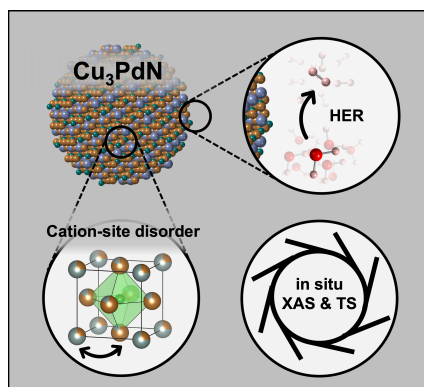
5 *In Situ* X-ray Study on Cation-Site Disordered Cu₃PdN Nanoparticles for Hydrogen Evolution Electrocatalysis

The content of this chapter was published in *Small* 21, 33, (2025) by Sani Y. Harouna-Mayer, Jagadesh Kopula Kesavan, Francesco Caddeo, Lian Belgardt, Chia-Shuo Hsu, Lars Klemeyer, Lizzi Kipping, Melike Gumus Akcaalan, Tjark R.L. Groene, Andrea Köppen, Heshmat Noei, Olivier Mathon, Ann-Christin Dippel, and Dorota Koziej.

My contribution to this work comprises: synthesis of Cu₃PdN nanoparticles, analysis of HRTEM, SAED, STEM:EDX, and UV-Vis spectroscopy data; measurement and analysis of PXRD data and *in-situ* TS data; and review of TMNs as electrocatalysts for the HER.

5.1 Abstract

Transition metal nitrides (TMNs) are emerging as a promising class of materials for application in optoelectronics as well as energy conversion and storage, but they remain rather unexplored, mainly due to a lack of mechanistic understanding of their synthetic pathways. Here, a one-pot synthesis is demonstrated, which yields 3 nm phase-pure Cu₃PdN nanoparticles after the reaction of Cu methoxide and Pd acetylacetonate in benzylamine for 5 min at 140 °C. The structure of the initial complexes and their conversion to Cu₃PdN are revealed by *in situ* X-ray absorption spectroscopy measurements and elucidate nucleation and growth of the nitride nanocrystals by *in situ* total X-ray scattering measurements. Interestingly, extended X-ray absorption fine structure double-edge refinement reveals the presence of short-range cation-site disorder in the anti-perovskite structure of Cu₃PdN, which has not been observed before in the Cu₃PdN system. Additionally, the synthesized Cu₃PdN nanoparticles are tested for the electrocatalytic hydrogen evolution reaction, revealing an overpotential as low as $\eta_{10} = 212 \pm 11$ mV measured at 10 mA cm⁻².



5.2 Introduction

Transition metal nitrides (TMNs) are a versatile class of materials that exhibit properties of covalent compounds, ionic crystals and transition metals.^{44,137,138} The incorporation of the nitride (N^{3-}) anion into the metal sublattice causes expansion of the parent metal lattice and metal d-band broadening.¹³⁹⁻¹⁴¹ These unique electronic and bonding characteristics give rise to numerous applications particularly in energy conversion and storage.^{43,44,138,142,143} Recent studies explored several TMNs as materials of interest for electrochemical energy conversion, focusing on the influence of morphology¹⁴⁴⁻¹⁴⁶, defect engineering¹⁴⁷⁻¹⁴⁹, heteroatom doping^{150,151}, heterostructuring^{152,153} or alloying^{154,155} on their electrochemical performance. Despite the progress, challenges remain, such as achieving scalability, stability in aqueous media or cost-effective and green synthetic methods, since TMN synthesis typically involves steps at high temperatures and/or pressure.^{43,143} Further, the synthesis of TMNs involves reaction pathways that are still poorly understood. A deeper understanding of the synthesis and reaction mechanisms is crucial to fully explore the TMN space and develop TMN materials with desired chemical and physical properties with respect to their application.^{43,156,157}

Among TMNs, Cu_3N has emerged as a promising material since it is non-toxic and earth-abundant, showing potential for cost-efficient solar energy conversion, catalysis and optoelectronics.¹⁵⁸ Cu_3N exhibits the anti- ReO_3 structure with corner-shared N-centered Cu-N octahedra. The vacant cubic central position can be occupied by a dopant such as Pd forming e.g. Cu_3PdN which changes the electronic structure from semiconducting to semimetallic.¹⁵⁹⁻¹⁶³ Cu_3PdN has been proposed to be a node-line semimetal and topological superconductor.¹⁶⁴⁻¹⁶⁶ Further, Cu_3PdN shows good electrochemical catalytic activity and stability for nitrate reduction¹⁶⁷, CO_2 reduction^{168,169}, O_2 reduction¹⁷⁰ and formic acid oxidation¹⁷¹. So far there are no reports on its activity for the hydrogen evolution reaction (HER). Independent of the application, Cu_3PdN exhibits superior catalytic activity and/or stability over the Pd deficient Cu_3N ^{167,170} as well as N deficient Cu_3Pd ^{168,171} or Pd^{167,170,171} counterparts.

All reported solvothermal synthetic approaches for Cu_3PdN follow the same route: $Cu(NO_3)_2 \cdot 3H_2O$ and $Pd(acac)_2$ form 10 – 20 nm sized Cu_3PdN nanoparticles (NPs) after 5 - 60 min at 230 - 250 °C in oleylamine (OAm) and 1-octadecene or hexadecane (Table S5.1).^{55,167-171} The reaction temperature can be decreased to 190 °C if Au, Pt and Pt- Fe_3O_4 NP seeds are used.¹⁷² In the reported synthesis route, OAm is expected to be both reductant and nitrogen source. First, OAm is oxidized by the nitrate and Cu(II) to a primary aldimine which reacts with extant OAm to a secondary aldimine, releasing ammonia. Consequently, ammonia reacts with Cu(I) forming Cu_3PdN .⁵⁵ This mechanism has been proposed based on the analysis of the reaction byproducts using 1H nuclear magnetic resonance (NMR), which is sensitive to the organic species present at the end of the reaction, but does not give exhaustive information on the nature of the metal complexes leading to the formation of the Cu_3PdN NPs. Moreover, limited information is given on the phase purity of Cu_3PdN NPs obtained with the OAm route, since the published PXRDs patterns display a peak shape anisotropy that likely indicates the presence of bimetallic Cu_3Pd impurities.^{55,167-172}

Here, we report a rapid, one-pot synthesis route that yields phase pure, highly crystalline 3 nm Cu_3PdN NPs. Unlike aforementioned reports on Cu_3PdN synthesis,^{55,167-172} we can decrease the reaction temperature to 140 °C by replacing copper (II) nitrate trihydrate with copper (II) methoxide and dissolving it, jointly with palladium (II) acetylacetonate, in benzylamine instead of OAm. Similar to the Cu_3N synthesis,⁵⁴ benzylamine acts as ligand, reductant and nitrogen source.

First, we perform Rietveld refinement and extended X-ray absorption fine structure (EXAFS) analysis of *ex situ* PXRD and X-ray absorption spectroscopy (XAS) data, respectively, to demonstrate phase purity and to examine the local structure around Cu and Pd in the anti-perovskite Cu₃PdN crystal structure. We find that the as prepared 3 nm Cu₃PdN NPs display cation-site disorder, with the Cu and Pd atoms being distributed at the corners and at the face centers of the cation fcc sublattice, with partial occupancy. This is the first time that cation-site disorder is reported for the case of colloidal TMNs with the anti-perovskite structure.¹⁷³⁻¹⁷⁵

Additionally, using *in situ* high-energy resolution fluorescence detected X-ray absorption near-edge structure (HERFD-XANES) and pair distribution function (PDF) analysis of TS, we investigate the reaction pathways involving the Cu and Pd starting complexes during the synthesis of Cu₃PdN in benzylamine. HERFD-XANES is a powerful, element-specific technique that probes the emergence of the electronic structure of a material and monitors the coordination of metal centers during the synthesis, including the formation and transformation of metal-organic complexes and intermediates into the desired crystalline nanomaterial, thereby shedding light on the reaction mechanism.^{91,176} Meanwhile, PDF analysis investigates the atomic structure of a material and thus allows to monitor the nucleation and growth of Cu₃PdN NPs.⁶⁶ Hence, *in situ* HERFD-XANES complemented by *in situ* PDF provides both electronic and structural insights, giving a comprehensive picture of the synthetic pathways together with the appearance of a metallic Cu₃Pd impurities for extended reaction times.

Finally, we test the electrocatalytic properties of the as synthesized Cu₃PdN NPs for the HER, showing good catalytic activity with an overpotential of $\eta_{10} = 212 \pm 11$ mV measured at 10 mA cm⁻² and excellent stability with no change of the overpotential after 10000 linear sweep voltammetry (LSV) cycles. Figure 5.1 shows a schematic representation of the work conducted in this report.

5.3 Results and Discussion

We perform the solvothermal synthesis of Cu₃PdN nanoparticles by reacting Cu(OCH₃)₂ and Pd(acac)₂ in benzylamine, which acts both as the solvent and nitrogen source. The reaction is carried out at 140 °C under inert atmosphere in a custom-made heating cell that enables precise control of reaction parameters such as the reaction temperature, reaction time, ramp rate and stirring of the reaction solution.⁹⁶ The reaction yields Cu₃PdN nanoparticles with sizes of ~3.5 nm for reaction times of 5 to 15 min as shown in Figure S5.1. Figure 5.2a shows a high resolution transmission electron microscopy (HRTEM) image of the Cu₃PdN nanoparticles after 5 minutes reaction time. The identified lattice spacing of 1.9 Å, 2.2 Å and 2.7 Å correspond to the (200), (111), and (110) planes, respectively, and are highlighted in Figure 5.2b. The corresponding selected area electron diffraction (SAED) pattern displays diffraction peaks with position and intensities consistent with the anti-perovskite crystal structure of Cu₃PdN as shown in Figure 5.2c. The elemental color mapping with overlay and line scan confirm that the nanoparticles are composed of Cu, Pd and N atoms and their signals overlap uniformly as shown in Figure 5.2d and 5.2e. We determine the composition of the as-synthesized nanoparticles by elemental analysis to be Cu₃ · 06 PdN₁ · 00, consistent with the expected Cu₃PdN stoichiometry, where the high nitrogen content is attributed to surface-bound benzylamine. Figure 5.2f shows the UV-vis spectra of Cu₃PdN nanoparticles. Unlike previous study that reported an indirect bandgap of 0.2 eV, we observe a direct optical bandgap of 0.61 eV. The discrepancies may arise due to the particle size being four times smaller and, more importantly, the absence of impurities in our sample.⁵⁵ Further studies of the optical

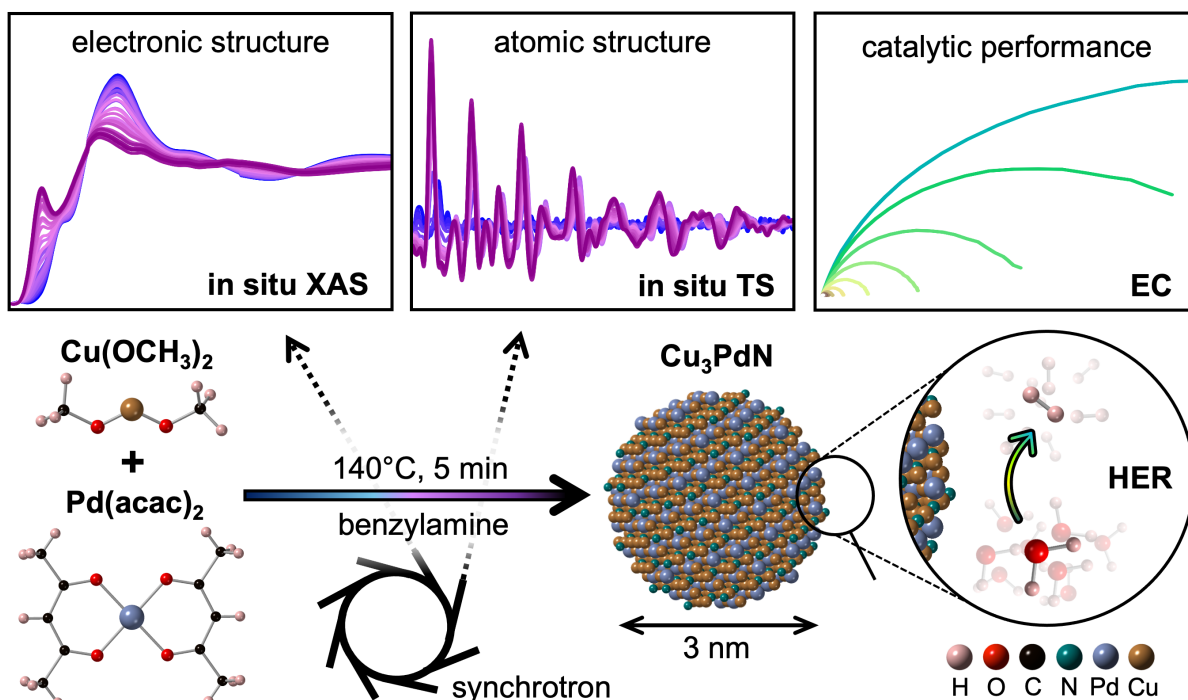


Figure 5.1: Schematic illustration of the present work. The reaction of Cu(II) methoxide and Pd(II) acetylacetonate, which yields Cu_3PdN nanoparticles after 5 min at 140°C in benzylamine, is studied using *in situ* X-ray absorption spectroscopy (XAS) and *in situ* total scattering (TS). The synthesized Cu_3PdN nanoparticles are tested for their electrochemical (EC) catalytic activity of the hydrogen evolution reaction (HER).

properties are beyond the scope of this work. The thermogravimetric analysis (TGA) of the obtained Cu_3PdN nanoparticles in nitrogen atmosphere (Figure S5.2) depicts a weight loss at low temperature below 160°C due to the removal of residual organics and a second one at temperature above 250°C likely due to the reduction of Cu_3PdN to bimetallic/metallic.⁵⁵

Cu_3Pd might form as a secondary phase during the synthesis of Cu_3PdN , thus we first check the phase purity of the obtained Cu_3PdN nanoparticles via Rietveld refinement of the PXRD patterns, as shown in Figure 5.2g. The PXRD patterns of Cu_3PdN and Cu_3Pd are very similar, with subtle differences in peak intensity and position, since both structures share the same space group and exhibit a slightly different lattice parameter as illustrated in Figure S5.3. In Figure S5.4, we simulate two-phase PXRD patterns with different phase ratios of $\text{Cu}_3\text{PdN}:\text{Cu}_3\text{Pd}$. The presence of a Cu_3Pd impurity generates a peak-shape anisotropy, which is most prominently visible at the most intense (111) reflection at around $2\Theta = 41^\circ$ (assuming Cu K-alpha radiation, $q = 2.9 \text{ \AA}^{-1}$). This peak shape anisotropy is present in most of the PXRD patterns of previously reported Cu_3PdN syntheses^{55,167–172}, confirming that the presence of Cu_3Pd impurity is often overlooked. The PXRD patterns of our Cu_3PdN nanoparticles prepared with a reaction time of 5, 10 and 15 minutes are reported in Figure S5.5 and confirm the absence of Cu_3Pd impurities. The Cu_3Pd phase appears only after reaction times longer than 15 minutes, as also confirmed by our *in situ* TS study discussed below.

The nitride phase purity of synthesized Cu_3PdN NPs is further confirmed by the X-ray photoelectron spectroscopy (XPS). The core level Cu 2p, Pd 3d and N 1s spectra of synthesized Cu_3PdN NPs are depicted in Figure 5.2h-j. The Cu binding energies (BE) of the main peaks at 932.69 eV and 952.54 eV are assigned to Cu 2p_{3/2} and Cu 2p_{1/2}, respectively, and these binding energies are related to the monovalent Cu (I) species.^{55,167–171} In addition to the main Cu (I)

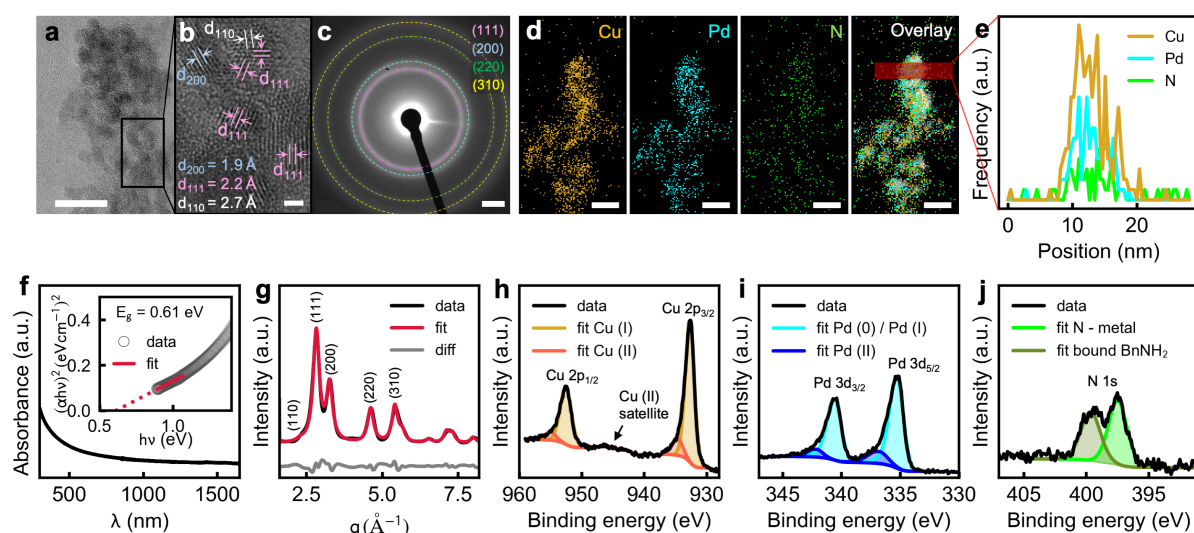


Figure 5.2: Ex situ characterization of Cu₃PdN NPs grown after 5 min reaction time. **a** HRTEM of Cu₃PdN NP agglomerate. **b** Zoom of a showing polydisperse spherical NPs. **c** SAED of a Cu₃PdN assembly. **d** STEM:EDX elemental mapping of Cu, Pd and N and an overlay of the mapped elements on the original STEM image. **e** EDX elemental line profiles of the area highlighted in c showing evenly distributed Cu, Pd and N. **f** UV-vis absorption spectrum of Cu₃PdN NPs redispersed in N-methyl-2-pyrrolidone with its corresponding Tauc plot, assuming a direct allowed transition as an inset. The dotted red trace shows the extrapolation of the linear fit shown as a solid red trace. **g** PXRD Rietveld refinement. XPS core-level spectra of **h** Cu 2p, **i** Pd 3d and **j** N 1s. Scales: a: 10 nm; b: 1 nm; c: 2 1/nm; d: 10 nm.

peaks, a less intense peak at 934.66 eV and 955.03 eV and the presence of a very weak-intense satellite peak around 941 – 946 eV are related to Cu (II), which is found in all the other reports of Cu₃PdN.^{55,167–171} The Pd 3d_{5/2} and 3d_{3/2} core level components at 335.23 eV and 340.46 eV, respectively, are related to Pd (0)/Pd (I). The secondary weak intense peaks at 335.97 eV and 341.49 eV are related to the Pd (II).¹⁶⁷ From the peak fitting analysis, the Cu (II) and Pd (II) contributions are around 13.5 % and 7.9 %, respectively. The N 1s core level spectrum is deconvoluted into two peaks at 397.47 eV and 399.63 eV are related to the metal-nitrogen bond and residual benzylamine bound to the surface of the Cu₃PdN NPs, respectively.

To further confirm the phase purity, we perform EXAFS analysis, which allows to determine the local structure around the absorbing atom.¹⁷⁷ In addition to being an element-specific technique, EXAFS is well suited for multielement materials, allowing to obtaining insights such as atomic rearrangements, defects and disorders.

The attempt to refine the *ex situ* EXAFS data of both Cu and Pd K-edges using the ordered anti-perovskite crystal structure does not yield a satisfactory agreement, as shown in Figure S5.6. A careful look at the Fourier-transformed Pd K-edge data compared with the simulated spectrum (Figure S5.7) reveals the presence of a peak around 1.6 Å might be originating from the scattering contribution of Pd-N distances in the first coordination shell of Pd atoms. This is a clear indication of the presence of a partial short-range cation-site disorder in the Cu₃PdN NPs, where the Cu and Pd atoms are located at the corners and at the face centers of the cation fcc sublattice, with partial occupancy, as shown in Figure 5.2j. This result is further supported by the oxidation state of the Cu cation. In the ordered structure, the average oxidation state of Cu is +1⁵⁵ and it is expected to be < +1 for the structure with cation-site disorder. The maximum of the first derivative of Cu K-edge XANES of Cu₃PdN in Figure S5.8 is slightly higher (8979.7 eV) than the reference Cu foil (8979.0 eV) and lower than the Cu₃N (8980.28 eV). Furthermore,

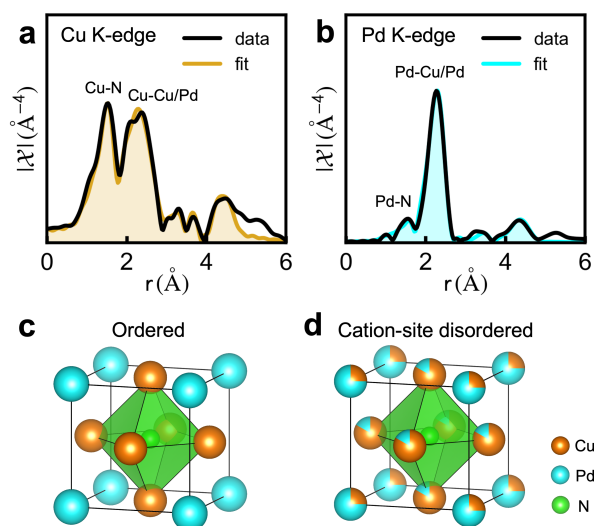


Figure 5.3: EXAFS fits showing the cation-site disorder. a Cu K-edge EXAFS fit. **b** Pd K-edge EXAFS fit. **c** Ordered and **d** cation-site disordered antiperovskite unit cell of Cu_3PdN .

when compared to the literature value for Cu_3N and Cu_2O (8980.5 eV) in which the oxidation state of Cu is +1^{178,179}, our sample's edge position is slightly at lower energy ($\Delta E = 0.8$ eV). This clearly emphasizes that the average oxidation state of Cu in Cu_3PdN is $< +1$, which further hints to the presence of cation-site disorder in our Cu_3PdN NPs. We therefore perform a double-edge EXAFS refinement, utilizing both Cu K-edge and Pd K-edge EXAFS data which allows to resolve the local structure around the Cu and Pd atom and to quantitatively assess the cation-site occupancy. The multi-shell fitting method employed uses the physical constraints given by the crystallographic structure, which includes the lattice parameter and the Cu-Pd and Pd-Pd distances. The many-body amplitude reduction factor (S_0^2) and the energy origin shift (ΔE_0) were considered as fixed parameters.¹⁸⁰ Further details of the EXAFS analysis is given in the supporting information. The Fourier-transformed EXAFS spectra, and their best fits are shown in Figure 5.3a and 5.3b and in Figure S5.6. It is important to note and it is common that the cation-site disorder induces a local distortion partially, leading to the short Cu – Pd bond length of 0.08 – 0.1 Å in the second shell without affecting the lattice symmetry.¹⁸¹ The EXFAS fit of our Cu_3PdN NPs confirms the presence of partial short-range cation-site disorder where about 25 % of the Pd atoms exchanged their lattice position. The interatomic distances, the disorder fraction (1-x) and Debye-Waller factors obtained from the fit can be found in Table S5.3. This short-range cation-site disorder occurs mainly due to low cation mobility, fast growth rate at the low temperature and short reaction times employed during the synthesis, which favors the formation of the disordered over the ordered structures.¹⁸² The short- and long-range disorder have already been experimentally observed and theoretically predicted in II-IV- N_2 wurtzite-derived structures^{175,183–186} (e.g. MgSnN_2 , ZnGeN_2) and other TMNs.^{187–189} The cation-site disorder in the nitride system is highly beneficial and allows to control and tune the properties such as band gap, ion and thermal conductivity.^{190,191} Nevertheless, it is important to highlight that this type of cation-site disorder has not been reported before for the case of colloidal anti-perovskite structured nitride systems, especially in Cu_3PdN .

The analysis of *ex situ* PXRD and EXAFS measurements demonstrates the phase purity of the obtained Cu_3PdN NPs and reveals cation-site disorder within the anti-perovskite crystal lattice. To elucidate the reaction pathways leading to the Cu_3PdN NPs as in 5.4a, we employ *in situ* Cu K-edge HERFD-XANES and PDF of *in situ* TS data. Figure 5.4b shows the *in situ* Cu K-edge HERFD-XANES data. The initial spectrum, blue trace, shows the Cu species in the

initial reaction solution at room temperature. The last spectrum, purple trace, shows the final product Cu₃PdN after 10 min at 140 °C. The reaction solution is heated up to the reaction temperature of 140 °C with a heating rate of 10 °C min⁻¹. The time at which the reaction temperature is reached is defined as 0 min. The room temperature XANES spectrum exhibits a pre-edge peak at 8977 eV, feature A in Figure 5.4b, which is the fingerprint of Cu²⁺ originating from the quadrupole-allowed 1s-3d transition.^{192,193} Feature B at the rising edge, at 8983 eV, is due to the 1s to unoccupied 4p transition.^{192,193} A clear, intense rising edge transition feature is evident for a square-planar coordination.^{194,195} At elevated temperature, the pre-edge feature A, disappears, while the white-line intensity, feature D, decreases, and the edge energy is shifted towards lower energy as indicated by the arrows in Figure 5.4b. This is a clear indication of the reduction of Cu²⁺ to Cu¹⁺. Further, we attribute the simultaneous increase in the intensity of feature B to a linear coordination of Cu¹⁺ with two N as present in Cu₃PdN, which confirms the formation of the nitride phase.¹⁹⁴

We apply the multivariate curve resolution by multivariate curve resolution by alternating least squares (MCR-ALS) method to the *in situ* HERFD-XANES data and extract the evolution of two distinct Cu components during the reaction, indicating that the initial Cu complex directly reduces to the final Cu₃PdN phase with no intermediates, as soon as the reaction temperature reaches 140 °C, as shown in Figure 5.4c. Their corresponding eigenvalue profile is shown in Figure S5.11, while the full-time series of individual Cu K-edge HERFD-XANES spectra, including their MCR-ALS contributions, can be found in Figure S5.12. By comparing the recovered spectra with FEFF¹³¹ simulations, we attribute the starting Cu complex formed when Cu(OCH₃)₂ is dissolved in benzylamine (BnNH₂) to [Cu₂(BnNH₂)₄(OCH₃)₂]²⁺, Figure 5.4d, left panel. In this complex, two Cu ions are bridged and coordinated with two amine molecules and two methoxy groups in a square planar configuration, as visualised in Figure 5.4a. In addition to FEFF, the structure of the Cu complex is confirmed by EXAFS refinement of the initial spectrum, as shown in Figure S5.13, in which the first coordination around Cu is 2 O atoms at 1.92 Å and 2 N atoms at 1.98 Å. This complex is similar to the one reported already when Cu(I) is dissolved in methanol and BnNH₂ at room temperature.¹⁹⁶ Moreover, we identify the Pd complex present in the reaction solution at room temperature and Cu₃PdN 10 min after reaching 140 °C by *ex situ* Pd K-edge XANES in Figure 5.4d, right panel. When the Pd(acac)₂ is dissolved in BnNH₂, the acetylacetonate ligand is released and the Pd²⁺ ion center is coordinated with four BnNH₂ molecules in a square-planar configuration, forming [Pd(BnNH₂)₄]²⁺, Figure 5.4a.¹⁹⁷ The Cu K-edge and Pd K-edge XANES spectra of the initial precursors and final product, together with their corresponding FEFF simulated spectra, are shown in Figure 5.4d. The FEFF simulated spectra of Cu₃PdN are based on a 2x2x2 supercell (Figure S5.14), which allows for introducing partial cation-site disorder without site occupancies.

We complement the *in situ* HERFD-XANES results with *in situ* PDF analysis as shown in Figure 5.4e. Consistent with the HERFD-XANES, PDF analysis shows the prompt formation of Cu₃PdN NPs upon reaching the reaction temperature of 140 °C, indicated by the emergence of distinct features at high *r* and the shift of the first peak from ~2.1 to 2.0 Å and the second peak from ~2.9 to 2.7 Å. The first and second peaks are highlighted in green and orange, respectively, in Figure 5.4e, and the evolution of the peak position is displayed in Figure S5.16. The first and second shell interatomic distances, corresponding to the first and second peak in the PDF, are consistently highlighted in the representation of the starting complexes [Cu₂(BnNH₂)₄(OCH₃)₂]²⁺ and the Cu₃PdN unit cell in Figure 5.4a. Here we assume the ordered anti-perovskite structure without cation-disorder since the PDF hardly has sensitivity to the cation-disorder in a high symmetry structure like Cu₃PdN, as shown by PDF simulations in Figure S5.17. The *in situ* PDF data is compared to PDF simulations of the starting complexes

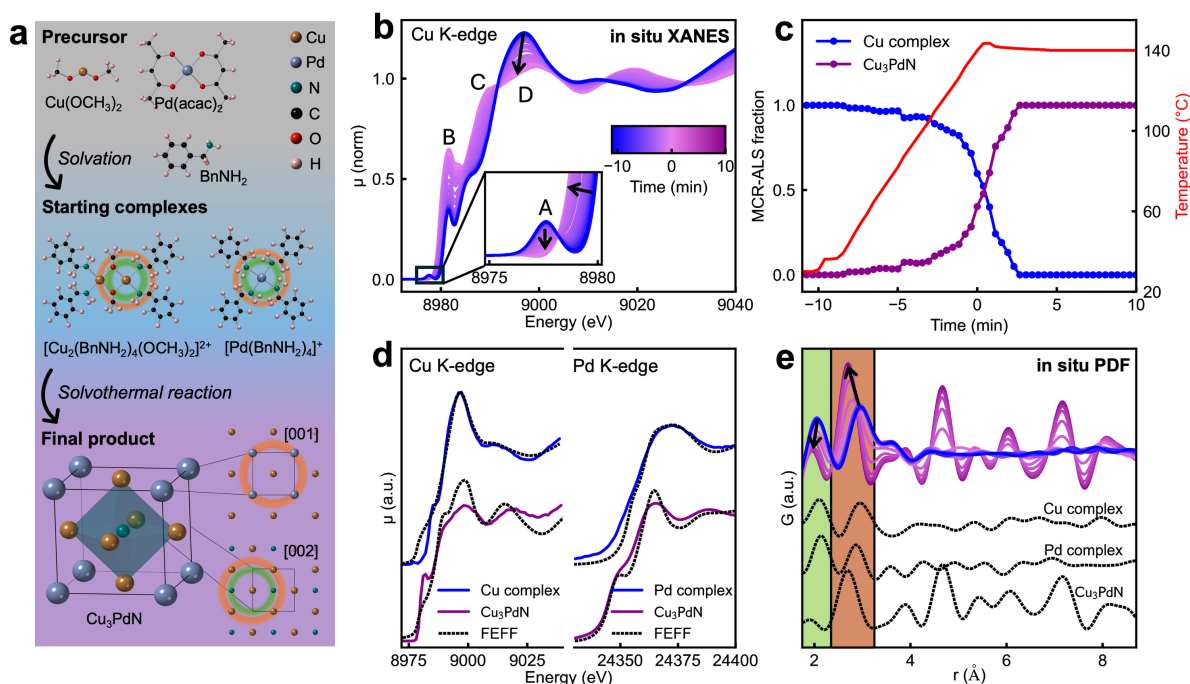


Figure 5.4: *In situ* XANES and PDF analysis of the reaction to Cu_3PdN . **a** Schematic of reaction mechanism. The $\text{Cu}(\text{OCH}_3)_2$ and $\text{Pd}(\text{acac})_2$ precursors dissolve in benzylamine to form $[\text{Cu}_2(\text{BnNH}_2)_4(\text{OCH}_3)_2]^{2+}$ and $[\text{Pd}(\text{BnNH}_2)_4]^+$ complexes, respectively, which form Cu_3PdN upon heating. The first shell and second shell around the metal atoms are highlighted by green and orange circles, respectively. **b** *In situ* Cu K-edge HERFD-XANES data and **c** corresponding MCR-ALS analysis of the *in situ* Cu K-edge HERFD-XANES show the formation of Cu_3PdN from the Cu starting complex without intermediates. **d** XANES spectra of the starting complexes and cation-site disordered Cu_3PdN at Cu K-edge and Pd K-edge compared to FEFF simulations. The left panel shows the recovered spectra of the Cu starting complex and final product Cu_3PdN from MCR-ALS analysis. The right panel shows *ex situ* XANES spectra of Pd starting complex and Cu_3PdN . The spectra are in good agreement with the FEFF simulations of the respective structures. **e** *In situ* PDFs $G(r)$. The *in situ* PDF data is compared to PDF simulations of the Cu and Pd starting complexes and Cu_3PdN phase in dashed black traces.

and the Cu_3PdN phase shown as dashed traces in Figure 5.4e. The initial PDF, blue trace, matches the superposition of the PDF simulations of the Cu and Pd complex, and the last PDF, purple trace, matches the PDF simulation of phase-pure Cu_3PdN as shown in Figure 5.4e. In Figure S5.16c we analyze the *in situ* PDF by a linear combination of the initial PDF and the final PDF, which shows consistent reaction pathways to the MCR-ALS findings of Cu K-edge HERFD-XANES. Figure S5.18 shows the full time-series of the individual PDFs. A detailed description of the analysis procedures and data processing routines are given in the Supporting Information.

For reaction times exceeding 15 min at 140 °C, *in situ* time-resolved PDF refinements (Figure S5.19-S5.21) reveal a further reduction of Cu_3PdN to the bimetallic Cu_3Pd phase, which completes within 40 min. The phase transformation is indicated by a peak shift to lower r , corresponding to a decrease in the lattice constant as nitrogen atoms leave the crystal lattice. In this context, our *ex situ* PXRD and EXAFS characterization, combined with *in situ* XANES and PDF analysis, provides a comprehensive view of the reaction pathway during synthesis, highlighting that an accurate control of the reaction parameters is needed to achieve phase pure Cu_3PdN NPs.

Phase purity is particularly important when evaluating the electrocatalytic performance of

a material. For example, Cu₃PdN has shown superior electrochemical activity for processes such as CO₂ reduction¹⁶⁸ and formic acid oxidation¹⁷¹ compared to the metallic Cu₃Pd phase. Interestingly, the electrocatalytic performance of Cu₃PdN NPs for the HER, the cathodic compartment of a water splitting cell, has not been reported so far. We therefore deposited our Cu₃PdN NPs on a glassy carbon electrode and tested their electrochemical performance for the HER in acidic media, using a 0.5 M H₂SO₄ aqueous solution as the electrolyte. For comparison, the bare glassy carbon electrode and 20 wt% Pt/C deposited on glassy carbon with the same catalyst loading were also tested under the same conditions. The linear sweep voltammetry (LSV) scan in Figure 5.5a reveals an overpotential of $\eta_{10} = 212 \pm 11$ mV measured at 10 mA cm⁻² and an onset potential of $\eta_1 = 67 \pm 12$ mV defined at 1 mA cm⁻². The Tafel plot in Figure 5.5b displays a slope of 125 mV/dec suggesting that the HER on Cu₃PdN follows the two-step Volmer-Heyrovský mechanism:¹⁹⁸



where in the first step (5.1) protons are discharged to form adsorbed hydrogen (H_{ads}) followed by the electrochemical desorption of an H₂ molecule during the second step (5.2). A Tafel slope close to 120 mV/dec is often attributed to the Volmer reaction being the rate-determining step, although recent studies also suggest that such a slope can be obtained for the Heyrovský reaction being the rate-determining step when the surface of the catalyst is highly covered with adsorbed hydrogen species.¹⁹⁹ We also determine the double layer capacitance (C_{dl}) of the electrode from cyclic voltammetry measurements as shown in Figures 5.5c and S5.22, suggesting that the Cu₃PdN NPs display a high number of active site and an electrochemically active surface area (ECSA) about 21 times higher than the bare glassy carbon electrode. We further assess the stability of the Cu₃PdN NPs during HER operation as shown in Figure 5.5d. We perform 10000 repeated LSV cycles and recorded a small cathodic shift of about 5 mV after refreshing the electrolyte, suggesting that the Cu₃PdN NPs show remarkable stability during HER operation. The stability of Cu₃PdN NPs in the electrolyte and during long-term electrochemical tests is further confirmed by PXRD and XPS measurements, Figure S5.24 and S5.25. We further investigate the charge transfer kinetics at the electrode-electrolyte interface via electrochemical impedance spectroscopy (EIS). In Figure 5.5e we show a typical Nyquist plot, displaying the presence of a single semicircle with decreasing diameter moving to more cathodic potentials, which suggests that the process is dominated by a charge transfer resistance with the absence of additional processes such as diffusion and mass transport limitations. We model the data with a simple equivalent circuit comprising a resistor (R_s) in series with a parallel combination of a charge transfer resistance (R_{CT}) and a constant phase element as shown in Figure S5.23. Figure 5.5f shows the dependence of the obtained R_{CT} as a function of the applied potential. At the overpotential of $\eta_{10} = 212$ mV, R_{CT} drops to 9.5 Ω, indicating an efficient charge transfer resistance at the catalyst-electrolyte interface. We further obtain a Tafel plot utilizing the R_{CT} extracted from the EIS fitting (inset in Figure 5.5f), revealing a slope of 125 mV/dec, which is identical to the one obtained with the voltammetric analysis. This indicates that the HER at the surface of Cu₃PdN proceeds under pure charge transfer kinetics, without limitations arising from mass transfer diffusion.

Figure 5.5g presents a comparative overview of the overpotentials and Tafel slopes reported in the literature for various nitrides during HER. The activity of the Cu₃PdN NPs obtained in this study compares favorably with that of other reported metal nitrides, as the overpotential

of most tested nitrides falls within the range of 100 – 250 mV. It is noteworthy that many of the reported nitrides are either supported on a porous substrate (e.g. Ni₂N on nickel foam²⁰⁰) or are synthesized as composites (e.g. Mo₂N-Mo₂C²⁰¹⁻²⁰³). These strategies effectively lower the overpotential required for the HER, by utilizing a catalyst support with a very large surface area or by leveraging the synergistic catalytic properties of composite heterostructures. Adopting these approaches could further enhance the performance of Cu₃PdN in future studies. Nevertheless, our findings indicate that phase pure Cu₃PdN NPs are a promising electrocatalyst for the HER in acidic media.

5.4 Conclusion

This study presents the one-pot synthesis of phase-pure, highly crystalline Cu₃PdN NPs with an average size of 3 nm using benzylamine as a solvent at 140 °C, which is, so far, the lowest reported reaction temperature for Cu₃PdN synthesis. The Rietveld refinement of the *ex situ* PXRD patterns demonstrates the phase purity of the obtained Cu₃PdN NPs, shedding light on the occurrence of Cu₃Pd impurities often overlooked in previous reports. Crucially, the double-edge EXAFS analysis reveals the occurrence of disorder in the anti-perovskite crystal lattice, with about 25 % of the Pd atoms interchanging their position with adjacent Cu atoms, generating a disordered structure with partial cation-site occupancy. The significantly smaller size of the synthesized Cu₃PdN NPs, less than half of the previously reported colloidal Cu₃PdN, provides a high surface area, making them highly suitable for application in electrocatalysis. We showcase that Cu₃PdN is suitable for the HER, revealing remarkable stability and an overpotential of 212(11) mV at 10 mA cm⁻² which is comparable to many other reported nitride catalysts. Supporting Cu₃PdN on porous substrates with a large surface area such as Ni foam could be a strategy to further lower the overpotential required for the HER. Furthermore, additional *in situ/operando* investigations are needed to unveil the HER mechanism at the surface of Cu₃PdN NPs.

We further monitor the reaction pathway leading to the formation of Cu₃PdN NPs in benzylamine, employing *in situ* HERFD-XANES and PDF analysis of *in situ* TS data. We observe that the solvation of the Cu and Pd precursors leads to the formation of [Cu₂(BnNH₂)₄(OCH₃)₂]²⁺ and [Pd(BnNH₂)₂]²⁺ as starting complexes which then directly react and convert to Cu₃PdN immediately after reaching the reaction temperature of 140 °C. For an extended reaction time (>15 min), further reduction of Cu₃PdN to bimetallic Cu₃Pd occurs, emphasizing that a meticulous control of the reaction parameters can prevent the formation of impurities.

In conclusion, our study offers comprehensive insights into the structural and mechanistic aspects of Cu₃PdN NP formation. The ability to control the cation-site disorder through parameters such as heating rate, reaction temperature and time or precursor concentrations could enable to tailor properties like the band gap, electronic conductivity and electrocatalytic activity. Additionally, tuning those reaction parameters could impact the size and size distribution of the Cu₃PdN NPs. The methodologies and findings presented here can be applied to other TMNs, opening avenues for optimizing their properties and expanding their potential applications in energy conversion and beyond.

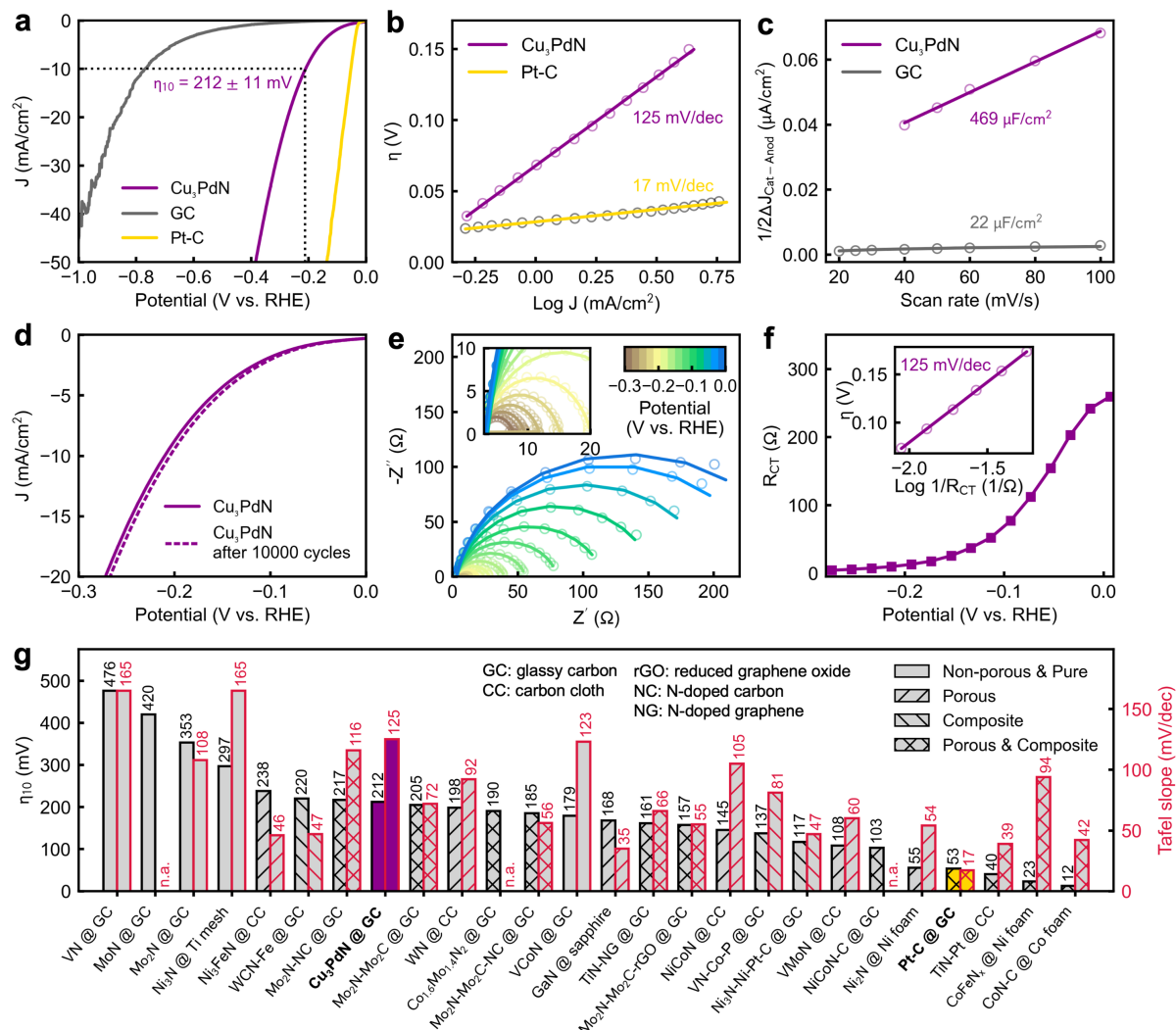


Figure 5.5: Electrocatalytic performance of Cu₃PdN NPs for the HER. **a** Typical LSV curve of Cu₃PdN NPs deposited on glassy carbon, compared with Pt-C and bare glassy carbon electrode, measured at a scan rate of 10 mV/s. **b** Tafel plot obtained from the LSV curves. **c** double layer capacitances obtained from the half-slope of the capacitive currents extracted from cyclic voltammetry measurements at increasing scan rates. **d** LSV scans before and after 10000 LSV cycles to assess the stability of the electrode. **e** Nyquist plot obtained via EIS measurements. **f** Dependence of the charge transfer resistance obtained by fitting the EIS data, along with the Tafel plot obtained using the RCT extracted from the impedance fitting (inset). **g** Comparison of the obtained overpotential and Tafel slope, highlighted with a colored bar and bold label, with other transition metal nitrides from the literature; missing data points are noted as n.a.: not available.^{200–222}

5.5 Experimental Section

Chemicals

All Chemicals were purchased from commercial sources and used without further purification: $\text{Cu}(\text{OCH}_3)_2$ (Thermo Scientific, 98%), $\text{Pd}(\text{acac})_2$ (Sigma Aldrich, 99%), benzylamine (Sigma Aldrich, 99%), hexane (Sigma Aldrich, 99%), N-methyl-2-pyrrolidon (VWR, 99.8%), H_2SO_4 (Carl Roth, 96%), methanol (VWR, 99.8%), NAFION (Ion-Power, 5% in methanol). All chemicals used for the syntheses were stored and handled in the glove box under inert atmosphere (Ar 6.0, $c(\text{H}_2\text{O}) > 0.1$ ppm, $c(\text{O}_2) > 0.1$ ppm).

Synthesis

In a typical synthesis, a stock solution is prepared in the glove box by adding $\text{Cu}(\text{OCH}_3)_2$ (37.7 mg, 0.3 mmol) and $\text{Pd}(\text{acac})_2$ (30.5 mg, 0.1 mmol) to 5 mL of benzylamine and stirring until all precursors are dissolved. Subsequently, a quantity of 2.5 mL was transferred to the inlet of the heating cell. Instead, for *in situ* reactions, a quantity of 0.3 mL was transferred to the respective reaction container for *in situ* XAS or *in situ* TS, respectively, as explained below. Consequently, the reaction container was assembled in the heating cell, taken out of the glovebox and heated to 140 °C with a heating rate of 10 °C min⁻¹ under vigorous stirring. After the desired reaction time at 140 °C the heating cell was cooled to room temperature. After the synthesis, the NPs were washed 3 times with hexane and centrifuged for 10 min at 10000 rpm. After the last centrifugation step, the nanocrystals were dried under nitrogen flow. The NP dispersion for HRTEM, STEM:EDX, STEM and UV-vis characterization were prepared by redispersing the NPs in N-methyl-2-pyrrolidon after the last centrifugation step and discarding the supernatant before drying under nitrogen flow to prevent agglomeration of the synthesized NPs.

Heating cell

The synthesis is carried out in a custom-made heating cell which enables precise control of the ramp rate, reaction temperature and reaction time, allows for stirring and operates under solvothermal conditions. The heating cell consists of a metal body and isolating polyether ether ketone (PEEK) (Bieglo) elements. Four heating elements (Cartridge heaters, 24 V, 50 W, Maxi watt) and a temperature sensor (Pt1000, Honeywell) were used to control the temperature with a temperature controller (Model 336, Lakeshore Cryotronics) and a power supply (EA-PS 310060-340, Elektro-Automatik). For the reaction, the heating cell is mounted on top of a magnetic stirring motor (Cimarec i, Thermo Scientific). The reaction takes place in a PEEK inlet as reaction container. The heating cell is also used for *in situ* XAS and *in situ* TS experiments. *In situ* XAS experiments take place in a PEEK inlet with 0.2 mm wall thickness in reflection geometry. *In situ* TS experiments take place in a fused silica inlet with 0.5 mm wall thickness in transmission geometry. The heating cell is discussed in detail in the literature.⁹⁶ We note that the synthesis is also feasible in a conventional autoclave. The reaction requires vigorous stirring in addition to an inert atmosphere which can be achieved by placing the reaction solution and a stirring magnet in the autoclave and heating the autoclave in an oil bath on a magnetic stirring plate. However, precise control over the reaction time is not possible in the conventional autoclave.

In situ High Energy Resolution Fluorescence Detected X-ray Absorption Near Edge Structure (HERFD-XANES)

In situ Cu K-edge HERFD-XANES measurements were performed at ID26¹³² and ID24²²³ beamlines of the European Synchrotron Radiation Facility (ESRF), Grenoble, France. The incident x-ray energy was chosen using the reflection from the Si(111) double crystal monochromator (DCM) and varied from 8970 to 9060 eV at ID26 (radius of curvature $R = 1$ m) and 8970-9040 eV at ID24-DCM ($R = 0.5$ m). The spectra were acquired in HERFD mode, using a 5-analyzer crystal

spectrometer in Johann geometry. To detect the maximum intensity of the Cu K α_1 emission line (8046 eV), we used five spherically bent Si(444) crystals¹³³ aligned at the Bragg angle of 79.4°. The HERFD-XANES spectra were recorded in a continuous scan mode every 20-25 s in the energy range of 8970-9060 eV with a step size of 0.2 eV. The overall energy resolution is about 1.70 eV of FWHM at the Cu K α_1 emission line. The beam spot size was about 200x200 μm^2 , and the beam position on the cell was moved after 2-5 scans to avoid sample damage due to the long exposure to x-rays. The details of the beam damage study can be found in the SI. The *ex situ* powder samples were measured as pellets diluted with cellulose.

In situ Total Scattering (TS) and Pair Distribution Function (PDF) analysis

In situ TS data was acquired at beamline P21.1 of PETRA III at Deutsches Elektronen-Synchrotron DESY, Hamburg, Germany. Scattering images were recorded every 1 s at an x-ray energy of 101.39 keV ($\lambda = 0.1222 \text{ \AA}$) using a 2D X-ray detector (PerkinElmer XRD1621, Varex Imaging Corp.) with 2048 x 2048 pixels and a pixel size of 200x200 μm^2 and a sample-to-detector distance of 0.604 m, obtained from a calibration with a LaB₆ powder standard packed into the fused silica inlet of the heating cell. A detailed description of the PDF analysis procedures is given in the supporting information. The code used for data processing of the PDF data is available at https://gitlab.rrz.uni-hamburg.de/BAS0906/shm_2024_cu3pdn.

X-ray photoelectron spectroscopy (XPS)

The XPS system employed in this work is located in the DESY NanoLab (<https://jlsrf.org/index.php/lsf/article/view/140>) in Hamburg, Germany. It is equipped with a monochromated Al K α source ($h\nu = 1486.6 \text{ eV}$) and a Phoibos 150 hemispherical energy analyzer with a base pressure of 1.5×10^{-10} mbar. The pristine Cu₃PdN powder sample is directly deposited on the carbon tape. The sample on the glassy carbon (GC) electrode (1x1 cm²) after the electrochemical test is washed 5 times with deionized water and 3 times with ethanol. After drying, the samples are then loaded into the UHV chamber and measured after evacuation. The details of the deposition of Cu₃PdN on the GC electrode is given in the section of Electrochemical characterization. The XPS data are analyzed using the Casaxps software. The surface contaminated aliphatic carbon C 1s peak at 284.41 eV is used to calibrate the binding energies. The GL30 (Gaussian 70% & Lorentzian 30%) type profile is used as a fitting function after subtracting the Shirley type background.

Electrochemical characterization

The working electrode for the electrochemical measurements was prepared by deposition of the NPs onto an L-shaped glassy carbon electrode with a surface area of 0.78 cm². Specifically, 40 μL of a 2 mg/mL dispersion of Cu₃PdN in methanol were drop-casted for six times onto the glassy carbon electrode. Afterwards, a NAFION solution was prepared by mixing 290 μL of methanol with 2 μL of a 5% NAFION dispersion in methanol. 40 μL of the obtained NAFION dispersion were drop-casted onto the glassy carbon electrode with the Cu₃PdN nanoparticles for three times. All the electrochemical measurements were conducted in 0.5M H₂SO₄ employing the typical three-electrode configuration using a graphite rod and an Ag/AgCl (3M KCl) as counter and reference electrodes, respectively. Prior to the measurement, the electrolyte was degassed by flushing Ar for about 15 minutes. The polarization curves were recorded by liner-sweep voltammetry at a scan rate of either 10 or 1 mV/s in a potential range of 0 to -1 V vs. RHE. All polarization curves were not corrected for iR drop. The double-layer capacitances (C_{dl}) were estimated by cyclic voltammetry using a previously reported method.²²⁴ Cyclic voltammetry scans were carried out in a 60 mV potential window around the open circuit potential, where no Faradaic processes occur, with variable scan rates, from 10 to 100 mV/s. The double-layer capacitances (C_{dl}) were extracted from the half slope of the linearly fitted curves of the capacitive currents ($J_{anodic} - J_{cathodic}$) versus the scan rates. EIS measurements

were carried out in a potential window from 0 to -0.35 V vs. RHE with a potential step of 20 mV, an AC sinus amplitude of 10 mV (mean square root voltage $V_{\text{rms}} = 7.07$ mV), a frequency range of 100 kHz – 0.1 Hz and an equilibration time of 30 s between each potential step. The EIS spectra were fitted using the software EC-Lab from Biologic. For all the electrochemical measurements, the potentials acquired with the Ag/AgCl reference electrodes were converted to the RHE scale using the equation E (V vs. RHE) = E (V vs. Ag/AgCl (3 M KCl)) + 0.197 + 0.059 x pH. All electrochemical measurements were recorded using a Biologic SP-150 potentiostat.

Powder X-ray Diffraction (PXRD) & Rietveld Refinement

PXRD patterns were acquired on a Bruker Advanced D8 with Cu $K\alpha$ -radiation of 8.0478 keV ($\lambda = 1.5406$ Å). Rietveld refinements and PXRD simulations were carried out with GSASII.⁶⁹ Instrumental parameters have been retrieved by refining a LaB₆ standard.

High-Resolution Transmission Electron Microscopy (HRTEM)

HRTEM images were collected using a JEOLJEM-2200FS (JEOL Ltd.) with an acceleration voltage of 200 kV. The synthesized sample was dispersed in N-methyl-2-pyrrolidone and deposited on a gold grid.

STEM:EDX

STEM:EDX images were collected using a Regulus 8220 (Hitachi High Technologies Corp.) with an acceleration voltage of 30 kV and the BFSTEM acquisition mode.

UV-vis

UV-visible spectra were collected with a Cary 60 UV-vis spectrometer (Agilent Technologies Inc.) in a quartz cuvette. The sample was dispersed in N-methyl-2-pyrrolidone.

Elemental analysis

The Cu concentration was determined using Flame Atomic Absorption Spectroscopy (F-AAS) with a Soolar S Series spectrometer (Thermo Scientific). The Pd concentration was determined using Inductively Coupled Plasma Optical Emission Spectroscopy (ICP-OES) using a Spectro Arcos spectrometer (SPECTRO Analytical Instruments GmbH). The N concentration was determined using a EuroEA3000 CHNS-O Analyzer (EuroVektor S.p.A.).

Statistical analysis

The details of the data processing, treatment of every technique used in this work are explained in their respective subsections in the supporting information.

Acknowledgements

This research was supported by the European Research Council (LINCHPIN project, grant no. 818941), the Deutsche Forschungsgemeinschaft (DFG) through the Cluster of Excellence “Advanced Imaging of Matter” (EXC 2056, project ID 390715994) and by the Bundesministerium für Bildung und Forschung (BMBF) via the project 05K22GU7 (LUCENT II). We acknowledge Marvin Skiba and Moritz Dybowski for TGA and UV-vis measurements, respectively. We also acknowledge DESY (Hamburg, Germany), a member of the Helmholtz Association, and ESRF (Grenoble, France) for the provision of experimental facilities. Parts of this research were carried out at PETRA III using beamlines P21.1 and P64 and at ESRF using beamlines ID26, ID24 and BM23 under proposals MA5366⁷⁹ and HC-4929²²⁵. We thank the beamline staff for the support with the experiments: at ID26 Dr. Pieter Glatzel, at P21.1 Dr. Fernando Igoa Dr. Jiatu Liu and at P64 Dr. Wolfgang Caliebe.

S5 Supporting information

Table S5.1: Review of Cu₃PdN solvothermal synthesis routines.

Reference	Precursors	Solvent/ Ligand	Temp.	Reaction time	Morphology Composite	Particle size/ Crystallite size/ Lat. par.	Degassing
Vaughn et al. 2014 ¹⁷⁰	Cu(NO ₃) ₂ · 3 H ₂ O & Pd(acac) ₂	1-octadecene & OAM	240 °C	5 min to 15 min	Quasi-cubic	16(2) nm 8 nm 3.82 Å	10 min @ 120 °C
Jia et al. 2016 ¹⁷¹	Cu(NO ₃) ₂ · 3 H ₂ O & Pd(acac) ₂	1-octadecene & OAM	250 °C	30 min	Spherical	11.3(25) nm 11.2 nm	10 min @ 120 °C
Lord et al. 2019 ¹⁷²	Cu(NO ₃) ₂ · 3 H ₂ O & Pd(acac) ₂ + metal NP seeds	1-octadecene & OAM	190 °C	30 min	Heterostructures / Cu ₃ PdN @ Pt/Pd	-	60 min @ 120 °C
Li et al. 2021 ¹⁶⁹	Cu(NO ₃) ₂ · 3 H ₂ O & Pd(acac) ₂	1-octadecene & OAM	245 °C	20 min	Quasi-cubic	20(2) nm - -	-
Jia et al. 2021 ¹⁶⁸	Cu(NO ₃) ₂ · 3 H ₂ O & Pd(acac) ₂	1-octadecene & OAM	230 °C	15 min	Spherical / on rGO	16 nm 4.0(46) nm 3.81 Å	5 min @ 120 °C
Parvizian et al. 2022 ⁵⁵	Cu(NO ₃) ₂ · 3 H ₂ O & Pd(acac) ₂	hexadecane & OAM	240 °C	5 min to 60 min	Cubic	10.2 nm 4.5(11) nm 3.83 Å	30 min @ 50 °C
Yao et al. 2023 ¹⁶⁷	Cu(NO ₃) ₂ · 3 H ₂ O & Pd(acac) ₂	1-octadecene & OAM	240 °C	15 min	Spherical / on activated carbon	18 nm	10 min @ 120 °C
This work	Cu(OCH ₃) ₂ & Pd(acac) ₂	benzylamine	140 °C	5 min to 15 min	Spherical	3.5(10) nm 3.5(10) nm 3.83 Å	-

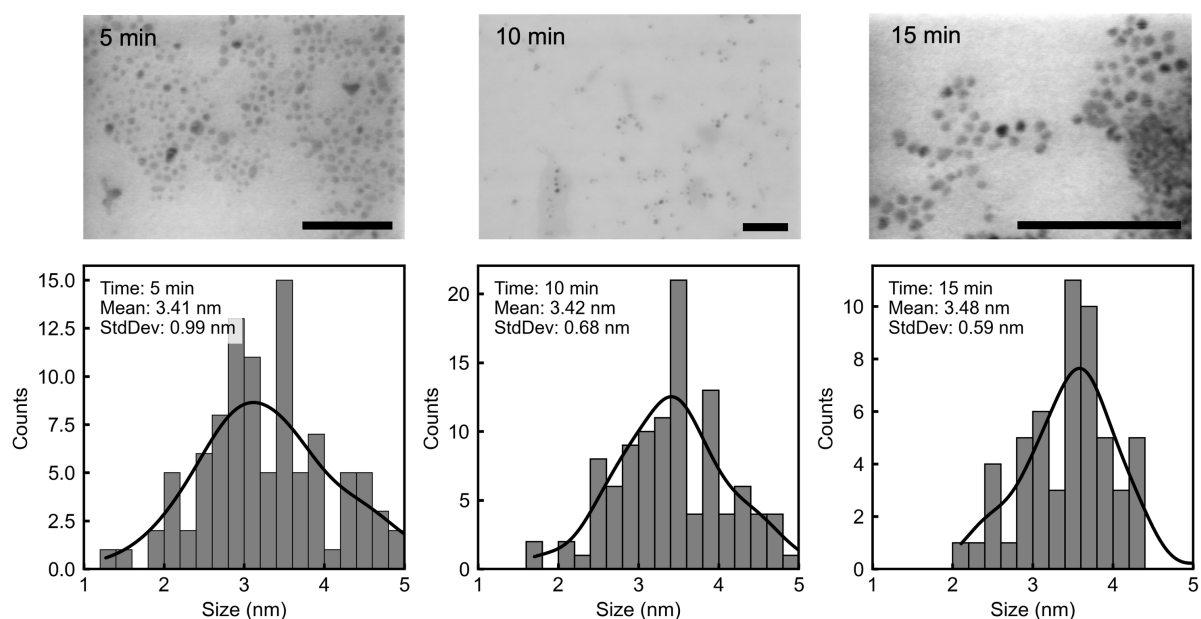


Figure S5.1: STEM images and size distribution of Cu₃PdN grown for 5, 10 and 15 min reaction time at 140 °C. Number of measured particles (n): 5 min: 103, 10 min: 107, 15 min: 56. Scalebar 50 nm.

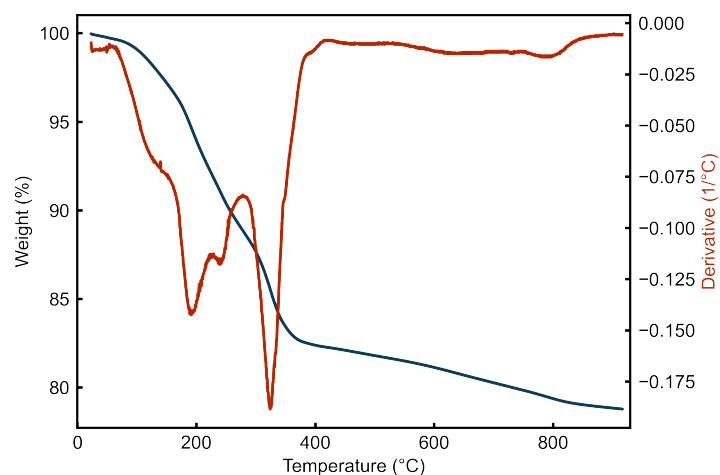


Figure S5.2: TGA performed under a nitrogen atmosphere of Cu_3PdN 15 min reaction time at 140 °C.

Phase impurity

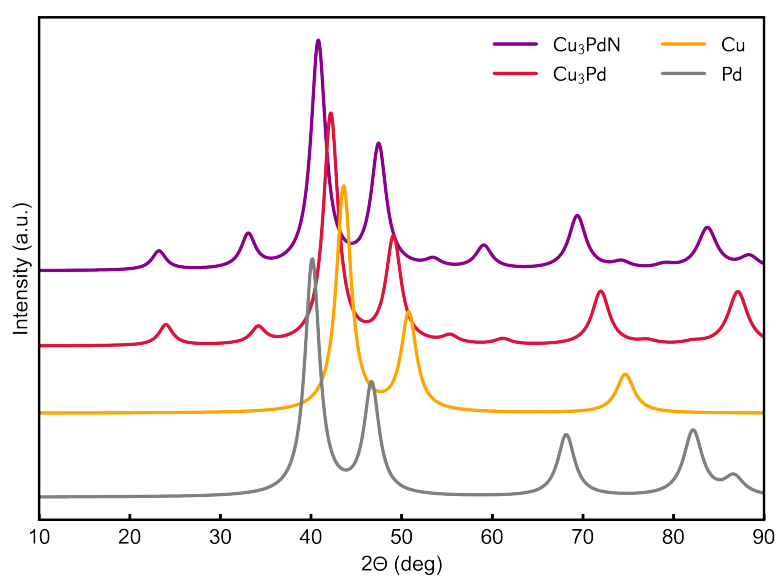


Figure S5.3: Simulated PXRD pattern of Cu_3PdN , Cu_3Pd , Cu and Pd. All patterns are simulated with GSASII⁶⁹ using Cu $K\alpha$ -radiation ($\lambda = 1.5406 \text{ \AA}$) and a crystallite size of 5 nm.

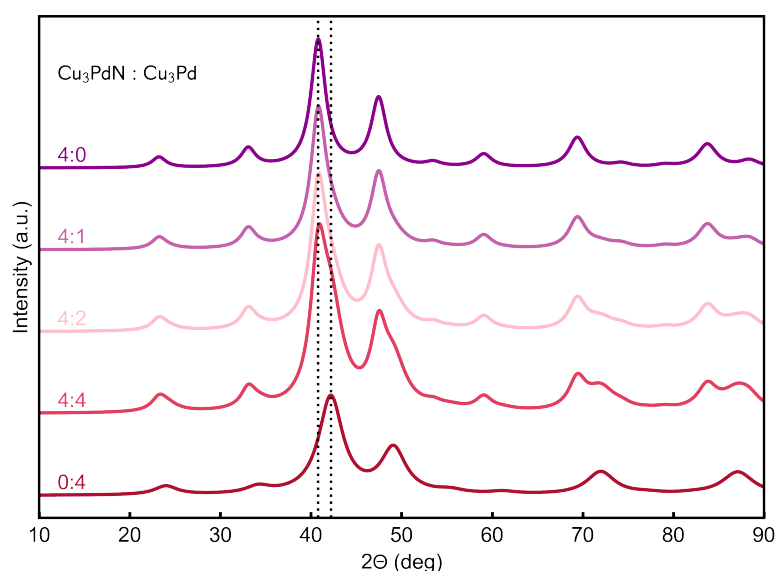


Figure S5.4: Simulated two-phase PXRD pattern of Cu_3PdN and Cu_3Pd at varying phase ratios. All patterns are simulated with GSASII⁶⁹ using Cu $K\alpha$ -radiation ($\lambda = 1.5406 \text{ \AA}$). Cu_3PdN and Cu_3Pd phases are simulated with a crystallite size of 5 and 3 nm, respectively. The simulated two-phase PXRD patterns comprise individual computed patterns of the two phases with the respective crystallite size which are added with the respective phase ratios.

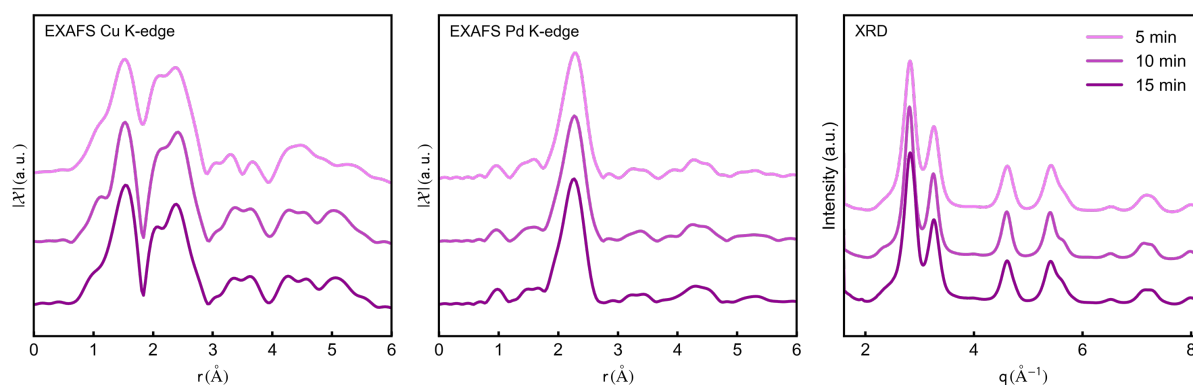


Figure S5.5: Waterfall plot of EXAFS Cu K-edge, EXAFS Pd K-edge and PXRD of Cu_3PdN grown for 5, 10 and 15 min reaction time at 140°C .

EXAFS refinements

The cation-site disorder in Cu_3PdN nanoparticles is determined by EXAFS refinement on ordered and disordered structural models, as shown in Figure S5.6. Below we describe the refinement procedures for the ordered and disordered models. More details on the EXAFS data processing and the refinement procedure are available in the section **Technical information on XANES and EXAFS analysis**. Cu_3PdN exhibits the anti-perovskite structure which consists of corner-shared, N-centered Cu-N octahedra with a Pd atom in the central cubic position. In the ordered case, the local coordination around Cu in the first shell is Cu-N at 1.91 \AA ; the second shell is composed of Cu-Cu and Cu-Pd coordination at 2.70 \AA and the third shell is Cu-Cu coordination at 3.86 \AA . In the case of Pd, the first coordination is Pd-Cu at 2.70 \AA , second coordination is Pd-N at 3.25 \AA and the third shell coordination is Pd-Pd at 3.86 \AA . Based on these components including the multiple scattering components, the Cu and Pd K-edge data

were fitted in the case of ordered structure and fits are shown in Figure S5.6. In the case of disordered structure, two crystallographic models are considered. They are (i) ordered anti-perovskite structure: as explained above and (ii) fully disordered anti-perovskite structure: Pd and Cu are fully displaced their positions. The scattering components of both structures are used as linear combination to fit the data. i.e. $S_0^2 \cdot x$ and $S_0^2 \cdot (1-x)$ and x is considered as a refining parameter. Obviously, the Cu – N, Pd – N, Cu – Cu and Pd – Pd scattering components are not common to both edges. The Debye-Waller (DW) factors for multiple scattering components are fixed to twice the single scattering ones which is necessary to limit the free parameters for the fit. The DW factors for some of the components in the second and third coordination shell are high due to the cation disorder. It is also seen in figure S5.7 that the intensity of the peaks in the simulated spectra is high compared to the experimental data. The scattering components used for the fit and their corresponding distance variation parameter and DW factors with graphical representations are listed in Table S5.2. The refinement results of all the three samples are shown in Table S5.3 and the spectra with best fits in R-space and in k-space are shown in Figure S5.6.

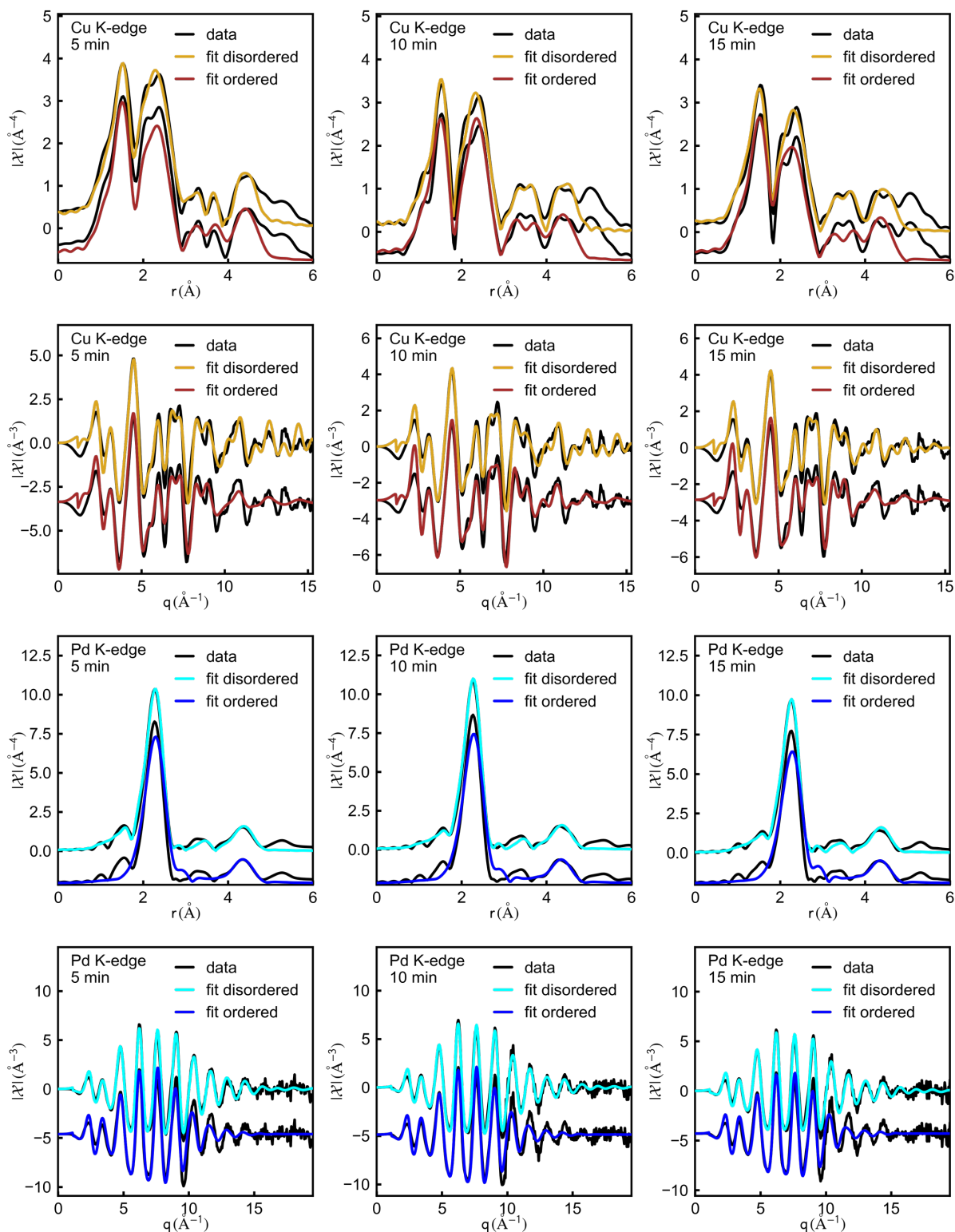


Figure S5.6: Double-edge Cu K-edge and Pd K-edge EXAFS fit of Cu_3PdN using the disordered and ordered anti-perovskite structure of Cu_3PdN for NPs grown for 5, 10 and 15 min reaction time at 140°C . Refined parameters are shown in Table S5.2 and S5.3

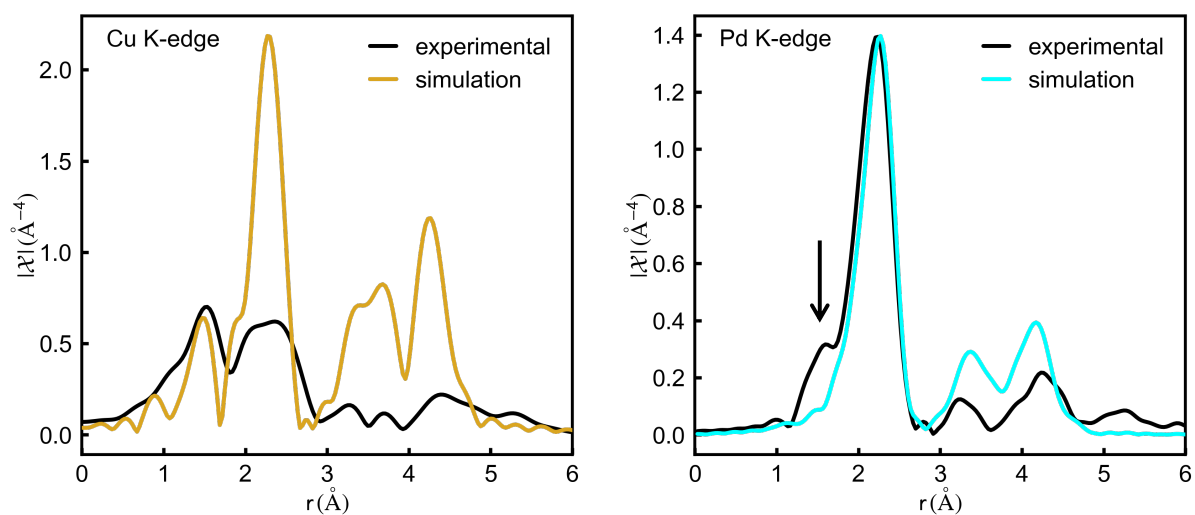


Figure S5.7: Comparison of experimental and FEFF-simulated Fourier-transformed Cu K-edge and Pd K-edge EXAFS data of ordered Cu_3PdN . The simulated data is multiplied by a factor of 0.25. A clear peak at 1.6 Å, indicated by an arrow arising from the Pd-N coordination in the Pd K-edge experimental spectrum, emphasizes the presence of the cation site disorder. The low intensity of the peaks related to the second and the third coordination in the experimental data, compared to the simulated ones, due to the high DW values, further confirms the disorder in the cation lattice.

Figure S5.8: First derivative XANES spectra of Cu_3PdN grown for 5, 10 and 15 min reaction time at 140 °C compared with the reference Cu_3N and Cu foil.

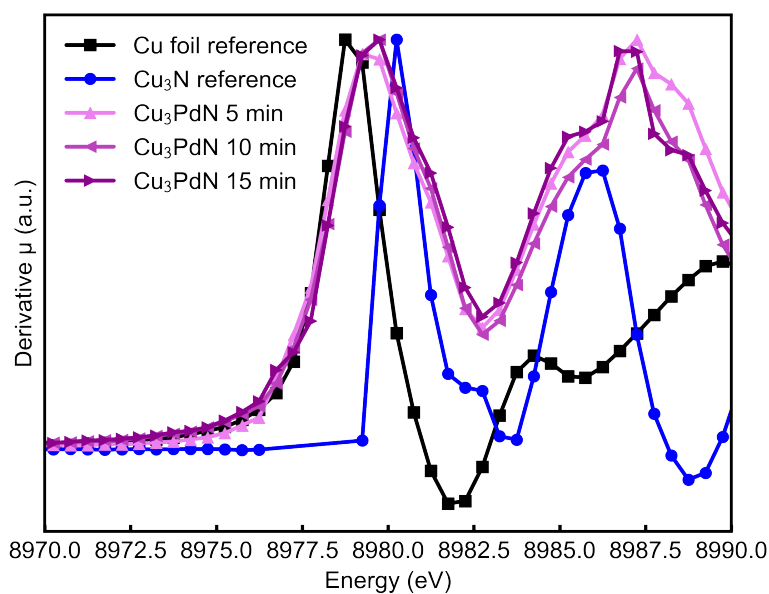


Table S5.2: The scattering paths used to fit the corresponding Cu and Pd K-edge EXAFS data in the case of the disordered structure. The graphical description is Cu: orange; Pd: cyan; N: green.

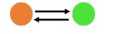
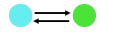

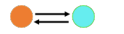
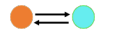
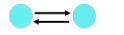
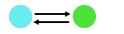
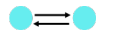
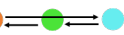
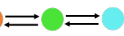
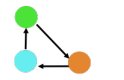
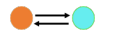

No	Scattering path (legs)	Edge	Degeneracy (n)	$\frac{1}{2}R_{\text{path}}$ (Å)	Distance variation parameter	Debye-Waller factor	Graphical description
1	Cu - N1 - Cu	Cu	2	1.91	Δr_1	σ_{Cu1}^2	
2	Pd - N1 - Pd	Pd	2	2.00	Δr_2	σ_{Pd1}^2	
3	Cu - Cu1 - Cu	Cu	12	2.69	Δr_3	σ_{Cu2}^2	
4	Cu - Pd1 - Cu	Cu & Pd	8	2.71	Δr_4	σ_{Cu3}^2	
5	Cu - Pd1 - Cu	Cu & Pd	4	2.63	Δr_5	σ_{Cu4}^2	
6	Pd - Pd1 - Pd	Pd	4	2.73	Δr_6	σ_{Pd2}^2	
7	Pd - N2 - Pd	Pd	8	3.34	$\sqrt{3} \Delta r_2$	σ_{Pd3}^2	
8	Pd - Pd2 - Pd	Pd	6	3.83	$\sqrt{2} \Delta r_4$	σ_{Pd4}^2	
9	Cu - N1 - Cu2 - Cu	Cu & Pd	4	3.83	$\sqrt{2} \Delta r_4$	$2 \sigma_{\text{Pd4}}^2$	
10	Cu - N1 - Cu2 - N1 - Cu	Cu & Pd	2	3.83	$\sqrt{2} \Delta r_4$	$2 \sigma_{\text{Pd4}}^2$	
11	Pd - N1 - Cu1 - Pd	Pd	48	3.97	$2 \Delta r_2$	$2 \sigma_{\text{Pd1}}^2$	
12	Pd - Cu2 - Pd	Cu & Pd	24	4.70	$\sqrt{3} \Delta r_4$	σ_{Cu5}^2	
13	Cu - Cu3 - Cu	Cu	16	4.70	$\sqrt{3} \Delta r_3$	σ_{Cu6}^2	

Table S5.3: EXAFS refined parameters. The error is given by the standard deviation of the refined parameter and shown in the parentheses. Cu K E₀ is calculated from the maximum of the first derivative of the corresponding XANES spectra.

Sample/Results	5 min	10 min	15 min
Cu K E ₀ (eV)	8979.60	8979.59	8979.65
x (%)	69.3(39)	76.5(43)	75.7(44)
R _{Cu-N1} (Å)	1.908(7)	1.909(6)	1.917(2)
$\sigma_{\text{Cu-N1}}^2$	0.0039(6)	0.0048(5)	0.0046(5)
R _{Pd-N1} (Å)	2.001(6)	1.999(9)	2.004(8)
$\sigma_{\text{Pd-N1}}^2$	0.0035(17)	0.0038(25)	0.0040(78)
R _{Cu-Pd1} (Å)	2.641(7)	2.630(7)	2.635(6)
$\sigma_{\text{Cu-Pd1}}^2$	0.0050(6)	0.0047(7)	0.0048(6)
R _{Cu-Cu1} (Å)	2.711(11)	2.726(18)	2.724(16)
$\sigma_{\text{Cu-Cu1}}^2$	0.0242(10)	0.0249(18)	0.0266(15)
R _{Cu-Pd1} (Å)	2.697(16)	2.689(19)	2.700(8)
$\sigma_{\text{Cu-Pd1}}^2$	0.0098(7)	0.0107(7)	0.0114(7)
R _{Pd-Pd1} (Å)	2.731(23)	2.730(22)	2.738(30)
$\sigma_{\text{Pd-Pd1}}^2$	0.0092(8)	0.0079(8)	0.0075(7)
R _{Pd-N2} (Å)	3.240(71)	3.262(55)	3.300(17)
$\sigma_{\text{Pd-N2}}^2$	0.0121(27)	0.0132(24)	0.0143(23)
R _{Cu-Cu2} (Å)	3.862(32)	3.861(31)	3.872(42)
$\sigma_{\text{Cu-Cu2}}^2$	0.0131(36)	0.0113(31)	0.0135(44)
R _{Cu-Cu3} (Å)	4.705(14)	4.707(16)	4.718(27)
$\sigma_{\text{Cu-Cu3}}^2$	0.0241(29)	0.0248(25)	0.0265(23)
R _{Pd-Cu2} (Å)	4.718(27)	4.722(31)	4.728(37)
$\sigma_{\text{Pd-Cu2}}^2$	0.0169(11)	0.0179(11)	0.0176(12)

PXRD and Rietveld Refinement Analysis

We test the hypothesis of cation disorder with PXRD. First, in Figure S5.9, we compare simulations for PXRD patterns of the ordered Cu₃PdN structure without atomic displacements (approach A), the Cu₃PdN structure with fully displaced Cu and Pd atoms (approach B), and fully displaced N atoms (approach C) and partially displaced Cu/Pd or N with adjusted atomic site occupancy to match the ratio of the displacement as determined by the EXAFS fit. We note that the structure of displaced Cu/Pd and displaced N, approach B and C, respectively, is identical in the first coordination shell but varies beyond. The simulated patterns exhibit little changes in relative peak intensity, most notably for peak (100) at $q = 1.6 \text{ \AA}^{-1}$ and (110) at $q = 2.3 \text{ \AA}^{-1}$, corresponding to $2\Theta = 23^\circ$ and $2\Theta = 33^\circ$, respectively, considering Cu K-alpha radiation. The peak intensity (100) and (110) notably decreases in the case of the displaced Cu and Pd model. Our PXRD pattern and literature reports display a similar pattern.^{55,167-172} However, the peak intensities in PXRD patterns are influenced by atomic displacement parameters (ADP), which are typically included in Rietveld refinement procedures to account for the uncertainty of the atomic position within the crystal lattice due to thermal vibration or static disorder.⁶¹ In Figure S5.10, we conduct Rietveld refinements using the ideal Cu₃PdN

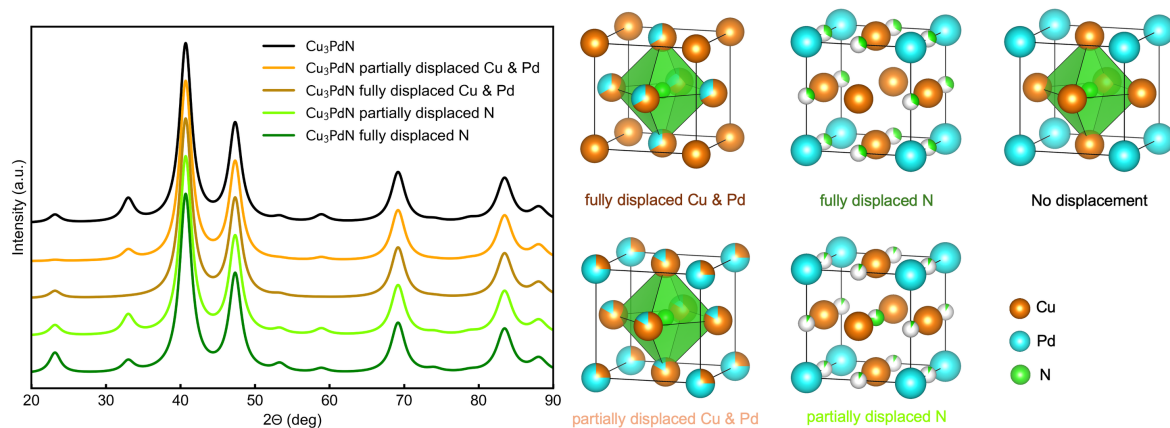


Figure S5.9: PXRD simulations of Cu₃PdN with no displacements, partially and fully displaced Cu & Pd or N atoms.

structure and partially displaced N atoms or Cu and Pd atoms. Table S5.4 lists the refined parameters. The refinements demonstrate good agreement across all models, although the refinement with partially displaced N atoms has unphysical ADP values indicating unlikely N displacement. Hence, with Rietveld refinements alone we cannot differentiate between the ordered Cu₃PdN and the disordered structure, *i.e.* the displacement of Cu and Pd, but exclude the potential displacement of N atoms.

Table S5.4: Retrieved Parameters of Rietveld Refinement Results of Cu₃PdN at 5, 10 and 15 min reaction time at 140 °C. *Displaced atom. The displacement takes place in { $a/2$, $a/2$, 0} from the original position of the atom for Cu, Pd and N. Unphysical values are marked in red.

Displacement	5 min			10 min			15 min		
	-	Cu/Pd	N	-	Cu/Pd	N	-	Cu/Pd	N
R _W (%)	3.813	3.757	3.716	4.956	4.587	4.825	3.873	4.063	3.995
χ ²	41.67	40.54	39.62	115.3	98.54	108.9	57.33	63.29	61.15
a (Å)	3.838	3.838	3.838	3.847	3.838	3.847	3.833	3.833	3.833
size (nm)	2.6	2.7	2.7	3.3	3.3	3.3	2.7	2.9	2.9
U _{iso} Cu (Å ⁻²)	0.0030	0.0070	0.0038	0.0041	0.0112	0.0083	0.0041	0.0102	0.0059
U _{iso} Pd* (Å ⁻²)					0.0224				0.0257
U _{iso} Pd (Å ⁻²)	0.0385	0.0288	0.0393	0.0358	0.0115	0.0269	0.0447	0.0027	0.0411
U _{iso} Cu* (Å ⁻²)		0.0286				0.0137			0.0168
U _{iso} N (Å ⁻²)	0.7424	0.2763	0.2267	0.5781	0.0780	0.0055	0.0623	0.0712	0.7641
U _{iso} N* (Å ⁻²)		27.10			1.956				-119.5

Technical information on XANES and EXAFS analysis

The XANES and EXAFS data shown in this report have been acquired at different beamlines as listed in Table S5.5.

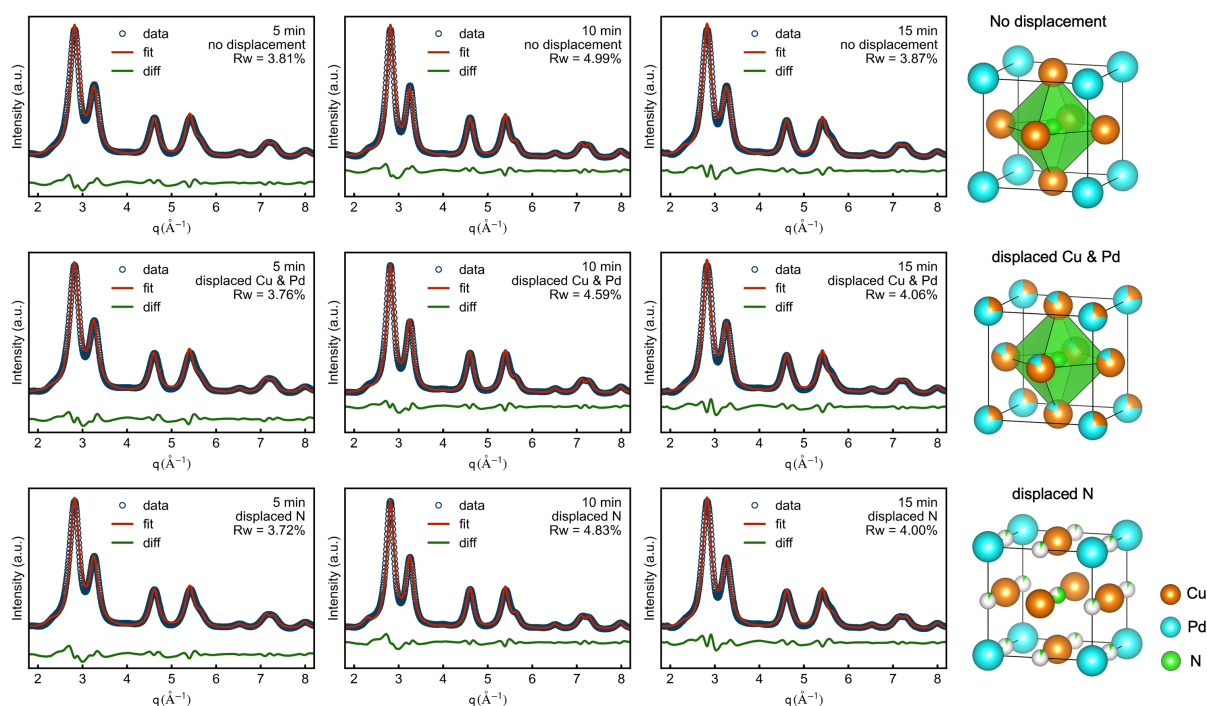


Figure S5.10: Rietveld refinements of Cu_3Pd at 5, 10 and 15 min reaction time at $140\text{ }^\circ\text{C}$. The patterns were refined using GSASII⁶⁹. Refined parameters are listed in Table S5.4

Table S5.5: Summary of the beamlines and synchrotrons utilized for collecting XAS data, as referenced in the figures of this report.

	Method	Beamline, Synchrotron
Figure 5.1	Cu K-edge HERFD-XANES	ID24, ESRF
Figure 5.3	Cu & Pd K-edge EXAFS	BM23, ESRF
Figure 5.4	Cu K-edge HERFD-XANES	ID24, ESRF
	Pd K-edge XANES	P64, DESY
Figure S5.5	Cu & Pd K-edge EXAFS	BM23, ESRF
Figure S5.6	Cu & Pd K-edge EXAFS	BM23, ESRF
Figure S5.7	Cu & Pd K-edge EXAFS	BM23, ESRF
Figure S5.8	Cu K-edge XANES	BM23, ESRF
Figure S5.12	Cu K-edge HERFD-XANES	ID24, ESRF
Figure S5.13	Cu K-edge EXAFS	P64, DESY
Figure S5.15	Cu K-edge HERFD-XANES	ID26, ESRF

In situ HERFD-XANES data were preliminarily viewed using the PyMCA software package²²⁶ and processed using a self-written Python code based on available packages. The data was imported using Silx²²⁷, treated with a Whittaker filter²²⁸ and further processed with the NumPy²²⁹ and SciPy²³⁰ packages. *Ex situ* powder samples XANES data were pre-treated using the Athena²³¹ of the Demeter software package.

The pretreatment process for all EXAFS spectra was performed using the Athena program of the Demeter IFEFFIT software package, and the data were analyzed Artemis code of the Demeter software package²³¹ using simulated scattering paths calculated by FEFF 6.0. The Fourier transform of the EXAFS spectra were obtained in the range of $3 - 13.5\text{ \AA}^{-1}$ and $3 - 18.5\text{ \AA}^{-1}$ with k3 weight for both Cu K and Pd K-edge data, respectively. The data were fitted in R space in

the range of 1 – 4.7 Å. The many-body amplitude reduction factor (S_0^2 (Cu)=0.955, S_0^2 (Pd)=0.935) and the common energy origin shift (ΔE_0 (Cu) = 5.05, ΔE_0 (Pd) = 4.68) were fixed to the values obtained from a fit of the Cu and Pd foils spectra, respectively. The fitting parameters were the interatomic distances (R), the Debye-Waller factors (σ^2), and x. The goodness of the fit (R) was below 0.01 for all the spectra.

The Multivariate Curve Resolution by Alternating Least Squares (MCR-ALS)²³² method is briefly reviewed, followed by detailed fit results. MCR-ALS is an emerging data analysis technique used to extract the reaction pathway from *in situ* XANES data. It allows for modelling an experimental dataset D (including q spectra), as the product of an S matrix, composed of N (with $N < q$) pure spectra and a matrix C, whose elements correspond to signal-related concentration profiles.

$$D = CS^T + E \quad (5.3)$$

Here, in the case of time-resolved XANES spectra, D is the experimental data with each row corresponding to a measured spectrum, rows of S are spectra of uncorrelated variables and columns of C are the concentration profiles of each component over time. E represents the error matrix associated to the reconstruction. For this MCR-ALS analysis we used the Graphical User Interface (GUI) by Jaumot and co-workers which is freely available using MATLAB R2011b.^{130,233} After guessing of initial C and S, which we do by means of the purest variables detection method so called SIMPLISMA algorithm²³⁴ with allowed noise parameter is fixed to 3 %, a set of linear equations is iteratively solved, alternatingly keeping C or S constant until the change in the standard deviation of E falls below a certain convergence criterion. For MCR-ALS, the data were analyzed in the energy range of 8970-9060 eV for Cu K-edge and 24280-24450 eV for Pd K-edge data sets. The optimization routine successfully converged after 50 iterations, resulting in the final ALS quality control parameters such as lack of fit, R^2 and σ . The quality estimates of a converged fit arise from the unexplained residuals E, or the difference between the experimental data and the model, with a lack of fit is given by

$$\text{Lack of fit (\%)} = 100 \cdot \sqrt{\frac{\sum_{i,j} e_{ij}^2}{\sum_{i,j} d_{ij}^2}} \quad (5.4)$$

Where d_{ij} is a data matrix element and e_{ij} is the corresponding element of the residual matrix E. Additionally, the variance explained in the model can be estimated from

$$R^2 = \frac{\sum_{i,j} d_{ij}^2 - \sum_{i,j} e_{ij}^2}{\sum_{i,j} d_{ij}^2} \quad (5.5)$$

and the standard deviation of the residuals is given by

$$\sigma = \frac{\sum_{i,j} e_{ij}^2}{nm} \quad (5.6)$$

Where n, m refers to the dimensions of D.

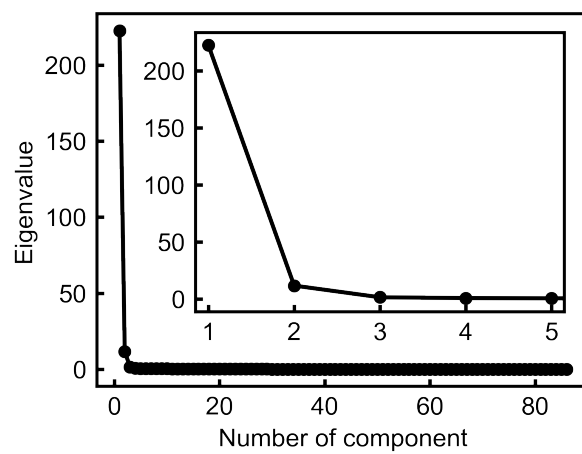


Figure S5.11: Eigen value profile of MCR-ALS analysis.

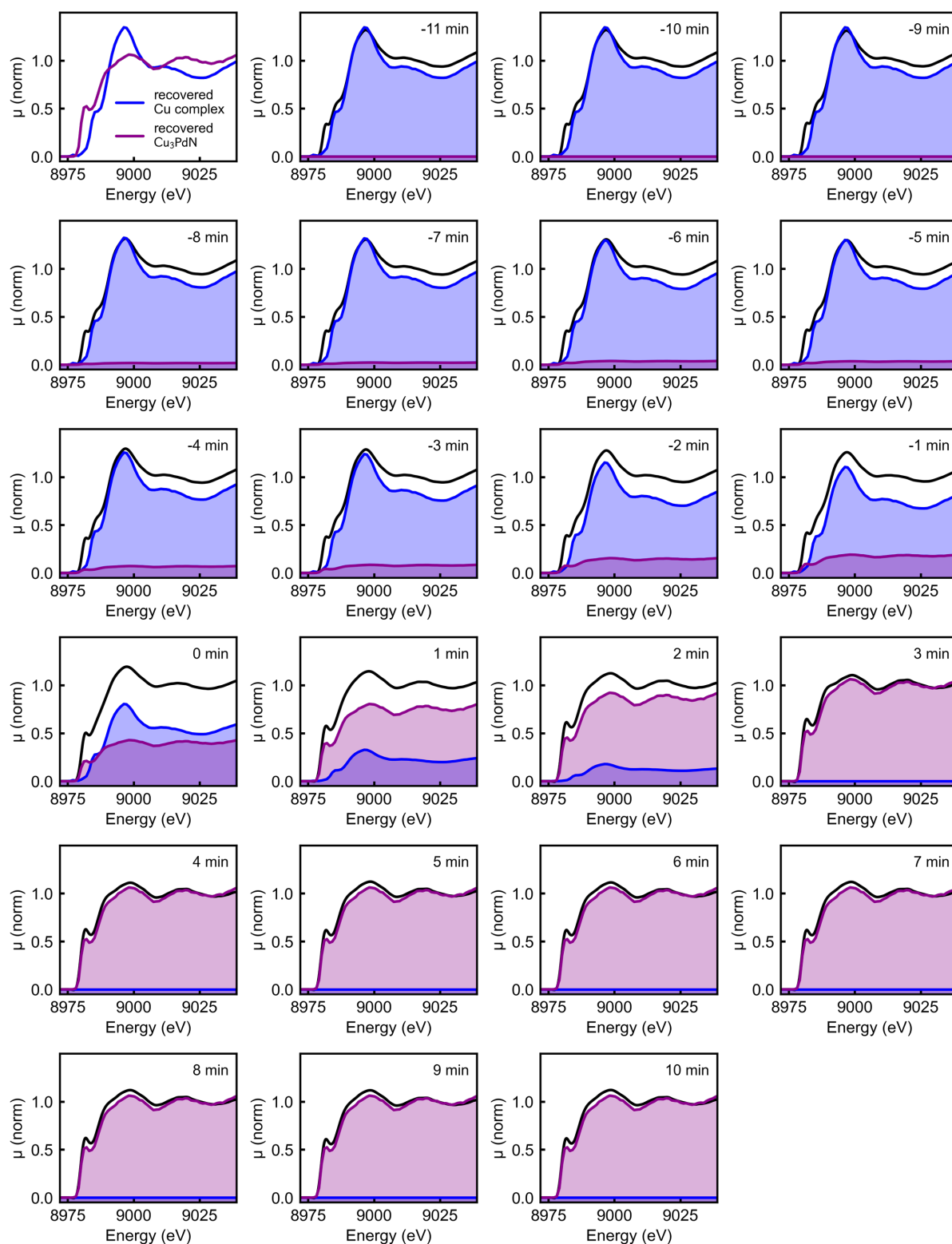


Figure S5.12: Time series of Cu K-edge HERFED-XANES spectra compared with contributions from MCR-ALS recovered spectra which are shown in Figure 5.4b,c. The black curve shows the measured spectra. The blue and violet curve show the MCR-ALS recovered contribution of the Cu complex and Cu_3PdN , respectively.

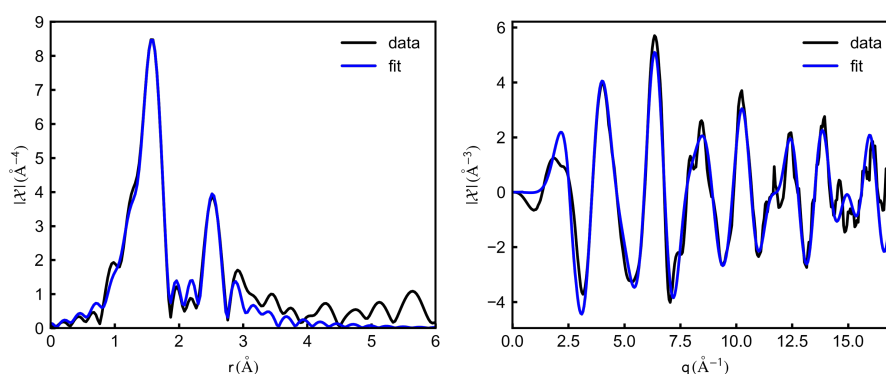


Figure S5.13: Fourier transformed Cu K-edge EXAFS data of the initial complex fitted using the complex shown in Figure 5.4. The fit reveals that the first coordination shell is composed of 2 N atoms and 2 O atoms at 1.92 Å and at 1.98 Å, respectively. The second shell is composed of 4 C atoms and 1 Cu atom at 2.92 Å and at 3.04 Å, respectively which clearly corresponds to the complex shown in Figure 5.4

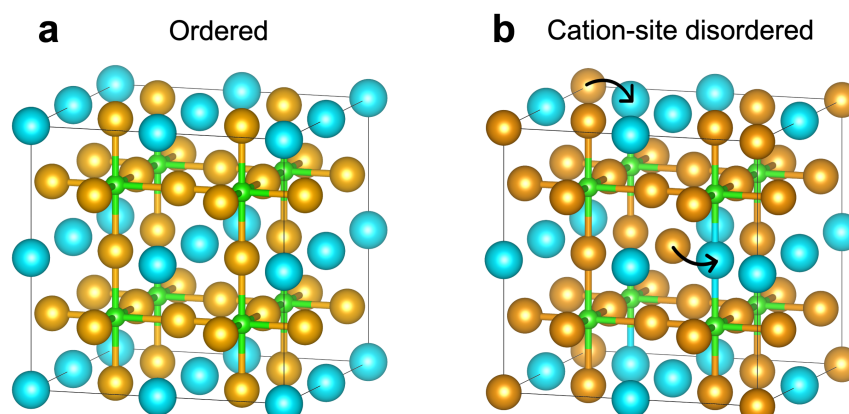


Figure S5.14: Ordered and cation-site disordered $2 \times 2 \times 2$ supercell of Cu_3PdN . a Ordered anti-perovskite supercell. b Disordered supercell in which two Pd atoms are interchanged with adjacent Cu atoms, which amounts to 25% disorder.

Beam Damage Study

The beam damage study is carried out before starting the actual *in situ* measurements. Figure S5.15 shows the XANES spectra of the precursor solution measured at room temperature. When we expose the sample with x-ray at the same spot, we observe the sample is reduced after 90 seconds. Thus, we measure 4 scans (20 sec/scan) at the same spot and after that we moved to the new spot on the sample. In this way, we avoid the beam damage, and all the *in situ* scans are carried out at the same condition.

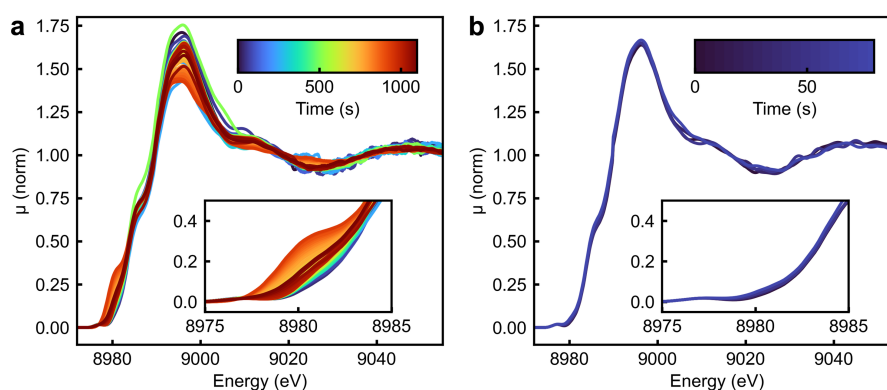


Figure S5.15: Beam damage study on Cu₃PdN precursor solution measured at room temperature (20 s/scan). Fifty-five spectra measured at the same spot. b Four spectra measured at the same spot.

Technical notes on PDF analysis of TS

The *in situ* total scattering (TS) data for pair distribution function (PDF) analysis were acquired every 1 s using 2D detectors. The 2D scattering images were azimuthally integrated to 1D with PyFAI.¹³⁶ Consequently, the integrated scattering patterns were averaged to 60. The 1D scattering patterns are eventually processed to PDFs using PDFgetX3.²³⁵ Table S5.6 gives the values used to process and Fourier transform the scattering patterns to the PDF.

Table S5.6: Values used for processing the PDF.

	q_{\min} (\AA^{-1})	q_{\max} (\AA^{-1})	$q_{\max, \text{inst}}$ (\AA^{-1})	r_{poly}
<i>In situ</i> PDF: Figure 5.4e, S5.16, S5.18	0.4	10.3	17.5	0.9
<i>In situ</i> PDF: Figure S5.19-S5.21	0.7	16.3	18.3	0.9

The *in situ* PDF data shown in Figure 5.4e, S5.16, S5.18 focuses on the early stages of the reaction, which shows the NP nucleation and precursor conversion to the nitride, while the *in situ* PDF data shown in Figure S5.19-S5.21 focuses on the growth of the NPs and the phase transition of Cu₃PdN to Cu₃Pd. Due to the low scattering from the non-crystalline species present at the early stage of the reaction and a very high background contribution of the sample environment to the scattering signal, the PDF shown in Figure 5.4e, S5.16, S5.18 is obtained by using a low upper cut-off frequency q_{\max} which sacrifices r -resolution but reduces noise in the PDF data. The crystalline materials at the later stages of the reaction allow for a higher upper cut-off frequency q_{\max} without increasing the noise level in the PDF, as is used in Figure S5.19-S5.21. Moreover, different background subtraction approaches have proven most reliable for the early-stage and late-stage PDF data sets, as explained below. The background scattering images are acquired by measuring the same sample environment but without the addition of the precursor salts to the reaction solution at the same temperature ramping and processing the background scattering images as explained above. The background data was then subtracted from the data of the same temperature. Two different approaches are used to set the scale for background subtraction of the TS data. The data used in Figure 5.4e, S5.16, S5.18 is background subtracted by maximizing the maximum intensity of the PDF between $r = 1.9$ and 4.0 \AA . The data used for Figure S5.19-S5.21 is background subtracted by fitting a Gaussian with a linear baseline to the glass peak at ~ 1.6 \AA and reducing the amplitude using the following function:

$$y = a \cdot \exp\left(\frac{-(x - x_0)^2}{2 \cdot \left(\frac{FWHM}{2.35482}\right)^2}\right) + m \cdot x + y_0 \quad (5.7)$$

x_0 is the position, a is the amplitude and FWHM is the full width at half maximum of the peak. m is the slope and y_0 is the intersection of the baseline with the y-axis. Table S5.7 shows the restraints used for the fitting.

Table S5.7: Boundaries used for Gaussian fit as shown in Equation 5.

Parameter	Lower boundary	Upper boundary
x_0 (Å)	1.5	1.7
a (Å)	0.0	–
FWHM (Å)	0.3	0.8
m (Å ⁻²)	-1.0	1.0
y_0 (Å ⁻³)	–	–

The *in situ* PDF data was refined using the diffpy-CMI library. The refinement was carried out sequentially, meaning the refined value of a parameter was used as the initial value for the refinement of the next time step. Table S5.8 shows the parameters used for the refinement, their restraints and the initial value for the refinement of the first time step. The refinement algorithm is shown in Table S5.9. N ADP is fixed to 0.35 Å⁻² throughout the refinement due to its strong correlation to the N occupancy. q_{damp} and q_{broad} are determined to 0.0281 and 0.0222 Å⁻¹, respectively, by refining the PDF of a LaB₆ standard filled in the heating cell.

Table S5.8: Initial values and boundaries of PDF refinement parameter.

Parameter	Initial value	Lower boundary	Upper boundary
Scale	0.3	0.0	–
Lattice parameter (Å)	3.84	–	–
Spherical domain size (Å)	30	15	–
N occupancy	1.0	0.0	1.0
δ_2 (Å ⁻²)	3.5	1.5	10.0
N U_{iso} (Å ⁻²)	0.35	0.35	0.35
Cu U_{11} (Å ⁻²)	0.05	0.0001	0.5
Cu U_{22} (Å ⁻²)	0.05	0.0001	0.5
Pd U_{iso} (Å ⁻²)	0.05	0.0001	0.5

Table S5.9: PDF refinement algorithm.

Refinement step	Included parameter for refinement
1	Scale
2	Scale, Particle size
3	Scale, Lattice parameter
4	Scale, N occupancy
5	Scale, Cu U_{11} , Cu U_{22} , Pd U_{iso}
6	Scale, δ_2
7	Scale, Particle size, Lattice parameter, N occupancy, Cu U_{11} , Cu U_{22} , Pd U_{iso} , δ_2

The code for the processing of the PDF data, including azimuthal integration of detector images, background subtraction approaches, averaging and Fourier transforming, as well as PDF refinement procedures, is available at: https://gitlab.rrz.uni-hamburg.de/BAS0906/shm_2024_cu3pdn.

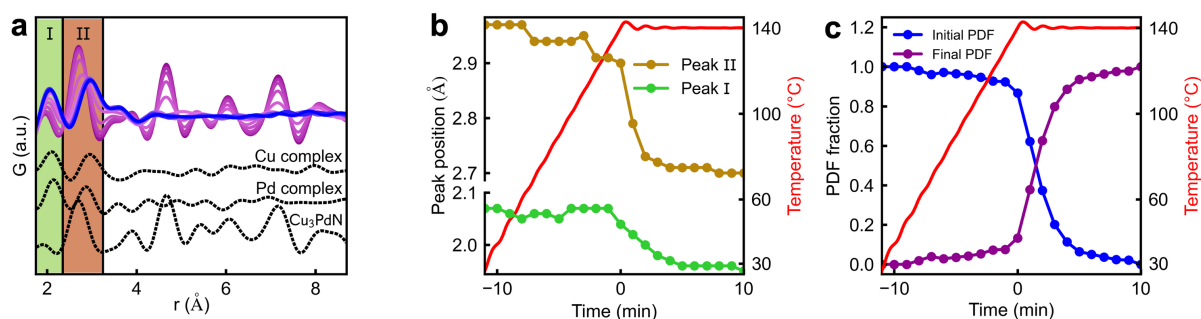


Figure S5.16: *In situ* PDF analysis of the reaction to Cu_3PdN . **a** *In situ* PDFs $G(r)$. The *in situ* PDF data is compared to PDF simulations of the Cu and Pd starting complexes and Cu_3PdN phase in dashed black traces. The first peak, peak I, highlighted in green, comprises the nearest neighbour interatomic distances Cu – N, Cu – O, Pd – N of the starting complexes as well as Cu – N of Cu_3PdN . The second peak, peak II, highlighted in orange, comprises the second neighbour interatomic distances Cu – Cu, Cu – C, and Pd – C of the starting complexes as well as Cu – Cu and Cu – Pd distances of Cu_3PdN nanoparticles. Purely organic pair interatomic distances are not listed due to their weak scattering and weak contributions to the PDF signal. **b** Peak position of the first and second peak versus the reaction time. **c** PDF fraction of the linear combination of the initial PDF at $t = -11$ min and the last PDF at $t = 10$ min versus the reaction time.

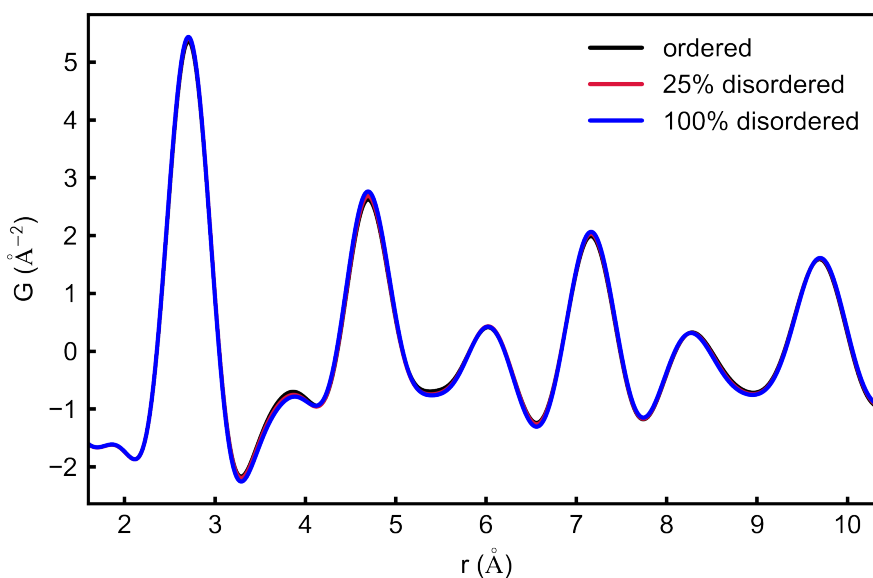


Figure S5.17: PDF simulation comparison of ordered and disordered Cu_3PdN . The ordered structure is the ideal anti-perovskite structure of Cu_3PdN without cation-disorder. In the 25% disordered structure, 25% of the Pd atoms interchange their position with 8% of the Cu atoms to account for the stoichiometry of Cu_3PdN ($25\% / 3 \approx 8\%$). In the 100% disordered structure, all Pd atoms interchange their position with 33% of the Cu atoms. The parameters used in the PDF simulations are the same as the initial values for the PDF refinements, as listed in Table S5.8.

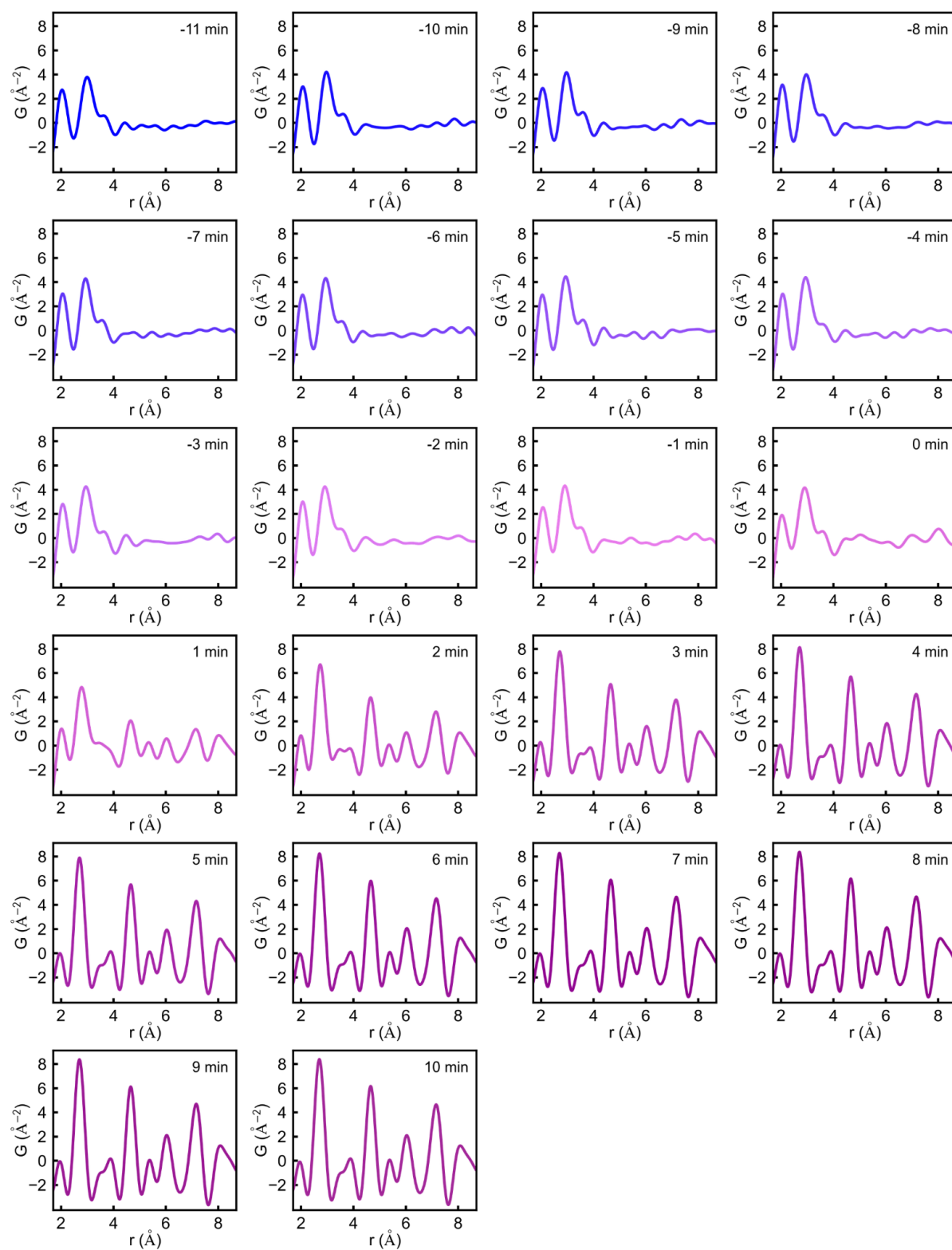


Figure S5.18: Time series of PDFs, which are shown in Figure 5.4 and Figure S5.16

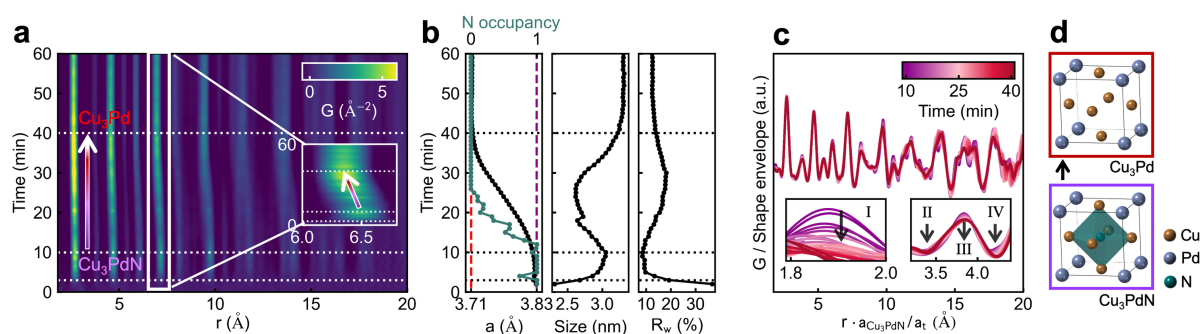


Figure S5.19: *In situ* PDF of the reduction of Cu_3PdN to bimetallic Cu_3Pd at advanced reaction times. a *in situ* time-resolved PDFs $G(r)$. The different regions are highlighted by horizontal dashed lines. At ~ 3 min after reaching 140°C , Cu_3PdN nanocrystals are emerging. The phase transformation takes place between ~ 10 and ~ 40 min. Cu_3PdN and Cu_3Pd have similar crystal structures and hence very similar PDFs. The phase transformation is mainly visible by a peak shift to lower r , which is due to the decrease of the lattice parameter when N leaves the crystal lattice. The inset shows a zoom of the peak at ~ 6.5 Å. b PDF refinement results. The phase transformation can be refined by using only the Cu_3PdN phase and freeing the N occupancy. The first panel shows the decrease of the refined N occupancy and the lattice parameter, a . The second panel shows the refined spherical domain size. The third panel shows the goodness of the fit parameter R_w . c Overlay of normalized PDFs during the phase transformation. To account for the peak shifts during the phase transformation, each PDF x-axis is normalized by the respective refined lattice parameter a_t . To account for the change of intensity dampening due to the change of the domain size each PDF is normalized by the respective refined shape envelope. The insets zoom on selected N-Cu (I, IV), N-N (III), N-Pd (II) distances. The decrease of the intensities at the respective distances can be attributed to vanishing N. d Unit cells of Cu_3PdN and Cu_3Pd .

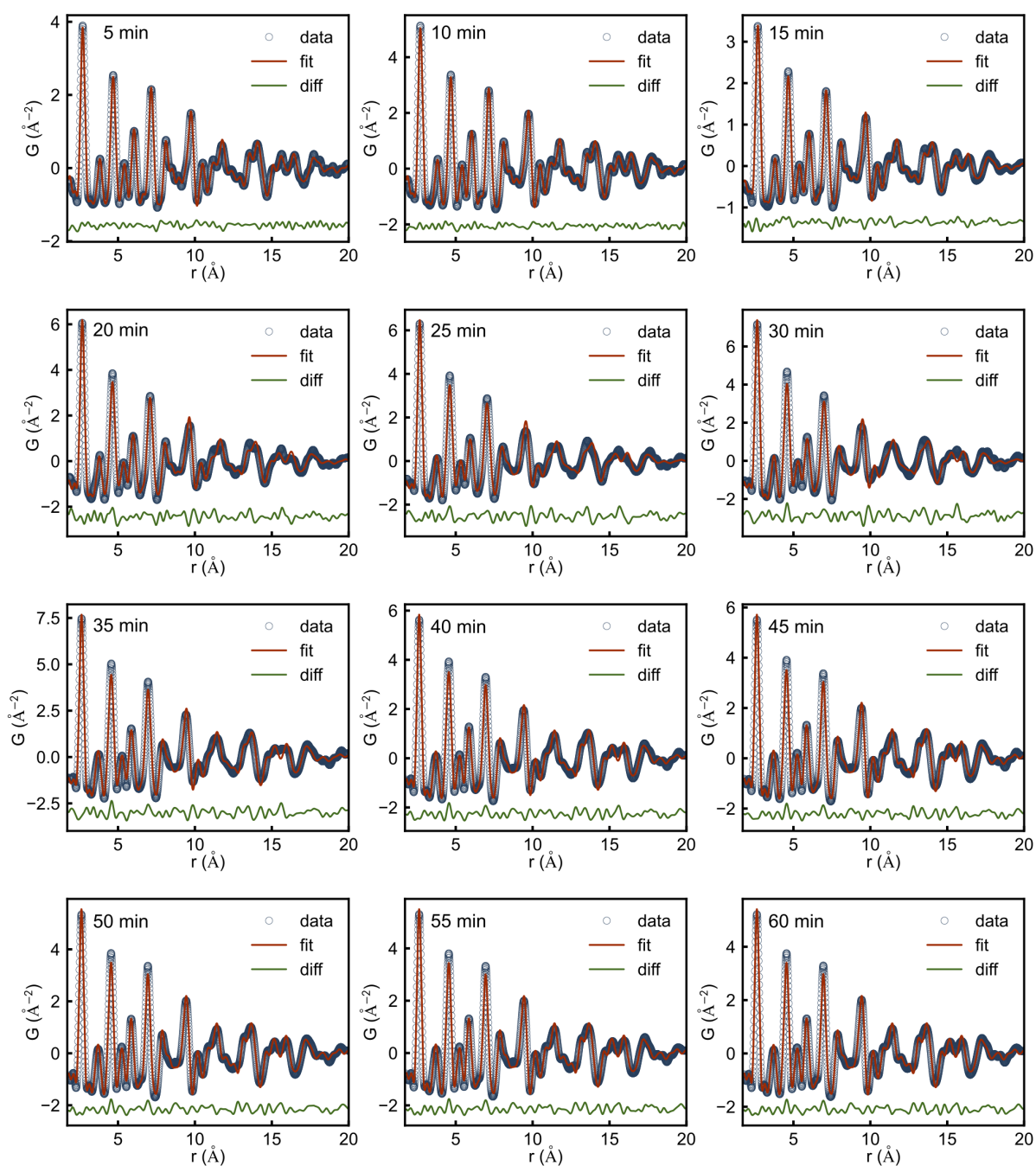


Figure S5.20: Time series of PDF refinements 5 to 60 minutes reaction time at 140 °C. Refined parameters are shown in Figure S5.21.

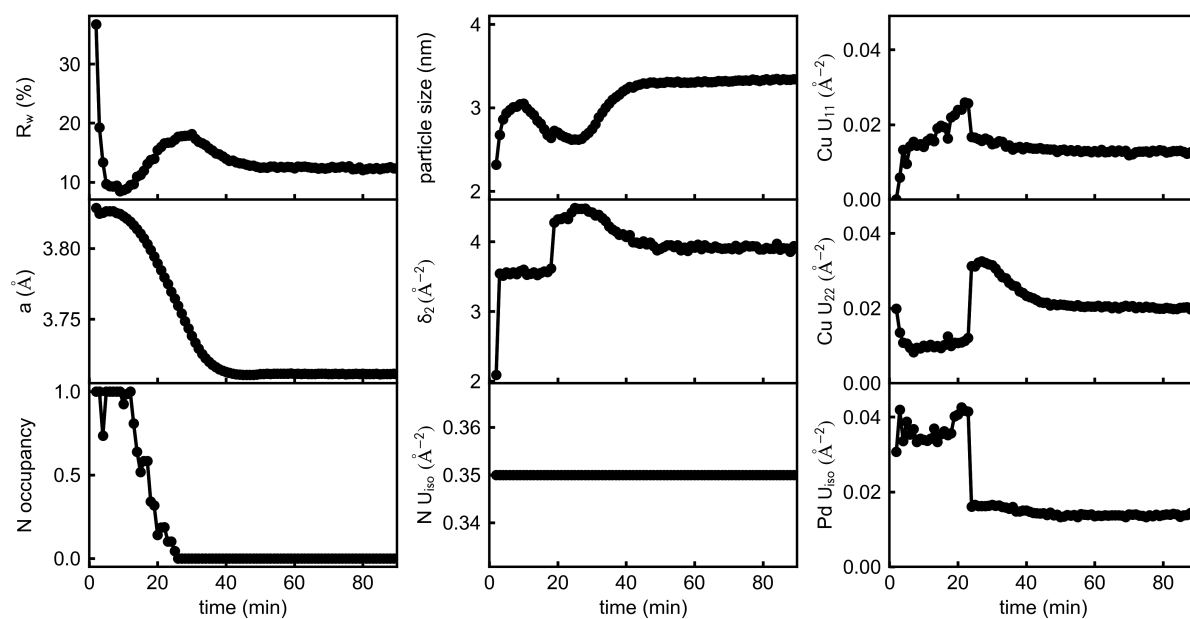


Figure S5.21: Detailed representation of refined parameters of PDF refinements shown in Figure S5.19 and S5.20.

Electrocatalysis of HER

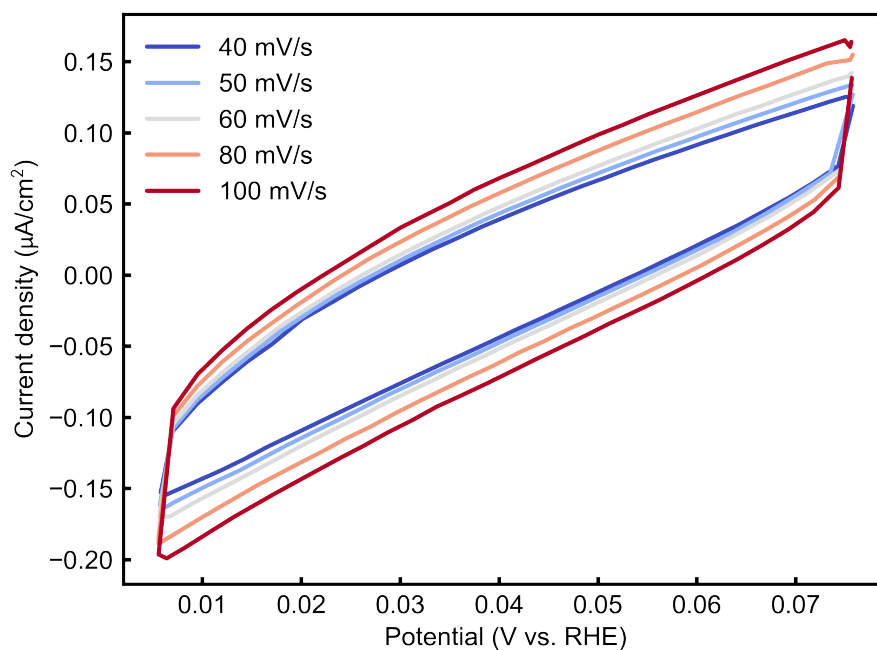


Figure S5.22: Cyclic voltammetry measurement.

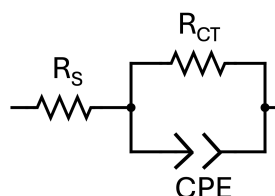


Figure S5.23: Representation of the simple equivalent circle used to fit the EIS data. R_S : solution resistance, R_{CT} : charge transfer resistance, CPE: constant phase element.

Stability of Cu_3PdN during EC

First, we test the stability of Cu_3PdN in the electrolyte. Therefore, 10 mg of Cu_3PdN NPs are dispersed in 5 mL of 0.5 M H_2SO_4 electrolyte for 20 h. Consequently, the Cu_3PdN is washed and centrifuged 3 times with water, and 3 times with ethanol for 5 min at 10000 rpm. Finally, the product is dried under nitrogen flow and measured by PXRD. Figure S5.24 shows the PXRD pattern that confirms the presence of anti-perovskite nitride phase without any additional bimetallic, metallic or oxide crystalline phases.

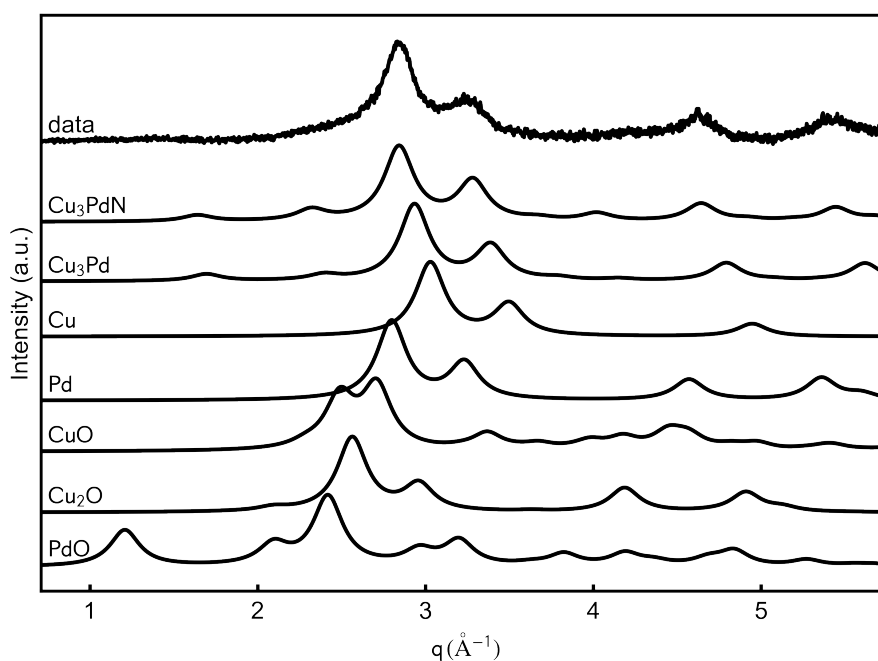


Figure S5.24: PXRD of Cu_3PdN after being dispersed in 0.5M H_2SO_4 electrolyte. The experimental data is compared to PXRD simulations of Cu_3PdN , Cu_3Pd , Cu, Pd, CuO, Cu_2O and PdO. All patterns are simulated using GSASII⁶⁹ and assuming a crystallite size of 3 nm.

Further, we test the stability of Cu_3PdN by comparing XPS before and after EC. Figure S5.25 shows Cu 2p, Pd 3d, N 1s and O 1s XP spectra before and after EC. The pristine sample is measured on a carbon tape. XPS after EC is directly measured on the GC working electrode. Despite the low intensity compared to the pristine sample due to the very low concentration of the sample deposited (300 - 400 μg) on the GC electrode, all the features are the same as the pristine sample, confirming the stability of the Cu_3PdN during the electrochemical measurement. However, the Cu 2p spectral feature is negatively shifted by about 0.7 eV, and the corresponding N 1s is positively shifted by 1.2 eV, which could be due to the low charge density of Cu compared to the pristine sample. Furthermore, the O 1s core-level spectrum

is deconvoluted into 3 obvious peaks related to metal-oxygen, OH, and COOH contributions as in the pristine sample. Together with the presence of Cu(II) and Pd(II), it is clear that a thin layer of amorphous metal oxide and hydroxide is formed on the surface of nitride NPs.⁵⁵ Despite this, it further proves that the Cu₃PdN NPs are highly stable during the electrochemical measurements.

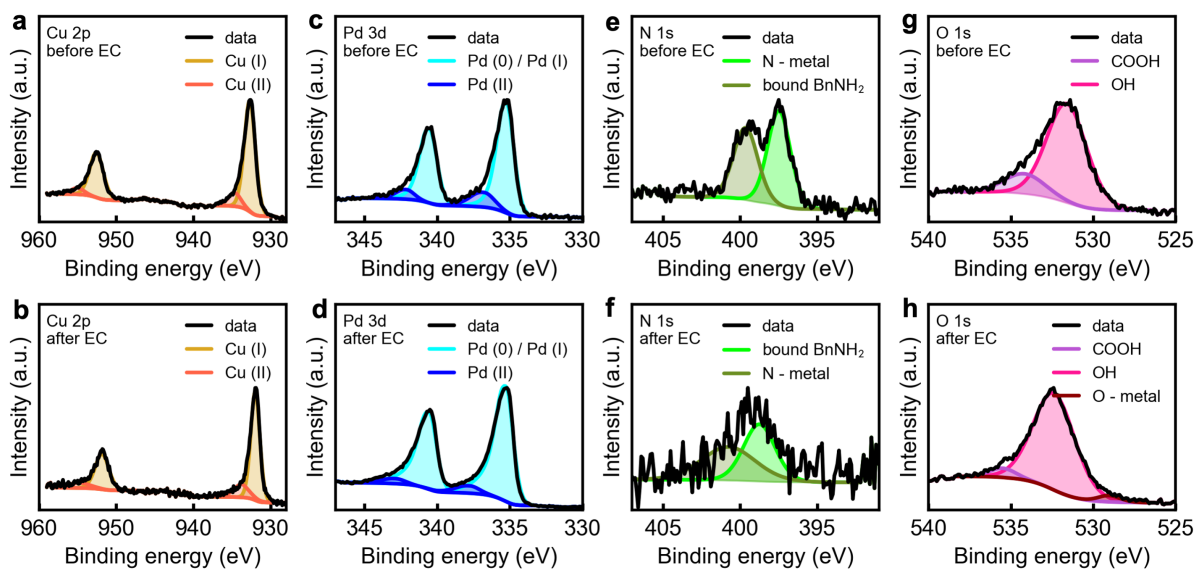


Figure S5.25: XPS core-level spectra of Cu₃PdN before and after EC. Cu 2p a before and b after EC, Pd 3d c before and d after EC, N 1s e before and f after EC, O 1s g before and h after EC.

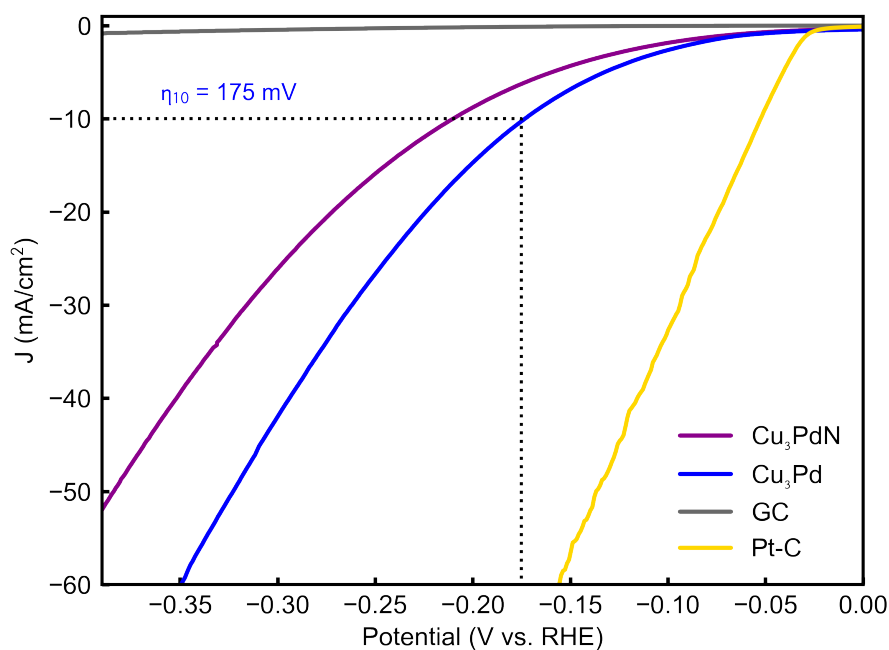


Figure S5.26: LSV of Cu₃Pd compared to Cu₃PdN, Pt-C and GC, showing an overpotential of 175 mV.

Table S5.10: Overview of TMN-based electrocatalysts for HER. GC: glassy carbon, CC: carbon cloth, rGO: reduced graphene oxide, NC: N-doped carbon, NG: N-doped graphene, n.a.: not available.

Material	Substrate	Medium	η_{10} (mV)	Tafel slope (mV/dec)	Reference
$\text{Co}_{0.6}\text{Mo}_{1.4}\text{N}_2$	GC	0.1 M HClO_4	190	n.a.	204
CoFeN_x	Ni-foam	1 M KOH	23	94	208
$\text{CoN}-\text{Co}$	Co-foam	1 M KOH	12	41.6	219
Cu_3PdN	GC	0.5 M H_2SO_4	212	122	This work
GaN	sapphire	0.5 M H_2SO_4	168	35	217
Mo_2N	GC	1 M KOH	353	108	206
$\text{Mo}_2\text{N}-\text{MoC}$	GC	0.5 M H_2SO_4	205	72	203
$\text{Mo}_2\text{N}-\text{Mo}_2\text{C}-\text{NC}$	GC	0.5 M H_2SO_4	185	56	202
$\text{Mo}_2\text{N}-\text{Mo}_2\text{C}-\text{rGO}$	GC	0.5 M H_2SO_4	157	55	201
$\text{Mo}_2\text{N}-\text{NC}$	GC	0.5 M H_2SO_4	217	116	213
MoN	GC	0.1 M HClO_4	420	n.a.	204
Ni_2N	Ni-foam	1 M KOH	55	54	200
Ni_3FeN	CC	1 M KOH	238	46	210
Ni_3FeN	GC	1 M KOH	158	46	209
Ni_3N	Ti mesh	0.5 M K-Bi	297	165	214
$\text{Ni}_3\text{N}-\text{Ni}-\text{Pt}-\text{C}$	GC	0.5 M H_2SO_4	117	47	220
NiCoN	CC	1 M NaOH	145	105	211
$\text{NiCoN}-\text{C}$	GC	1 M KOH	103	n.a.	218
$\text{Pt}-\text{C}$	GC	0.5 M H_2SO_4	53	17	This work
$\text{TiN}-\text{NG}$	GC	0.5 M H_2SO_4	161	66	212
$\text{TiN}-\text{Pt}$	CC	0.5 M H_2SO_4	40	39	215
WCoN	GC	1 M KOH	179	123	222
VMoN	CC	0.5 M H_2SO_4	108	60	216
VN	GC	1 M KOH	476	165	222
$\text{VN}-\text{Co}-\text{P}$	GC	1 M KOH	137	81	221
$\text{WCN}-\text{Fe}$	GC	0.5 M H_2SO_4	220	47	205
WN	CC	0.5 M H_2SO_4	198	92	207
–	GC	0.5 M H_2SO_4	768	366	This work

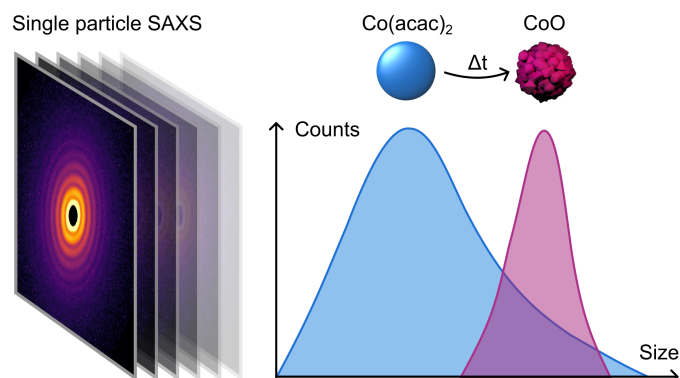
6 Single-Particle X-ray Scattering Reveals a High Local Supersaturation of Precursors as the Origin of CoO Nanoassembly Formation

The content of this chapter was published in arXiv, (2025) by Sani Y. Harouna-Mayer, Lars Klemeyer, Cecilia A. Zito, Johan Bielecki, Xuemei Cheng, Davide Derelli, Armando D. Estillore, Tjark L. R. Groene, Tjark R.L. Groene, Lukas V. Haas, Romain Letrun, Chan Kim, Jayanath C. P. Koliyadu, Abhishek Mall, Parichita Mazumder, Diogo V. M. Melo, Adam R. Round, Amit K. Samanta, Abhisakh Sarma, Zhou Shen, Xiao Sun, Patrik Vagovic, Tamme Wollweber, Richard Bean, Jochen Küpper, Henry N. Chapman, Dorota Koziej, and Kartik Ayyer.

My contribution to this work comprises: synthesis and sample preparation of CoO nanoparticle assemblies, collection and analysis of EM, TS, conventional SAXS data, and analysis of SP-SAXS classes.

6.1 Abstract

Single-particle small-angle X-ray scattering (SP-SAXS) enables quantitative morphological analysis by recording diffraction snapshots from isolated particles using X-ray free-electron laser (XFEL) pulses. Unlike conventional X-ray techniques, which average over the entire illuminated sample volume, SP-SAXS resolves low-contrast, less abundant, or transient species within heterogeneous particle populations that would otherwise remain hidden. Here, we apply SP-SAXS to investigate the solvothermal formation of CoO nanocrystal assemblies from a $\text{Co}(\text{acac})_3$ precursor in benzyl alcohol. The single-particle data reveal amorphous, uniform-density $\text{Co}(\text{acac})_2$ spheres as transient intermediates that directly crystallize into cavernous CoO nanocrystal assemblies, which explains why CoO forms as hierarchical aggregates rather than as isolated nanocrystals. These results demonstrate that SP-SAXS provides a powerful framework for disentangling morphological heterogeneity in nanoparticle formation processes.



6.2 Introduction

The emergence of nanomaterials in solution is governed by complex chemical and structural transformations that ultimately dictate their composition, structure, morphology, and functionality. The rational design of nanomaterials with tailored properties therefore requires mechanistic insight into their formation pathways.^{80,236,237} In many systems, nanomaterials do not form through the straightforward monomer-by-monomer growth described by classical nucleation theory but rather follow nonclassical pathways involving metastable intermediates such as pre-nucleation clusters, dense liquid phases, amorphous precipitates, or the assembly of nanoscale building blocks into hierarchical architectures.^{1,4,7} These multi-step routes have been reported across a wide range of material classes, yet they continue to pose significant challenges for mechanistic understanding and predictive control.^{8,12,238–240}

Among the most powerful methods for investigating nanomaterial formation are X-ray techniques at synchrotron sources.¹⁴ For instance, wide-angle X-ray scattering (WAXS) provides access to atomic arrangements, while small-angle X-ray scattering (SAXS) probes particle size, shape, and morphology.^{34,241} X-ray absorption spectroscopy (XAS) offers element-specific insight into the electronic structure and chemical environment of the absorbing atom.⁵⁷ Complementary optical spectroscopies such as ultraviolet, visible, and infrared (UV/Vis/IR) spectroscopy are sensitive to organic species, optical band-gap transitions, and plasmonic resonances.²⁴² Similar to SAXS, dynamic light scattering (DLS) probes the particle size, but it assumes a hard sphere model and is not applicable to broad or multimodal size distributions.²⁴³ Such methods provide comprehensive information about nanoparticle formation and can be applied *in situ*, enabling real-time monitoring of the evolution of the electronic, atomic, and mesoscopic structure. However, they inherently average over the illuminated sample volume, which may obscure structural or chemical heterogeneity within particle ensembles.³⁵ The analytical ultracentrifugation (AUC) enables the deconvolution of particle size distributions from sedimentation profiles of colloidal nanoparticle dispersions. However, it relies on assumptions about particle density, shape, and frictional ratio, and thus cannot accurately resolve heterogeneous, complex, or anisotropic morphologies.¹³

In contrast, individual particles can be directly imaged during formation in solution using *in situ* electron microscopy (EM) or from quenched aliquots via cryogenic (cryo-)EM, which, however, require elaborate sample preparation, and are prone to electron-beam-induced damage and confinement effects, and only very small sample volumes can be probed.²⁴⁴ Similarly, atomic force microscopy (AFM) can resolve surface morphology and size distributions of deposited nanoparticles but is limited to dried samples and small surface areas. In summary, all conventional methods which allow the study of nanomaterial formation mechanisms

either lose information by averaging over the whole sample volume, or only allow very small sample quantities and might be further altered due to sample preparation or beam-damage.

Here, we introduce single-particle small-angle X-ray scattering (SP-SAXS), which enables the morphological analysis of very large numbers of individual particles using an X-ray free-electron laser (XFEL). The ultrashort and extremely intense XFEL pulses used in SP-SAXS ensure that diffraction is recorded before the onset of X-ray-induced damage, effectively capturing an undistorted structural snapshot of each particle.²⁴⁵

We apply SP-SAXS to a model system, the solvothermal synthesis of CoO nanocrystal assemblies from a $\text{Co}(\text{acac})_3$ precursor in benzyl alcohol at 160 °C. Previous complementary *in situ* X-ray studies followed the reaction from the molecular precursor to the final assemblies by combining XAS with WAXS and SAXS.⁹¹ XAS revealed the rapid reduction of Co^{3+} to Co^{2+} and identified $\text{Co}(\text{acac})_2$ as a stable intermediate, which gradually transformed into rock-salt CoO. Time-resolved WAXS and SAXS analyses showed that crystallite and assembly growth proceeded concurrently, with CoO nanocrystals expanding from ~ 3 nm to ~ 6 nm and the corresponding spherical assemblies from ~ 20 nm to ~ 60 nm over the course of the reaction. This work provided a comprehensive picture of the chemical reduction, nucleation, and growth steps. However, one central question remained unresolved: why does CoO emerge and grow as an assembly? The data revealed an interconnected evolution of nanocrystals and assemblies but could not disentangle whether the assemblies originate from the crystallization of amorphous intermediates or from particle aggregation, due to the averaging over entire reaction volume of the applied *in situ* X-ray methods. By analyzing scattering patterns from individual CoO assemblies and pre-assembly entities extracted from the reaction solution during the early stages of assembly formation, we identify uniform amorphous uniform-density spheres as transient intermediates, that subsequently crystallize into cavernous superstructures. This single-particle perspective provides the missing mechanistic link and explains why CoO forms as assemblies rather than as dispersed nanocrystals.

6.3 Results

Figure 6.1 illustrates the experimental and analytical workflow of conventional SAXS in comparison with SP-SAXS. In conventional SAXS, measured at a synchrotron or laboratory X-ray source, each diffraction pattern represents the sum of scattering contributions from all species within the illuminated sample volume. In contrast, SP-SAXS collects diffraction patterns from individual particles that are delivered in a dilute aerosol or liquid jet at an XFEL. The single-particle diffraction patterns are typically noisy, incomplete, and un-oriented. To obtain high-resolution data, a large ensemble of similar single-particle diffraction patterns are identified, orientationally aligned, and averaged. Each averaged dataset forms a class, whose relative hit ratio reflects the population of the corresponding particle type within the sample. The SP-SAXS data processing routine follows similar principles to single-particle imaging (SPI) or coherent diffractive imaging (CDI), in which the individual diffraction patterns are mapped in three-dimensional diffraction space and phase reconstructed.^{73,74} In SP-SAXS, we analyze the averaged two-dimensional diffraction images and their radial integrations.

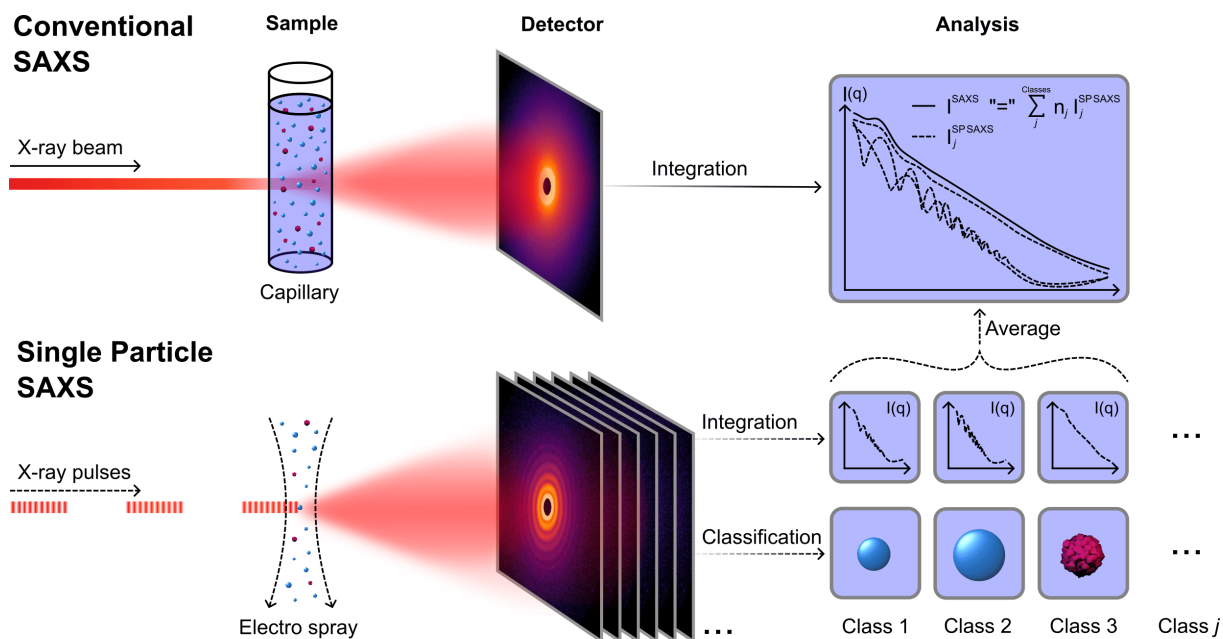


Figure 6.1: Experimental and analytical workflow of single-particle SAXS (SP-SAXS) compared to conventional SAXS. In conventional SAXS, the diffraction pattern comprises scattering contributions of all species within the illuminated sample volume of the X-ray beam from a synchrotron or laboratory source. In SP-SAXS, diffraction patterns from individual particles are averaged into classes, each representing a distinct particle population within the sample. The relative hit ratio of each class, n_j , reflects the concentration of the corresponding particle species j . In principle, the sum of all SP-SAXS class diffraction patterns, $I_j^{\text{SP-SAXS}}$, reproduces the total diffraction pattern obtained in conventional SAXS, I^{SAXS} .

To elucidate the CoO nanocrystal assembly formation pathway, we perform SP-SAXS on reaction aliquots collected at three early reaction times during the emergence of the CoO assemblies: 20, 30, and 40 min. In total, we collect 650 000 single particle diffraction snapshots with an average hit rate of 2.1 %, from which 60 distinct classes are identified across the combined dataset of the three aliquots. Table S6.1 lists all classes including their total hit rate and relative occupancies across the different reaction times. Figures S6.1 and S6.2 display the diffraction images and corresponding radial integrations of all classes.

In Figure 6.2, we show representative diffraction patterns of selected classes. The scattering profiles can be assigned either to amorphous, uniform-density spheres – referred to as sphere classes, or to nanocrystal assemblies – referred to as assembly classes. The sphere classes exhibit isotropic ring patterns in their diffraction images, and the corresponding radial integrations display the characteristic oscillations of monodisperse spherical form factors with an overall q^{-4} intensity decay. At higher q values $> 3 \text{ nm}^{-1}$, the intensity increases systematically in all sphere classes, which originates from diffuse scattering from the amorphous structure of the spherical particles. The assembly classes, in contrast, display sharp low- q peaks in the diffraction images, arising from the internal fractal arrangement of nanocrystals within the assemblies. Their radial integrations typically feature one intensity bump around 0.2 nm^{-1} , followed by a smooth decay – closely resembling the SAXS profile observed after full conversion of the intermediate into CoO assemblies.⁹¹ We estimate the assembly size from the position of the intensity bump. The sphere patterns are modeled using a spherical form factor, incorporating a Gaussian size distribution to account for minor variations in particle size within each sphere class. We note that some sphere classes fit well in the low- q region of the first fringes, but the model tends to underestimate the intensity for $q > 0.5 \text{ nm}^{-1}$. This weak

deviation suggests the onset of structural inhomogeneity, possibly early crystallization within a subset of spheres; however, the effect is subtle and should be regarded as a qualitative trend rather than a quantitative indicator of structural evolution. Synthesis, sample preparation, SP-SAXS data processing, and the fitting procedure and size determination of the classes' diffraction patterns are described in the Supporting Information in detail.

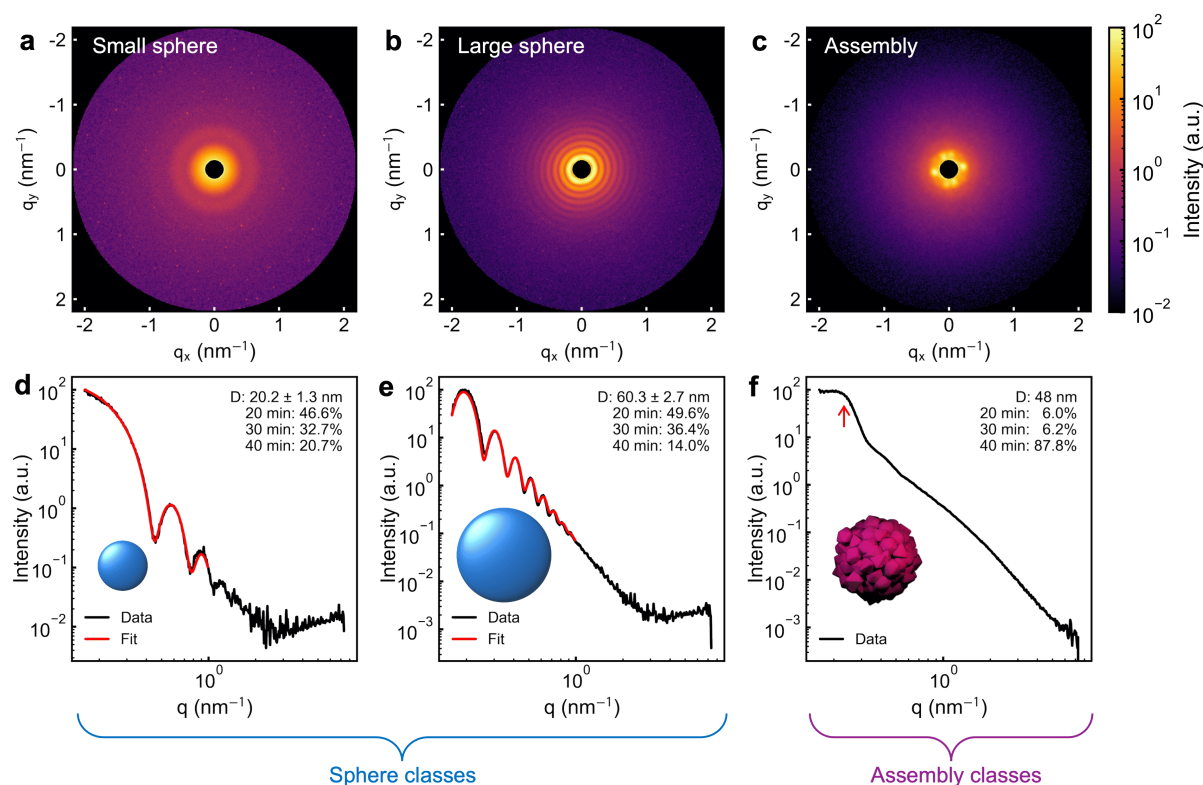


Figure 6.2: Representative diffraction images (a-c) and corresponding radial integrations (d-f) of selected SP-SAXS classes. The diameter D of the sphere classes is fitted with the a spherical form factor, where the error represents the standard deviation of the Gaussian distribution. The diameter of the assembly classes is estimated by the intensity bump maximum as marked by the red arrow. The relative occupancy of each class at 20, 30, and 40 min reflects the temporal evolution of the populations.

Figure 6.3a-c show the summed radial integrations of the sphere, assembly, and all classes at the different reaction times. The summed sphere classes show a steady q^{-4} slope, due to smearing of spherical form factor oscillations of the overall polydisperse ensemble, and a positive slope at high q due to the diffuse scattering of the amorphous spheres. The summed assembly classes radial integrations exhibit the characteristic low q intensity bump associated with the internal nanocrystal arrangement within the assemblies. At reaction times 20 and 30 min, the scattering contribution from the assembly classes is indistinguishable in the radial integration sum of all classes whereas at 40 min the assembly classes dominate the scattering profile due to its increasing concentration. Figure 6.3d-f show the size distributions of the sphere and assembly classes at the respective reaction times, revealing a progressive increase in the fraction of assemblies over time.

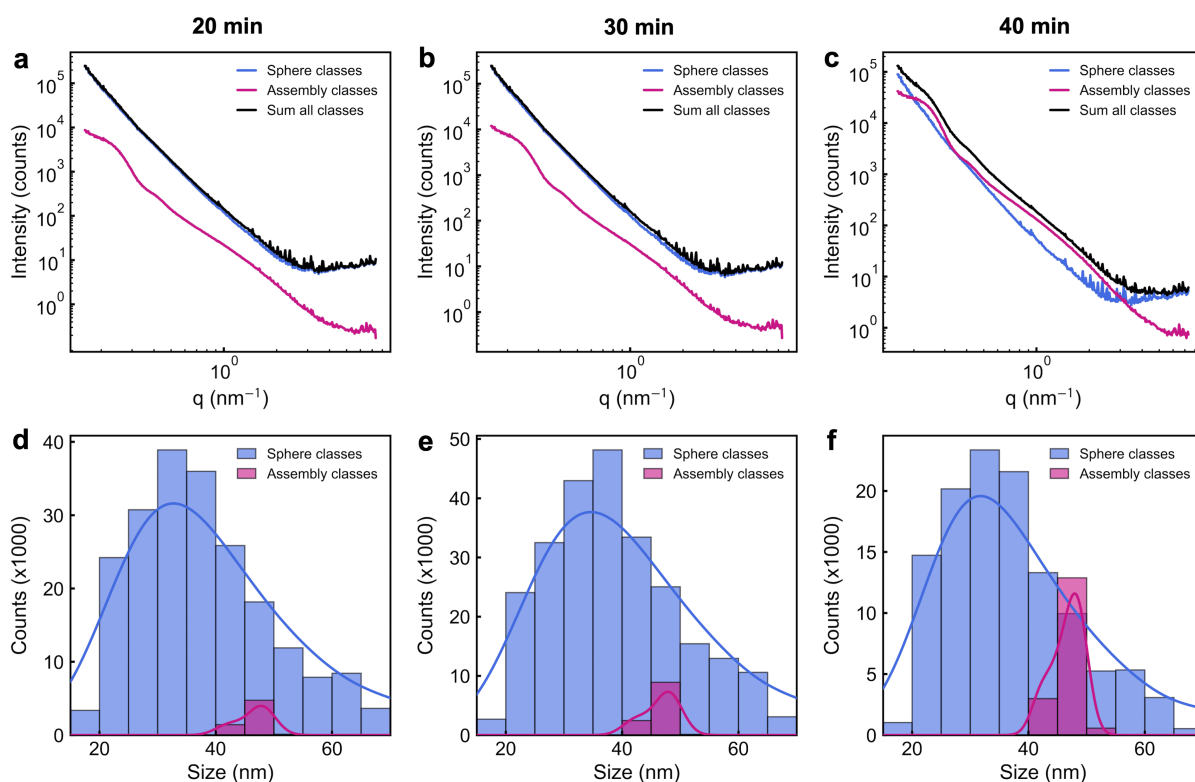


Figure 6.3: SP-SAXS analysis of the reaction aliquots at 20, 30, and 40 min. (a-c) Summed radial integrations of the sphere, assembly, and all classes. (d-f) Histogram of the size distribution of the sphere and assembly classes. The solid trace shows a kernel density estimate of the histograms.

Altogether, the SP-SAXS analysis reveals a population evolution from amorphous, uniform-density spheres to nanocrystal assemblies, as illustrated in Figure 6.4. To interpret these morphological observations, we relate the SP-SAXS results to the chemical transformation pathway established in earlier *in situ* X-ray studies: Initially, the precursor $\text{Co}(\text{acac})_3$ is dissolved in benzyl alcohol, where it reduces to the intermediate $\text{Co}(\text{acac})_2$, which subsequently transforms into CoO .⁹¹ The SP-SAXS findings indicate that $\text{Co}(\text{acac})_2$ phase-separates into spherical amorphous precipitates upon reduction, owing to its low solubility in benzyl alcohol. The comparable size range of these amorphous spheres and the emerging assemblies suggests a direct structural transformation rather than secondary aggregation of individual nanocrystals. Crystallization is likely initiated from high local supersaturation of $\text{Co}(\text{acac})_2$ inside the precipitate volume. During crystallization, the higher density of CoO compared to $\text{Co}(\text{acac})_2$ causes the spherical precipitates to contract, giving rise to cavernous polycrystalline assemblies instead of dense crystalline entities.

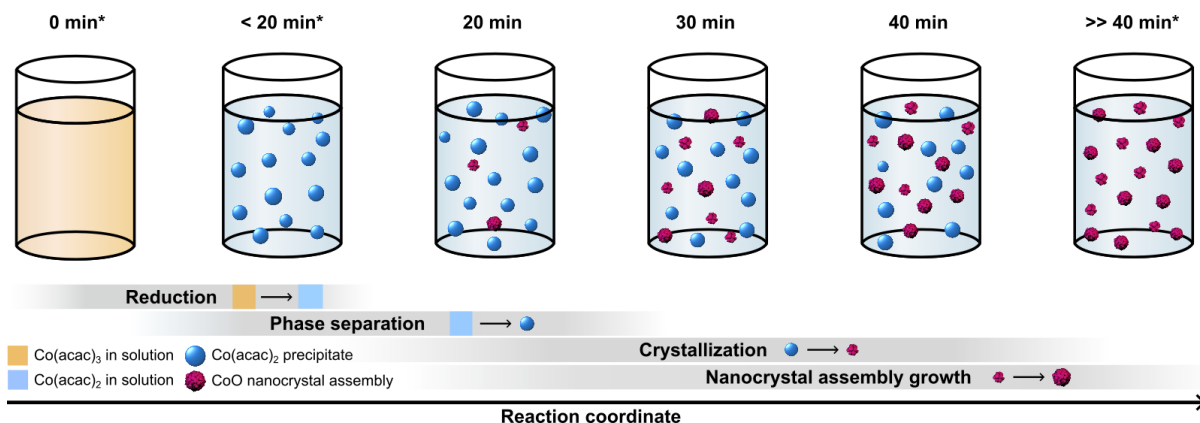


Figure 6.4: Schematic illustration of the proposed formation pathway of CoO nanocrystal assemblies after the reaction of $\text{Co}(\text{acac})_3$ in benzyl alcohol. Initially, $\text{Co}(\text{acac})_3$ reduces to $\text{Co}(\text{acac})_2$, which subsequently phase-separates to spherical amorphous precipitates. With increasing reaction time, these $\text{Co}(\text{acac})_2$ precipitates crystallize into CoO nanocrystal assemblies. The asterisks (*) denote extrapolated reaction states before and after the measured time points of 20, 30, and 40 min.

The $\text{Co}(\text{acac})_2$ spheres can easily be overlooked in conventional SAXS measurements, as their smooth intensity decay lacks distinct features in the SAXS regime and may be mistaken for background scattering. In electron microscopy (EM) images, these spheres can also be misinterpreted as organic aggregates or reaction byproducts unrelated to the assembly formation mechanism. Moreover, because of the poor solubility of $\text{Co}(\text{acac})_2$ in benzyl alcohol, a significant fraction of the spheres may be lost during sample washing and redispersion. For instance, spherical aggregates are found in the supernatant after washing the reaction mixture with ethanol, as shown in Figure S6.7a,b. This likely explains why the spherical $\text{Co}(\text{acac})_2$ particles were not observed in previous studies, where the samples were washed several times with ethanol prior to EM analysis.⁹¹ To further confirm the precipitation behavior of $\text{Co}(\text{acac})_2$, Figure S6.7c,d show EM images of commercial $\text{Co}(\text{acac})_2$ dissolved in benzyl alcohol and ethanol, both showing precipitation of spherical particles similar to those detected in the reaction solution and supernatant.

6.4 Conclusion

In conclusion, the single-particle perspective provided by SP-SAXS offers unprecedented insight into nanoparticle formation pathways by quantitatively resolving distinct particle populations that may be obscured in conventional measurements. Applied to the solvothermal synthesis of CoO, SP-SAXS reveals that intermediate amorphous $\text{Co}(\text{acac})_2$ spheres crystallize into CoO nanocrystal assemblies, elucidating why CoO emerges as hierarchical aggregates rather than as dispersed nanocrystals. Beyond this specific case, SP-SAXS represents a broadly applicable approach for studying morphological and structural heterogeneity in complex systems. Extending the concept to single-particle wide-angle X-ray scattering (SP-WAXS), achieved by reducing the sample-to-detector distance, would allow quantitative access to atomic-scale order similar to serial femtosecond crystallography (SFX).⁷⁵ A multimodal two-detector configuration could further combine SP-SAXS and SP-WAXS, bridging the full range from atomic to mesoscopic structure. Looking ahead, the realization of *in situ* SP-SAXS and SP-WAXS experiments, where small volumes of the reaction mixture are continuously injected

into the XFEL beam, will open the way toward real-time visualization of nanoparticle nucleation and growth at the single-particle level, transforming our ability to directly observe matter in formation.

Acknowledgements

This research was supported by the Deutsche Forschungsgemeinschaft (DFG) through the Cluster of Excellence “Advanced Imaging of Matter” (EXC 2056, project ID 390715994) and by the European Research Council (LINCHPIN project, grant no. 818941). We acknowledge European XFEL in Schenefeld, Germany, for provision of X-ray free-electron laser beamtime at SPB/SFX SASE1 under proposal number 2995 as well as DESY (Hamburg, Germany), a member of the Helmholtz Association, for the provision of synchrotron beamtime at beamline P21.1¹³⁵ and P62. We thank the beamline staffs for the support with the experiments: at P62, Dr. Sylvio Haas; at P21.1, Dr. Martin v. Zimmermann, Dr. Ann-Christin Dippel, Dr. Fernando Igoa, Dr. Jiatu Liu, Philipp Glaeveccke, and Olof Gutowski. Further, we thank Stefan Werner from University of Hamburg for the TEM measurements, and we acknowledge financial support from the Open Access Publication Fund of University of Hamburg.

S6 Supporting information

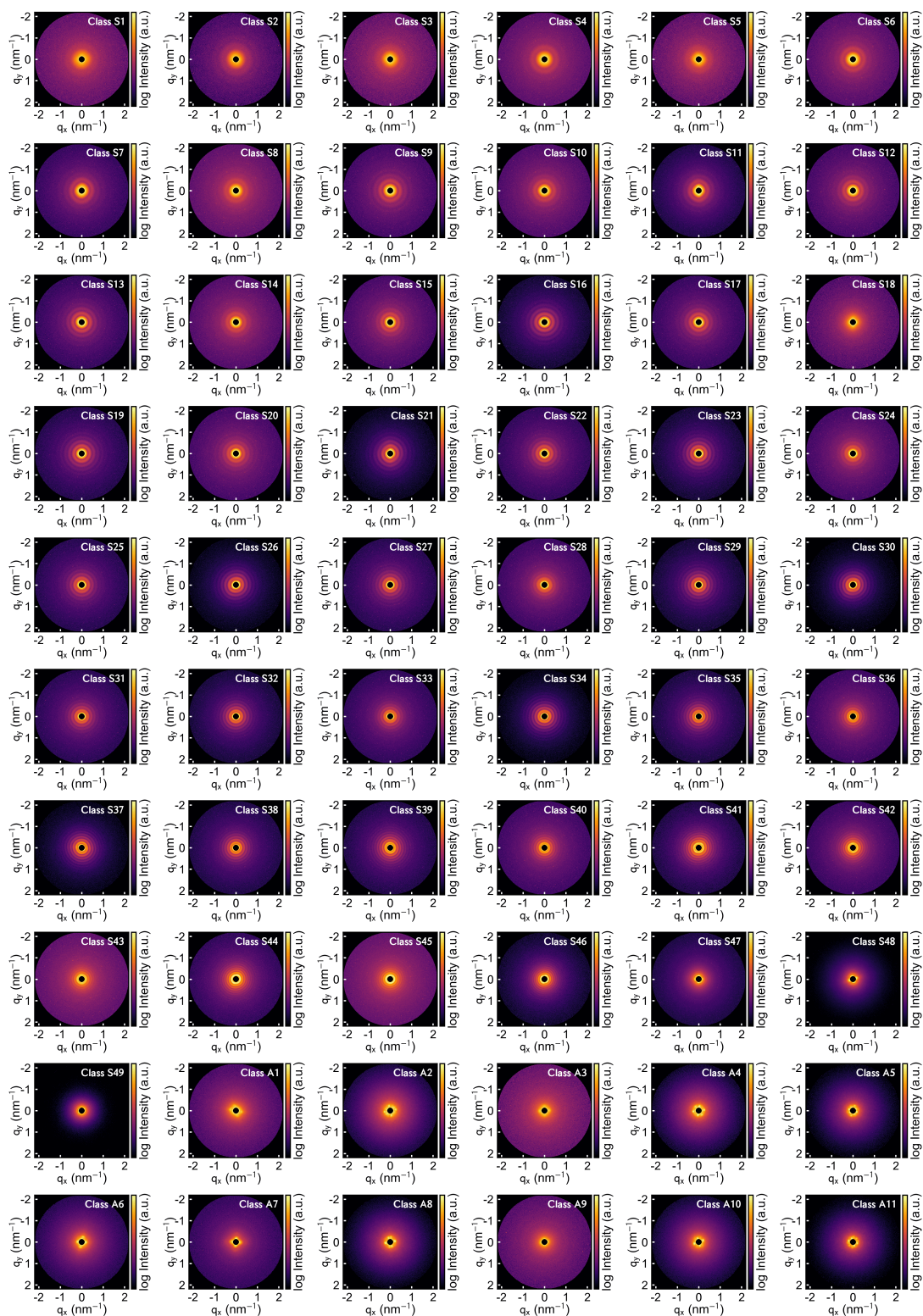


Figure S6.1: Diffraction images of all SP-SAXS classes.

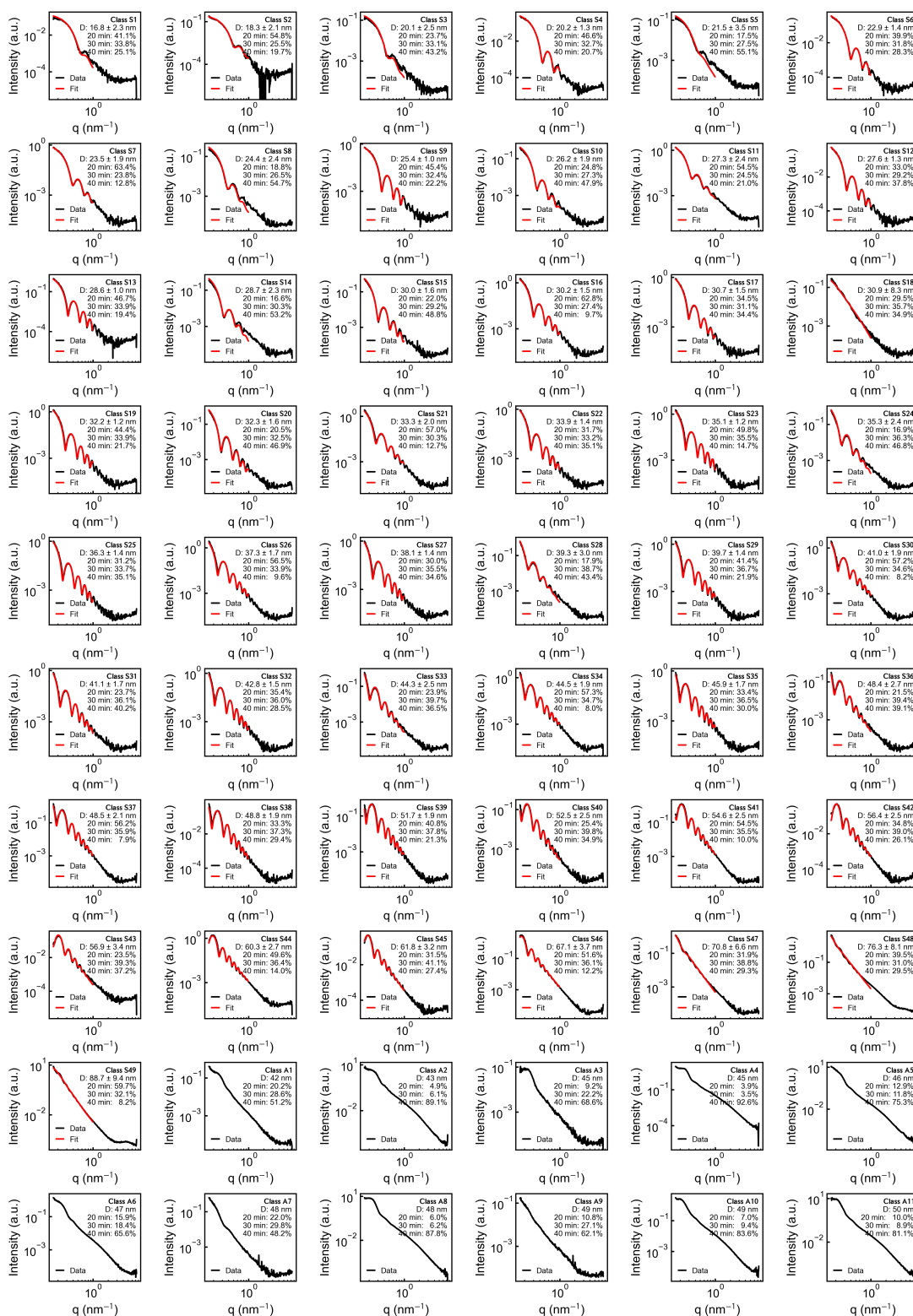


Figure S6.2: Radial integration of all SP-SAXS classes including their determined diameter D and relative occupancy of the measured reaction times 20, 30, and 40 min.

Table S6.1: List of all SP-SAXS classes with class number (#), their classification into sphere (S) or assembly (A) classes, determined particle sizes, relative occupancies at the different reaction times (20, 30, and 40 min), total number of hits per class, and the hit ratio of each class relative to the total number of hits across all classes.

#	Diameter (nm)	20 min (%)	30 min (%)	40 min (%)	No. hits	Hit ratio (%)
S1	16.8 ± 2.3	41.1	33.8	25.1	4333	0.0067
S2	18.3 ± 2.1	54.8	25.5	19.7	2771	0.0043
S3	20.1 ± 2.5	23.7	33.1	43.2	3280	0.0051
S4	20.2 ± 1.3	46.6	32.7	20.7	15237	0.0237
S5	21.5 ± 3.5	17.5	27.5	55.1	3090	0.0048
S6	22.9 ± 1.4	39.9	31.8	28.3	14541	0.0226
S7	23.5 ± 1.9	63.4	23.8	12.8	8776	0.0137
S8	24.4 ± 2.4	18.8	26.5	54.7	18100	0.0282
S9	25.4 ± 1.0	45.4	32.4	22.2	13540	0.0211
S10	26.2 ± 1.9	24.8	27.3	47.9	16331	0.0254
S11	27.3 ± 2.4	54.5	24.5	21.0	9984	0.0155
S12	27.6 ± 1.3	33.0	29.2	37.8	14975	0.0233
S13	28.6 ± 1.0	46.7	33.9	19.4	12581	0.0196
S14	28.7 ± 2.3	16.6	30.3	53.2	16025	0.0249
S15	30.0 ± 1.6	22.0	29.2	48.8	16310	0.0254
S16	30.2 ± 1.5	62.8	27.4	9.7	9894	0.0154
S17	30.7 ± 1.5	34.5	31.1	34.4	16396	0.0255
S18	30.9 ± 8.3	29.5	35.7	34.9	4160	0.0065
S19	32.2 ± 1.2	44.4	33.9	21.7	13113	0.0204
S20	32.3 ± 1.6	20.5	32.5	46.9	17880	0.0278
S21	33.3 ± 2.0	57.0	30.3	12.7	9569	0.0149
S22	33.9 ± 1.4	31.7	33.2	35.1	17933	0.0279
S23	35.1 ± 1.2	49.8	35.5	14.7	12412	0.0193
S24	35.3 ± 2.4	16.9	36.3	46.8	16678	0.0260
S25	36.3 ± 1.4	31.2	33.7	35.1	17124	0.0267
S26	37.3 ± 1.7	56.5	33.9	9.6	12365	0.0192
S27	38.1 ± 1.4	30.0	35.5	34.6	16589	0.0258
S28	39.3 ± 3.0	17.9	38.7	43.4	16164	0.0252
S29	39.7 ± 1.4	41.4	36.7	21.9	14393	0.0224
S30	41.0 ± 1.9	57.2	34.6	8.2	9600	0.0149
S31	41.1 ± 1.7	23.7	36.1	40.2	18259	0.0284
S32	42.8 ± 1.5	35.4	36.0	28.5	15901	0.0248
S33	44.3 ± 2.5	23.9	39.7	36.5	19276	0.0300
S34	44.5 ± 1.9	57.3	34.7	8.0	9581	0.0149
S35	45.9 ± 1.7	33.4	36.5	30.0	15587	0.0243
S36	48.4 ± 2.7	21.5	39.4	39.1	15322	0.0238
S37	48.5 ± 2.1	56.2	35.9	7.9	8394	0.0131
S38	48.8 ± 1.9	33.3	37.3	29.4	13871	0.0216
S39	51.7 ± 1.9	40.8	37.8	21.3	10418	0.0162
S40	52.5 ± 2.5	25.4	39.8	34.9	15325	0.0239
S41	54.6 ± 2.5	54.5	35.5	10.0	6836	0.0106
S42	56.4 ± 2.5	34.8	39.0	26.1	13104	0.0204
S43	56.9 ± 3.4	23.5	39.3	37.2	13076	0.0204
S44	60.3 ± 2.7	49.6	36.4	14.0	8262	0.0129
S45	61.8 ± 3.2	31.5	41.1	27.4	13832	0.0215
S46	67.1 ± 3.7	51.6	36.1	12.2	7288	0.0113
S47	70.8 ± 6.6	31.9	38.8	29.3	17887	0.0278
S48	76.3 ± 8.1	39.5	31.0	29.5	10107	0.0157
S49	88.7 ± 9.4	59.7	32.1	8.2	1777	0.0028
A1	42	20.2	28.6	51.2	5813	0.0090
A2	43	4.9	6.1	89.1	1054	0.0016
A3	45	9.2	22.2	68.6	3459	0.0054
A4	45	3.9	3.5	92.6	814	0.0013
A5	46	12.9	11.8	75.3	1103	0.0017
A6	47	15.9	18.4	65.6	3581	0.0056
A7	48	22.0	29.8	48.2	9831	0.0153
A8	48	6.0	6.2	87.8	938	0.0015
A9	49	10.8	27.1	62.1	4950	0.0077
A10	49	7.0	9.4	83.6	1876	0.0029
A11	50	10.0	8.9	81.1	798	0.0012
Σ	-	35.3	42.9	21.8	642461	100.0000

Experimental

Single particle small-angle X-ray scattering (SP-SAXS):

The SP-SAXS measurements were performed at the Single Particle, Biomolecules and Clusters/Serial Femtosecond Crystallography (SPB/SFX) end-station at the European X-ray Free Electron Laser (EuXFEL)²⁴⁶. X-ray pulses with photon energy of 6 keV and average pulse energy of 1.2 μJ were focused to a diameter of around 250 nm. The sample dispersion was aerosolized and transported to the X-ray interaction region using an electrospray and aerodynamic lens stack injection system²⁴⁷. Diffraction patterns were collected at an average rate of 3420 frames/second in 10 bursts of 342 frames per second on the AGIPD-1M detector²⁴⁸ placed 700 mm downstream of the interaction point.

An average of 2.0 % of the patterns contained statistically significant diffraction from single

particles above the background scattering, primarily from the carrier gas. Of these 794 902 patterns, 150 200 were discarded due to instabilities in the electrospray, during which very large droplets were produced. The other 644 702 patterns were first converted to photons using previously described procedures⁷⁴, and then classified into 50 classes using the *Dragonfly* software²⁴⁹. This classification is performed using the EMC algorithm²⁵⁰, where intensity models on the detector are determined which maximize the likelihood of generating the observed diffraction patterns using a Poisson noise model. The process was repeated from a random initial guess 5 times, yielding very similar results.

The results of this classification are shown in Figure S6.1 and Figure S6.2, in the classes labeled S1-S49. A second round of classification was performed with all patterns belonging to class averages which deviated from dense spherical particles, the results of which are marked as A1-A11 in the same figures.

Size determination SP-SAXS sphere classes:

The sphere classes were modeled using a custom Python script. The spherical form factor $f(q, r)$ is given by

$$f(q, r) = \frac{\sin(qr) - qr \cos(qr)}{(qr)^3}, \quad (6.1)$$

where q is the magnitude of the scattering vector and $r = D/2$ the particle radius, and the intensity of monodisperse spherical particles would be

$$I_{\text{mono}}(q) \propto f^2(q, r). \quad (6.2)$$

To account for size polydispersity within a class, we assume a Gaussian probability density function $p(r_0, \sigma)$ of the particle radii,

$$p(r, r_0, \sigma) = \frac{1}{\sqrt{2\pi} \sigma} \exp \left[-\frac{(r - r_0)^2}{2\sigma^2} \right], \quad (6.3)$$

where r_0 is the mean radius and σ is the standard deviation. The scattering intensity of a polydisperse ensemble, $I_{\text{poly}}(q)$, is then calculated by summing the form-factor contributions of N discrete radii in a $\pm 3\sigma$ -range weighted by their probability:

$$I_{\text{poly}}(q) \propto f_{\text{poly}}^2(q, r_0, \sigma) = \sum_{n=1}^N p(r_n, r_0, \sigma) \cdot f^2(q, r_n). \quad (6.4)$$

To reduce the influence of the high-intensity low- q region during fitting, we minimize the residual χ^2 using relative intensity weights via

$$\chi^2 = \sum_i \left[\frac{I_i - I_{\text{model}}(q_i)}{I_i} \right]^2. \quad (6.5)$$

The parameters r_0 , σ , and a scale factor were refined by minimizing χ^2 using the Levenberg–Marquardt algorithm implemented in SciPy's `optimize.least_squares` function.²³⁰

Size determination SP-SAXS assembly classes:

The particle sizes of the assembly classes were estimated by assuming a uniform density for

the spherical assemblies, following the approach of Grote et al.⁹¹ The SP-SAXS profiles do not extend into the Guinier regime, which prevents reliable form-factor fitting. Instead, the assembly sizes were obtained directly from the position of the first intensity oscillation in the scattering profile. Specifically, we determine the size from either the maximum or the subsequent local minimum of the first intensity bump, as illustrated in Figure S6.3.

The zero of the first derivative of equation 6.1 and 6.2 gives the particle diameter of the first intensity oscillation maximum $q_{1,\max}$ and the subsequent minimum $q_{2,\min}$ via:

$$D_{1,\max} = \frac{11.54}{q_{1,\max}}, \quad D_{2,\min} = \frac{15.45}{q_{2,\min}}. \quad (6.6)$$

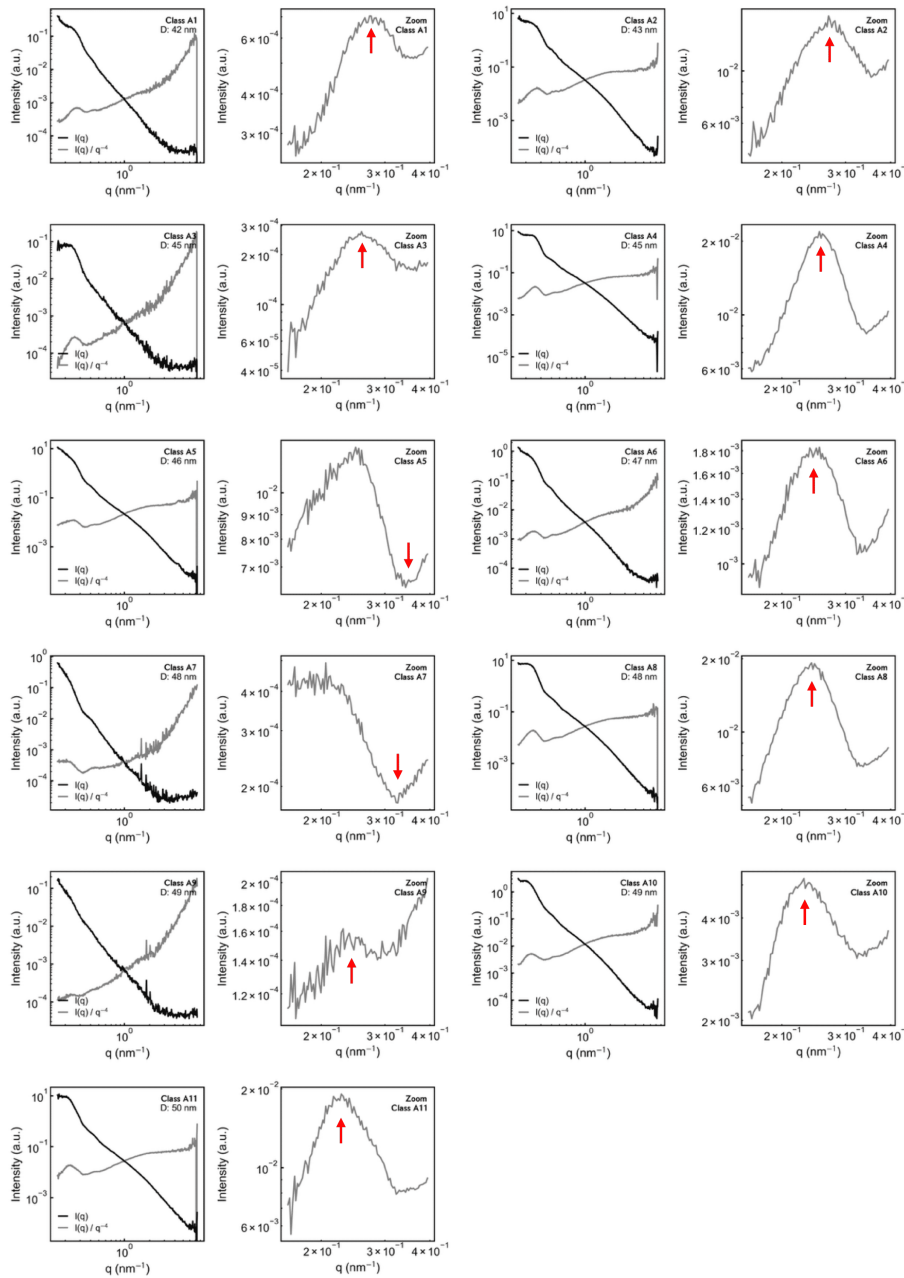


Figure S6.3: Radial integration of SP-SAXS assembly classes. The upwards facing red arrow indicates the local maximum, $q_{1,\max}$, and the downwards facing red arrow indicated subsequent minimum, $q_{2,\min}$, of the first intensity bump, which was used to determine the size of the assembly. To better see the intensity bump the data is divided by q^{-4} .

Synthesis:

All chemicals were purchased from commercial sources and used without further purification: $\text{Co}(\text{acac})_3$ (Sigma-Aldrich, 99.99%), $\text{Co}(\text{acac})_2$ (Acros, 99.9%), benzyl alcohol (Sigma-Aldrich, >99%), and ethanol (VWR, absolute grade).

The synthesis is performed as described by Grote et al.⁹¹ $\text{Co}(\text{acac})_3$ (179.1 mg, 0.5 mmol) is added to 5 mL of benzyl alcohol and stirred for 10 min at room temperature. 0.8 mL of the reaction solution are then transferred to the reaction container of the reactor, which is described in detail by Grote et al.. After assembling the reaction container in the reactor, it is first heated to 60 °C with an heating rate of 1 °C/s for 5 min, and then heated to 160 °C with the same heating rate. The time of the beginning of the reaction (t_0) is defined at the point where the heating of the reaction solution from 60 °C to 160 °C starts. All mentions of the reaction times are relative to t_0 . For the SP-SAXS measurements the reaction was stopped after 20, 30, and 40 min, and the reactor was cooled with a cold metal block. Figures S6.4, S6.5, and S6.6 show conventional SAXS, PDF, and TEM data, respectively, of the 20, 30, and 40 min samples. The samples for the reference EM measurements of $\text{Co}(\text{acac})_2$ precipitates shown in Figure S6.7c,d were prepared by stirring $\text{Co}(\text{acac})_2$ (55.4 mg, 0.2 mmol) in 2 mL benzyl alcohol or ethanol for 30 min at room temperature.

Sample preparation:

The SP-SAXS samples were prepared by centrifuging the quenched reaction solution in ethanol for 5 min at 3500 rpm, discarding the supernatant, and collecting the residue. The residue was then weighed and redispersed in a 10 mmol ammonium acetate ethanol solution to obtain a concentration of 0.075 mg/mL.

Conventional SAXS samples were prepared either by directly filling the reaction solution in a capillary or by centrifuging at 3500 rpm for 5 min in ethanol, redispersing the residue in ethanol and filling the capillary with the dispersion.

PDF samples were measured from dry powder after centrifuging at 3500 rpm for 5 min in ethanol.

EM samples were prepared by depositing one drop of the sample solution on a TEM grid and washing the grid with a few drops of ethanol.

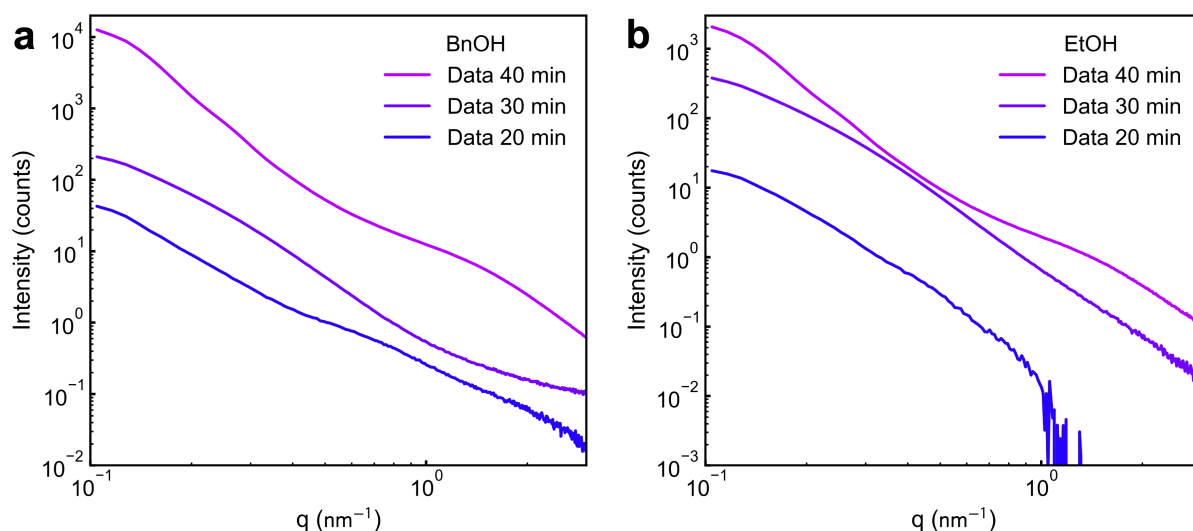


Figure S6.4: Conventional SAXS data of (a) reaction solutions in benzyl alcohol (BnOH) after 20, 30, and 40 min reaction time and (b) the reaction solutions redispersed in ethanol (EtOH) after centrifuging at 3500 rpm for 5 min. Both the BnOH and EtOH data show similar scattering profiles at the respective time points. Both data sets were measured at the lower part of capillary, which showed sample precipitation, making a comparison of the conventional SAXS to the summed SP-SAXS data, which is measured from very diluted particles, difficult.

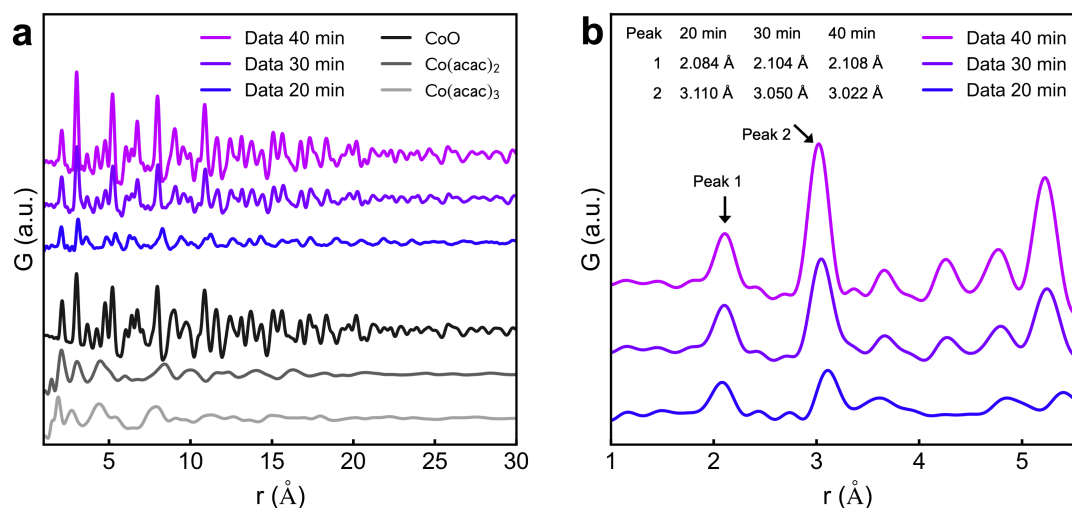


Figure S6.5: (a) Pair distribution function (PDF) of total X-ray scattering data of 20, 30, and 40 min samples compared to PDF simulations of rock-salt CoO, Co(acac)₂²⁵¹, and Co(acac)₃²⁵² structures. The 30 and 40 min PDF closely matches the CoO simulation, while the 20 min sample shows features of both CoO and Co(acac)₂, which confirms the proposed phase transition of Co(acac)₂ to CoO. (b) Zoom of the experimental PDFs. The inset lists the peak position of the first and second peak. A detailed PDF analysis is beyond the scope of this paper, but available in the literature.⁹¹

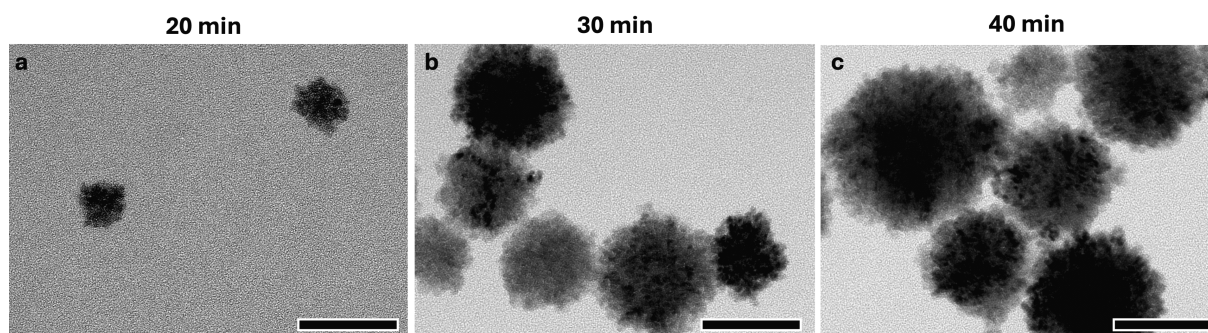


Figure S6.6: TEM images of CoO nanocrystal assemblies of reaction aliquots of (a) 20 min, (b) 30 min, and (c) 40 min. Scale bars 50 nm.

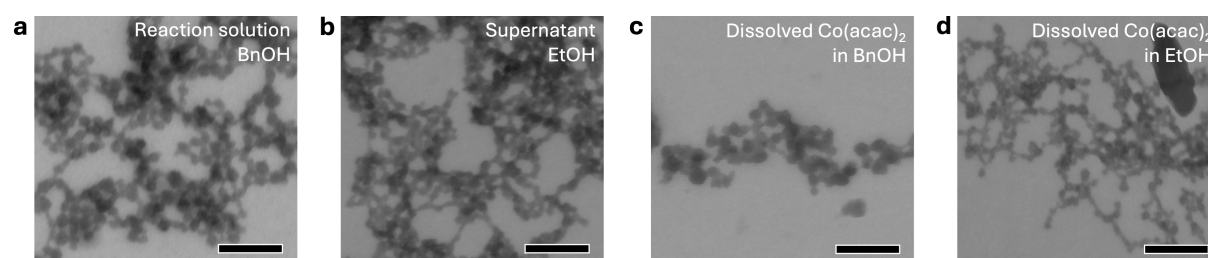


Figure S6.7: STEM images of spherical aggregates from solutions in benzyl alcohol (BnOH) or ethanol (EtOH). (a) Quenched reaction solution of the reaction of $\text{Co}(\text{acac})_3$ in BnOH after 20 min reaction time. (b) Supernatant of washed reaction solution of (a) after centrifugation for 5 min at 3500 rpm in EtOH. Control experiments: commercial $\text{Co}(\text{acac})_2$ dissolved in (c) BnOH and (d) EtOH for 30 min. Scale bars: 100 nm.

Reproducibility of the synthesis:

The reaction kinetics observed in this study appear slightly slower than those reported by Grote et al.⁹¹ based on the comparison of SAXS, EM, and PDF data. This difference is related to slight variations in the reactor inlet design, as discussed elsewhere.¹⁵ The overall trends are similar.

Furthermore, we occasionally observe crumpled sheet- or rose-like particles with sizes of approximately 0.5-1.0 μm , as shown in Figure S6.8. These particles are beyond the detection limit of our SP-SAXS set-up and appear more frequently at 20 min, while they are rarely seen at 30 or 40 min. Similar rose-like structures were also reported by Grote et al.⁹¹ at reaction times earlier than 20 min. Given their disappearance as the reaction progresses, we attribute these particles to side reactions that do not affect the formation of CoO nanocrystal assemblies.

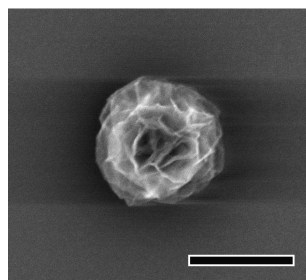


Figure S6.8: SEM image of a rose-like particle from a 20 min reaction aliquot. Scale bar: 500 nm.

Electron microscopy (EM):

Scanning electron microscopy (SEM) and scanning transmission electron microscopy (STEM) images were collected using a Regulus 8220 (Hitachi High Technologies Corp.) with an acceleration voltage of 30 keV. Transmission electron microscopy (TEM) images were collected using a JEM 1011 (JEOL Ltd.) with an acceleration voltage of 100 keV.

Conventional SAXS:

SAXS data was acquired at beamline P62 of PETRA III at Deutsches Elektronen-Synchrotron DESY, Hamburg, Germany. The particle dispersions were filled in a 1 mm diameter borosilicate capillary and diffraction images were recorded for 30 s at an X-ray energy of 24.30 keV ($\lambda = 0.5102 \text{ \AA}$) using a two-dimensional X-ray detector (EIGER2 X 9M, Dectris Ltd.) with 3108×3262 pixels and a pixel size of $75 \times 75 \mu\text{m}^2$ and a sample-to-detector distance of 4.946 m, obtained from a calibration with a silver behenate standard packed into a capillary. The diffraction images were integrated using PyFAI¹³⁶.

Total X-ray scattering (TS) and pair distribution function (PDF) analysis:

TS data was acquired at beamline P21.1¹³⁵ of PETRA III at Deutsches Elektronen-Synchrotron DESY, Hamburg, Germany. The powder sample was packed in a 1 mm diameter borosilicate capillary and diffraction images were recorded for 60 s at an X-ray energy of 101.39 keV ($\lambda = 0.1222 \text{ \AA}$) using a two-dimensional X-ray detector (PerkinElmer XRD1621, Varex Imaging Corp.) with 2048×2048 pixels and a pixel size of $200 \times 200 \mu\text{m}^2$ and a sample-to-detector distance of 0.301 m, obtained from a calibration with a LaB_6 powder standard packed into a capillary. The diffraction images were integrated using PyFAI¹³⁶. The experimental PDFs were calculated using PDFgetX3²³⁵ with values $q_{\text{max,inst}} = 25.0 \text{ \AA}^{-1}$, $q_{\text{max}} = 22.5 \text{ \AA}^{-1}$, $q_{\text{min}} = 1.0 \text{ \AA}^{-1}$, and $r_{\text{poly}} = 0.9$. The PDF simulations were calculated using DiffPy-CMI⁷¹ with the same values as the experimental PDF calculations.

7 Conclusions

This thesis introduces new synthetic, experimental, and analytical methodologies for metal oxide and metal nitride nanoparticles, and provides mechanistic insight into their nucleation and growth by resolving their structural evolution using complementary X-ray techniques. Figure 7.1 provides a schematic summary of the formation pathways of the main systems studied – Cu_3PdN , Fe_3O_4 , and CoO – together with their corresponding experimental setups.

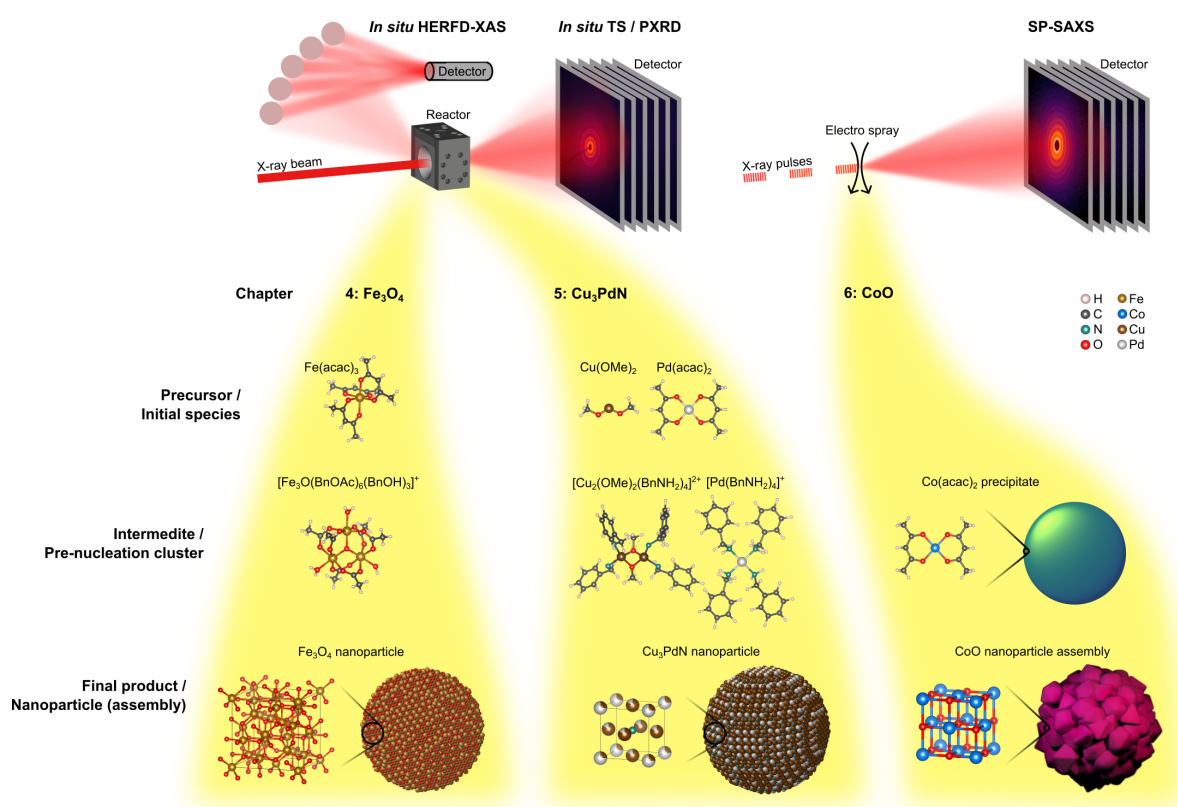


Figure 7.1: Formation mechanisms of Fe_3O_4 , Cu_3PdN , and CoO nanostructures alongside schematic illustrations of associated experimental setups used to study the respective reaction.

First, we present a versatile reactor that integrates XAS, WAXS, and SAXS experiments at synchrotron sources on a single experimental platform (Chapter 4). The reactor enables to study solvothermal syntheses under autoclave-like, inert conditions, and provides precise control over the reaction temperature between $-20\text{ }^\circ\text{C}$ and $200\text{ }^\circ\text{C}$, pressures up to 8 bar, magnetic stirring, and the controlled injection of gases or liquids.

The capabilities of this reactor are demonstrated in the study of the reaction of $\text{Fe}(\text{acac})_3$ to Fe_3O_4 in benzyl alcohol (Chapter 4). *In situ* TS together with HERFD-XAS reveal the formation of a ferric acetate $[\text{Fe}_3\text{O}(\text{AcOR})(\text{ROH})_3]^+$ complex preceding crystallization. Complementary *in situ* ATR-IR measurements show the thermal decomposition of acetylacetonate to benzyl

acetate, which supports the formation of ferric acetate as the intermediate. Together, these results uncover a nonclassical formation mechanism for Fe_3O_4 nanoparticles and highlight the strength of the reactor in combining multiple analytical techniques to resolve nucleation and growth processes in solution. Moreover, the modular reactor design allows straightforward extension to additional techniques, such as dynamic light scattering or UV/Vis spectroscopy, providing access to complementary aspects of nanoparticle formation. Beyond Fe_3O_4 , it is broadly applicable for a wide range of solution-based synthesis. In particular, its air-tight conditions enable the *in situ* investigation of highly sensitive synthesis such as for metal nitrides.

Building on these capabilities, the reactor is applied to the study of a novel one-pot synthesis of phase-pure Cu_3PdN nanoparticles (Chapter 5). *In situ* TS and HERFD-XAS measurements reveal the formation of $[\text{Cu}(\text{OMe})_2(\text{BnNH}_2)_4]^{2+}$ and $[\text{Pd}(\text{BnNH}_2)_4]^+$ complexes upon dissolution of the precursors $\text{Cu}(\text{OMe})_2$ and $\text{Pd}(\text{acac})_2$ in the solvent BnNH_2 . The Rietveld refinements of the *ex situ* PXRD patterns confirm the phase purity of the obtained Cu_3PdN nanoparticles and clarify the presence of Cu_3Pd impurities that have frequently gone unnoticed in previous reports. In contrast to all previously reported colloidal Cu_3PdN syntheses, the route introduced here proceeds at a reaction temperature of only 140 °C, which is ~ 100 °C lower than in earlier studies. The significantly smaller size of the synthesized Cu_3PdN nanoparticles, less than half that reported for previously described colloidal Cu_3PdN , provides in a high surface area, making them particularly well suited for electrocatalytic applications. We showcase that Cu_3PdN is suitable for the hydrogen evolution reaction, revealing remarkable stability and good catalytic activity. The double-edge EXAFS analysis reveals pronounced disorder within the anti-perovskite crystal lattice, where approximately 25 % of the Pd atoms interchange positions with adjacent Cu atoms, resulting in a disordered structure with partial cation-site occupancies. This phenomenon likely originates from high cation mobilities combined with short reaction times and is reported here for the first time for colloidal nitride nanoparticles. The methodologies and insights gained from the study of Cu_3PdN nanoparticle formation are transferable to other metal nitride systems, opening avenues to optimize their properties and expand their potential applications in energy conversion and beyond. Most importantly, controlling the degree of cation-site disorder through parameters such as heating rate, reaction temperature, reaction time, or precursor concentration could provide a powerful handle to deliberately tune key material properties, including the band gap, electronic conductivity, and electrocatalytic activity.

In the preceding studies on Fe_3O_4 and Cu_3PdN nanoparticle formation, complementary X-ray scattering and spectroscopy techniques at synchrotron sources provided detailed insights into nucleation and growth processes. Despite the rich structural and chemical information accessible with such conventional analytical X-ray techniques, transient, dilute, or low-contrast species may remain unresolved because the measured signal represents an average over the entire illuminated sample volume. This limitation was overcome by introducing SP-SAXS at XFELs. Using CoO nanoassembly formation as a case study, we demonstrate that, although previous XAS, WAXS, and SAXS measurements successfully clarified precursor conversion and CoO crystallization, they could not explain why CoO forms hierarchical assemblies rather than isolated nanocrystals. By applying SP-SAXS to reaction aliquots, spherical amorphous $\text{Co}(\text{acac})_2$ precipitates were identified as intermediate species that contract during crystallization into cavernous CoO assemblies, thereby resolving the origin of the hierarchical structures. This result highlights how the single-particle perspective provided by SP-SAXS can address mechanistic questions that remain inaccessible to even the most comprehensive ensemble-averaged *in situ* characterizations.

Altogether, this thesis extends the methodological toolbox by introducing synthesis approaches and experimental strategies for investigating nanoparticles – providing new means to watch nanoparticles form.

Appendix

The appendix of this thesis presents unpublished preliminary studies. Chapter A1 shows *in situ* X-ray scattering investigations of tin-doped iron oxide nanoparticles and illustrates how the introduction of a tin precursor modifies the reaction pathway and the resulting iron oxide crystal structure. Chapter A2 describes a synthetic route toward phase-pure Cu_3N nanoparticles enabled by the addition of an acetylacetonate precursor. Chapter A3 discusses crystallographic phase and morphology of side reaction products during the formation of CoO nanoassemblies. Finally, Chapter A4 presents a fabrication route for nanotextured TiO_2 films grown on sapphire substrates.

A1 *In situ* X-ray Scattering Study on $\text{Sn:Fe}_x\text{O}_y$

Iron oxide nanoparticles constitute one of the most extensively studied classes of nanomaterials due to their broad applicability in biomedicine, environmental remediation, electronics, and catalysis.²⁵³⁻²⁵⁶ Their appeal arises from their non-toxicity, low-cost synthesis, elemental abundance, and rich polymorphism. In particular, hematite (Fe_2O_3) and magnetite (Fe_3O_4) represent the most abundant iron oxide polymorphs, with hematite being the thermodynamically most stable bulk phase, while magnetite is often favored at small crystallite sizes.^{257,258} The magnetic, electronic, and catalytic properties of iron oxides strongly depend on particle size, morphology, and crystallographic structure, all of which can be tailored by controlling reaction parameters such as precursor chemistry, reaction temperature and time, as well as heteroatom doping. Nevertheless, the underlying formation pathways of iron oxides, including the transformation of iron species during synthesis, are often poorly understood.¹²⁴

In Chapter 4 we revealed the nonclassical formation of Fe_3O_4 nanoparticles from iron(III) acetylacetonate ($\text{Fe}(\text{acac})_3$) precursor in benzyl alcohol (BnOH) using *in situ* X-ray techniques. Upon reaching the reaction temperature of $180\text{ }^\circ\text{C}$, $\text{Fe}(\text{acac})_3$ converts into an intermediate $[\text{Fe}_3\text{O}(\text{AcOR})_6(\text{ROH})_3]^+$ complex, from which Fe_3O_4 nanoparticles subsequently form. Building on this work, the present chapter reports preliminary *in situ* X-ray scattering studies of the same synthesis, but with the addition of tin(IV) chloride (SnCl_4) yielding tin-doped iron oxide ($\text{Sn:Fe}_x\text{O}_y$) nanoparticles.

Figure A1.1 shows *in situ* PXRD data recorded during the synthesis of iron oxide nanoparticles with tin-doping concentrations ranging from 0 to 16 %, together with PXRD calculations of various metallic and oxide iron and tin phases, of which only Fe_3O_4 and Fe_2O_3 can be assigned to experimental patterns across all datasets. The percentages refer to the molar ratio of the tin relative to the iron precursor. The 0 % dataset represents the pristine iron oxide nanoparticle synthesis, which is the same dataset discussed in Chapter 4. Further, to better compare the progress of the different reactions, Figure A1.2 shows PXRD patterns at identical reaction time points for the different tin concentrations together with PXRD calculations of Fe_3O_4 and Fe_2O_3 . The reaction time of 0 min corresponds to the point at which the reaction temperature of $180\text{ }^\circ\text{C}$ is reached. Prior to this point, all PXRD datasets are similar and do

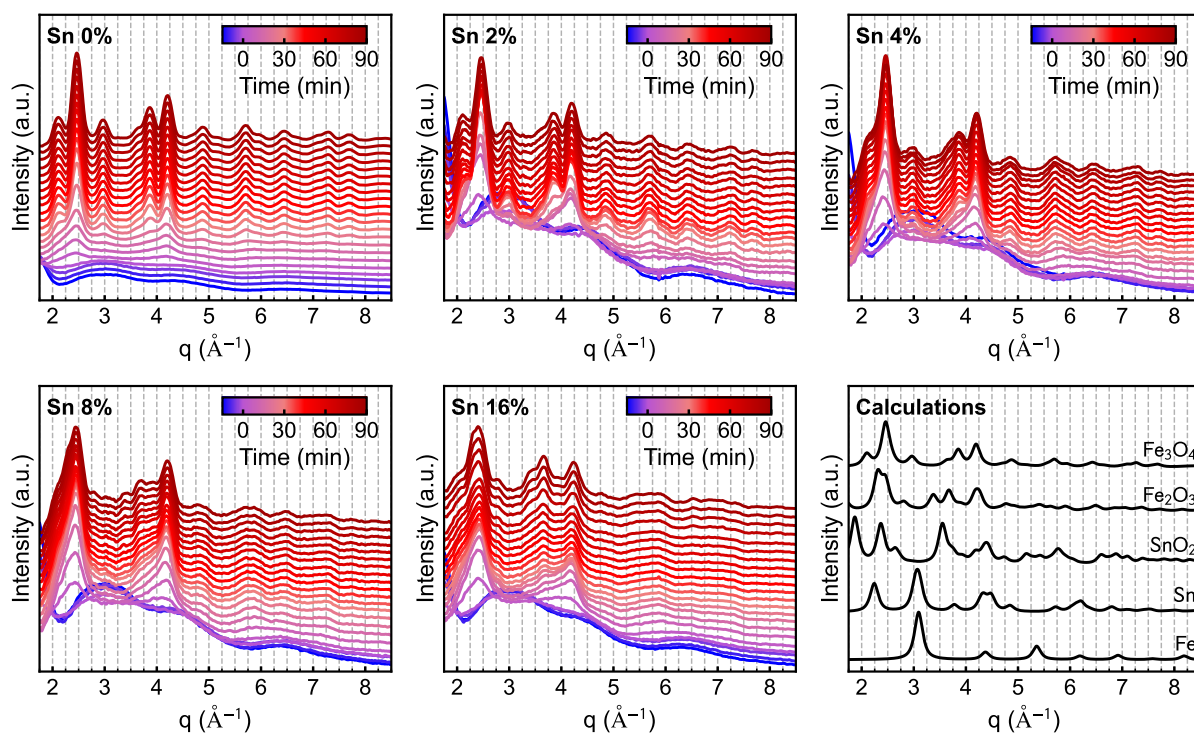


Figure A1.1: *In situ* PXRD waterfall plots of Sn:Fe_xO_y nanoparticle syntheses with different Sn concentrations compared to PXRD calculations.

not exhibit any Bragg reflection indicating that no crystalline phase forms up to this point. The early-stage PXRD patterns of the doped samples appear more intense than those of the undoped sample; however, this effect arises from the normalization of each dataset to the maximum intensity of the final pattern at 90 min, which is lower for the doped samples than for the undoped reference. This indicates a decrease in overall crystallinity upon the addition of tin. This becomes evident upon inspection of the PXRD data at extended reaction times. At approximately 15 min, Bragg reflections emerge, indicating the formation of iron oxide phases. For the undoped sample, the reflections are consistent with the Fe₃O₄ structure. Increasing tin concentrations lead to a progressive broadening of the reflections, attributable to a reduction in crystallite size and increased structural disorder, as well as to the emergence of a secondary Fe₂O₃ phase alongside Fe₃O₄. A similar trend has been observed for the same synthesis performed under microwave heating.²⁵⁹ In contrast to the present synthesis carried out in the *in situ* reactor,¹⁵ the PXRD patterns of Sn:Fe_xO_y nanoparticles obtained from the microwave-assisted synthesis exhibit intense and sharp Fe₂O₃ Bragg reflections alongside broad Fe₃O₄ Bragg reflections, indicating the presence of large Fe₂O₃ crystallites and small Fe₃O₄ crystallites. Despite identical nominal reaction temperatures, this discrepancy may arise from a lower effective temperature in the *in situ* reactor, caused by the temperature sensor being positioned outside the reaction solution.

In situ PDFs of the same datasets are shown in Figure A1.3. Figure A1.4 compares PDF patterns of same reaction time point of the different tin concentrations with PDF calculations of observed phases. The early-stage *in situ* PDFs of different tin concentrations exhibit the same features and overall trends, suggesting an identical transformation of the iron precursor Fe(acac)₃ into the pre-nucleation cluster [Fe₃O(AcOR)₆(ROH)₃]⁺. With increasing tin concentration, the PDF patterns at the beginning of the reaction show an increasingly intense peak at ~2.3 Å. This feature originates from the addition of SnCl₄; however, based on the PDF data alone and in the absence of a dedicated structural refinement, it cannot be determined

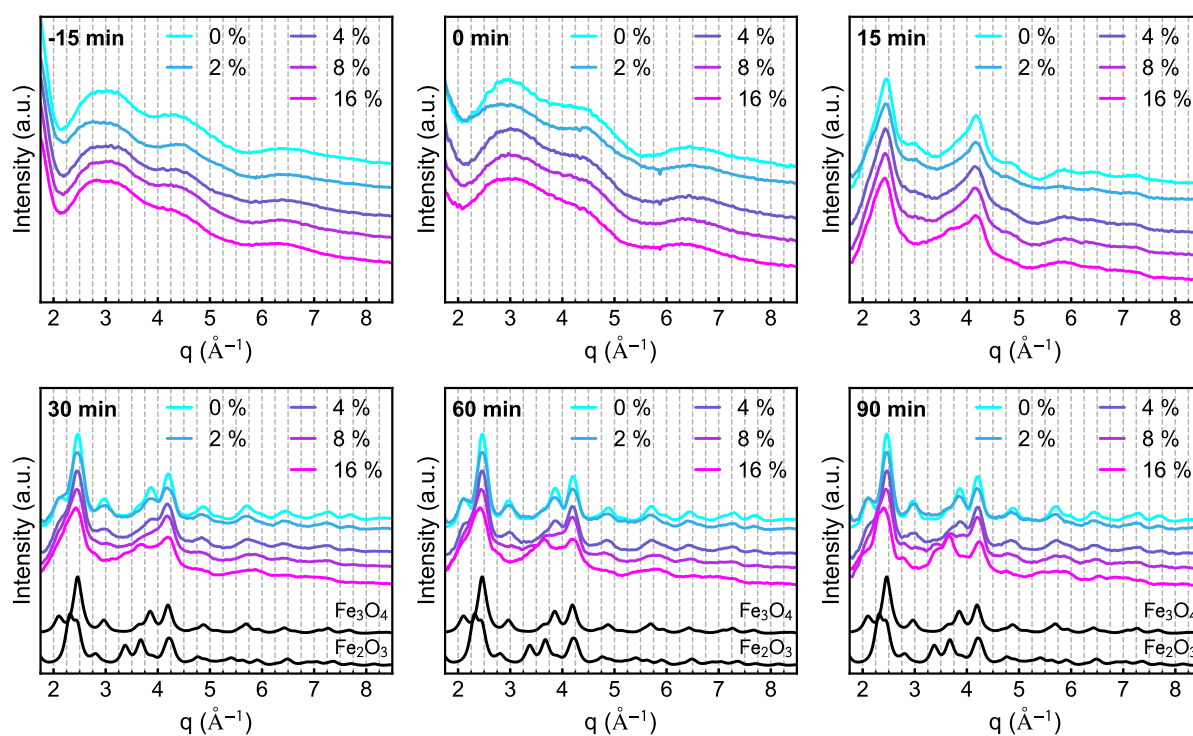


Figure A1.2: Comparison of PXRD patterns from different Sn concentrations at selected reaction time points compared to calculated Fe_3O_4 and Fe_2O_3 patterns.

whether this contribution arises from intact SnCl_4 species or from tin coordinated to organic ligands upon solvation in the reaction solution. The PDF patterns at -15 min all exhibit a decaying wavy background, best visible between 7 and 9 Å, due to solvation spheres of BnOH surrounding $\text{Fe}(\text{acac})_3$.²⁶⁰ As observed in the PXRD data, increasing tin concentration leads to the formation of Fe_2O_3 contributions at extended reaction times, as evident by the shift of the most intense PDF peak at ~ 3.5 Å to higher r -values, and the increase of the PDF peak amplitude of the first peak at ~ 2.0 Å relative to the most intense PDF peak. Further, the coherent domain size of the formed crystalline phases at extended reaction times reduces with increasing tin concentration, as seen by the reduction of high- r features in the PDFs.

To compare the reaction progression for different tin concentrations, Figure A1.5 shows the evolution of the peak maximum positions and amplitudes of the first three PDF peaks. The PDF peaks comprise contributions from all species within the reaction volume, which complicates the disentanglement of individual peak contributions and the overall analysis, particularly upon addition of the tin precursor that results in multiple species being present throughout the reaction. Moreover, the peak maximum positions extracted from the *in situ* PDFs do not yield sub-Å-accurate interatomic distances, and the peak amplitudes are influenced by several factors, including structural disorder, crystallite size, and atomic identity, further complicating a direct comparison between different tin concentrations. Nevertheless, these data allow a qualitative assessment of trends that reflect the overall course of the reactions.

The peak contributions are dominated by interatomic pair correlations involving iron atoms, owing to the prevalence of iron-containing species in the reaction mixture and the substantially higher scattering power of iron compared to organic atoms.⁶⁶ Hence, the dominant interatomic pair correlations are assigned to iron species and are summarized in Table A1.1 together with the corresponding distances of the first three PDF peaks. These peaks are consistently highlighted in yellow, green, and red (Peaks I, II, and III, respectively) in Figure A1.4, Figure A1.5, and Table A1.1.

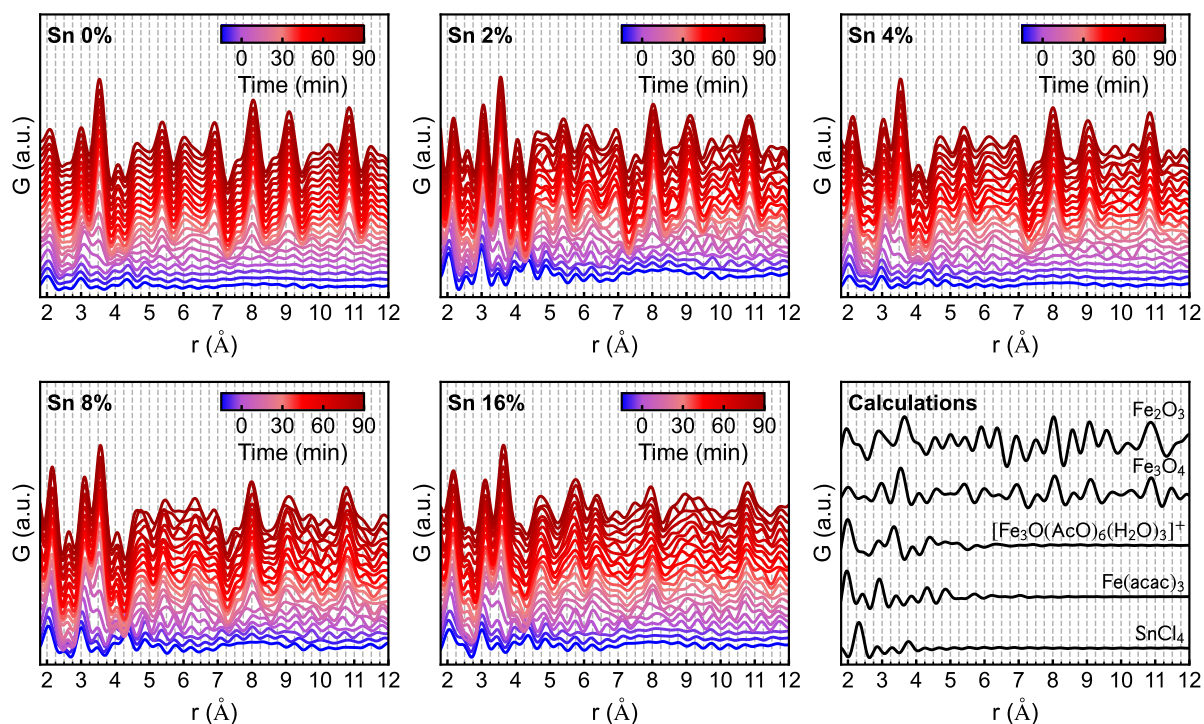


Figure A1.3: *In situ* PDF waterfall plots of Sn:Fe_xO_y nanoparticle syntheses with different Sn concentrations compared to PDF calculations.

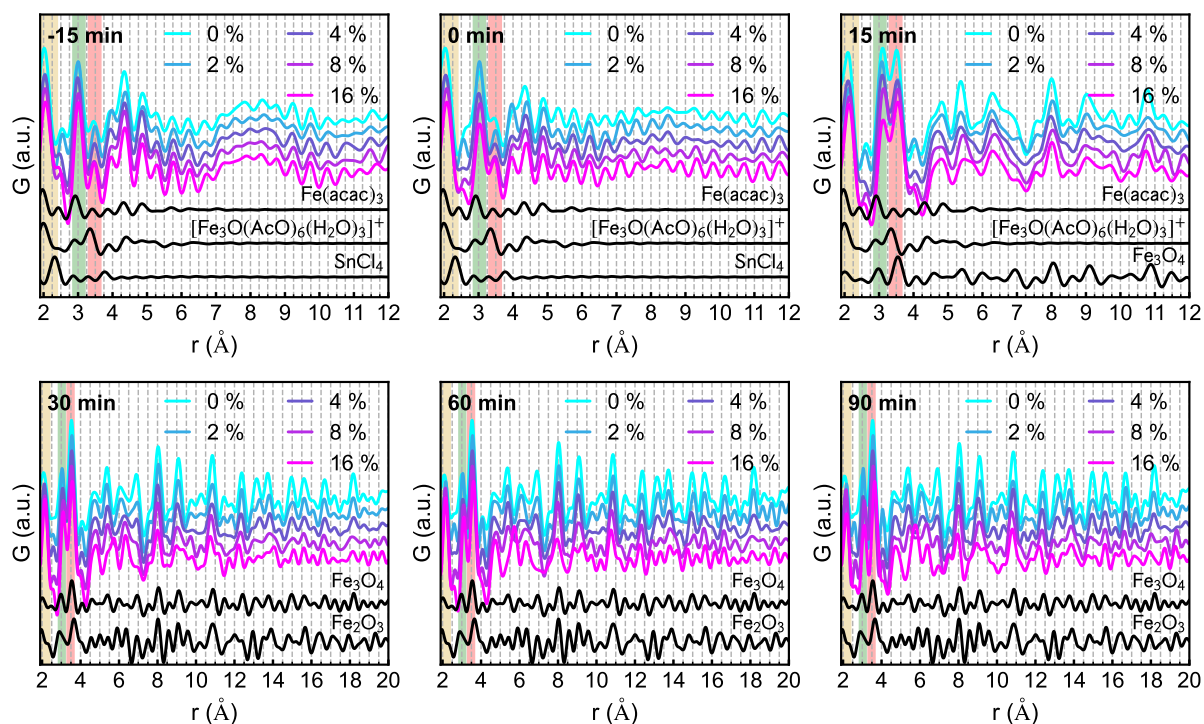


Figure A1.4: Comparison of PDF patterns from different Sn concentrations at selected reaction time points at relevant r -ranges compared to observed PDF calculations. The first three peaks are highlighted in yellow, green, and red, respectively.

Table A1.1: Atomic correlation of the main contributions of the observed iron species to the first three PDF peaks and their interatomic distances. Fe⁶ and Fe⁴ denote the Fe center in FeO₆-octahedra and FeO₄-tetrahedra, respectively, and italic letters *c*, *e*, or *f* denote corner-, edge-, or face-shared polyhedra, respectively.

	Fe(acac) ₃	[Fe ₃ O(AcOR) ₆ (ROH) ₃] ⁺	Fe ₃ O ₄	Fe ₂ O ₃
Peak I	Fe–O (~2.0 Å)	Fe–O (~2.0 Å)	Fe ⁶ -O (~2.1 Å)	Fe ⁶ -O (~2.1 Å)
Peak II	Fe–C (~2.9 Å)	Fe–C (~3.0 Å)	<i>e</i> –Fe ⁶ –Fe ⁶ (~3.0 Å)	<i>f</i> –Fe ⁶ –Fe ⁶ (~2.9 Å)
Peak III	Fe–C (~3.3 Å)	Fe–Fe (~3.3 Å)	<i>c</i> –Fe ⁶ –Fe ⁴ (~3.5 Å)	<i>c</i> –Fe ⁶ –Fe ⁶ (~3.7 Å)

The reaction stages can be traced from the evolution of the peak positions: Peaks I and II exhibit plateaus before ~0 min, corresponding to the prevalence of the initial iron species Fe(acac)₃, and after ~30 min, when Sn:Fe_xO_y has formed. The intermediate region between these plateaus is associated with the presence of the intermediate species [Fe₃O(AcOR)₆(ROH)₃]⁺. Overall, tin addition to the reaction results in an increase of the peak positions. Tin has a larger ionic radius than iron, leading to an expansion of the average first coordination shell, as reflected by the position of Peak I, and an increase in position of Peak II and III at extended reaction times due the expansion of the iron oxide crystal lattice from potential interstitial or substitution tin-doping. The data presented here do not allow a clear determination of the tin species present throughout the reaction; however, the increased position of Peak II between 0 and 30 min for the 8 and 16 % reactions may suggest the formation of an intermediate tin species, assuming that the intermediate iron species [Fe₃O(AcOR)₆(ROH)₃]⁺ is not altered by the introduction of tin. Before 15 min, the position of Peak III is highly noisy and does not permit a meaningful comparison. Beyond this point, the 16 % dataset exhibits a steady increase in peak position associated with the formation of Fe₂O₃. The peak position continues to shift until the final time point at 90 min, showing that the transformation toward Fe₂O₃ is still ongoing.

Similar to the PDF peak positions, the amplitudes also reflects distinct reaction stages. The relative peak amplitudes of Peak III remain close to zero until a sudden increase at ~0 min, marking the onset of formation of the intermediate cluster [Fe₃O(AcOR)₆(ROH)₃]⁺. With increasing tin concentration, this onset shifts to earlier reaction times. A comparable trend is observed in the evolution of the position of Peak I, indicating an accelerated reaction progression upon the addition of tin.

In summary, this chapter presents preliminary *in situ* PXRD and PDF studies of the synthesis of Sn:Fe_xO_y nanoparticles in BnOH from Fe(acac)₃ and varying concentrations of SnCl₄ ranging from 0 to 16 molar %. The undoped 0 % reaction yields Fe₃O₄ nanoparticles, whereas the addition of SnCl₄ leads to the formation of a secondary Fe₂O₃ phase alongside Fe₃O₄. Furthermore, the data show that the presence of SnCl₄ reduces the coherent domain size of the nanoparticles and accelerates the overall reaction progression. The introduction of SnCl₄ into the reaction solution may result in the formation of HCl, which could exert a catalytic effect by accelerating the reaction kinetics and/or promoting the direct formation of Fe₂O₃ or a phase transformation from Fe₃O₄ to Fe₂O₃.

A comprehensive understanding of the formation pathways of Sn:Fe_xO_y requires dedicated PDF refinements to follow the structural evolution of both tin and iron species throughout the reaction, as well as Rietveld PXRD or PDF refinements to elucidate the formation of the Sn:Fe_xO_y structure at different tin concentrations. In addition, *in situ* EXAFS or XANES analysis could element-specifically track the local chemical environment of tin and iron. Complementary SAXS and TEM measurements would further provide insight into particle

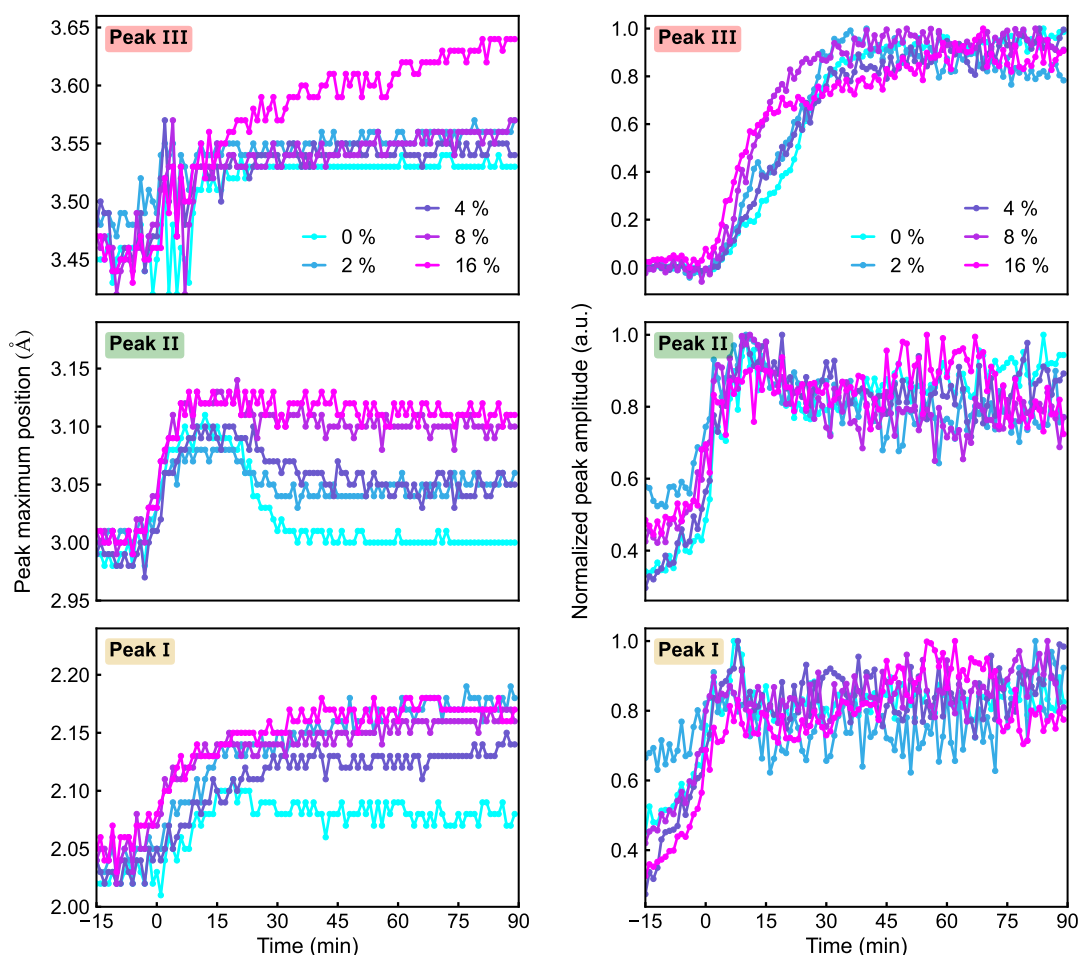


Figure A1.5: Evolution of maximum positions and amplitudes for different tin concentrations of the first three peaks. The amplitudes are normalized by the maximum amplitude within each dataset.

size and morphology, while elemental analysis would yield the actual tin concentrations of the nanoparticles. The rich polymorphism of iron oxides implies a wide range of possible structural configurations, rendering the determination of the Sn:Fe_xO_y structure particularly nontrivial. Tin may occupy substitutional or interstitial sites within the iron oxide lattices and may further modify the connectivity of Sn- or FeO_x polyhedra within the underlying structural motifs, giving rise to multiple plausible local and extended structures.^{261–264}

Looking ahead, this synthesis route could be applied to fabricate Sn:Fe₂O₃ electrodes for photoelectrochemical water splitting. Fe₂O₃ is a promising catalyst for the oxygen evolution reaction, for which tin doping has been shown to significantly enhance its catalytic activity.^{259,265–268} Fe₂O₃ films have previously been produced by depositing Fe₃O₄ nanoparticles onto a substrate followed by thermal treatment to induce their transformation to Fe₂O₃.^{259,269,270} Since the addition of tin already promotes the formation of Fe₂O₃ during the synthesis, this approach could reduce the calcination temperature required to obtain Sn:Fe₂O₃ electrodes, while directly introducing tin dopants to yield an efficient catalyst.²⁷¹

Experimental

Chemicals

All chemicals were purchased from commercial sources: Fe(acac)₃ (Sigma Aldrich, 99.9%), benzyl alcohol (Sigma Aldrich, 99.8%), SnCl₄ (Sigma Aldrich, 99.995%); and were stored and handled in the glove box under an inert atmosphere: Ar 6.0 purity, c(H₂O) < 0.1 ppm, c(O₂) < 0.1 ppm.

Synthesis

In a typical synthesis, a stock solution was prepared in the glove box by dissolving Fe(acac)₃ (352.2 mg, 1.0 mmol) in 5 mL of BnOH under stirring until complete dissolution of the iron precursor was achieved. Further, 2.34, 4.68, 9.32 or 18.64 μ L of SnCl₄, corresponding to 0.02 mmol, 0.04 mmol, 0.08 mmol, or 0.16 mmol, respectively, were added to the stock solution to obtain nominal tin-doping levels of 2, 4, 8, or 16 at.%.

An aliquot of 80 μ L of the resulting solution was then transferred to the reactor inlet. After assembly, the reactor was removed from the glove box and heated to 180 °C at a heating rate of 10 °C min⁻¹ under vigorous stirring.

In situ scattering

The data were acquired at beamline P21.1 at PETRA III at Deutsches Elektronen-Synchrotron DESY, Hamburg, Germany.¹³⁵ Two-dimensional scattering patterns were recorded every 1 s at an X-ray energy of 101.39 keV ($\lambda = 0.1222$ Å) using an X-ray area detector (PerkinElmer XRD1621, Varex Imaging Corp.) equipped with a 2048x2048 pixel array and a pixel size of 200x200 μ m². A LaB₆ powder standard packed in the reaction inlet was used to calibrate the sample-to-detector distance of 0.390 m, as well as instrumental parameter $q_{\text{damp}} = 0.0494$ Å⁻¹ and $q_{\text{broad}} = 0.0374$ Å⁻¹. Azimuthal integration and detector calibration were carried out using pyFAI¹³⁶. PDF calculations were performed using diffpy-CMI⁷¹ and PXRD calculations were conducted with GSAS-II⁶⁹. Background subtraction was carried out by scaling the background pattern to the data pattern without introducing negative intensities in the range between 1.05 Å⁻¹ and 1.45 Å⁻¹. The PXRD and PDF analysis was performed on the same datasets. PDFs were calculated with values $q_{\text{min}} = 1.1$ Å⁻¹, $q_{\text{max}} = 14.2$ Å⁻¹, $q_{\text{max,inst}} = 24.0$ Å⁻¹, and $r_{\text{poly}} = 0.9$.

Author contributions

My contribution to this work comprises the analysis of *in situ* X-ray scattering data. The data was acquired by Cecilia Zito, Francesco Caddeo, Jagadesh Kopula Kesavan, Tjark R. L. Gröne, Lars Klemeyer, Philip Ulmen, Brian Jessen, and myself. Francesco Caddeo and Paul Kühn proposed the concept of tin-doping.

A2 Synthesis of - the Role of Acetylacetonate on Phase-purity

Copper nitride Cu_3N is a relatively underexplored, metastable direct semiconductor that has attracted attention due to its low cost, non-toxicity, and promising potential for applications in solar cells, high-density optical data storage, and electrocatalysis.^{163,272,273} Cu_3N crystallizes in the rather open cubic anti- ReO_3 lattice composed of corner-shared NCu_6 octahedra. This structural motif allows interstitial heteroatom incorporation, enabling deliberate tuning of the electronic structure toward semimetallic or metallic behavior,^{55,274} as demonstrated in Chapter 5 for Cu_3PdN .

Due to its metastability, the synthesis of phase-pure Cu_3N is challenging and, in most cases, requires elevated reaction temperatures and multiple reaction steps.^{55,158,163,272} A low-temperature one-pot synthesis has been reported in which ultras-small (~ 2 nm) Cu_3N nanoparticles are obtained from copper(II) methoxide ($\text{Cu}(\text{OMe})_2$) in benzylamine (BnNH_2) at a reaction temperature of 140°C .⁵⁴ Despite numerous attempts in our laboratory, this synthetic route could not be reproduced, as the resulting nanoparticles consistently exhibited significant copper oxide impurities. This chapter discusses an alternative approach toward the synthesis of stable, phase-pure Cu_3N nanoparticles by introducing copper(II) acetylacetonate ($\text{Cu}(\text{acac})_2$) into the reported reaction scheme.

Figure A2.1 shows the PXRD patterns and corresponding Rietveld refinements of nanoparticles synthesized using different molar precursor ratios of $\text{Cu}(\text{OMe})_2:\text{Cu}(\text{acac})_2$, as well as syntheses based on $\text{Cu}(\text{OMe})_2$ with the addition of acetylacetone (acacH). A precursor ratio of 3:1 $\text{Cu}(\text{OMe})_2:\text{Cu}(\text{acac})_2$ yields phase-pure Cu_3N nanoparticles, whereas all other investigated compositions exhibit copper oxide impurities. The refined phase fractions and crystallite sizes are summarized in Table A2.1. The sample prepared following the reported reaction scheme⁵⁴ using $\text{Cu}(\text{OMe})_2$ as the sole precursor exhibits a cupric oxide (CuO) impurity of $\sim 20\%$. Replacing 25% of the $\text{Cu}(\text{OMe})_2$ with $\text{Cu}(\text{acac})_2$ results in phase-pure Cu_3N . In contrast, further increasing the $\text{Cu}(\text{acac})_2$ fraction to 50, 75, or 100% leads to the predominance of the cuprous oxide (Cu_2O) phase, with only minor Cu_3N fractions of 10–20%.

Since the addition of acetylacetonate (acac) in the right ratio leads to phase purity, the use of acetylacetone (acacH) was explored as a potential alternative with a similar effect. However, the tested $\text{Cu}(\text{OMe})_2:\text{acacH}$ molar ratios of 4:1 and 4:4 resulted in pronounced copper oxide impurities of approximately 30% and 70%, respectively. To more closely reproduce the effective 3:1 $\text{Cu}(\text{OMe})_2:\text{Cu}(\text{acac})_2$ ratio of either the ligands OMe and acac , or copper ion and acac , future experiments should explore molar ratios of 3:1 $\text{OMe}:\text{acacH}$ or 3:2 $\text{Cu}(\text{II}):\text{acacH}$, which may provide a suitable route to achieve phase-pure Cu_3N .

To evaluate the ambient stability of the phase-pure Cu_3N nanoparticles, Figure A2.2 compares PXRD patterns and corresponding Rietveld refinements of the 3:1 $\text{Cu}(\text{OMe})_2:\text{Cu}(\text{acac})_2$ batch measured directly after synthesis and washing, as well as after exposure to air for periods ranging from 1 to 19 days. Even after 19 days, no crystalline oxide phase is observed in the PXRD patterns. However, the refined Cu_3N crystallite size shows a slight decrease over time, as summarized in Table A2.2. This trend may indicate the gradual formation of a thin amorphous oxide layer on the surface of the Cu_3N nanoparticles upon prolonged exposure to air.

In summary, this chapter introduces a synthesis route for phase-pure ~ 3 nm Cu_3N nanoparticles using $\text{Cu}(\text{OMe})_2$ and $\text{Cu}(\text{acac})_2$ precursors in a 3:1 molar ratio in BnNH_2 at 140°C . Deviations from this precursor ratio lead to the formation of copper oxide impurities, high-

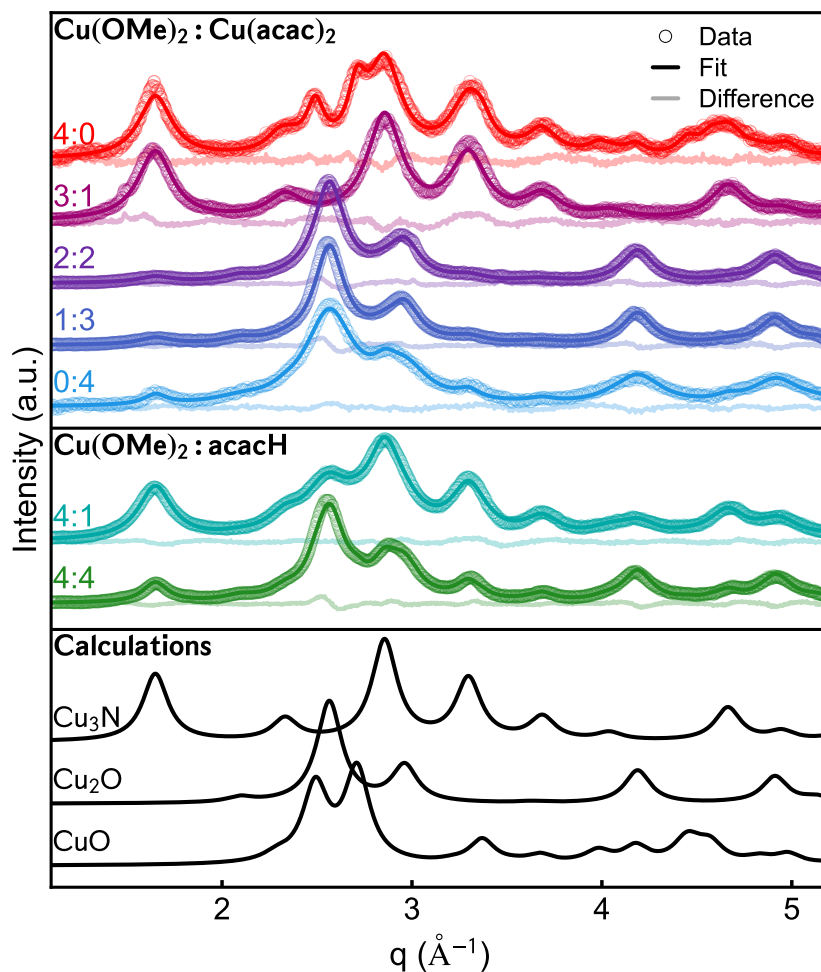


Figure A2.1: PXRD patterns and Rietveld refinements of nanoparticles synthesized using different precursor ratios, compared to PXRD calculations of the observed phases.

Table A2.1: Rietveld-refined phase fractions and crystallite sizes of Cu_3N , CuO , and Cu_2O .

Precursors Ratio	$\text{Cu}(\text{OMe})_2:\text{Cu}(\text{acac})_2$					$\text{Cu}(\text{OMe})_2:\text{acacH}$	
	4:0	3:1	4:4	1:3	0:4	4:1	4:4
Scale Cu_3N	0.80	1.00	0.16	0.18	0.13	0.69	0.32
Size Cu_3N (nm)	3.0	3.2	3.0	3.0	4.4	2.9	4.1
Scale CuO	0.20	0.00	0.00	0.00	0.00	0.06	0.05
Size CuO (nm)	5.7	–	–	–	–	3.4	6.6
Scale Cu_2O	0.00	0.00	0.84	0.82	0.87	0.24	0.63
Size Cu_2O (nm)	–	–	3.2	3.3	2.1	2.1	3.3
Rw (%)	1.67	1.90	1.38	1.60	1.37	1.15	1.50

Table A2.2: Rietveld-refined crystallite sizes of phase-pure Cu_3N synthesized with a 3:1 $\text{Cu}(\text{OMe})_2:\text{Cu}(\text{acac})_2$ precursor ratio after exposure to air for different durations.

	Time in air (day)	0	1	5	14	19
Size Cu_3N (nm)		3.2	2.9	2.8	2.8	2.7
Rw (%)		1.90	1.82	1.73	1.94	1.34

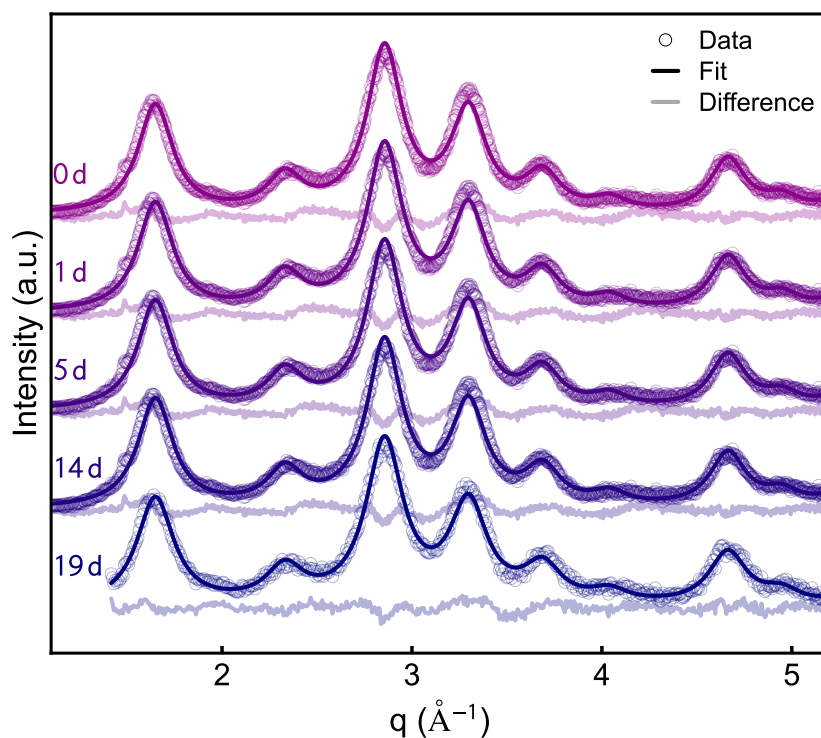


Figure A2.2: PXRD patterns and Rietveld refinements of phase-pure Cu_3N nanoparticles synthesized with a 3:1 $\text{Cu}(\text{OMe})_2:\text{Cu}(\text{acac})_2$ precursor ratio after exposure to air for different durations.

lighting the decisive role of acetylacetonate in controlling phase-purity. While the empirical effectiveness of $\text{Cu}(\text{acac})_2$ addition is demonstrated, a mechanistic understanding of how acetylacetonate influences precursor conversion, nucleation, and phase selection remains unresolved.

A deeper insight into the synthesis mechanism could be obtained through *in situ* X-ray characterization techniques by monitoring precursor transformations, nucleation, and crystallization. Complementary optical spectroscopic methods such as *in situ* ATR-IR or UV/Vis spectroscopy could be employed to track organic species, including acetylacetonate and methoxide ligands, and to elucidate their role in stabilizing reactive intermediates. Furthermore, *ex situ* surface-sensitive techniques such as X-ray photoelectron spectroscopy (XPS) could provide detailed information on surface composition, ligand termination, and potential oxidation processes of the Cu_3N nanoparticles after synthesis.

Looking ahead, the reaction scheme presented here offers a promising platform for the controlled one-pot and low-temperature synthesis of phase-pure nitride nanomaterials beyond Cu_3N . The deliberate use of chelating ligands such as acetylacetonate to steer precursor chemistry and phase selection may be transferable to other binary or ternary metal nitrides. Extending this approach could enable access to metastable nitride phases with tailored compositions and properties, providing new opportunities for applications in optoelectronics, catalysis, and energy-related technologies.

Experimental

Chemicals

All chemicals were purchased from commercial sources: $\text{Cu}(\text{OMe})_2$ (Thermo Scientific, 98%),

Cu(acac)₂ (Sigma Aldrich, 99.9%), acetylacetone (Sigma Aldrich, > 99.995%), benzylamine (Sigma Aldrich, 99.8%), hexane (Sigma Aldrich, 99%); and were stored and handled in the glove box under an inert atmosphere: Ar 6.0 purity, c(H₂O) < 0.1 ppm, c(O₂) < 0.1 ppm.

Synthesis

The reaction solution was prepared inside a glove box by adding Cu(OMe)₂ and/or Cu(acac)₂, or acetylacetone (acacH), and in 35 mL of benzylamine in a 45 mL Teflon liner equipped with a stirring magnet. The employed masses and corresponding molar concentrations are summarized in Table A2.3. Subsequently, the Teflon liner was assembled in an autoclave, and the autoclave was then removed from the glove box, and placed in a preheated oil bath at 140 °C for 2 h under vigorous stirring. After completion of the reaction, the autoclave was removed from the oil bath and allowed to cool naturally to room temperature. Following the synthesis, the nanoparticles were washed three times with hexane and centrifuged for 10 min at 10 000 rpm. After the final centrifugation step, the nanoparticles were dried under a nitrogen flow.

Table A2.3: Weights or volumes and molar concentrations of the precursors used to prepare the 5 mL stock solutions for Cu₃N syntheses.

Precursors Ratio	Cu(OMe) ₂ :Cu(acac) ₂					Cu(OMe) ₂ :acacH	
	4:0	3:1	4:4	1:3	0:4	4:1	4:4
Cu(OMe)₂							
w (mg)	50.0	37.5	25.0	12.5	0.0	50.0	50.0
c (mmol/ml)	0.08	0.06	0.04	0.02	0.00	0.08	0.08
Cu(acac)₂							
w (mg)	0.0	26.2	52.4	78.5	104.72	-	-
c (mmol/ml)	0.00	0.02	0.04	0.06	0.08	-	-
acacH							
V (μL)	-	-	-	-	-	10.3	41.1
c (mmol/ml)	-	-	-	-	-	0.02	0.08

Powder X-ray Diffraction (PXRD) & Rietveld Refinement

PXRD patterns were acquired on a Bruker Advanced D8 with Cu K α -radiation of 8.048 keV ($\lambda = 1.541 \text{ \AA}$). Rietveld refinements and PXRD calculations were carried out with GSASII.⁶⁹ Instrumental parameters have been retrieved by refining a LaB₆ standard. In the Rietveld refinements, only the phase scale factors, spherical crystallite size, and background were refined. The lattice parameters and atomic displacement parameters were fixed, as summarized in Table A2.4. PXRD calculations were performed assuming a crystallite size of 4 nm for all phases.

Table A2.4: Fixed parameters for Rietveld refinements.

Phase	Lattice parameter	Atomic displacement parameter
Cu₃N	a = 3.814 Å	Cu: U ₁₁ = 0.0013 Å ² , U ₂₂ = 0.0035 Å ² N: U _{iso} = 0.005 Å ²
CuO	a = 4.686 Å, b = 3.423 Å c = 5.129 Å, $\beta = 99.54^\circ$	Cu: U ₁₁ = 0.0057 Å ² , U ₂₂ = 0.0079 Å ² , U ₃₃ = 0.0045 Å ² O: U ₁₁ = 0.0068 Å ² , U ₂₂ = 0.0111 Å ² , U ₃₃ = 0.0056 Å ²
Cu₂O	a = 4.247 Å	Cu: U _{iso} = 0.01 Å ² O: U _{iso} = 0.01 Å ²

Author contributions

My contribution to this work comprises the concept of introducing acetylacetonate to achieve phase purity, as well as the analysis of the PXRD data. The synthesis and PXRD measurements were carried out by Jagadesh Kopula Kesavan, Paul Kühn, and myself.

A3 X-ray and Electron Diffraction of CoO Nanoassemblies and Intermediate Phases

This chapter presents preliminary PXRD and electron microscopy analyses of different intermediate reaction time points during the formation of CoO nanoassemblies from cobalt(III) acetylacetonate ($\text{Co}(\text{acac})_3$) in benzyl alcohol (BnOH). Previous *in situ* X-ray studies on the same synthesis have shown that the precursor $\text{Co}(\text{acac})_3$ is first converted into cobalt(II) acetylacetonate ($\text{Co}(\text{acac})_2$), from which rock-salt CoO nanoassemblies subsequently form.⁹¹ The single-particle small-angle X-ray scattering (SP-SAXS) analysis presented in Chapter 6 further revealed that $\text{Co}(\text{acac})_2$, due to its poor solubility in BnOH, forms spherical, amorphous precipitates that contract during crystallization into cavernous CoO assemblies. This explains the formation of hierarchical nanoassemblies rather than isolated CoO nanoparticles.

In this reaction, all intermediate species are fully converted into rock-salt CoO nanoassemblies after approximately 90 min.⁹¹ In the present work, electron microscopy and PXRD analyses of reaction aliquots collected at 20, 30, and 40 min reveal the presence of additional morphologies and contributions from cobalt hydroxide ($\text{Co}(\text{OH})_2$) and a hexagonal CoO phase alongside the previously identified amorphous $\text{Co}(\text{acac})_2$ spherical precipitates and the emerging rock-salt CoO nanoassemblies. Hereafter, the cubic rock-salt CoO phase is referred to as c-CoO, in contrast to the hexagonal CoO phase, denoted as h-CoO.

Figure A3.1 shows transmission and scanning electron microscopy (TEM and SEM) images acquired at the intermediate reaction stages. Amorphous $\text{Co}(\text{acac})_2$ spheres and c-CoO nanoassemblies with sizes of a few tens of nanometers are highlighted by blue and violet arrows, respectively. In addition, micrometer-sized, rose-like crumbled sheet structures are present, as indicated by green arrows. These rose-like morphologies are most frequently observed at 20 min and occur with decreasing frequency as the reaction time increases. At 30 min, the images further show nanoparticle assemblies (highlighted by red arrows) that are larger than the c-CoO nanoassemblies, with overall sizes of approximately 100 to 300 nm and internal grain sizes of about 10 nm. These grains are noticeably larger than those of the c-CoO nanoassemblies, which typically range from 3 to 7 nm.⁹¹

Figure A3.2 shows PXRD patterns collected at the different reaction times together with corresponding Rietveld refinements, as well as simulated reference patterns and structural representations of the identified phases $\text{Co}(\text{OH})_2$, c-CoO, and h-CoO.

The 20 min PXRD pattern can be assigned to layered $\text{Co}(\text{OH})_2$, in agreement with reported diffraction data for $\text{Co}(\text{OH})_2$ films.²⁷⁵ $\text{Co}(\text{OH})_2$ crystallizes in a hexagonal structure composed of layered edge-sharing CoO_6 octahedra normal to the (001) direction, with hydrogen atoms located between the layers (Figure A3.2e). We fit the 20 min pattern using an uniaxial model along (001) to account for the sheet-like morphology observed in the electron microscopy images (Figure A3.2f). The refinement yields an equatorial crystallite size of ~ 9 Å and an axial size of < 1 Å. In addition, the refined lattice parameter c , along the (001) direction, expands by $> 50\%$ compared to the initial lattice parameter, suggesting the interstratification of additional species between the layered CoO_6 octahedra.

We note that the simplified structural model employed for the refinement of the $\text{Co}(\text{OH})_2$ phase does not permit the extraction of precise structural parameters. In particular, it does not account for structural disorder frequently observed in layered hydroxides, such as stacking faults, turbostratic disorder, or interstratification, all of which contribute to reflection broadening that can be misinterpreted to crystallite effects.²⁷⁶ Moreover, the model does not

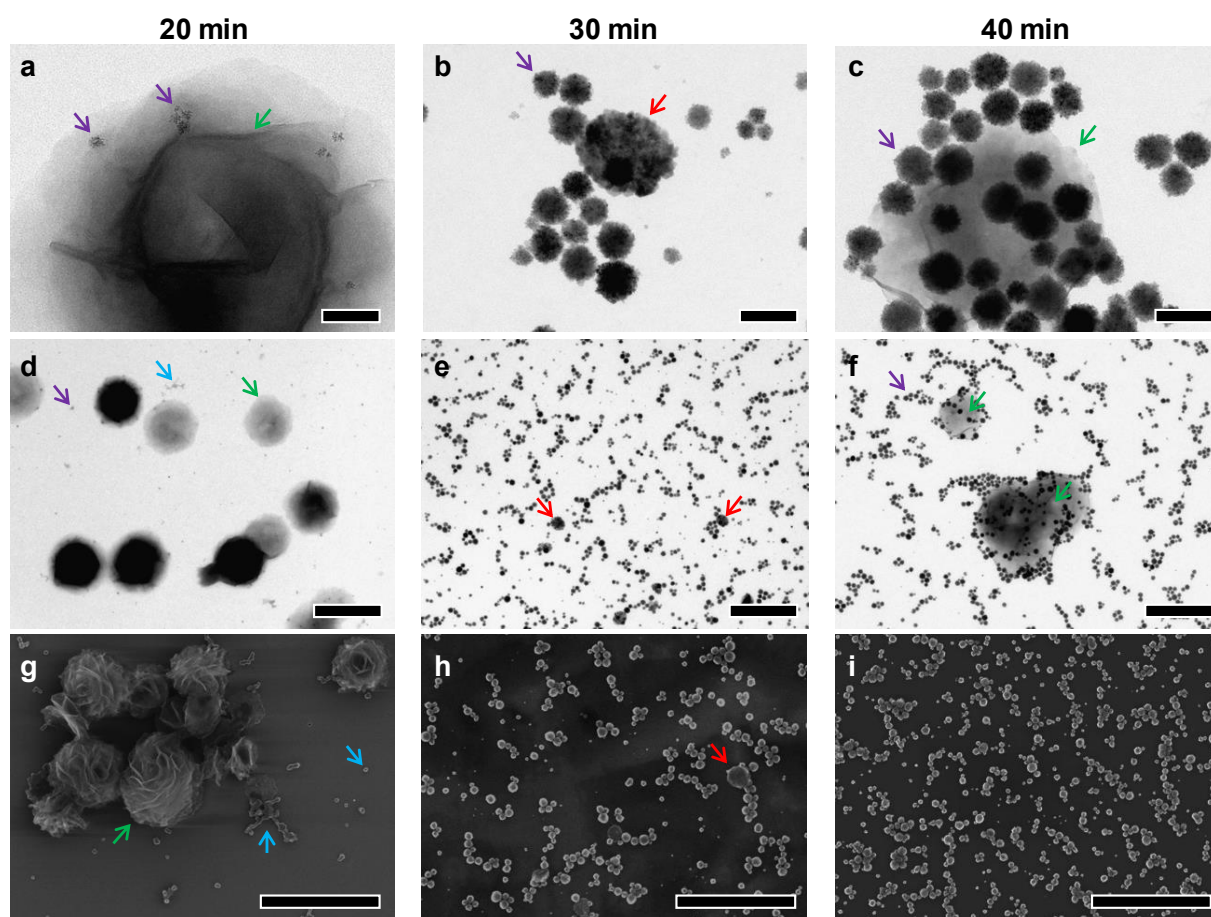


Figure A3.1: TEM images (top and middle row) and SEM images (bottom row) of different reaction time points. The colored arrows highlight representative particles of the four different morphologies: violet: c-CoO nanoassemblies, blue: $\text{Co}(\text{acac})_2$ spherical aggregates, green: $\text{Co}(\text{OH})_2$ rose-like crumbled sheets, red: h-CoO nanoparticle assemblies noticeably larger than the c-CoO assemblies. Scalebars: a-c: 100 nm, d-i: 1 μm .

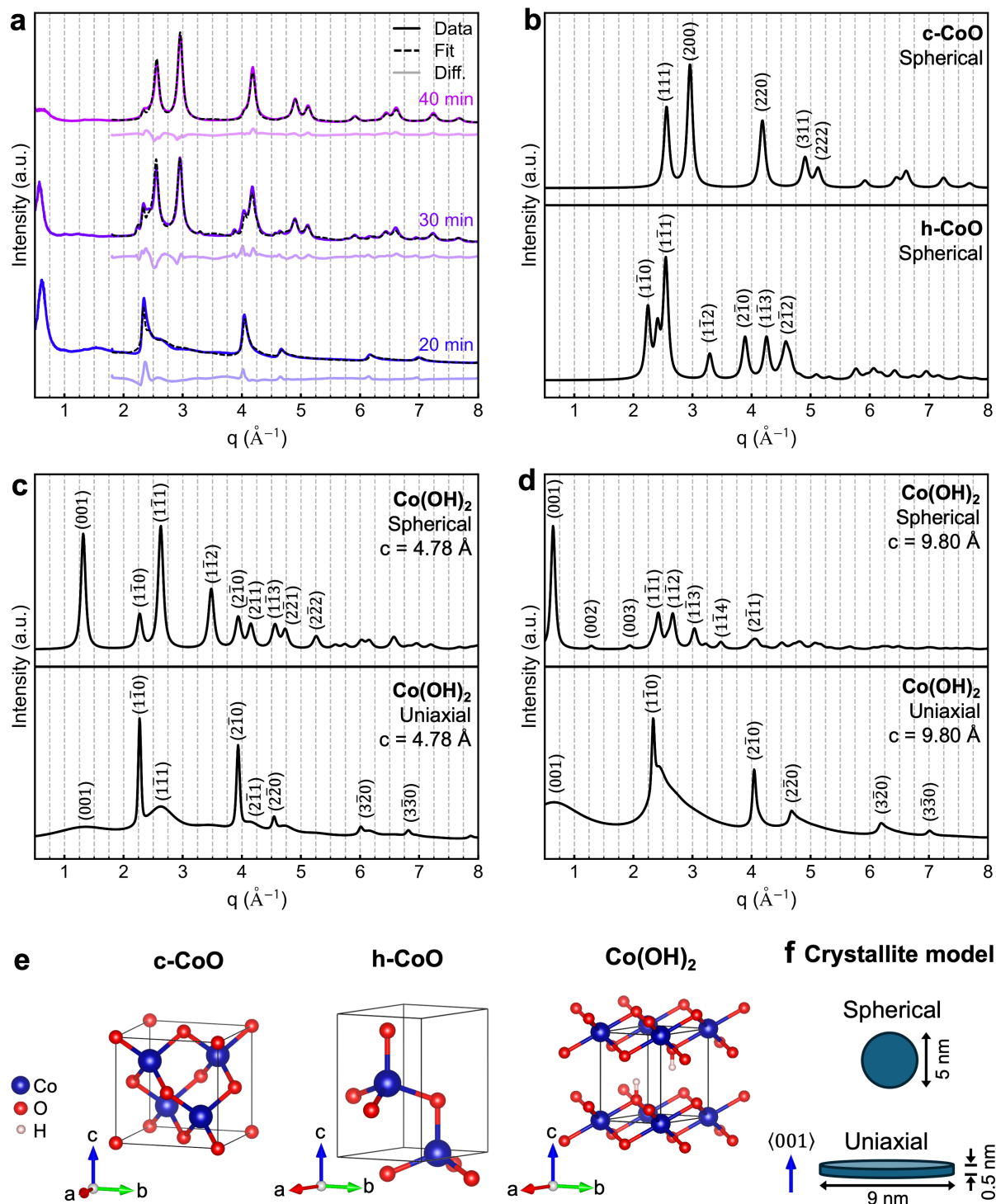


Figure A3.2: PXRD patterns and corresponding multiphase Rietveld refinements at different reaction time points, compared with individual PXRD simulations and structural representations of the identified phases. All spherical models were simulated assuming a diameter of 5 nm, while the uniaxial models were simulated with an axial size of 0.5 nm and an equatorial size of 9 nm.

consider possible intercalated species and the refined expansion of the c lattice parameter introduces an artificial distortion of the CoO_6 octahedra. Nevertheless, the approach provides a qualitative description of the observed structure. To illustrate the influence of the refined parameters, Figure A3.2c,d shows simulated PXRD patterns of $\text{Co}(\text{OH})_2$ using both spherical and uniaxial crystallite size models, including variations of the c lattice parameter. The uniaxial model produces pronounced $(hk0)$ reflections with shoulders toward higher q -values arising from the broadening of (hkl) reflections with $l \neq 0$. Such anisotropic peak shapes are characteristic of thin nanosheets comprising only a few atomic layers.²⁷⁷⁻²⁸³ Comparison of the simulated uniaxial pattern with the experimental data shows that the model significantly underestimates the intensity of the (001) reflection at $\sim 0.6 \text{ \AA}^{-1}$. For this reason, the (001) reflection was excluded from the Rietveld refinement range, which results in a large uncertainty of the refined c lattice parameter. However, the manually extracted q -position of this reflection allows the determination of c and thus directly provides the corresponding d -spacing of the layered structure.

Residual contributions of the reflections observed in the 20 min PXRD pattern are present in the 30 min and 40 min patterns, albeit with progressively decreasing intensity. This behavior is consistent with the electron microscopy observations, which show a diminishing occurrence of the rose-like particles as the reaction proceeds. In addition, the $\text{Co}(\text{OH})_2$ (001) reflection gradually shifts toward lower q with increasing reaction time. This shift corresponds to an increasing interlayer spacing and may be caused by the intercalation of additional or larger species between the layered CoO_6 octahedra. The extracted peak positions and corresponding d -spacings are listed in Table A3.1.

Table A3.1: q -position and d -spacing of the $\text{Co}(\text{OH})_2$ (001) reflection.

	20 min	30 min	40 min
q (\AA^{-1})	0.71	0.59	0.45
d (\AA)	9.9	10.7	13.4

Both the 30 min and 40 min PXRD patterns exhibit intense reflections consistent with the cubic rock-salt CoO structure (c - CoO , $Fm\bar{3}m$). In addition, the 30 min pattern shows weak reflections that can be assigned to the hexagonal CoO phase (h - CoO , $P6_3mc$). Since the h - CoO reflections are absent in the 20 min and 40 min datasets, they are attributed to the large nanoparticle assemblies observed only in the 30 min electron microscopy images (Figure A3.1). The 30 min and 40 min PXRD patterns were refined using the CoO phases together with the $\text{Co}(\text{OH})_2$ structure with all structural parameters fixed to the values obtained from the 20 min refinement.

The refined parameter for all datasets are summarized in Table A3.2. The refinements show the diminishing $\text{Co}(\text{OH})_2$ and increasing c - CoO contribution over time, and the occurrence of a small h - CoO fraction at 30 min.

Given that a simplified structural model is employed for the refinement, Figure A3.3 further compares the experimental patterns with PXRD simulations of all experimentally reported structures with compositions Co , Co-O , Co-O-H , and Co-O-H-C available in The Materials Project database²⁸⁴, as well as cobalt acetylacetonate-related structures reported in the literature.^{251,252} None of these additional phases match the experimental patterns, apart from the identified uniaxial $\text{Co}(\text{OH})_2$, and spherical c - CoO and h - CoO structures.

Table A3.2: Rietveld refinement results. For c-CoO and h-CoO, a spherical crystallite size was assumed. For $\text{Co}(\text{OH})_2$, an uniaxial crystallite size model was applied along the (001) direction; its reported crystallite sizes correspond to equatorial size / axial size. Parameters marked with an asterisk (*) were held fixed during the refinement. Further, all atomic displacement parameters for all phases were fixed at 0.01 \AA^2 . The employed Rietveld refinement software⁶⁹ does not permit decimal nanometer values for fixed uniaxial crystallite sizes. Consequently, the corresponding values for $\text{Co}(\text{OH})_2$ in the 30 min and 40 min refinements were rounded.

	R_w (%)	Phase	Wt. frac. (%)	Size (nm)	a (Å)	c (Å)
20 min	10.8	c-CoO	6	1.6	4.263	-
		$\text{Co}(\text{OH})_2$	94	9.4 / 0.5	3.117	9.769
		h-CoO	-	-	-	-
30 min	9.5	c-CoO	43	5.2	4.272	-
		$\text{Co}(\text{OH})_2$	51	9* / 1*	3.117*	9.769*
		h-CoO	6	9.0	3.240	5.235
40 min	7.9	c-CoO	75	5.2	4.261	-
		$\text{Co}(\text{OH})_2$	25	9* / 1*	3.117*	9.769*
		h-CoO	-	-	-	-

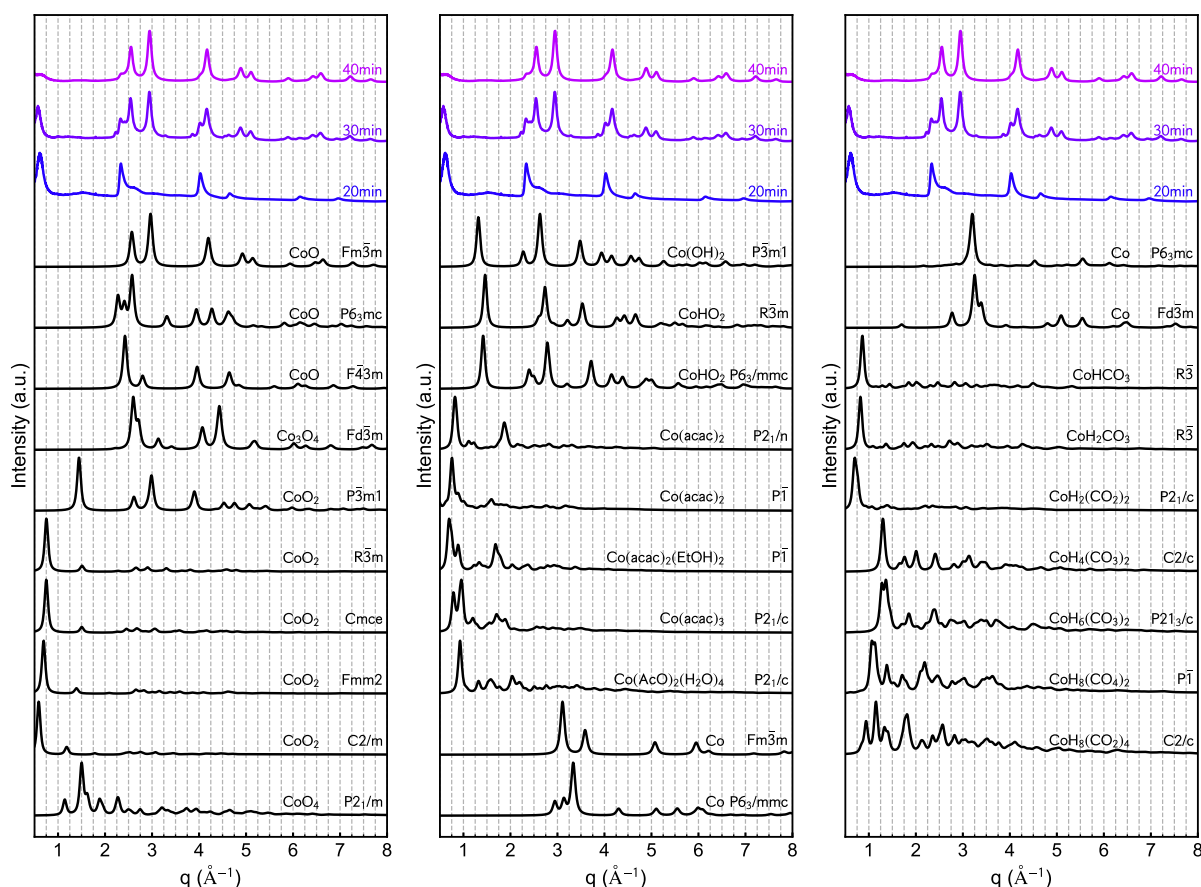


Figure A3.3: Simulated PXRD patterns of elemental cobalt, cobalt oxide, hydroxide, carbonate-related, and acetylacetonate phases. The structural models were obtained from crystallographic databases²⁸⁴ and literature sources^{251,252,285}. All simulations were calculated assuming a spherical crystallite size of 5 nm.

Figure A3.4 shows selected area electron diffraction (SAED) patterns acquired at the intermediate reaction times. Table A3.3 lists the first four diffraction ring positions and compares them with reference values for c-CoO and Co₃O₄. The SAED rings observed at 20 min (Figure A3.4a,b) can be attributed to a subset of Co₃O₄ reflections, suggesting the presence of a preferentially oriented structure. However, corresponding reflections are not observed in the 20 min PXRD pattern (Figure A3.2), indicating that this apparent Co₃O₄ signature may arise from electron-beam-induced phase-transition from Co(OH)₂ during the SAED measurement. SAED patterns at 30 min from regions containing the c-CoO nanoassemblies (Figure A3.4c,d) exhibit spotty diffraction rings that match the c-CoO structure. At a larger probed area (Figure A3.4e,f), these rings become more continuous due to the increased number of scattering c-CoO particles. In addition, these larger regions include the h-CoO nanoassemblies with crystallites that are larger than in the c-CoO nanoassemblies, giving rise to additional isolated diffraction spots in the SAED patterns. Since there are only few isolated diffraction spots, they cannot be unambiguously assigned h-CoO. By 40 min, the SAED patterns (Figure A3.4g-j) display diffraction rings that are entirely consistent with the c-CoO crystal structure.

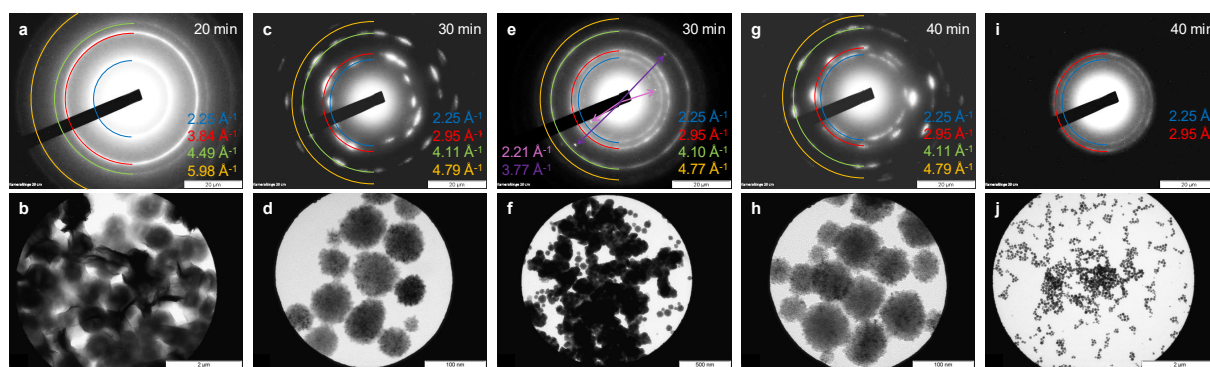


Figure A3.4: SAED patterns (top row) and corresponding TEM images (bottom row) at different reaction time points. The q -values of the highlighted peaks in the SAED images are determined using the camera constant of $76.261 \mu\text{m} \text{ \AA}^{-1}$. Scalebars: a: 20 μm , b: 2 μm , c: 20 μm , d: 100 nm, e: 20 μm , f: 500 nm, g: 20 μm , h: 100 nm, i: 20 μm , j: 2 μm .

Table A3.3: SAED ring positions compared to reference reflection positions of c-CoO and Co₃O₄. The letters in the column refer to the sub-figures of the corresponding SAED pattern in Figure A3.4.

Ring #	20 min	30 min		40 min		c-CoO		Co ₃ O ₄	
	a, b	c, d	e, f	g, h	i, j	hkl	q (\AA^{-1})	hkl	q (\AA^{-1})
1	2.25	2.51	2.51	2.51	2.51	111	2.55	220	2.21
2	3.84	2.95	2.95	2.95	2.95	200	2.95	422	3.83
3	4.49	4.11	4.10	4.11	-	220	4.17	440	4.42
4	5.98	4.79	4.77	4.79	-	311	4.89	731/533	5.00

In conclusion, this chapter reveals the presence of additional transient morphologies during the formation of c-CoO nanoassemblies from the crystallization of amorphous spherical Co(acac)₂ precipitates at reaction times of 20, 30, and 40 min. Rietveld refinements of the PXRD patterns, supported by comparison with simulated reference structures, allow the micrometer-sized rose-like crumpled sheets observed predominantly at 20 min to be assigned to layered Co(OH)₂. The refinement requires a uniaxial crystallite size model to account for the anisotropic peak shapes, consistent with thin nanosheet morphologies. However, the simplified structural model does not capture possible stacking disorder, turbostraticity, or

intercalation effects, and therefore provides only a qualitative description of the layered hydroxide phase.

At 30 min, additional reflections attributable to h-CoO are identified, corresponding to large nanoparticle assemblies with overall sizes of 100 to 300 nm and larger internal grain sizes compared to the c-CoO nanoassemblies. This h-CoO contribution is transient, being absent at 20 and 40 min, suggesting that it represents a metastable intermediate or side product.

Taken together, the combined PXRD refinements and electron microscopy analyses indicate that the observed $\text{Co}(\text{OH})_2$ sheets and h-CoO assemblies arise as side reaction products that do not fundamentally alter the dominant formation pathway of c-CoO nanoassemblies via amorphous $\text{Co}(\text{acac})_2$ spheres.

Experimental

Synthesis and sample preparation

All chemicals were purchased from commercial sources and used without further purification: $\text{Co}(\text{acac})_3$ (Sigma-Aldrich, 99.99%), benzyl alcohol (Sigma-Aldrich, >99%), and ethanol (VWR, absolute grade).

The CoO nanoassemblies were synthesized by heating a reaction solution of 0.1 mmol mL^{-1} $\text{Co}(\text{acac})_3$ in benzyl alcohol at 160°C for reaction times of 20, 30, or 40 min in a heating reactor. A detailed description of the synthesis procedure is provided in Section S6.

STEM and TEM samples were prepared by depositing one drop of the sample solution after the respective reaction time onto a TEM grid, followed by rinsing with a few drops of ethanol. PXRD samples were measured from dried powders of three combined synthesis batches for each reaction time obtained from centrifuging the reaction solution with the addition of ethanol at 3500 rpm for 5 min.

Powder X-ray Diffraction (PXRD)

PXRD measurements were performed on the powders packed in 2.1 mm borosilicate capillaries. The data were measured at beamline P21.1 at PETRA III at Deutsches Elektronen-Synchrotron DESY, Hamburg, Germany.¹³⁵ Two-dimensional scattering patterns were recorded for 60 s acquisition time at an X-ray energy of 101.31 keV ($\lambda = 0.1222 \text{ \AA}$) using an X-ray area detector (PILATUS3 X CdTe 2M, DECTRIS AG) equipped with a 1475×1679 pixel array and a pixel size of $172 \times 172 \mu\text{m}^2$. A LaB_6 powder standard packed in the capillary was used to calibrate the sample-to-detector distance of 0.801 m. Azimuthal integration and detector calibration were carried out using pyFAI¹³⁶. PXRD calculations were conducted with GSAS-II⁶⁹. A background measurement was performed on an empty capillary.

Electron microscopy (EM):

Scanning electron microscopy (SEM) images were collected using a Regulus 8220 (Hitachi High Technologies Corp.) with an acceleration voltage of 30 keV. Transmission electron microscopy (TEM) images and selected area electron diffraction (SAED) patterns were collected using a JEM 1011 (JEOL Ltd.) with an acceleration voltage of 100 keV.

Author contributions

My contribution to this work comprises the syntheses, the acquisition and analysis of the PXRD data, the measurement of SEM images, and the analysis of the electron microscopy data. SAED and TEM images were acquired by Stefan Werner.

A4 Fabrication of Nanotextured TiO₂ Thin-films

This chapter describes a fabrication route for epitaxial rutile TiO₂ on c-cut single crystal sapphire substrates by depositing TiO₂ nanorods (TNR) with the Langmuir-Blodgett (LB) technique followed by thermal treatment. The fabrication is described in detail in the experimental section below. The films exhibit a strong preferred orientation of the TiO₂ due to epitaxial sintering during the calcination process. This is evidenced by PXRD pattern shown in Figure A4.1. The reflections of the sample can be assigned to preferred oriented rutile with a small anatase impurity. The anatase phase exhibits smaller crystallite sizes than the rutile phase as indicated by peak broadening.

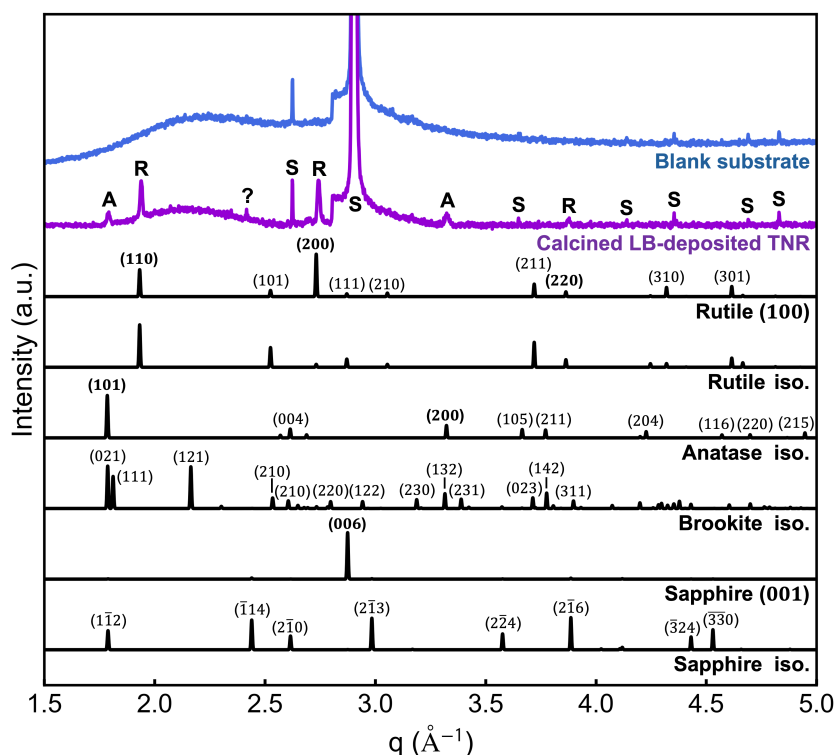


Figure A4.1: PXRD pattern of the calcined TNR film compared with the blank substrate and simulated patterns of titania and sapphire phases. The reflections of the calcined TNR film are assigned to preferentially oriented rutile (100), isotropic anatase, and the sapphire substrate, and are indexed with R, A, or S, respectively. One weak reflection at $\sim 2.4 \text{ \AA}^{-1}$ cannot be assigned to any phase and is therefore indexed with a question mark (?). Reflections in the simulated patterns are labeled by their Miller indices, and those assigned to the experimental pattern are highlighted in bold. The rutile (100) is simulated with 65 % and the sapphire (001) is simulated with 90 % preferred orientation. The other simulations assume isotropic (iso.) structures.

Experimental

Chemicals and materials

Ethanol (VWR chemicals, >99.9%), acetone (Sigma Aldrich, >99.9%), and chloroform (VWR chemicals, >99.8%, stabilized with 0.6% ethanol) were purchased from commercial sources. Deionized water was produced in-house using a Milli-Q IQ 7000 system (18.2 M Ω cm). Single-crystal sapphire (Al₂O₃) substrates were purchased from Crystal GmbH. The substrates have dimensions of 5x5x0.5 mm³, are polished on both sides to a surface roughness of <0.5 nm,

and are cut with the surface oriented along the (0001) plane and the edges along the (11 $\bar{2}$ 0) and (1 $\bar{1}$ 00) plane. Before the film fabrication, the substrates were cleaned in an ultrasonic bath for 15 min in acetone followed by 15 min in ethanol, and are subsequently rinsed with deionized water and dried with an air gun.

Synthesis

TiO₂ nanorods (TNR) were synthesized as described by Gordon et.al.²⁸⁶ The as-synthesized TNRs are dispersed in chloroform to obtain a concentration of ~ 20 mg mL. 40 μ L of this dispersion are added to a mixture of 2 mL chloroform and 0.5 mL ethanol, yielding a ~ 2.5 mL TNR stock dispersion with a concentration of ~ 0.3 mg mL.

Film fabrication

First, the Teflon reservoir of the Langmuir-Blodgett (LB) device (MicroTrough FilmwareX 4.2, Kibron Inc.) with an area of 280 000 mm² is filled with ~ 240 -250 mL deionized water to create a convex meniscus at the edges of the reservoir. Subsequently, 700 μ L of the TNR stock dispersion are added drop-wise to the water surface using a micropipette. The reservoir is left undisturbed for 30 min to 60 min to allow complete evaporation of the chloroform and the formation of a TNR monolayer at the water-air interface. The TNR monolayer is then compressed using a movable barrier at a speed of 3 mm min⁻¹ to a target area of 5000 mm². The sapphire substrate is dip-coated into the reservoir at a speed of 0.5 mm min⁻¹. This dipping procedure is repeated twice, resulting in the transfer of four TNR monolayers onto the substrate. Prior to the LB deposition, one side of the sapphire substrate is covered with Scotch tape to prevent coating on both sides. After deposition, the tape is removed, and residual adhesive is cleaned by wiping the surface with a tissue soaked in acetone. The LB-TNR film is subsequently dried overnight in a vacuum oven at 60 °C and 5 mbar. Finally, the LB-TNR film is calcined at 1000 °C with a heating rate of 100 °C min⁻¹ for 24 h, followed by natural cooling to room temperature.

Powder X-ray Diffraction (PXRD)

PXRD patterns were acquired on a Bruker Advanced D8 with Cu K α -radiation of 8.048 keV ($\lambda = 1.541$ Å). PXRD calculations were performed using CrystalDiffract 7 (CrystalMaker Software Ltd.).

Author contributions

My contribution to this work comprises the thermal treatment of the deposited films, and acquisition and analysis of the PXRD data. The LB-deposition was carried out by Yogesh Mahor and Tomasz Kacperski. TNRs were synthesized by Yogesh Mahor, Sophia Bittinger, and Finn Dobschall.

Bibliography

- (1) Lee, J.; Yang, J.; Kwon, S. G.; Hyeon, T. *Nonclassical nucleation and growth of inorganic nanoparticles*, *Nature Reviews Materials* 1, 8, **2016**, DOI: <https://doi.org/10.1038/natrevmats.2016.34>.
- (2) Baek, W.; Chang, H.; Bootharaju, M. S.; Kim, J. H.; Park, S.; Hyeon, T. *Recent Advances and Prospects in Colloidal Nanomaterials*, *JACS Au* 1, 11, **2021**, DOI: <https://doi.org/10.1021/jacsau.1c00339>.
- (3) Baig, N.; Kammakakam, I.; Falath, W. *Nanomaterials: a review of synthesis methods, properties, recent progress, and challenges*, *Materials Advances* 2, 6, **2021**, DOI: <https://doi.org/10.1039/D0MA00807A>.
- (4) Jun, Y.-S.; Zhu, Y.; Wang, Y.; Ghim, D.; Wu, X.; Kim, D.; Jung, H. *Classical and Nonclassical Nucleation and Growth Mechanisms for Nanoparticle Formation*, *Annual Review of Physical Chemistry* 73, **2022**, DOI: <https://doi.org/10.1146/annurev-physchem-082720-100947>.
- (5) Gibbs, Josiah Willard *On the equilibrium of heterogeneous substances*, *Transactions of the Connecticut Academy of Arts and Sciences* 3, **1876**.
- (6) Debenedetti, P. G.; Kim, Y.-Y.; Meldrum, F. C.; Tanaka, H. *Special Topic Preface: Nucleation—Current understanding approaching 150 years after Gibbs*, *The Journal of Chemical Physics* 160, 10, **2024**, DOI: <https://doi.org/10.1063/5.0203119>.
- (7) Gebauer, D.; Raiteri, P.; Gale, J. D.; Cölfen, H. *On classical and non-classical views on nucleation*, *American Journal of Science* 318, 9, **2018**, DOI: <https://doi.org/10.2475/09.2018.05>.
- (8) Jia, C.; Xiao, A.; Zhao, J.; Wang, P.; Fang, X.; Zhang, H.; Guan, B. *A New Perspective on Crystal Nucleation: A Classical View on Non-Classical Nucleation*, *Crystal Growth & Design* 24, 1, **2024**, DOI: <https://doi.org/10.1021/acs.cgd.3c01078>.
- (9) Jin, B.; Liu, Z.; Tang, R. *Recent experimental explorations of non-classical nucleation*, *CrystEngComm* 22, 24, **2020**, DOI: <https://doi.org/10.1039/D0CE00480D>.
- (10) Anderson, M. W.; Bennett, M.; Cedeno, R.; Cölfen, H.; Cox, S. J.; Cruz-Cabeza, A. J.; De Yoreo, J. J.; Drummond-Brydson, R.; Dudek, M. K.; Fichthorn, K. A.; Finney, A. R.; Ford, I.; Galloway, J. M.; Gebauer, D.; Grossier, R.; Harding, J. H.; Hare, A.; Horváth, D.; Hunter, L.; Kim, J.; Kimura, Y.; Kirschhock, C. E. A.; Kiselev, A. A.; Kras, W.; Kuttner, C.; Lee, A. Y.; Liao, Z.; Maini, L.; Nilsson Lill, S. O.; Pellens, N.; Price, S. L.; Rietveld, I. B.; Rimer, J. D.; Roberts, K. J.; Rogal, J.; Salvalaglio, M.; Sandei, I.; Schuszter, G.; Sefcik, J.; Sun, W.; Ter Horst, J. H.; Ukrainczyk, M.; Van Driessche, A. E. S.; Veessler, S.; Vekilov, P. G.; Verma, V.; Whale, T.; Wheatcroft, H. P.; Zeglinski, J. *Understanding crystal nucleation mechanisms: where do we stand? General discussion*, *Faraday Discussions* 235, **2022**, DOI: <https://doi.org/10.1039/D2FD90021A>.
- (11) Thanh, N. T. K.; Maclean, N.; Mahiddine, S. *Mechanisms of Nucleation and Growth of Nanoparticles in Solution*, *Chemical Reviews* 114, 15, **2014**, DOI: <https://doi.org/10.1021/cr400544s>.

- (12) Finney, A. R.; Salvalaglio, M. *Molecular simulation approaches to study crystal nucleation from solutions: Theoretical considerations and computational challenges*, WIREs Computational Molecular Science 14, 1, **2024**, DOI: <https://doi.org/10.1002/wcms.1697>.
- (13) Cölfen, H. *Analytical ultracentrifugation in colloid and polymer science: new possibilities and perspectives after 100 years*, Colloid and Polymer Science 301, 7, **2023**, DOI: <https://doi.org/10.1007/s00396-023-05130-0>.
- (14) Bøjesen, E. D.; Iversen, B. B. *The chemistry of nucleation*, CrystEngComm 18, 43, **2016**, DOI: <https://doi.org/10.1039/c6ce01489e>.
- (15) Harouna-Mayer, S. Y.; Gumus Akcaalan, M.; Kopula Kesavan, J.; Groene, T. R. L.; Klemeyer, L.; Hussak, S.-A.; Grote, L.; Derelli, D.; Caddeo, F.; Zito, C.; Stütze, P.; Speer, D.; Dippel, A.-C.; Detlefs, B.; Appiarius, Y.; Jacobi Von Wangelin, A.; Koziej, D. *Modular reactor for in situ X-ray scattering, spectroscopy and ATR-IR studies of solvothermal nanoparticle synthesis*, Journal of Synchrotron Radiation 33, 1, **2026**, DOI: <https://doi.org/10.1107/S1600577525009634>.
- (16) Harouna-Mayer, S. Y.; Kopula Kesavan, J.; Caddeo, F.; Belgardt, L.; Hsu, C.-S.; Klemeyer, L.; Kipping, L.; Akcaalan, M. G.; Groene, T. R.; Köppen, A.; Noei, H.; Mathon, O.; Dippel, A.-C.; Koziej, D. *Cation-Site Disordered Cu₃PdN Nanoparticles for Hydrogen Evolution Electrocatalysis*, Small 21, **2025**, DOI: <https://doi.org/10.1002/smll.202506838>.
- (17) Harouna-Mayer, S. Y.; Klemeyer, L.; Zito, C. A.; Bielecki, J.; Cheng, X.; Derelli, D.; Estillore, A. D.; Groene, T. L. R.; Haas, L. V.; Letrun, R.; Kim, C.; Koliyadu, J. C. P.; Mall, A.; Mazumder, P.; Melo, D. V. M.; Round, A. R.; Samanta, A. K.; Sarma, A.; Shen, Z.; Sun, X.; Vagovic, P.; Wollweber, T.; Bean, R.; Küpper, J.; Chapman, H. N.; Koziej, D.; Ayyer, K. *Single-Particle X-ray Scattering Reveals a High Local Supersaturation of Precursors as the Origin of CoO Assembly Formation*, 2025, DOI: <https://doi.org/10.48550/arXiv.2512.08488>.
- (18) Karthika, S.; Radhakrishnan, T. K.; Kalaichelvi, P. *A Review of Classical and Nonclassical Nucleation Theories*, Crystal Growth & Design 16, 11, **2016**, DOI: <https://doi.org/10.1021/acs.cgd.6b00794>.
- (19) Arshadi, S.; Moghaddam, J.; Eskandarian, M. *LaMer diagram approach to study the nucleation and growth of Cu₂O nanoparticles using supersaturation theory*, Korean Journal of Chemical Engineering 31, 11, **2014**, DOI: <https://doi.org/10.1007/s11814-014-0130-3>.
- (20) Gebauer, D.; Cölfen, H. *Prenucleation clusters and non-classical nucleation*, Nano Today 6, 6, **2011**, DOI: <https://doi.org/10.1016/j.nantod.2011.10.005>.
- (21) Grote, L., *Imaging nanomaterials in solution – A multimodal approach using in situ X-ray ptychography, spectroscopy and scattering*, Doctoral thesis, **2022**, Available at: <https://ediss.sub.uni-hamburg.de/handle/ediss/9811>.
- (22) Derelli, D., *Investigating Nanostructured Materials by Multi-modal in situ X-ray Methods*, Doctoral thesis, **2024**, Available at: <https://ediss.sub.uni-hamburg.de/handle/ediss/10963>.
- (23) Klemeyer, L., *Investigating the emergence of electronic and atomic structure during the synthesis of transition-metal sulfides*, Doctoral thesis, **2025**, Available at: <https://ediss.sub.uni-hamburg.de/handle/ediss/11745>.

-
- (24) Plummer, L. K.; Hutchison, J. E. *Understanding the Effects of Iron Precursor Ligation and Oxidation State Leads to Improved Synthetic Control for Spinel Iron Oxide Nanocrystals*, *Inorganic Chemistry* 59, 20, **2020**, DOI: <https://doi.org/10.1021/acs.inorgchem.0c02040>.
- (25) Horner, O.; Neveu, S.; de Montredon, S.; Siaugue, J.-M.; Cabuil, V. *Hydrothermal synthesis of large maghemite nanoparticles: influence of the pH on the particle size*, *Journal of Nanoparticle Research* 11, 5, **2009**, DOI: <https://doi.org/10.1007/s11051-008-9582-x>.
- (26) Roth, H.-C.; Schwaminger, S. P.; Schindler, M.; Wagner, F. E.; Berensmeier, S. *Influencing factors in the CO-precipitation process of superparamagnetic iron oxide nano particles: A model based study*, *Journal of Magnetism and Magnetic Materials* 377, **2015**, DOI: <https://doi.org/10.1016/j.jmmm.2014.10.074>.
- (27) LaMer, V. K.; Dinegar, R. H. *Theory, Production and Mechanism of Formation of Monodispersed Hydrosols*, *Journal of the American Chemical Society* 72, 11, **1950**, DOI: <https://doi.org/10.1021/ja01167a001>.
- (28) Kwon, S. G.; Hyeon, T. *Formation Mechanisms of Uniform Nanocrystals via Hot-Injection and Heat-Up Methods*, *Small* 7, 19, **2011**, DOI: <https://doi.org/10.1002/smll.201002022>.
- (29) Kulpa-Greszta, M.; Tomaszewska, A.; Dziedzic, A.; Pązik, R. *Rapid hot-injection as a tool for control of magnetic nanoparticle size and morphology*, *RSC Advances* 11, 34, **2021**, DOI: <https://doi.org/10.1039/D1RA02977K>.
- (30) Kwon, S. G.; Piao, Y.; Park, J.; Angappane, S.; Jo, Y.; Hwang, N.-M.; Park, J.-G.; Hyeon, T. *Kinetics of Monodisperse Iron Oxide Nanocrystal Formation by "Heating-Up" Process*, *Journal of the American Chemical Society* 129, 41, **2007**, DOI: <https://doi.org/10.1021/ja074633q>.
- (31) Muscas, G.; Singh, G.; Glomm, W. R.; Mathieu, R.; Kumar, P. A.; Concas, G.; Agostinelli, E.; Peddis, D. *Tuning the Size and Shape of Oxide Nanoparticles by Controlling Oxygen Content in the Reaction Environment: Morphological Analysis by Aspect Maps*, *Chemistry of Materials* 27, 6, **2015**, DOI: <https://doi.org/10.1021/cm5038815>.
- (32) Baumgartner, J.; Dey, A.; Bomans, P. H. H.; Le Coadou, C.; Fratzl, P.; Sommerdijk, N. A. J. M.; Faivre, D. *Nucleation and growth of magnetite from solution*, *Nature Materials* 12, 4, **2013**, DOI: <https://doi.org/10.1038/nmat3558>.
- (33) Zheng, W.; Hauwiller, M. R.; Liang, W.-I.; Ophus, C.; Ercius, P.; Chan, E. M.; Chu, Y.-H.; Asta, M.; Du, X.; Alivisatos, A. P.; Zheng, H. *Real time imaging of two-dimensional iron oxide spherulite nanostructure formation*, *Nano Research* 12, 11, **2019**, DOI: <https://doi.org/10.1007/s12274-019-2531-4>.
- (34) Leffler, V.; Ehlert, S.; Förster, B.; Dulle, M.; Förster, S. *Nanoparticle Heat-Up Synthesis: In Situ X-ray Diffraction and Extension from Classical to Nonclassical Nucleation and Growth Theory*, *ACS Nano* 15, 1, **2021**, DOI: <https://doi.org/10.1021/acs.nano.0c07359>.
- (35) Li, J.; Deepak, F. L. *In Situ Kinetic Observations on Crystal Nucleation and Growth*, *Chemical Reviews* 122, 23, **2022**, DOI: <https://doi.org/10.1021/acs.chemrev.1c01067>.
- (36) Kim, B. H.; Shin, K.; Kwon, S. G.; Jang, Y.; Lee, H.-S.; Lee, H.; Jun, S. W.; Lee, J.; Han, S. Y.; Yim, Y.-H.; Kim, D.-H.; Hyeon, T. *Sizing by Weighing: Characterizing Sizes of Ultrasmall-Sized Iron Oxide Nanocrystals Using MALDI-TOF Mass Spectrometry*, *Journal of the American Chemical Society* 135, 7, **2013**, DOI: <https://doi.org/10.1021/ja310030c>.

- (37) Jensen, K. M. Ø.; Andersen, H. L.; Tyrsted, C.; Bøjesen, E. D.; Dippel, A.-C.; Lock, N.; Billinge, S. J. L.; Iversen, B. B.; Christensen, M. *Mechanisms for Iron Oxide Formation under Hydrothermal Conditions: An in Situ Total Scattering Study*, ACS Nano 8, 10, **2014**, DOI: <https://doi.org/10.1021/nn5044096>.
- (38) Scheck, J.; Wu, B.; Drechsler, M.; Rosenberg, R.; Van Driessche, A. E. S.; Stawski, T. M.; Gebauer, D. *The Molecular Mechanism of Iron(III) Oxide Nucleation*, The Journal of Physical Chemistry Letters 7, 16, **2016**, DOI: <https://doi.org/10.1021/acs.jpcllett.6b01237>.
- (39) Ai, Z.; Deng, K.; Wan, Q.; Zhang, L.; Lee, S. *Facile Microwave-Assisted Synthesis and Magnetic and Gas Sensing Properties of Fe₃O₄ Nanoroses*, The Journal of Physical Chemistry C 114, 14, **2010**, DOI: <https://doi.org/10.1021/jp910514f>.
- (40) Nikam, A. V.; Prasad, B. L. V.; Kulkarni, A. A. *Wet chemical synthesis of metal oxide nanoparticles: a review*, CrystEngComm 20, 35, **2018**, DOI: <https://doi.org/10.1039/c8ce00487k>.
- (41) Shanker, G. S.; Ogale, S. *Faceted Colloidal Metallic Ni₃N Nanocrystals: Size-Controlled Solution-Phase Synthesis and Electrochemical Overall Water Splitting*, ACS Applied Energy Materials 4, 3, **2021**, DOI: <https://doi.org/10.1021/acsaem.0c02674>.
- (42) Parvizian, M.; De Roo, J. *Precursor chemistry of metal nitride nanocrystals*, Nanoscale 13, 45, **2021**, DOI: <https://doi.org/10.1039/d1nr05092c>.
- (43) Wang, H.; Li, J.; Li, K.; Lin, Y.; Chen, J.; Gao, L.; Nicolosi, V.; Xiao, X.; Lee, J.-M. *Transition metal nitrides for electrochemical energy applications*, Chemical Society Reviews 50, 2, **2021**, DOI: <https://doi.org/10.1039/D0CS00415D>.
- (44) Yang, Z.-G.; Xu, H.-M.; Shuai, T.-Y.; Zhan, Q.-N.; Zhang, Z.-J.; Huang, K.; Dai, C.; Li, G.-R. *Recent progress in the synthesis of transition metal nitride catalysts and their applications in electrocatalysis*, Nanoscale 15, 28, **2023**, DOI: <https://doi.org/10.1039/D3NR01607B>.
- (45) Luo, Q.; Lu, C.; Liu, L.; Zhu, M. *A review on the synthesis of transition metal nitride nanostructures and their energy related applications*, Green Energy & Environment 8, 2, **2023**, DOI: <https://doi.org/10.1016/j.gee.2022.07.002>.
- (46) Sidana, H. K.; Mir, R. A.; Pandey, O. *Synthesis of molybdenum nitride (Mo₂N) nanoflakes via in-situ reduction-nitridation*, Journal of Alloys and Compounds 736, **2018**, DOI: <https://doi.org/10.1016/j.jallcom.2017.09.268>.
- (47) Bai, P.; Xing, W.; Yan, Z. *Synthesis and characterization of mesostructured tungsten nitride by using tungstic acid as the precursor*, Journal of Porous Materials 13, 2, **2006**, DOI: <https://doi.org/10.1007/s10934-006-7027-4>.
- (48) Wang, L.; Shen, Q.; Zhao, D.; Lu, J.; Liu, W.; Zhang, J.; Bao, K.; Zhou, Q. *Chemical synthesis of hexagonal indium nitride nanocrystallines at low temperature*, Journal of Crystal Growth 471, **2017**, DOI: <https://doi.org/10.1016/j.jcrysgro.2017.05.005>.
- (49) Choi, D.; Blomgren, G. E.; Kumta, P. N. *Fast and Reversible Surface Redox Reaction in Nanocrystalline Vanadium Nitride Supercapacitors*, Advanced Materials 18, 9, **2006**, DOI: <https://doi.org/10.1002/adma.200502471>.
- (50) Huang, T.; Mao, S.; Zhou, G.; Wen, Z.; Huang, X.; Ci, S.; Chen, J. *Hydrothermal synthesis of vanadium nitride and modulation of its catalytic performance for oxygen reduction reaction*, Nanoscale 6, 16, **2014**, DOI: <https://doi.org/10.1039/C4NR02646B>.

-
- (51) Choi, D.; Kumta, P. N. *Synthesis and Characterization of Nanostructured Niobium and Molybdenum Nitrides by a Two-Step Transition Metal Halide Approach*, *Journal of the American Ceramic Society* 94, 8, **2011**, DOI: <https://doi.org/10.1111/j.1551-2916.2011.04412.x>.
- (52) Gao, Z.; Wan, Y.; Xiong, G.; Guo, R.; Luo, H. *Synthesis of aluminum nitride nanoparticles by a facile urea glass route and influence of urea/metal molar ratio*, *Applied Surface Science* 280, **2013**, DOI: <https://doi.org/10.1016/j.apsusc.2013.04.075>.
- (53) Choi, J.; Gillan, E. G. *Solvothermal Synthesis of Nanocrystalline Copper Nitride from an Energetically Unstable Copper Azide Precursor*, *Inorganic Chemistry* 44, 21, **2005**, DOI: <https://doi.org/10.1021/ic050497j>.
- (54) Deshmukh, R.; Zeng, G.; Tervoort, E.; Staniuk, M.; Wood, D.; Niederberger, M. *Ultrasmall Cu₃N Nanoparticles: Surfactant-Free Solution-Phase Synthesis, Nitridation Mechanism, and Application for Lithium Storage*, *Chem. Mater.* **2015**.
- (55) Parvizian, M.; Duràn Balsa, A.; Pokratath, R.; Kalha, C.; Lee, S.; Van den Eynden, D.; Ibáñez, M.; Regoutz, A.; De Roo, J. *The Chemistry of Cu₃N and Cu₃PdN Nanocrystals***, *Angewandte Chemie International Edition* 61, 31, **2022**, DOI: <https://doi.org/10.1002/anie.202207013>.
- (56) Wang, D.; Li, Y. *Controllable synthesis of Cu-based nanocrystals in ODA solvent*, *Chemical Communications* 47, 12, **2011**, DOI: <https://doi.org/10.1039/c0cc04902f>.
- (57) Koziej, D. *Revealing Complexity of Nanoparticle Synthesis in Solution by in Situ Hard X-ray Spectroscopy—Today and Beyond*, *Chemistry of Materials* 28, 8, **2016**, DOI: <https://doi.org/10.1021/acs.chemmater.6b00486>.
- (58) Als-Nielsen, J., *Elements of Modern X-ray Physics*, John Wiley & Sons, **2011**, ISBN: 978-1-119-99731-3.
- (59) Willmott, P., *An introduction to synchrotron radiation: techniques and applications*, John Wiley & Sons, **2019**, ISBN: 978-1-119-28039-2.
- (60) Mobilio, S., *Synchrotron Radiation: Basics, Methods and Applications*, Springer Berlin Heidelberg, Berlin, Heidelberg, **2015**, ISBN: 978-3-642-55314-1 978-3-642-55315-8.
- (61) Egami, T.; Billinge, S. J. L., *Underneath the Bragg Peaks: Structural Analysis of Complex Materials*, Elsevier Science, **2012**, ISBN: 978-0-08-097141-4.
- (62) Billinge, S.; Jensen, A. P. K.; Billinge, S.; Jensen, A. P. K., *Atomic Pair Distribution Function Analysis: A Primer*, Oxford University Press, Oxford, New York, **2023**, ISBN: 978-0-19-888580-1.
- (63) Newville, M., *Fundamentals of XAFS*, Consortium for Advanced Radiation Sources, Chicago, IL, **2008**.
- (64) Glatzel, P.; Juhin, A. In *Local Structural Characterisation*; John Wiley & Sons, Ltd: 2013, DOI: <https://doi.org/10.1002/9781118681909.ch2>.
- (65) Iglesias-Juez, A.; Chiarello, G. L.; Patience, G. S.; Guerrero-Pérez, M. O. *Experimental methods in chemical engineering: X-ray absorption spectroscopy—XAS, XANES, EXAFS*, *The Canadian Journal of Chemical Engineering* 100, 1, **2022**, DOI: <https://doi.org/10.1002/cjce.24291>.
- (66) Christiansen, T. L.; Cooper, S. R.; Jensen, K. M. Ø. *There's no place like real-space: elucidating size-dependent atomic structure of nanomaterials using pair distribution function analysis*, *Nanoscale Advances* 2, 6, **2020**, DOI: <https://doi.org/10.1039/D0NA00120A>.

- (67) Roelsgaard, M.; Kløve, M.; Christensen, R.; Bertelsen, A. D.; Broge, N. L. N.; Kantor, I.; Sørensen, D. R.; Dippel, A.-C.; Banerjee, S.; Zimmermann, M. V.; Glaevecke, P.; Gutowski, O.; Jørgensen, M. R. V.; Iversen, B. B. *A reactor for time-resolved X-ray studies of nucleation and growth during solvothermal synthesis*, *Journal of Applied Crystallography* 56, 3, **2023**, DOI: <https://doi.org/10.1107/S1600576723002339>.
- (68) Brown, P. J.; Fox, A. G.; Maslen, E. N.; O'Keefe, M. A.; Willis, B. T. M. In *International Tables for Crystallography Volume C: Mathematical, physical and chemical tables*; Springer, Dordrecht: 2006, DOI: <https://doi.org/10.1107/97809553602060000600>.
- (69) Toby, B. H.; Von Dreele, R. B. *GSAS-II: the genesis of a modern open-source all purpose crystallography software package*, *Journal of Applied Crystallography* 46, 2, **2013**, DOI: <https://doi.org/10.1107/S0021889813003531>.
- (70) Billinge, S. J. L.; Farrow, C. L. *Towards a robust ad hoc data correction approach that yields reliable atomic pair distribution functions from powder diffraction data*, *Journal of Physics: Condensed Matter* 25, 45, **2013**, DOI: <https://doi.org/10.1088/0953-8984/25/45/454202>.
- (71) Juhás, P.; Farrow, C.; Yang, X.; Knox, K.; Billinge, S. *Complex modeling: a strategy and software program for combining multiple information sources to solve ill posed structure and nanostructure inverse problems*, *Acta Crystallographica Section A: Foundations and Advances* 71, 6, **2015**, DOI: <https://doi.org/10.1107/S2053273315014473>.
- (72) Farrow, C. L.; Billinge, S. J. L. *Relationship between the atomic pair distribution function and small-angle scattering: implications for modeling of nanoparticles*, *Acta Crystallographica Section A Foundations of Crystallography* 65, 3, **2009**, DOI: <https://doi.org/10.1107/S0108767309009714>.
- (73) Sobolev, E.; Zolotarev, S.; Giewekemeyer, K.; Bielecki, J.; Okamoto, K.; Reddy, H. K. N.; Andreasson, J.; Ayyer, K.; Barak, I.; Bari, S.; Barty, A.; Bean, R.; Bobkov, S.; Chapman, H. N.; Chojnowski, G.; Daurer, B. J.; Dörner, K.; Ekeberg, T.; Flückiger, L.; Galzitskaya, O.; Gelisio, L.; Hauf, S.; Hogue, B. G.; Horke, D. A.; Hosseinizadeh, A.; Ilyin, V.; Jung, C.; Kim, C.; Kim, Y.; Kirian, R. A.; Kirkwood, H.; Kulyk, O.; Küpper, J.; Letrun, R.; Loh, N. D.; Lorenzen, K.; Messerschmidt, M.; Mühlig, K.; Ourmazd, A.; Raab, N.; Rode, A. V.; Rose, M.; Round, A.; Sato, T.; Schubert, R.; Schwander, P.; Sellberg, J. A.; Sikorski, M.; Silenzi, A.; Song, C.; Spence, J. C. H.; Stern, S.; Sztuk-Dambietz, J.; Teslyuk, A.; Timneanu, N.; Trebbin, M.; Uetrecht, C.; Weinhausen, B.; Williams, G. J.; Xavier, P. L.; Xu, C.; Vartanyants, I. A.; Lamzin, V. S.; Mancuso, A.; Maia, F. R. N. C. *Megahertz single-particle imaging at the European XFEL*, *Communications Physics* 3, 1, **2020**, DOI: <https://doi.org/10.1038/s42005-020-0362-y>.
- (74) Ayyer, K.; Xavier, P. L.; Bielecki, J.; Shen, Z.; Daurer, B. J.; Samanta, A. K.; Awel, S.; Bean, R.; Barty, A.; Bergemann, M.; Ekeberg, T.; Estillore, A. D.; Fangohr, H.; Giewekemeyer, K.; Hunter, M. S.; Karnevskiy, M.; Kirian, R. A.; Kirkwood, H.; Kim, Y.; Koliyadu, J.; Lange, H.; Letrun, R.; Lübke, J.; Michelat, T.; Morgan, A. J.; Roth, N.; Sato, T.; Sikorski, M.; Schulz, F.; Spence, J. C. H.; Vagovic, P.; Wollweber, T.; Worbs, L.; Yefanov, O.; Zhuang, Y.; Maia, F. R. N. C.; Horke, D. A.; Küpper, J.; Loh, N. D.; Mancuso, A. P.; Chapman, H. N. *3D diffractive imaging of nanoparticle ensembles using an x-ray laser*, *Optica* 8, 1, **2021**, DOI: <https://doi.org/10.1364/OPTICA.410851>.
- (75) Barends, T. R. M.; Stauch, B.; Cherezov, V.; Schlichting, I. *Serial femtosecond crystallography*, *Nature Reviews Methods Primers* 2, 1, **2022**, DOI: <https://doi.org/10.1038/s43586-022-00141-7>.

-
- (76) Elam, W.; Ravel, B.; Sieber, J. *A new atomic database for X-ray spectroscopic calculations*, *Radiation Physics and Chemistry* 63, 2, **2002**, DOI: [https://doi.org/10.1016/S0969-806X\(01\)00227-4](https://doi.org/10.1016/S0969-806X(01)00227-4).
- (77) Newville, M., *XrayDB*, Software, **2025**, Available at: <https://github.com/xraypy/XrayDB>.
- (78) Spasyuk, D.; Mikhchian, M.; Blanchard, P.; Vu, M.; Reid, J.; Bergen, E.; Chen, N.; Desmau, M.; Chernikov, R.; Pan, Y.; Lin, J.; Grosvenor, A. *Canadian Light Source XAS Database Data*, 2025, DOI: <https://doi.org/10.20383/103.01329>.
- (79) Caddeo, F.; Gröne, T. L. R.; Gumus Akcaalan, M.; Hsu, C.-S.; Hussak, S.-A.; Klemeyer, L.; Kopula Kesavan, J.; Koziej, D. *in situ photon-in-photon-out spectroscopic studies with high temporal, spatial and energy resolution during emergence of transition metal su*, in collab. with Mathon, O., 2024, DOI: <https://doi.org/10.15151/ESRF-ES-1442330861>.
- (80) Heiligtag, F. J.; Niederberger, M. *The fascinating world of nanoparticle research*, *Materials Today* 16, 7, **2013**, DOI: <https://doi.org/10.1016/j.mattod.2013.07.004>.
- (81) Yin, Y.; Talapin, D. *The chemistry of functional nanomaterials*, *Chemical Society Reviews* 42, 7, **2013**, DOI: <https://doi.org/10.1039/C3CS90011H>.
- (82) Boles, M. A.; Ling, D.; Hyeon, T.; Talapin, D. V. *The surface science of nanocrystals*, *Nature Materials* 15, 2, **2016**, DOI: <https://doi.org/10.1038/nmat4526>.
- (83) Cansell, F.; Aymonier, C. *Design of functional nanostructured materials using supercritical fluids*, *The Journal of Supercritical Fluids* 47, 3, **2009**, DOI: <https://doi.org/10.1016/j.supflu.2008.10.002>.
- (84) Deshmukh, R.; Niederberger, M. *Mechanistic Aspects in the Formation, Growth and Surface Functionalization of Metal Oxide Nanoparticles in Organic Solvents*, *Chemistry – A European Journal* 23, 36, **2017**, DOI: <https://doi.org/10.1002/chem.201605957>.
- (85) Terraschke, H., *Nanostructured Materials: Applications, Synthesis and In-Situ Characterization*, Walter de Gruyter GmbH & Co KG, **2023**, ISBN: 978-3-11-045909-8.
- (86) Jensen, K. M. Ø.; Tyrsted, C.; Bremholm, M.; Iversen, B. B. *In Situ Studies of Solvothermal Synthesis of Energy Materials*, *ChemSusChem* 7, 6, **2014**, DOI: <https://doi.org/10.1002/cssc.201301042>.
- (87) Nyborg-Broge, N. L.; Søndergaard-Pedersen, F.; Roelsgaard, M.; Hassing-Hansen, X.; Brummerstedt-Iversen, B. *Mapping the redox chemistry of common solvents in solvothermal synthesis through in situ X-ray diffraction*, *Nanoscale* 12, 15, **2020**, DOI: <https://doi.org/10.1039/D0NR01240H>.
- (88) Zhu, H.; Huang, Y.; Ren, J.; Zhang, B.; Ke, Y.; Jen, A. K.-Y.; Zhang, Q.; Wang, X.-L.; Liu, Q. *Bridging Structural Inhomogeneity to Functionality: Pair Distribution Function Methods for Functional Materials Development*, *Advanced Science* 8, 6, **2021**, DOI: <https://doi.org/10.1002/advs.202003534>.
- (89) Grosso, D.; Boissière, C.; Smarsly, B.; Brezesinski, T.; Pinna, N.; Albouy, P. A.; Amenitsch, H.; Antonietti, M.; Sanchez, C. *Periodically ordered nanoscale islands and mesoporous films composed of nanocrystalline multimetallic oxides*, *Nature Materials* 3, 11, **2004**, DOI: <https://doi.org/10.1038/nmat1206>.

- (90) Andersen, C. W.; Borfecchia, E.; Bremholm, M.; Jørgensen, M. R. V.; Vennestrøm, P. N. R.; Lamberti, C.; Lundegaard, L. F.; Iversen, B. B. *Redox-Driven Migration of Copper Ions in the Cu-CHA Zeolite as Shown by the In Situ PXRD/XANES Technique*, *Angewandte Chemie International Edition* 56, 35, **2017**, DOI: <https://doi.org/10.1002/anie.201703808>.
- (91) Grote, L.; Zito, C. A.; Frank, K.; Dippel, A.-C.; Reisbeck, P.; Pitala, K.; Kvashnina, K. O.; Bauters, S.; Detlefs, B.; Ivashko, O.; Pandit, P.; Rebber, M.; Harouna-Mayer, S. Y.; Nickel, B.; Koziej, D. *X-ray studies bridge the molecular and macro length scales during the emergence of CoO assemblies*, *Nature Communications* 12, 1, **2021**, DOI: <https://doi.org/10.1038/s41467-021-24557-z>.
- (92) Beyer, K. A.; Zhao, H.; Borkiewicz, O. J.; Newton, M. A.; Chupas, P. J.; Chapman, K. W. *Simultaneous diffuse reflection infrared spectroscopy and X-ray pair distribution function measurements*, *Journal of Applied Crystallography* 47, 1, **2014**, DOI: <https://doi.org/10.1107/S1600576713028410>.
- (93) Staniuk, M.; Hirsch, O.; Kränzlin, N.; Böhlen, R.; van Beek, W.; Abdala, P. M.; Koziej, D. *Puzzling Mechanism behind a Simple Synthesis of Cobalt and Cobalt Oxide Nanoparticles: In Situ Synchrotron X-ray Absorption and Diffraction Studies*, *Chemistry of Materials* 26, 6, **2014**, DOI: <https://doi.org/10.1021/cm500090r>.
- (94) Thum, L.; Arzmann, M.; Zizak, I.; Grüneberger, R.; Steigert, A.; Grimm, N.; Wallacher, D.; Schlatmann, R.; Amkreutz, D.; Gili, A. *In situ cell for grazing-incidence x-ray diffraction on thin films in thermal catalysis*, *Review of Scientific Instruments* 95, 3, **2024**, DOI: <https://doi.org/10.1063/5.0179989>.
- (95) Grunwaldt, J.-D.; Ramin, M.; Rohr, M.; Michailovski, A.; Patzke, G. R.; Baiker, A. *High pressure in situ x-ray absorption spectroscopy cell for studying simultaneously the liquid phase and the solid/liquid interface*, *Review of Scientific Instruments* 76, 5, **2005**, DOI: <https://doi.org/10.1063/1.1914787>.
- (96) Klemeyer, L.; Gröne, T. L. R.; Zito, C. d. A.; Vasylieva, O.; Gumus Akcaalan, M.; Harouna-Mayer, S. Y.; Caddeo, F.; Steenbock, T.; Hussak, S.-A.; Kesavan, J. K.; Dippel, A.-C.; Sun, X.; Köppen, A.; Saveleva, V. A.; Kumar, S.; Bester, G.; Glatzel, P.; Koziej, D. *Utilizing High X-ray Energy Photon-In Photon-Out Spectroscopies and X-ray Scattering to Experimentally Assess the Emergence of Electronic and Atomic Structure of ZnS Nanorods*, *Journal of the American Chemical Society* 146, 49, **2024**, DOI: <https://doi.org/10.1021/jacs.4c10257>.
- (97) Şahin, E. O.; Tüysüz, H.; K. Chan, C.; Moon, G.-h.; Dai, Y.; Schmidt, W.; Lim, J.; Scheu, C.; Weidenthaler, C. *In situ total scattering experiments of nucleation and crystallisation of tantalum-based oxides: from highly dilute solutions via cluster formation to nanoparticles*, *Nanoscale* 13, 1, **2021**, DOI: <https://doi.org/10.1039/D0NR07871A>.
- (98) Derelli, D.; Frank, K.; Grote, L.; Mancini, F.; Dippel, A.-C.; Gutowski, O.; Nickel, B.; Koziej, D. *Direct Synthesis of CuPd Icosahedra Supercrystals Studied by In Situ X-Ray Scattering*, *Small* 20, 32, **2024**, DOI: <https://doi.org/10.1002/smll.202311714>.
- (99) Chupas, P. J.; Chapman, K. W.; Kurtz, C.; Hanson, J. C.; Lee, P. L.; Grey, C. P. *A versatile sample-environment cell for non-ambient X-ray scattering experiments*, *Journal of Applied Crystallography* 41, 4, **2008**, DOI: <https://doi.org/10.1107/S0021889808020165>.

-
- (100) Becker, J.; Bremholm, M.; Tyrsted, C.; Pauw, B.; Jensen, K. M. Ø.; Eltzholt, J.; Christensen, M.; Iversen, B. B. *Experimental setup for in situ X-ray SAXS/WAXS/PDF studies of the formation and growth of nanoparticles in near- and supercritical fluids*, *Journal of Applied Crystallography* 43, 4, **2010**, DOI: <https://doi.org/10.1107/S0021889810014688>.
- (101) Bare, S. R.; Yang, N.; Kelly, S. D.; Mickelson, G. E.; Modica, F. S. *Design and operation of a high pressure reaction cell for in situ X-ray absorption spectroscopy*, *Catalysis Today* 126, 1, **2007**, DOI: <https://doi.org/10.1016/j.cattod.2006.10.007>.
- (102) Testemale, D.; Brugger, J. In *International Tables for Crystallography, Volume I: X-ray absorption spectroscopy and related techniques*; International Union of Crystallography / Wiley-VCH: 2024, DOI: <https://doi.org/10.1107/S1574870722003238>.
- (103) Yi, Z.; Dumée, L. F.; Garvey, C. J.; Feng, C.; She, F.; Rookes, J. E.; Mudie, S.; Cahill, D. M.; Kong, L. *A New Insight into Growth Mechanism and Kinetics of Mesoporous Silica Nanoparticles by in Situ Small Angle X-ray Scattering*, *Langmuir* 31, 30, **2015**, DOI: <https://doi.org/10.1021/acs.langmuir.5b01637>.
- (104) Tominaka, S.; Yamada, H.; Hiroi, S.; Kawaguchi, S. I.; Ohara, K. *Lepidocrocite-Type Titanate Formation from Isostructural Prestructures under Hydrothermal Reactions: Observation by Synchrotron X-ray Total Scattering Analyses*, *ACS Omega* 3, 8, **2018**, DOI: <https://doi.org/10.1021/acsomega.8b01693>.
- (105) Yamada, H.; Tominaka, S.; Ohara, K.; Liu, Z.; Okubo, T.; Wakihara, T. *Structural Evolution of Amorphous Precursors toward Crystalline Zeolites Visualized by an in Situ X-ray Pair Distribution Function Approach*, *The Journal of Physical Chemistry C* 123, 46, **2019**, DOI: <https://doi.org/10.1021/acs.jpcc.9b07232>.
- (106) Klemeyer, L.; Caddeo, F.; Gröne, T. L. R.; Harouna-Mayer, S. Y.; Jessen, B.; Zito, C. A.; Kopula Kesavan, J.; Dippel, A.-C.; Igoa Saldaña, F.; Mathon, O.; Glatzel, P.; Koziej, D. *Spatially Resolved In Situ X-ray Absorption Spectroscopy Studies of ZnS Nanoparticle Synthesis at the Water-Toluene Interface*, *ACS Nano* 19, 28, **2025**, DOI: <https://doi.org/10.1021/acsnano.5c02875>.
- (107) Pinna, N.; Grancharov, S.; Beato, P.; Bonville, P.; Antonietti, M.; Niederberger, M. *Magnetite Nanocrystals: Nonaqueous Synthesis, Characterization, and Solubility*, *Chemistry of Materials* 17, 11, **2005**, DOI: <https://doi.org/10.1021/cm050060+>.
- (108) Evans, J. S. O.; Francis, R. J.; O'Hare, D.; Price, S. J.; Clark, S. M.; Flaherty, J.; Gordon, J.; Nield, A.; Tang, C. C. *An apparatus for the study of the kinetics and mechanism of hydrothermal reactions by in situ energy dispersive x-ray diffraction*, *Review of Scientific Instruments* 66, 3, **1995**, DOI: <https://doi.org/10.1063/1.1146451>.
- (109) Fingland, B. R.; Ribeiro, F. H.; Miller, J. T. *Simultaneous Measurement of X-ray Absorption Spectra and Kinetics: A Fixed-bed, Plug-flow Operando Reactor*, *Catalysis Letters* 131, 1, **2009**, DOI: <https://doi.org/10.1007/s10562-009-0026-8>.
- (110) Van Beek, W.; Safonova, O. V.; Wiker, G.; Emerich, H. *SNBL, a dedicated beamline for combined in situ X-ray diffraction, X-ray absorption and Raman scattering experiments*, *Phase Transitions* 84, 8, **2011**, DOI: <https://doi.org/10.1080/01411594.2010.549944>.
- (111) Schaef, H.; Windisch, C.; McGrail, B.; Martin, P.; Rosso, K. *Brucite [Mg(OH)₂] carbonation in wet supercritical CO₂: An in situ high pressure X-ray diffraction study*, *Geochimica et Cosmochimica Acta* 75, 23, **2011**, DOI: <https://doi.org/10.1016/j.gca.2011.09.029>.

- (112) Borkiewicz, O. J.; Shyam, B.; Wiaderek, K. M.; Kurtz, C.; Chupas, P. J.; Chapman, K. W. *The AMPIX electrochemical cell: a versatile apparatus for in situ X-ray scattering and spectroscopic measurements*, *Journal of Applied Crystallography* 45, 6, **2012**, DOI: <https://doi.org/10.1107/S0021889812042720>.
- (113) Heidenreich, N.; Rütt, U.; Köppen, M.; Inge, A. K.; Beier, S.; Dippel, A.-C.; Suren, R.; Stock, N. *A multi-purpose reaction cell for the investigation of reactions under solvothermal conditions*, *Review of Scientific Instruments* 88, 10, **2017**, DOI: <https://doi.org/10.1063/1.4999688>.
- (114) Yao, S.; Yang, C.; Zhao, H.; Li, S.; Lin, L.; Wen, W.; Liu, J.; Hu, G.; Li, W.; Hou, Y.; Ma, D. *Reconstruction of the Wet Chemical Synthesis Process: The Case of Fe₅C₂ Nanoparticles*, *The Journal of Physical Chemistry C* 121, 9, **2017**, DOI: <https://doi.org/10.1021/acs.jpcc.7b00198>.
- (115) Hoffman, A. S.; Singh, J. A.; Bent, S. F.; Bare, S. R. *In situ observation of phase changes of a silica-supported cobalt catalyst for the Fischer–Tropsch process by the development of a synchrotron-compatible in situ/operando powder X-ray diffraction cell*, *Journal of Synchrotron Radiation* 25, 6, **2018**, DOI: <https://doi.org/10.1107/S1600577518013942>.
- (116) Kalantzopoulos, G. N.; Lundvall, F.; Checchia, S.; Lind, A.; Wragg, D. S.; Fjellvåg, H.; Arstad, B. *In Situ Flow MAS NMR Spectroscopy and Synchrotron PDF Analyses of the Local Response of the Brønsted Acidic Site in SAPO-34 during Hydration at Elevated Temperatures*, *ChemPhysChem* 19, 4, **2018**, DOI: <https://doi.org/10.1002/cphc.201700973>.
- (117) Wang, H.; Mo, G.; Zhong, J.; Liu, Y.; Qian, L.; Yao, L.; Xing, X.; Chen, Z.; Wu, Z. *A capillary sample cell used for in-situ SAXS, XRD, and XAFS measurements during hydrothermal synthesis*, *Nuclear Instruments and Methods in Physics Research Section A: Accelerators, Spectrometers, Detectors and Associated Equipment* 1031, **2022**, DOI: <https://doi.org/10.1016/j.nima.2022.166605>.
- (118) Prinz, N.; Strübbe, S.; Bauer, M.; Zobel, M. *Structural transitions during Ni nanoparticle formation by decomposition of a Ni-containing metal–organic framework using in situ total scattering*, *New Journal of Chemistry* 47, 24, **2023**, DOI: <https://doi.org/10.1039/D3NJ00493G>.
- (119) Testemale, D.; Pokrovski, G. S.; Lahera, E.; Prat, A.; Kieffer, I.; Delnet, W.; Proux, O.; Louvel, M.; Sanchez-Valle, C.; Hazemann, J. L. *In situ X-ray absorption spectroscopy using the FAME autoclave: a window into fluid–mineral–melt interactions in the Earth’s crust*, *High Pressure Research* 44, 3, **2024**, DOI: <https://doi.org/10.1080/08957959.2024.2380916>.
- (120) Kim, D.; Lee, N.; Park, M.; Kim, B. H.; An, K.; Hyeon, T. *Synthesis of Uniform Ferrimagnetic Magnetite Nanocubes*, *Journal of the American Chemical Society* 131, 2, **2009**, DOI: <https://doi.org/10.1021/ja8086906>.
- (121) Fantechi, E.; Roca, A. G.; Sepúlveda, B.; Torruella, P.; Estradé, S.; Peiró, F.; Coy, E.; Jurga, S.; Bastús, N. G.; Nogués, J.; Puntes, V. *Seeded Growth Synthesis of Au-Fe₃O₄ Heterostructured Nanocrystals: Rational Design and Mechanistic Insights*, *Chemistry of Materials* 29, 9, **2017**, DOI: <https://doi.org/10.1021/acs.chemmater.7b00608>.
- (122) Nobile, C.; Cozzoli, P. D. *Synthetic Approaches to Colloidal Nanocrystal Heterostructures Based on Metal and Metal-Oxide Materials*, *Nanomaterials* 12, 10, **2022**, DOI: <https://doi.org/10.3390/nano12101729>.

-
- (123) Niederberger, M.; Garnweitner, G.; Buha, J.; Polleux, J.; Ba, J.; Pinna, N. *Nonaqueous synthesis of metal oxide nanoparticles: Review and indium oxide as case study for the dependence of particle morphology on precursors and solvents*, Journal of Sol-Gel Science and Technology 40, 2, **2006**, DOI: <https://doi.org/10.1007/s10971-006-6668-8>.
- (124) Mikhailova, M. A.; Chernyshov, I. Y.; Illarionov, G. A.; Kolchanov, D. S.; Kuchur, O. A.; Vinogradov, A. V.; Morozova, S. M.; Morozov, M. I. *Revisiting syntheses of Fe₃O₄ nanoparticles in water and lower alcohols and their resistive switching properties*, Journal of Materials Chemistry C 10, 1, **2022**, DOI: <https://doi.org/10.1039/D1TC03825G>.
- (125) Anson, C. E.; Bourke, J. P.; Cannon, R. D.; Jayasooriya, U. A.; Molinier, M.; Powell, A. K. *Crystal Structures of the Isomorphous Prototypic Oxo-Centered Trinuclear Complexes [Cr₃O(OOCCH₃)₆(H₂O)₃]Cl · 6 H₂O and [Fe₃O(OOCCH₃)₆(H₂O)₃]Cl · 6 H₂O*, Inorganic Chemistry 36, 6, **1997**, DOI: <https://doi.org/10.1021/ic960960f>.
- (126) Bauer, M.; Kauf, T.; Christoffers, J.; Bertagnolli, H. *Investigations into the metal species of the homogeneous iron(iii) catalyzed Michael addition reactions*, Physical Chemistry Chemical Physics 7, 13, **2005**, DOI: <https://doi.org/10.1039/b501204j>.
- (127) Levish, A.; Winterer, M. *In situ cell for x-ray absorption spectroscopy of low volatility compound vapors*, Review of Scientific Instruments 91, 6, **2020**, DOI: <https://doi.org/10.1063/5.0006721>.
- (128) Okudera, H.; Yoshiasa, A.; Murai, K.-i.; Okube, M.; Takeda, T.; Kikkawa, S. *Local structure of magnetite and maghemite and chemical shift in Fe K-edge XANES*, Journal of Mineralogical and Petrological Sciences 107, 3, **2012**, DOI: <https://doi.org/10.2465/jmps.110624>.
- (129) Piquer, C.; Laguna-Marco, M. A.; Roca, A. G.; Boada, R.; Guglieri, C.; Chaboy, J. *Fe K-Edge X-ray Absorption Spectroscopy Study of Nanosized Nominal Magnetite*, The Journal of Physical Chemistry C 118, 2, **2014**, DOI: <https://doi.org/10.1021/jp4104992>.
- (130) Jaumot, J.; Gargallo, R.; de Juan, A.; Tauler, R. *A graphical user-friendly interface for MCR-ALS: a new tool for multivariate curve resolution in MATLAB*, Chemometrics and Intelligent Laboratory Systems 76, 1, **2005**, DOI: <https://doi.org/10.1016/j.chemolab.2004.12.007>.
- (131) J. Rehr, J.; J. Kas, J.; D. Vila, F.; P. Prange, M.; Jorissen, K. *Parameter-free calculations of X-ray spectra with FEFF9*, Physical Chemistry Chemical Physics 12, 21, **2010**, DOI: <https://doi.org/10.1039/B926434E>.
- (132) Gauthier, C.; Solé, V. A.; Signorato, R.; Goulon, J.; Mogueiline, E. *The ESRF beamline ID26: X-ray absorption on ultra dilute sample*, Journal of Synchrotron Radiation 6, **1999**, DOI: <https://doi.org/10.1107/S0909049598016835>.
- (133) Glatzel, P.; Harris, A.; Marion, P.; Sikora, M.; Weng, T.-C.; Guilloud, C.; Lafuerza, S.; Rovezzi, M.; Detlefs, B.; Ducotté, L. *The five-analyzer point-to-point scanning crystal spectrometer at ESRF ID26*, Journal of Synchrotron Radiation 28, 1, **2021**, DOI: <https://doi.org/10.1107/S1600577520015416>.
- (134) Newville, M. *Larch: An Analysis Package for XAFS and Related Spectroscopies*, Journal of Physics: Conference Series 430, 1, **2013**, DOI: <https://doi.org/10.1088/1742-6596/430/1/012007>.

- (135) V. Zimmermann, M.; Ivashko, O.; Igoa Saldaña, F.; Liu, J.; Glaevecke, P.; Gutowski, O.; Nowak, R.; Köhler, K.; Winkler, B.; Schöps, A.; Schulte-Schrepping, H.; Dippel, A.-C. *P21.1 at PETRA III – a high-energy X-ray diffraction beamline for physics and chemistry*, *Journal of Synchrotron Radiation* 32, 3, **2025**, DOI: <https://doi.org/10.1107/S1600577525002826>.
- (136) Kieffer, J.; Wright, J. P. *PyFAI: a Python library for high performance azimuthal integration on GPU*, *Powder Diffraction* 28, **2013**, DOI: <https://doi.org/10.1017/S0885715613000924>.
- (137) Sun, W.; Bartel, C. J.; Arca, E.; Bauers, S. R.; Matthews, B.; Orvañanos, B.; Chen, B.-R.; Toney, M. F.; Schelhas, L. T.; Tumas, W.; Tate, J.; Zakutayev, A.; Lany, S.; Holder, A. M.; Ceder, G. *A map of the inorganic ternary metal nitrides*, *Nature Materials* 18, 7, **2019**, DOI: <https://doi.org/10.1038/s41563-019-0396-2>.
- (138) Jamil, R.; Ali, R.; Loomba, S.; Xian, J.; Yousaf, M.; Khan, K.; Shabbir, B.; McConville, C. F.; Mahmood, A.; Mahmood, N. *The role of nitrogen in transition-metal nitrides in electrochemical water splitting*, *Chem Catalysis* 1, 4, **2021**, DOI: <https://doi.org/10.1016/j.checat.2021.06.014>.
- (139) Calais, J.-L. *Band structure of transition metal compounds*, *Advances in Physics* 26, 6, **1977**, DOI: <https://doi.org/10.1080/00018737700101473>.
- (140) Papaconstantopoulos, D. A.; Pickett, W. E.; Klein, B. M.; Boyer, L. L. *Electronic properties of transition-metal nitrides: The group-V and group-VI nitrides VN, NbN, TaN, CrN, MoN, and WN*, *Physical Review B* 31, 2, **1985**, DOI: <https://doi.org/10.1103/PhysRevB.31.752>.
- (141) Lengauer, W.; Eder, A. In *Carbides: Transition Metal Solid State Chemistry*, 2005, DOI: <https://doi.org/10.1002/0470862106.ia156>.
- (142) Xie, J.; Xie, Y. *Transition Metal Nitrides for Electrocatalytic Energy Conversion: Opportunities and Challenges*, *Chemistry – A European Journal* 22, 11, **2016**, DOI: <https://doi.org/10.1002/chem.201501120>.
- (143) Zhong, Y.; Xia, X.; Shi, F.; Zhan, J.; Tu, J.; Fan, H. J. *Transition Metal Carbides and Nitrides in Energy Storage and Conversion*, *Advanced Science* 3, 5, **2016**, DOI: <https://doi.org/10.1002/advs.201500286>.
- (144) Han, Y.; Yue, X.; Jin, Y.; Huang, X.; Shen, P. K. *Hydrogen evolution reaction in acidic media on single-crystalline titanium nitride nanowires as an efficient non-noble metal electrocatalyst*, *Journal of Materials Chemistry A* 4, 10, **2016**, DOI: <https://doi.org/10.1039/C5TA09976E>.
- (145) Vadahanambi, S.; Park, H. *Carbon sheathed molybdenum nitride nanoparticles anchored on reduced graphene oxide as high-capacity sodium-ion battery anodes and supercapacitors*, *New Journal of Chemistry* 42, 8, **2018**, DOI: <https://doi.org/10.1039/C7NJ04764A>.
- (146) Wu, Z.; Wang, H.; Xiong, P.; Li, G.; Qiu, T.; Gong, W.-B.; Zhao, F.; Li, C.; Li, Q.; Wang, G.; Geng, F. *Molecularly Thin Nitride Sheets Stabilized by Titanium Carbide as Efficient Bifunctional Electrocatalysts for Fiber-Shaped Rechargeable Zinc-Air Batteries*, *Nano Letters* 20, 4, **2020**, DOI: <https://doi.org/10.1021/acs.nanolett.0c00717>.
- (147) Xiong, J.; Cai, W.; Shi, W.; Zhang, X.; Li, J.; Yang, Z.; Feng, L.; Cheng, H. *Salt-templated synthesis of defect-rich MoN nanosheets for boosted hydrogen evolution reaction*, *Journal of Materials Chemistry A* 5, 46, **2017**, DOI: <https://doi.org/10.1039/C7TA07566A>.

-
- (148) Liu, B.; He, B.; Peng, H.-Q.; Zhao, Y.; Cheng, J.; Xia, J.; Shen, J.; Ng, T.-W.; Meng, X.; Lee, C.-S.; Zhang, W. *Unconventional Nickel Nitride Enriched with Nitrogen Vacancies as a High-Efficiency Electrocatalyst for Hydrogen Evolution*, *Advanced Science* 5, 8, **2018**, DOI: <https://doi.org/10.1002/advs.201800406>.
- (149) Jin, H.; Li, L.; Liu, X.; Tang, C.; Xu, W.; Chen, S.; Song, L.; Zheng, Y.; Qiao, S.-Z. *Nitrogen Vacancies on 2D Layered W_2N_3 : A Stable and Efficient Active Site for Nitrogen Reduction Reaction*, *Advanced Materials* 31, 32, **2019**, DOI: <https://doi.org/10.1002/adma.201902709>.
- (150) Yan, H.; Tian, C.; Wang, L.; Wu, A.; Meng, M.; Zhao, L.; Fu, H. *Phosphorus-Modified Tungsten Nitride/Reduced Graphene Oxide as a High-Performance, Non-Noble-Metal Electrocatalyst for the Hydrogen Evolution Reaction*, *Angewandte Chemie* 127, 21, **2015**, DOI: <https://doi.org/10.1002/ange.201501419>.
- (151) Chen, Z.; Song, Y.; Cai, J.; Zheng, X.; Han, D.; Wu, Y.; Zang, Y.; Niu, S.; Liu, Y.; Zhu, J.; Liu, X.; Wang, G. *Tailoring the d-Band Centers Enables Co_4N Nanosheets To Be Highly Active for Hydrogen Evolution Catalysis*, *Angewandte Chemie International Edition* 57, 18, **2018**, DOI: <https://doi.org/10.1002/anie.201801834>.
- (152) Song, F.; Li, W.; Yang, J.; Han, G.; Liao, P.; Sun, Y. *Interfacing nickel nitride and nickel boosts both electrocatalytic hydrogen evolution and oxidation reactions*, *Nature Communications* 9, 1, **2018**, DOI: <https://doi.org/10.1038/s41467-018-06728-7>.
- (153) Li, Q.; Zhang, Q.; Sun, J.; Liu, C.; Guo, J.; He, B.; Zhou, Z.; Man, P.; Li, C.; Xie, L.; Yao, Y. *All Hierarchical Core-Shell Heterostructures as Novel Binder-Free Electrode Materials for Ultrahigh-Energy-Density Wearable Asymmetric Supercapacitors*, *Advanced Science* 6, 2, **2019**, DOI: <https://doi.org/10.1002/advs.201801379>.
- (154) Balamurugan, J.; Nguyen, T. T.; Aravindan, V.; Kim, N. H.; Lee, J. H. *Flexible Solid-State Asymmetric Supercapacitors Based on Nitrogen-Doped Graphene Encapsulated Ternary Metal-Nitrides with Ultralong Cycle Life*, *Advanced Functional Materials* 28, 44, **2018**, DOI: <https://doi.org/10.1002/adfm.201804663>.
- (155) Zhu, L.; Chen, Z.; Song, Y.; Wang, P.; Jiang, Y.; Jiang, L.; Zhou, Y.-N.; Hu, L. *Lower ammoniation activation energy of CoN nanosheets by Mn doping with superior energy storage performance for secondary ion batteries*, *Nanoscale* 10, 12, **2018**, DOI: <https://doi.org/10.1039/C7NR08893K>.
- (156) Gao, B.; Li, X.; Ding, K.; Huang, C.; Li, Q.; Chu, P. K.; Huo, K. *Recent progress in nanostructured transition metal nitrides for advanced electrochemical energy storage*, *Journal of Materials Chemistry A* 7, 1, **2019**, DOI: <https://doi.org/10.1039/C8TA05760E>.
- (157) Tareen, A. K.; Priyanga, G. S.; Behara, S.; Thomas, T.; Yang, M. *Mixed ternary transition metal nitrides: A comprehensive review of synthesis, electronic structure, and properties of engineering relevance*, *Progress in Solid State Chemistry* 53, **2019**, DOI: <https://doi.org/10.1016/j.progsolidstchem.2018.11.001>.
- (158) Paredes, P.; Rauwel, E.; Rauwel, P. *Surveying the Synthesis, Optical Properties and Photocatalytic Activity of Cu_3N Nanomaterials*, *Nanomaterials* 12, 13, **2022**, DOI: <https://doi.org/10.3390/nano12132218>.
- (159) Hahn, U.; Weber, W. *Electronic structure and chemical-bonding mechanism of Cu_3N , Cu_3NPd , and related $Cu(I)$ compounds*, *Physical Review B* 53, 19, **1996**, DOI: <https://doi.org/10.1103/PhysRevB.53.12684>.

- (160) Ji, A.; Yun, D.; Gao, L.; Cao, Z. *Crystalline thin films of stoichiometric Cu_3N and intercalated Cu_3NM_x ($M = \text{metals}$): Growth and physical properties*, *physica status solidi (a)* 207, 12, **2010**, DOI: <https://doi.org/10.1002/pssa.201026449>.
- (161) Cui, X. Y.; Soon, A.; Phillips, A. E.; Zheng, R. K.; Liu, Z. W.; Delley, B.; Ringer, S. P.; Stampfl, C. *First principles study of 3d transition metal doped Cu_3N* , *Journal of Magnetism and Magnetic Materials* 324, 19, **2012**, DOI: <https://doi.org/10.1016/j.jmmm.2012.05.021>.
- (162) Caskey, C. M.; Richards, R. M.; Ginley, D. S.; Zakutayev, A. *Thin film synthesis and properties of copper nitride, a metastable semiconductor*, *Materials Horizons* 1, 4, **2014**, DOI: <https://doi.org/10.1039/C4MH00049H>.
- (163) Jiang, A. *Preparation, structure, properties, and application of copper nitride (Cu_3N) thin films: A review*, *Journal of Materials Science*, **2018**.
- (164) Yu, R.; Weng, H.; Fang, Z.; Dai, X.; Hu, X. *Topological Node-Line Semimetal and Dirac Semimetal State in Antiperovskite Cu_3N* , *Physical Review Letters* 115, 3, **2015**, DOI: <https://doi.org/10.1103/PhysRevLett.115.036807>.
- (165) Quintela, C. X.; Campbell, N.; Shao, D. F.; Irwin, J.; Harris, D. T.; Xie, L.; Anderson, T. J.; Reiser, N.; Pan, X. Q.; Tsymbal, E. Y.; Rzechowski, M. S.; Eom, C. B. *Epitaxial thin films of Dirac semimetal antiperovskite Cu_3N* , *APL Materials* 5, 9, **2017**, DOI: <https://doi.org/10.1063/1.4992006>.
- (166) Wang, X.; Chen, J.; Xie, D. *Prospect of Node-Line Semimetal Cu_3N to Be a Topological Superconductor*, *Journal of Superconductivity and Novel Magnetism* 30, 10, **2017**, DOI: <https://doi.org/10.1007/s10948-017-4133-2>.
- (167) Yao, K.; Fang, Z.; Wang, J.; Wang, W.; Wang, M.; Yan, W.; Ye, M.; Jiang, B.; Wu, K.; Wei, X. *Regulating charge distribution of Cu_3PdN nanocrystals for nitrate electroreduction to ammonia*, *Chemical Communications* 59, 81, **2023**, DOI: <https://doi.org/10.1039/D3CC02791K>.
- (168) Jia, J.; Hao, X.; Chang, Y.; Jia, M.; Wen, Z. *Rational design of Cu_3PdN nanocrystals for selective electroreduction of carbon dioxide to formic acid*, *Journal of Colloid and Interface Science* 586, **2021**, DOI: <https://doi.org/10.1016/j.jcis.2020.10.112>.
- (169) Li, T.; Wang, J.; Zhu, S.; Delmo, E. P.; Sun, F.; Zhang, L.; Gu, M.; Shao, M. *Cu_3N nanocrystals for efficient CO_2 electrochemical reduction to methane*, *Electrochimica Acta* 371, **2021**, DOI: <https://doi.org/10.1016/j.electacta.2021.137793>.
- (170) Vaughn II, D. D.; Araujo, J.; Meduri, P.; Callejas, J. F.; Hickner, M. A.; Schaak, R. E. *Solution Synthesis of Cu_3PdN Nanocrystals as Ternary Metal Nitride Electrocatalysts for the Oxygen Reduction Reaction*, *Chemistry of Materials* 26, 21, **2014**, DOI: <https://doi.org/10.1021/cm5029723>.
- (171) Jia, J.; Shao, M.; Wang, G.; Deng, W.; Wen, Z. *Cu_3PdN nanocrystals electrocatalyst for formic acid oxidation*, *Electrochemistry Communications* 71, **2016**, DOI: <https://doi.org/10.1016/j.elecom.2016.08.009>.
- (172) Lord, R. W.; Holder, C. F.; Fenton, J. L.; Schaak, R. E. *Seeded Growth of Metal Nitrides on Noble-Metal Nanoparticles To Form Complex Nanoscale Heterostructures*, *Chemistry of Materials* 31, 12, **2019**, DOI: <https://doi.org/10.1021/acs.chemmater.9b01638>.
- (173) Sharan, A.; Lany, S. *Computational discovery of stable and metastable ternary oxynitrides*, *The Journal of Chemical Physics* 154, 23, **2021**, DOI: <https://doi.org/10.1063/5.0050356>.

-
- (174) Zakutayev, A. *Synthesis of Zn_2NbN_3 ternary nitride semiconductor with wurtzite-derived crystal structure*, *Journal of Physics: Condensed Matter* 33, 35, **2021**, DOI: <https://doi.org/10.1088/1361-648X/abfab3>.
- (175) Rom, C. L.; Smaha, R. W.; Melamed, C. L.; Schnepf, R. R.; Heinselman, K. N.; Mangum, J. S.; Lee, S.-J.; Lany, S.; Schelhas, L. T.; Greenaway, A. L.; Neilson, J. R.; Bauers, S. R.; Tamboli, A. C.; Andrew, J. S. *Combinatorial Synthesis of Cation-Disordered Manganese Tin Nitride $MnSnN_2$ Thin Films with Magnetic and Semiconducting Properties*, *Chemistry of Materials* 35, 7, **2023**, DOI: <https://doi.org/10.1021/acs.chemmater.2c03826>.
- (176) Glatzel, P.; Bergmann, U. *High resolution 1s core hole X-ray spectroscopy in 3d transition metal complexes—electronic and structural information*, *Coordination Chemistry Reviews* 249, 1, **2005**, DOI: <https://doi.org/10.1016/j.ccr.2004.04.011>.
- (177) Fornasini, P. In *Synchrotron Radiation: Basics, Methods and Applications*, Mobilio, S., Boscherini, F., Meneghini, C., Eds.; Springer: Berlin, Heidelberg, 2015, DOI: https://doi.org/10.1007/978-3-642-55315-8_6.
- (178) Bijani, S.; Gabás, M.; Subías, G.; García, J.; Sánchez, L.; Morales, J.; Martínez, L.; R. Ramos-Barrado, J. *XAS study of the reversible reactivity mechanism of micro- and nanostructured electrodeposited Cu_2O thin films towards lithium*, *Journal of Materials Chemistry* 21, 14, **2011**, DOI: <https://doi.org/10.1039/C0JM03565C>.
- (179) Xu, H.; Yamaguchi, S.; Mitsudome, T.; Mizugaki, T. *A copper nitride nanocube catalyst for highly efficient hydroboration of alkynes*, *Organic & Biomolecular Chemistry* 21, 7, **2023**, DOI: <https://doi.org/10.1039/D2OB02130G>.
- (180) Mijit, E.; Durandurdu, M.; Rodrigues, J. E. F. S.; Trapananti, A.; Rezvani, S. J.; Rosa, A. D.; Mathon, O.; Irifune, T.; Di Cicco, A. *Structural and electronic transformations of $GeSe_2$ glass under high pressures studied by X-ray absorption spectroscopy*, *Proceedings of the National Academy of Sciences of the United States of America* 121, 14, **2024**, DOI: <https://doi.org/10.1073/pnas.2318978121>.
- (181) Kopula Kesavan, J.; d'Acapito, F.; Scardi, P.; Stavrinadis, A.; Akgul, M. Z.; Burgués-Ceballos, I.; Konstantatos, G.; Boscherini, F. *Cation Disorder and Local Structural Distortions in $Ag_xBi_{1-x}S_2$ Nanoparticles*, *Nanomaterials* 10, 2, **2020**, DOI: <https://doi.org/10.3390/nano10020316>.
- (182) Schnepf, R. R.; Cordell, J. J.; Tellekamp, M. B.; Melamed, C. L.; Greenaway, A. L.; Mis, A.; Brennecka, G. L.; Christensen, S.; Tucker, G. J.; Toberer, E. S.; Lany, S.; Tamboli, A. C. *Utilizing Site Disorder in the Development of New Energy-Relevant Semiconductors*, *ACS Energy Letters* 5, 6, **2020**, DOI: <https://doi.org/10.1021/acsenergylett.0c00576>.
- (183) Fioretti, A. N.; Zakutayev, A.; Moutinho, H.; Melamed, C.; Perkins, J. D.; Norman, A. G.; Al-Jassim, M.; Toberer, E. S.; Tamboli, A. C. *Combinatorial insights into doping control and transport properties of zinc tin nitride*, *Journal of Materials Chemistry C* 3, 42, **2015**, DOI: <https://doi.org/10.1039/C5TC02663F>.
- (184) Melamed, C. L.; Pan, J.; Mis, A.; Heinselman, K.; Schnepf, R. R.; Woods-Robinson, R.; Cordell, J. J.; Lany, S.; Toberer, E. S.; Tamboli, A. C. *Combinatorial investigation of structural and optical properties of cation-disordered $ZnGeN_2$* , *Journal of Materials Chemistry C* 8, 26, **2020**, DOI: <https://doi.org/10.1039/D0TC01675F>.

- (185) Schnepf, R. R.; Levy-Wendt, B. L.; Tellekamp, M. B.; Ortiz, B. R.; Melamed, C. L.; Schelhas, L. T.; Stone, K. H.; Toney, M. F.; Toberer, E. S.; Tamboli, A. C. *Using resonant energy X-ray diffraction to extract chemical order parameters in ternary semiconductors*, *Journal of Materials Chemistry C* 8, 13, **2020**, DOI: <https://doi.org/10.1039/C9TC06699C>.
- (186) Huang, J.; Kang, J. *Cation disorder in MgSnN₂ and its effects on the electronic properties*, *Physical Review Materials* 8, 7, **2024**, DOI: <https://doi.org/10.1103/PhysRevMaterials.8.074604>.
- (187) Łopuszyński, M.; Majewski, J. A. *Ordering in ternary nitride semiconducting alloys*, *Physical Review B* 85, 3, **2012**, DOI: <https://doi.org/10.1103/PhysRevB.85.035211>.
- (188) Zhuk, S.; Kistanov, A. A.; Boehme, S. C.; Ott, N.; La Mattina, F.; Stiefel, M.; Kovalenko, M. V.; Siol, S. *Synthesis and Characterization of the Ternary Nitride Semiconductor Zn₂VN₃: Theoretical Prediction, Combinatorial Screening, and Epitaxial Stabilization*, *Chemistry of Materials* 33, 23, **2021**, DOI: <https://doi.org/10.1021/acs.chemmater.1c03025>.
- (189) Sirotti, E.; Wagner, L. I.; Jiang, C.-M.; Eichhorn, J.; Munnik, F.; Streibel, V.; Schilcher, M. J.; März, B.; Hegner, F. S.; Kuhl, M.; Höldrich, T.; Müller-Caspary, K.; Egger, D. A.; Sharp, I. D. *Beyond Cation Disorder: Site Symmetry-Tuned Optoelectronic Properties of the Ternary Nitride Photoabsorber ZrTaN₃*, *Advanced Energy Materials* 14, DOI: <https://doi.org/10.1002/aenm.202402540>.
- (190) Christian, T. M.; Beaton, D. A.; Mukherjee, K.; Alberi, K.; Fitzgerald, E. A.; Mascarenhas, A. *Amber-green light-emitting diodes using order-disorder Al_xIn_{1-x}P heterostructures*, *Journal of Applied Physics* 114, 7, **2013**, DOI: <https://doi.org/10.1063/1.4818477>.
- (191) Greenaway, A. L.; Melamed, C. L.; Tellekamp, M. B.; Woods-Robinson, R.; Toberer, E. S.; Neilson, J. R.; Tamboli, A. C. *Ternary Nitride Materials: Fundamentals and Emerging Device Applications*, *Annual Review of Materials Research* 51, 1, **2021**, DOI: <https://doi.org/10.1146/annurev-matsci-080819-012444>.
- (192) Geoghegan, B. L.; Liu, Y.; Peredkov, S.; Dechert, S.; Meyer, F.; DeBeer, S.; Cutsail, G. E. I. *Combining Valence-to-Core X-ray Emission and Cu K-edge X-ray Absorption Spectroscopies to Experimentally Assess Oxidation State in Organometallic Cu(I)/(II)/(III) Complexes*, *Journal of the American Chemical Society* 144, 6, **2022**, DOI: <https://doi.org/10.1021/jacs.1c09505>.
- (193) Wang, J.; Hsu, C.-S.; Wu, T.-S.; Chan, T.-S.; Suen, N.-T.; Lee, J.-F.; Chen, H. M. *In situ X-ray spectroscopies beyond conventional X-ray absorption spectroscopy on deciphering dynamic configuration of electrocatalysts*, *Nature Communications* 14, **2023**, DOI: <https://doi.org/10.1038/s41467-023-42370-8>.
- (194) Kau, L. S.; Spira-Solomon, D. J.; Penner-Hahn, J. E.; Hodgson, K. O.; Solomon, E. I. *X-ray absorption edge determination of the oxidation state and coordination number of copper. Application to the type 3 site in Rhus vernicifera laccase and its reaction with oxygen*, *Journal of the American Chemical Society* 109, 21, **1987**, DOI: <https://doi.org/10.1021/ja00255a032>.
- (195) Chaboy, J.; Muñoz-Páez, A.; Carrera, F.; Merklings, P.; Marcos, E. S. *Ab initio x-ray absorption study of copper K-edge XANES spectra in Cu(II) compounds*, *Physical Review B* 71, 13, **2005**, DOI: <https://doi.org/10.1103/PhysRevB.71.134208>.

-
- (196) Becker, S.; Behrens, U.; Schindler, S. *Synthesis, Structure and Reactivity of the Compound $[Cu(C_7H_7NH_2)Cl]_4$ derived from CuCl and Benzylamine ($C_7H_7NH_2$)*, *Zeitschrift für anorganische und allgemeine Chemie* 641, 2, **2015**, DOI: <https://doi.org/10.1002/zaac.201400395>.
- (197) Yin, X.; Shi, M.; Kwok, K. S.; Zhao, H.; Gray, D. L.; Bertke, J. A.; Yang, H. *Dish-like higher-ordered palladium nanostructures through metal ion-ligand complexation*, *Nano Research* 11, 6, **2018**, DOI: <https://doi.org/10.1007/s12274-018-1993-0>.
- (198) Anantharaj, S.; Ede, S. R.; Sakthikumar, K.; Karthick, K.; Mishra, S.; Kundu, S. *Recent Trends and Perspectives in Electrochemical Water Splitting with an Emphasis on Sulfide, Selenide, and Phosphide Catalysts of Fe, Co, and Ni: A Review*, *ACS Catalysis* 6, 12, **2016**, DOI: <https://doi.org/10.1021/acscatal.6b02479>.
- (199) Shinagawa, T.; Garcia-Esparza, A. T.; Takanebe, K. *Insight on Tafel slopes from a microkinetic analysis of aqueous electrocatalysis for energy conversion*, *Scientific Reports* 5, 1, **2015**, DOI: <https://doi.org/10.1038/srep13801>.
- (200) Ma, Z.; Li, Z.; Li, S.; Li, P.; Zhang, H. *Nanostructured Ni_2 thin films magnetron-sputtered on nickel foam as efficient electrocatalyst for hydrogen evolution reaction*, *Materials Letters* 229, **2018**, DOI: <https://doi.org/10.1016/j.matlet.2018.07.016>.
- (201) Yan, H.; Xie, Y.; Jiao, Y.; Wu, A.; Tian, C.; Zhang, X.; Wang, L.; Fu, H. *Holey Reduced Graphene Oxide Coupled with an Mo_2-Mo_2 Heterojunction for Efficient Hydrogen Evolution*, *Advanced Materials* 30, 2, **2018**, DOI: <https://doi.org/10.1002/adma.201704156>.
- (202) Cheng, R.; He, H.; Pu, Z.; Amiin, I. S.; Chen, L.; Wang, Z.; Li, G.; Mu, S. *Shrunken hollow Mo-N/Mo-C nanosphere structure for efficient hydrogen evolution in a broad pH range*, *Electrochimica Acta* 298, **2019**, DOI: <https://doi.org/10.1016/j.electacta.2018.12.128>.
- (203) Wang, W.; Liu, C.; Zhou, D.; Yang, L.; Zhou, J.; Yang, D. *In-situ synthesis of coupled molybdenum carbide and molybdenum nitride as electrocatalyst for hydrogen evolution reaction*, *Journal of Alloys and Compounds* 792, **2019**, DOI: <https://doi.org/10.1016/j.jallcom.2019.03.397>.
- (204) Cao, B.; Veith, G. M.; Neufeind, J. C.; Adzic, R. R.; Khalifah, P. G. *Mixed Close-Packed Cobalt Molybdenum Nitrides as Non-noble Metal Electrocatalysts for the Hydrogen Evolution Reaction*, *Journal of the American Chemical Society* 135, 51, **2013**, DOI: <https://doi.org/10.1021/ja4081056>.
- (205) Zhao, Y.; Kamiya, K.; Hashimoto, K.; Nakanishi, S. *Hydrogen Evolution by Tungsten Carbonitride Nanoelectrocatalysts Synthesized by the Formation of a Tungsten Acid/Polymer Hybrid In Situ*, *Angewandte Chemie International Edition* 52, 51, **2013**, DOI: <https://doi.org/10.1002/anie.201307527>.
- (206) Ma, L.; Ting, L. R. L.; Molinari, V.; Giordano, C.; Yeo, B. S. *Efficient hydrogen evolution reaction catalyzed by molybdenum carbide and molybdenum nitride nanocatalysts synthesized via the urea glass route*, *Journal of Materials Chemistry A* 3, 16, **2015**, DOI: <https://doi.org/10.1039/C5TA00139K>.
- (207) Shi, J.; Pu, Z.; Liu, Q.; Asiri, A. M.; Hu, J.; Sun, X. *Tungsten nitride nanorods array grown on carbon cloth as an efficient hydrogen evolution cathode at all pH values*, *Electrochimica Acta* 154, **2015**, DOI: <https://doi.org/10.1016/j.electacta.2014.12.096>.

- (208) Wang, Y.; Liu, D.; Liu, Z.; Xie, C.; Huo, J.; Wang, S. *Porous cobalt-iron nitride nanowires as excellent bifunctional electrocatalysts for overall water splitting*, *Chemical Communications* 52, 85, **2016**, DOI: <https://doi.org/10.1039/c6cc06608a>.
- (209) Jia, X.; Zhao, Y.; Chen, G.; Shang, L.; Shi, R.; Kang, X.; Waterhouse, G. I. N.; Wu, L.-Z.; Tung, C.-H.; Zhang, T. *Ni₃N Nanoparticles Derived from Ultrathin NiFe-Layered Double Hydroxide Nanosheets: An Efficient Overall Water Splitting Electrocatalyst*, *Advanced Energy Materials* 6, 10, **2016**, DOI: <https://doi.org/10.1002/aenm.201502585>.
- (210) Chen, Q.; Wang, R.; Yu, M.; Zeng, Y.; Lu, F.; Kuang, X.; Lu, X. *Bifunctional Iron–Nickel Nitride Nanoparticles as Flexible and Robust Electrode for Overall Water Splitting*, *Electrochimica Acta* 247, **2017**, DOI: <https://doi.org/10.1016/j.electacta.2017.07.025>.
- (211) Han, L.; Feng, K.; Chen, Z. *Self-Supported Cobalt Nickel Nitride Nanowires Electrode for Overall Electrochemical Water Splitting*, *Energy Technology* 5, 11, **2017**, DOI: <https://doi.org/10.1002/ente.201700108>.
- (212) Shanker, G. S.; Markad, G. B.; Jagadeeswararao, M.; Bansode, U.; Nag, A. *Colloidal Nanocomposite of TiN and N-Doped Few-Layer Graphene for Plasmonics and Electrocatalysis*, *ACS Energy Letters* 2, 10, **2017**, DOI: <https://doi.org/10.1021/acsenergylett.7b00741>.
- (213) Song, Y.-J.; Yuan, Z.-Y. *One-pot Synthesis of Mo₂/NC Catalysts with Enhanced Electrocatalytic Activity for Hydrogen Evolution Reaction*, *Electrochimica Acta* 246, **2017**, DOI: <https://doi.org/10.1016/j.electacta.2017.06.086>.
- (214) Xie, L.; Qu, F.; Liu, Z.; Ren, X.; Hao, S.; Ge, R.; Du, G.; Asiri, A. M.; Sun, X.; Chen, L. *In situ formation of a 3D core/shell structured Ni₃N@Ni–Bi nanosheet array: an efficient non-noble-metal bifunctional electrocatalyst toward full water splitting under near-neutral conditions*, *Journal of Materials Chemistry A* 5, 17, **2017**, DOI: <https://doi.org/10.1039/C7TA02333B>.
- (215) Wang, C.; Shi, H.; Liu, H.; Fu, J.; Wei, D.; Zeng, W.; Wan, Q.; Zhang, G.; Duan, H. *Quasi-atomic-scale platinum anchored on porous titanium nitride nanorod arrays for highly efficient hydrogen evolution*, *Electrochimica Acta* 292, **2018**, DOI: <https://doi.org/10.1016/j.electacta.2018.10.011>.
- (216) Wei, B.; Tang, G.; Liang, H.; Qi, Z.; Zhang, D.; Hu, W.; Shen, H.; Wang, Z. *Bimetallic vanadium-molybdenum nitrides using magnetron co-sputtering as alkaline hydrogen evolution catalyst*, *Electrochemistry Communications* 93, **2018**, DOI: <https://doi.org/10.1016/j.elecom.2018.07.012>.
- (217) Hu, H.; Chang, B.; Sun, X.; Huo, Q.; Zhang, B.; Li, Y.; Shao, Y.; Zhang, L.; Wu, Y.; Hao, X. *Intrinsic Properties of Macroscopically Tuned Gallium Nitride Single-Crystalline Facets for Electrocatalytic Hydrogen Evolution*, *Chemistry – A European Journal* 25, 44, **2019**, DOI: <https://doi.org/10.1002/chem.201901395>.
- (218) Lai, J.; Huang, B.; Chao, Y.; Chen, X.; Guo, S. *Strongly Coupled Nickel–Cobalt Nitrides/Carbon Hybrid Nanocages with Pt-Like Activity for Hydrogen Evolution Catalysis*, *Advanced Materials* 31, 2, **2019**, DOI: <https://doi.org/10.1002/adma.201805541>.
- (219) Song, F.; Li, W.; Yang, J.; Han, G.; Yan, T.; Liu, X.; Rao, Y.; Liao, P.; Cao, Z.; Sun, Y. *Interfacial Sites between Cobalt Nitride and Cobalt Act as Bifunctional Catalysts for Hydrogen Electrochemistry*, *ACS Energy Letters* 4, 7, **2019**, DOI: <https://doi.org/10.1021/acsenergylett.9b00738>.

-
- (220) Wang, C.; Sun, Y.; Tian, E.; Fu, D.; Zhang, M.; Zhao, X.; Ye, W. *Easy access to trace-loading of Pt on inert Ni₃N nanoparticles with significantly improved hydrogen evolution activity at entire pH values*, *Electrochimica Acta* 320, **2019**, DOI: <https://doi.org/10.1016/j.electacta.2019.134597>.
- (221) Yang, H.; Hu, Y.; Huang, D.; Xiong, T.; Li, M.; Balogun, M.-S.; Tong, Y. *Efficient hydrogen and oxygen evolution electrocatalysis by cobalt and phosphorus dual-doped vanadium nitride nanowires*, *Materials Today Chemistry* 11, **2019**, DOI: <https://doi.org/10.1016/j.mtchem.2018.10.004>.
- (222) Zhang, N.; Cao, L.; Feng, L.; Huang, J.; Kajiyoshi, K.; Li, C.; Liu, Q.; Yang, D.; He, J. *Co,N-Codoped porous vanadium nitride nanoplates as superior bifunctional electrocatalysts for hydrogen evolution and oxygen reduction reactions*, *Nanoscale* 11, **2019**.
- (223) Rosa, A. D.; Garbarino, G.; Rodrigues, J. E.; Mijit, E.; Jacobs, J.; Bugnazet, D.; Pasternak, S.; Berruyer, G.; Moyne, A.; Clavel, C.; Perrin, F.; Anzellini, S.; Meneghini, C.; Ocelli, F.; Zhan, X.; Ishimatsu, N.; Sakai, T.; Boccato, S.; Torchio, R.; Hernandez, J.-A.; Heath, C. J. S.; Dominijanni, S.; Morard, G.; Antonangeli, D.; Petitdemange, S.; Wehinger, B.; Mezouar, M.; Kovalskii, G.; Morgenroth, W.; Wilke, M.; Di Cicco, A.; Bouhifd, M. A.; Irifune, T.; Lomachenko, K. A.; Mathon, O. *New opportunities for high pressure X-ray absorption spectroscopy at ID24-DCM and BM23 with the Extremely Brilliant Source of the ESRF*, *High Pressure Research* 44, 3, **2024**, DOI: <https://doi.org/10.1080/08957959.2024.2364281>.
- (224) Zhang, H.; Li, X.; Hähnel, A.; Naumann, V.; Lin, C.; Azimi, S.; Schweizer, S. L.; Maijenburg, A. W.; Wehrspohn, R. B. *Bifunctional Heterostructure Assembly of NiFe LDH Nanosheets on NiCoP Nanowires for Highly Efficient and Stable Overall Water Splitting*, *Advanced Functional Materials* 28, 14, **2018**, DOI: <https://doi.org/10.1002/adfm.201706847>.
- (225) Koziej, D.; Jagadesh KOPULA KESAVAN; KLEMEYER, L.; REBBER, M. N.; Sani HAROUNA-MAYER; GRÖNE, T. L. R. *In situ photon-in photon-out spectroscopy measurements on ultra-small Cu₃N nanoparticles*, in collab. with GLATZEL, P., 2023, DOI: <https://doi.org/10.15151/ESRF-ES-657465136>.
- (226) Solé, V. A.; Papillon, E.; Cotte, M.; Walter, P.; Susini, J. *A multiplatform code for the analysis of energy-dispersive X-ray fluorescence spectra*, *Spectrochimica Acta Part B: Atomic Spectroscopy* 62, 1, **2007**, DOI: <https://doi.org/10.1016/j.sab.2006.12.002>.
- (227) Reuter, J. A.; Menzel, M. *SLIX: A Python package for fully automated evaluation of Scattered Light Imaging measurements on brain tissue*, *Journal of Open Source Software* 5, 54, **2020**, DOI: <https://doi.org/10.21105/joss.02675>.
- (228) Eilers, P. H. C. *A Perfect Smoother*, *Analytical Chemistry* 75, 14, **2003**, DOI: <https://doi.org/10.1021/ac034173t>.
- (229) Harris, C. R.; Millman, K. J.; van der Walt, S. J.; Gommers, R.; Virtanen, P.; Cournapeau, D.; Wieser, E.; Taylor, J.; Berg, S.; Smith, N. J.; Kern, R.; Picus, M.; Hoyer, S.; van Kerkwijk, M. H.; Brett, M.; Haldane, A.; Del Río, J. F.; Wiebe, M.; Peterson, P.; Gérard-Marchant, P.; Sheppard, K.; Reddy, T.; Weckesser, W.; Abbasi, H.; Gohlke, C.; Oliphant, T. E. *Array programming with NumPy*, *Nature* 585, 7825, **2020**, DOI: <https://doi.org/10.1038/s41586-020-2649-2>.

- (230) Virtanen, P.; Gommers, R.; Oliphant, T. E.; Haberland, M.; Reddy, T.; Cournapeau, D.; Burovski, E.; Peterson, P.; Weckesser, W.; Bright, J.; van der Walt, S. J.; Brett, M.; Wilson, J.; Millman, K. J.; Mayorov, N.; Nelson, A. R. J.; Jones, E.; Kern, R.; Larson, E.; Carey, C. J.; Polat, İ.; Feng, Y.; Moore, E. W.; VanderPlas, J.; Laxalde, D.; Perktold, J.; Cimrman, R.; Henriksen, I.; Quintero, E. A.; Harris, C. R.; Archibald, A. M.; Ribeiro, A. H.; Pedregosa, F.; van Mulbregt, P. *SciPy 1.0: fundamental algorithms for scientific computing in Python*, *Nature Methods* 17, 3, **2020**, DOI: <https://doi.org/10.1038/s41592-019-0686-2>.
- (231) Ravel, B.; Newville, M. *ATHENA, ARTEMIS, HEPHAESTUS: data analysis for X-ray absorption spectroscopy using IFFFIT*, *Journal of Synchrotron Radiation* 12, **2005**, DOI: <https://doi.org/10.1107/S0909049505012719>.
- (232) Juan, A. d.; Jaumot, J.; Tauler, R. *Multivariate Curve Resolution (MCR). Solving the mixture analysis problem*, *Analytical Methods* 6, 14, **2014**, DOI: <https://doi.org/10.1039/C4AY00571F>.
- (233) Jaumot, J.; de Juan, A.; Tauler, R. *MCR-ALS GUI 2.0: New features and applications*, *Chemometrics and Intelligent Laboratory Systems* 140, **2015**, DOI: <https://doi.org/10.1016/j.chemolab.2014.10.003>.
- (234) Windig, W.; Stephenson, D. A. *Self-modeling mixture analysis of second-derivative near-infrared spectral data using the SIMPLISMA approach*, *Analytical Chemistry* 64, 22, **1992**, DOI: <https://doi.org/10.1021/ac00046a015>.
- (235) Juhás, P.; Davis, T.; Farrow, C. L.; Billinge, S. J. L. *PDFgetX3: a rapid and highly automatable program for processing powder diffraction data into total scattering pair distribution functions*, *Journal of Applied Crystallography* 46, 2, **2013**, DOI: <https://doi.org/10.1107/S0021889813005190>.
- (236) Wu, K.-J.; Tse, E. C.; Shang, C.; Guo, Z. *Nucleation and growth in solution synthesis of nanostructures – From fundamentals to advanced applications*, *Progress in Materials Science* 123, **2022**, DOI: <https://doi.org/10.1016/j.pmatsci.2021.100821>.
- (237) Fu, H.; Gao, X.; Zhang, X.; Ling, L. *Recent Advances in Nonclassical Crystallization: Fundamentals, Applications, and Challenges*, *Crystal Growth & Design* 22, 2, **2022**, DOI: <https://doi.org/10.1021/acs.cgd.1c01084>.
- (238) Gebauer, D.; Gale, J. D.; Cölfen, H. *Crystal Nucleation and Growth of Inorganic Ionic Materials from Aqueous Solution: Selected Recent Developments, and Implications*, *Small* 18, 28, **2022**, DOI: <https://doi.org/10.1002/smll.202107735>.
- (239) Du, J. S.; Bae, Y.; De Yoreo, J. J. *Non-classical crystallization in soft and organic materials*, *Nature Reviews Materials* 9, 4, **2024**, DOI: <https://doi.org/10.1038/s41578-023-00637-y>.
- (240) Wang, X.; Li, K.; Qin, X.; Li, M.; Liu, Y.; An, Y.; Yang, W.; Chen, M.; Ouyang, J.; Gong, J. *Research on Mesoscale Nucleation and Growth Processes in Solution Crystallization: A Review*, *Crystals* 12, 9, **2022**, DOI: <https://doi.org/10.3390/cryst12091234>.
- (241) Whitehead, C. B.; Finke, R. G. *Particle formation mechanisms supported by in situ synchrotron XAFS and SAXS studies: a review of metal, metal-oxide, semiconductor and selected other nanoparticle formation reactions*, *Materials Advances* 2, 20, **2021**, DOI: <https://doi.org/10.1039/D1MA00222H>.
- (242) Bols, M. L.; Ma, J.; Rammal, F.; Plessers, D.; Wu, X.; Navarro-Jaén, S.; Heyer, A. J.; Sels, B. F.; Solomon, E. I.; Schoonheydt, R. A. *In Situ UV-Vis-NIR Absorption Spectroscopy and Catalysis*, *Chemical Reviews* 124, 5, **2024**, DOI: <https://doi.org/10.1021/acs.chemrev.3c00602>.

-
- (243) Jia, Z.; Li, J.; Gao, L.; Yang, D.; Kanaev, A. *Dynamic Light Scattering: A Powerful Tool for In Situ Nanoparticle Sizing*, *Colloids and Interfaces* 7, 1, **2023**, DOI: <https://doi.org/10.3390/colloids7010015>.
- (244) Ilett, M.; Afzali, M.; Abdulkarim, B.; Aslam, Z.; Foster, S.; Burgos-Ruiz, M.; Kim, Y.-Y.; Meldrum, F. C.; Drummond-Brydson, R. M. *Studying crystallisation processes using electron microscopy: The importance of sample preparation*, *Journal of Microscopy* 295, 3, **2024**, DOI: <https://doi.org/10.1111/jmi.13300>.
- (245) Chapman, H. N.; Fromme, P.; Barty, A.; White, T. A.; Kirian, R. A.; Aquila, A.; Hunter, M. S.; Schulz, J.; DePonte, D. P.; Weierstall, U.; Doak, R. B.; Maia, F. R. N. C.; Martin, A. V.; Schlichting, I.; Lomb, L.; Coppola, N.; Shoeman, R. L.; Epp, S. W.; Hartmann, R.; Rolles, D.; Rudenko, A.; Foucar, L.; Kimmel, N.; Weidenspointner, G.; Holl, P.; Liang, M.; Barthelmess, M.; Caleman, C.; Boutet, S.; Bogan, M. J.; Krzywinski, J.; Bostedt, C.; Bajt, S.; Gumprecht, L.; Rudek, B.; Erk, B.; Schmidt, C.; Hömke, A.; Reich, C.; Pietschner, D.; Strüder, L.; Hauser, G.; Gorke, H.; Ullrich, J.; Herrmann, S.; Schaller, G.; Schopper, F.; Soltau, H.; Kühnel, K.-U.; Messerschmidt, M.; Bozek, J. D.; Hau-Riege, S. P.; Frank, M.; Hampton, C. Y.; Sierra, R. G.; Starodub, D.; Williams, G. J.; Hajdu, J.; Timneanu, N.; Seibert, M. M.; Andreasson, J.; Røcker, A.; Jönsson, O.; Svenda, M.; Stern, S.; Nass, K.; Andritschke, R.; Schröter, C.-D.; Krasniqi, F.; Bott, M.; Schmidt, K. E.; Wang, X.; Grotjohann, I.; Holton, J. M.; Barends, T. R. M.; Neutze, R.; Marchesini, S.; Fromme, R.; Schorb, S.; Rupp, D.; Adolph, M.; Gorkhover, T.; Andersson, I.; Hirsemann, H.; Potdevin, G.; Graafsma, H.; Nilsson, B.; Spence, J. C. H. *Femtosecond X-ray protein nanocrystallography*, *Nature* 470, 7332, **2011**, DOI: <https://doi.org/10.1038/nature09750>.
- (246) Mancuso, A. P.; Aquila, A.; Batchelor, L.; Bean, R. J.; Bielecki, J.; Borchers, G.; Doerner, K.; Giewekemeyer, K.; Graceffa, R.; Kelsey, O. D.; Kim, Y.; Kirkwood, H. J.; Legrand, A.; Letrun, R.; Manning, B.; Lopez Morillo, L.; Messerschmidt, M.; Mills, G.; Raabe, S.; Reimers, N.; Round, A.; Sato, T.; Schulz, J.; Signe Takem, C.; Sikorski, M.; Stern, S.; Thute, P.; Vagovič, P.; Weinhausen, B.; Tschentscher, T. *The single particles, clusters and biomolecules and serial femtosecond crystallography instrument of the European XFEL: initial installation*, *Synchrotron Radiation* 26, 3, **2019**.
- (247) Bielecki, J.; Hantke, M. F.; Daurer, B. J.; Reddy, H. K. N.; Hasse, D.; Larsson, D. S. D.; Gunn, L. H.; Svenda, M.; Munke, A.; Sellberg, J. A.; Flueckiger, L.; Pietrini, A.; Nettelblad, C.; Lundholm, I.; Carlsson, G.; Okamoto, K.; Timneanu, N.; Westphal, D.; Kulyk, O.; Higashiura, A.; van der Schot, G.; Loh, N.-T. D.; Wysong, T. E.; Bostedt, C.; Gorkhover, T.; Iwan, B.; Seibert, M. M.; Osipov, T.; Walter, P.; Hart, P.; Bucher, M.; Ulmer, A.; Ray, D.; Carini, G.; Ferguson, K. R.; Andersson, I.; Andreasson, J.; Hajdu, J.; Maia, F. R. N. C. *Electrospray sample injection for single-particle imaging with x-ray lasers*, *Science Advances* 5, 5, **2019**.
- (248) Allahgholi, A.; Becker, J.; Delfs, A.; Dinapoli, R.; Göttlicher, P.; Graafsma, H.; Greiffenberg, D.; Hirsemann, H.; Jack, S.; Klyuev, A.; Krüger, H.; Kuhn, M.; Laurus, T.; Marras, A.; Mezza, D.; Mozzanica, A.; Poehlsen, J.; Shefer Shalev, O.; Sheviakov, I.; Schmitt, B.; Schwandt, J.; Shi, X.; Smoljanin, S.; Trunk, U.; Zhang, J.; Zimmer, M. *Megapixels@ Megahertz-The AGIPD high-speed cameras for the European XFEL*, *Nuclear Instruments and Methods in Physics Research Section A: Accelerators, Spectrometers, Detectors and Associated Equipment* 942, **2019**.
- (249) Ayer, K.; Lan, T.-Y.; Elser, V.; Loh, N. D. *Dragonfly: an implementation of the expand-maximize-compress algorithm for single-particle imaging*, *Journal of Applied Crystallography* 49, 4, **2016**, DOI: <https://doi.org/10.1107/S1600576716008165>.

- (250) Loh, N.-T. D.; Elser, V. *Reconstruction algorithm for single-particle diffraction imaging experiments*, Physical Review E—Statistical, Nonlinear, and Soft Matter Physics 80, 2, **2009**.
- (251) Vreshch, V. D.; Yang, J.-H.; Zhang, H.; Filatov, A. S.; Dikarev, E. V. *Monomeric Square-Planar Cobalt(II) Acetylacetonate: Mystery or Mistake?*, Inorganic Chemistry 49, 18, **2010**, DOI: <https://doi.org/10.1021/ic100963r>.
- (252) Chrzanowski, L. S. v.; Lutz, M.; Spek, A. L. *α -Tris(2,4-pentanedionato- κ^2 O,O')cobalt(III) at 240, 210, 180, 150 and 110K*, Acta Crystallographica Section C: Crystal Structure Communications 63, 7, **2007**, DOI: <https://doi.org/10.1107/S0108270107022950>.
- (253) Ogbezode, J. E.; Ezealigo, U. S.; Bello, A.; Anye, V. C.; Onwualu, A. P. *A narrative review of the synthesis, characterization, and applications of iron oxide nanoparticles*, Discover Nano 18, 1, **2023**, DOI: <https://doi.org/10.1186/s11671-023-03898-2>.
- (254) Kumar, S.; Kumar, M.; Singh, A. *Synthesis and characterization of iron oxide nanoparticles (Fe_2O_3 , Fe_3O_4): a brief review*, Contemporary Physics 62, 3, **2021**, DOI: <https://doi.org/10.1080/00107514.2022.2080910>.
- (255) Chaudhari, D.; Panda, G. *A brief overview on iron oxide nanoparticle synthesis, characterization, and applications*, Materials Today: Proceedings, **2023**, DOI: <https://doi.org/10.1016/j.matpr.2023.10.087>.
- (256) Ansari, K.; Ahmad, R.; Tanweer, M. S.; Azam, I. *Magnetic Iron Oxide Nanoparticles as a Tool for the Advancement of Biomedical and Environmental Application: A Review*, Biomedical Materials & Devices 2, 1, **2024**, DOI: <https://doi.org/10.1007/s44174-023-00091-y>.
- (257) Navrotsky, A.; Mazeina, L.; Majzlan, J. *Size-Driven Structural and Thermodynamic Complexity in Iron Oxides*, Science 319, 5870, **2008**, DOI: <https://doi.org/10.1126/science.1148614>.
- (258) Guo, H.; Barnard, A. S. *Naturally occurring iron oxide nanoparticles: morphology, surface chemistry and environmental stability*, J. Mater. Chem. A 1, 1, **2013**, DOI: <https://doi.org/10.1039/C2TA00523A>.
- (259) Kühn, *Tin doped iron oxide electrodes for photoelectrochemical water splitting*, Bachelor thesis, **2023**, Available at: https://www2.physnet.uni-hamburg.de/services/bibliothek/Examensarbeiten/bachelor/___Bachelorarbeiten/K%C3%BChn___Paul___2023.pdf.
- (260) Thompson, N. B.; Mulfort, K. L.; Tiede, D. M. *Toward a quantitative description of solvation structure: a framework for differential solution scattering measurements*, IUCrJ 11, 3, **2024**, DOI: <https://doi.org/10.1107/S2052252524003282>.
- (261) Berry, F. J.; Greaves, C.; Helgason, Ö.; McManus, J. *Synthesis and characterisation of tin-doped iron oxides*, Journal of Materials Chemistry 9, 1, **1999**, DOI: <https://doi.org/10.1039/a803861i>.
- (262) Radoń, A.; Kubacki, J.; Kądziołka-Gaweł, M.; Gębara, P.; Hawełek, Ł.; Topolska, S.; Łukowiec, D. *Structure and magnetic properties of ultrafine superparamagnetic Sn-doped magnetite nanoparticles synthesized by glycol assisted co-precipitation method*, Journal of Physics and Chemistry of Solids 145, **2020**, DOI: <https://doi.org/10.1016/j.jpcs.2020.109530>.
- (263) Lavanya Rathi, P.; Deepa, S. *Structural, magnetic, thermal and optical properties of Sn²⁺ cation doped magnetite nanoparticles*, Ceramics International 46, 3, **2020**, DOI: <https://doi.org/10.1016/j.ceramint.2019.09.294>.

-
- (264) Orlandi, M.; Mazzi, A.; Arban, G.; Bazzanella, N.; Rudatis, P.; Caramori, S.; Patel, N.; Fernandes, R.; Bignozzi, C. A.; Miotello, A. *On the effect of Sn-doping in hematite anodes for oxygen evolution*, *Electrochimica Acta* 214, **2016**, DOI: <https://doi.org/10.1016/j.electacta.2016.08.046>.
- (265) Tian, C. M.; Li, W.-W.; Lin, Y. M.; Yang, Z. Z.; Wang, L.; Du, Y. G.; Xiao, H. Y.; Qiao, L.; Zhang, J. Y.; Chen, L.; Qi, D.-C.; MacManus-Driscoll, J. L.; Zhang, K. H. L. *Electronic Structure, Optical Properties, and Photoelectrochemical Activity of Sn-Doped Fe₂O₃ Thin Films*, *The Journal of Physical Chemistry C* 124, 23, **2020**, DOI: <https://doi.org/10.1021/acs.jpcc.0c02875>.
- (266) Khan, W.; Minar, J.; Khan, S. A.; Asghar, H. *Theoretical analysis of an intermediate band in Sn-doped hematite with wide-spectrum solar response*, *Journal of Solid State Electrochemistry* 25, 2, **2021**, DOI: <https://doi.org/10.1007/s10008-020-04849-y>.
- (267) Hufnagel, A. G.; Hajiyani, H.; Zhang, S.; Li, T.; Kasian, O.; Gault, B.; Breitbach, B.; Bein, T.; Fattakhova-Rohlfing, D.; Scheu, C.; Pentcheva, R. *Why Tin-Doping Enhances the Efficiency of Hematite Photoanodes for Water Splitting—The Full Picture*, *Advanced Functional Materials* 28, 52, **2018**, DOI: <https://doi.org/10.1002/adfm.201804472>.
- (268) Ling, Y.; Li, Y. *Review of Sn-Doped Hematite Nanostructures for Photoelectrochemical Water Splitting*, *Particle & Particle Systems Characterization* 31, 11, **2014**, DOI: <https://doi.org/10.1002/ppsc.201400051>.
- (269) Chandrappa, K. G.; Venkatesha, T. V. *Electrochemical bulk synthesis of Fe₃O₄ and α -Fe₂O₃ nanoparticles and its ZnCo₂Fe₂O₃ composite thin films for corrosion protection*, *Materials and Corrosion* 65, 5, **2014**, DOI: <https://doi.org/10.1002/maco.201206630>.
- (270) Kazeminezhad, I.; Mosivand, S. *Phase Transition of Electrooxidized Fe₃O₄ to γ and α -Fe₂O₃ Nanoparticles Using Sintering Treatment*, *Acta Physica Polonica A* 125, 5, **2014**, DOI: <https://doi.org/10.12693/APhysPolA.125.1210>.
- (271) Widatallah, H. M.; Gismelseed, A. M.; Yousif, A. A.; Al-Rawas, A. D.; Al-Omari, I. A.; Al-Tai, S.; Elzain, M. E.; Johnson, C. *Structural and magnetic analysis of the transformation of Sn-doped magnetite to Sn-doped hematite by mechanical milling*, *Journal of Applied Physics* 97, 10, **2005**, DOI: <https://doi.org/10.1063/1.1850407>.
- (272) Ballester, M.; Marquez, A. P.; Blanco, E.; Manuel, J. M.; Rodriguez-Tapiador, M. I.; Fernandez, S. M.; Willomitzer, F.; Katsaggelos, A. K.; Marquez, E. *Comprehensive Optoelectronic Study of Copper Nitride: Dielectric Function and Bandgap Energies*, *Nanomaterials* 15, 20, **2025**, DOI: <https://doi.org/10.3390/nano15201577>.
- (273) Rodríguez-Tapiador, M. I.; Asensi, J. M.; Roldán, M.; Merino, J.; Bertomeu, J.; Fernández, S. *Copper Nitride: A Versatile Semiconductor with Great Potential for Next-Generation Photovoltaics*, *Coatings* 13, 6, **2023**, DOI: <https://doi.org/10.3390/coatings13061094>.
- (274) Birkett, M.; Savory, C. N.; Fioretti, A. N.; Thompson, P.; Muryn, C. A.; Weerakkody, A. D.; Mitrovic, I. Z.; Hall, S.; Treharne, R.; Dhanak, V. R.; Scanlon, D. O.; Zakutayev, A.; Veal, T. D. *Atypically small temperature-dependence of the direct band gap in the metastable semiconductor copper nitride Cu₃N*, *Physical Review B* 95, 11, **2017**, DOI: <https://doi.org/10.1103/PhysRevB.95.115201>.

- (275) Barauskienė, I.; Valatka, E. *Synthesis, structure and capacitive properties of cobalt hydroxide films on stainless steel substrates*, *Open Chemistry* 12, 11, **2014**, DOI: <https://doi.org/10.2478/s11532-014-0570-y>.
- (276) Thomas, G. S.; Kamath, P. V. *Line broadening in the PXRD patterns of layered hydroxides: The relative effects of crystallite size and structural disorder*, *Journal of Chemical Sciences* 118, 1, **2006**, DOI: <https://doi.org/10.1007/BF02708774>.
- (277) Seeck, O. H.; Murphy, B., *X-Ray Diffraction: Modern Experimental Techniques*, CRC Press, **2015**, ISBN: 978-981-4303-60-6.
- (278) Ryan, B. J.; Roling, L. T.; Panthani, M. G. *Anisotropic Disorder and Thermal Stability of Silicane*, *ACS Nano* 15, 9, **2021**, DOI: <https://doi.org/10.1021/acsnano.1c04230>.
- (279) Weber, D.; Schoop, L. M.; Duppel, V.; Lippmann, J. M.; Nuss, J.; Lotsch, B. V. *Magnetic Properties of Restacked 2D Spin 1/2 honeycomb RuCl₃ Nanosheets*, *Nano Letters* 16, 6, **2016**, DOI: <https://doi.org/10.1021/acs.nanolett.6b00701>.
- (280) Vazquez-Molina, D. A.; Mohammad-Pour, G. S.; Lee, C.; Logan, M. W.; Duan, X.; Harper, J. K.; Uribe-Romo, F. J. *Mechanically Shaped Two-Dimensional Covalent Organic Frameworks Reveal Crystallographic Alignment and Fast Li-Ion Conductivity*, *Journal of the American Chemical Society* 138, 31, **2016**, DOI: <https://doi.org/10.1021/jacs.6b05568>.
- (281) De Siena, M. C.; Creutz, S. E.; Regan, A.; Malinowski, P.; Jiang, Q.; Kluherz, K. T.; Zhu, G.; Lin, Z.; De Yoreo, J. J.; Xu, X.; Chu, J.-H.; Gamelin, D. R. *Two-Dimensional van der Waals Nanoplatelets with Robust Ferromagnetism*, *Nano Letters* 20, 3, **2020**, DOI: <https://doi.org/10.1021/acs.nanolett.0c00102>.
- (282) Favieres, C.; Vergara, J.; Magén, C.; Ibarra, M. R.; Madurga, V. *Building oriented nanosheets in thin films of Co-MT (MT = V, Cr, Cu, Zn, Cd, Hf) and the generation and enhancement of their magnetic anisotropy*, *Journal of Alloys and Compounds* 664, **2016**, DOI: <https://doi.org/10.1016/j.jallcom.2015.12.249>.
- (283) Hocking, R. K.; Gummow, R. J.; King, H. J.; Sabri, M.; Kappen, P.; Dwyer, C.; Chang, S. L. Y. *Direct Formation of 2D-MnO_x under Conditions of Water Oxidation Catalysis*, *ACS Applied Nano Materials* 1, 4, **2018**, DOI: <https://doi.org/10.1021/acsanm.8b00095>.
- (284) Jain, A.; Ong, S. P.; Hautier, G.; Chen, W.; Richards, W. D.; Dacek, S.; Cholia, S.; Gunter, D.; Skinner, D.; Ceder, G.; Persson, K. A. *Commentary: The Materials Project: A materials genome approach to accelerating materials innovation*, *APL Materials* 1, 1, **2013**, DOI: <https://doi.org/10.1063/1.4812323>.
- (285) Sobolev, A. N.; Miminoshvili, E. B.; Miminoshvili, K. E.; Sakvarelidze, T. N. *Cobalt diacetate tetrahydrate*, *Acta Crystallographica Section E: Structure Reports Online* 59, 10, **2003**, DOI: <https://doi.org/10.1107/S1600536803019093>.
- (286) Gordon, T. R.; Cargnello, M.; Paik, T.; Mangolini, F.; Weber, R. T.; Fornasiero, P.; Murray, C. B. *Nonaqueous Synthesis of TiO₂ Nanocrystals Using TiF₄ to Engineer Morphology, Oxygen Vacancy Concentration, and Photocatalytic Activity*, *Journal of the American Chemical Society* 134, 15, **2012**, DOI: <https://doi.org/10.1021/ja300823a>.

List of Abbreviations

acac	acetylacetonate
acacH	acetylacetone
ADP	atomic displacement parameter
AGIPD	Adaptive Gain Integrating Pixel Detector
ATR	attenuated total reflection
ATR-IR	attenuated total reflection infrared
BnNH₂	benzylamine
BnOH	benzyl alcohol
BW	bandwidth
DCM	double-crystal monochromator
DOS	density of states
EC	electrocatalysis
EMC	expand-maximize-compress algorithm
EXAFS	extended X-ray absorption fine structure
FEL	free electron laser
FFT	fast Fourier transformation
FFKM	perfluoro elastomer
FTIR	Fourier transformed infrared
FWHM	full width at half maximum
GC-MS	gas chromatography-mass spectrometry
HER	hydrogen evolution reaction
HERFD-XANES	high-energy resolution fluorescence detected X-ray absorption near-edge structure
HERFD-XAS	high-energy resolution fluorescence detected X-ray absorption spectroscopy
HRTEM	high resolution transmission electron microscopy
IR	infrared
LB	Langmuir-Blodgett
LSV	linear sweep voltammetry
MCR-ALS	multivariate curve resolution by alternating least squares
NC	nanocrystal

NMR nuclear magnetic resonance
NP nanoparticle
OAm oleylamine
OER oxygen evolution reaction
PDF pair distribution function
PEC photoelectrocatalysis
PEEK polyether ether ketone
PTFE polytetrafluoroethylene
PXRD powder X-ray diffraction
RDF radial distribution function
SAXS small-angle X-ray scattering
SAED selected area electron diffraction
SASE self-amplified spontaneous emission
SD standard deviation
SDD sample-to-detector distance
SEM scanning electron microscopy
SNR signal-to-noise ratio
SPB/SFX Single Particles, Clusters and Biomolecules / Serial Femtosecond Crystallography instrument
SPS single particle scattering
SP-SAXS single-particle small-angle X-ray scattering
SP-WAXS single-particle wide-angle X-ray scattering
STEM scanning transmission electron microscopy
TEM transmission electron microscopy
TGA thermogravimetric analysis
TMO transition metal oxide
TMN transition metal nitride
TS total scattering
WAXS wide-angle X-ray scattering
XANES X-ray absorption near edge structure
XAS X-ray absorption spectroscopy
XPS X-ray photoelectron spectroscopy
XRD X-ray diffraction
XFEL X-ray free electron laser

List of Figures

2.1	LaMer diagram.	5
2.2	Gibbs free energy for classical and nonclassical nucleation pathways.	5
3.1	Overview of X-ray methods.	8
3.2	Schematic of an X-ray scattering experiment.	10
3.3	Atomic form factors of selected elements	11
3.4	Bragg and Laue condition.	14
3.5	PXRD simulations of bulk Cu and Cu nanoparticles.	15
3.6	PDF simulations of bulk Cu and Cu nanoparticles.	16
3.7	SAXS simulations of spherical nanoparticles.	18
3.8	Absorption coefficient of selected elements.	19
3.9	Normalized X-ray absorption spectrum of copper(II) oxide.	20
3.10	Total energy diagram illustrating electronic transitions of Cu(II).	22
3.11	Conventional vs. HERFD-XAS of copper(II) oxide.	23
4.1	Design of the reactor.	29
4.2	Thermal, pressure and transmission characteristics of the glass inlet.	31
4.3	PXRD of CuO nanoparticles at different concentrations and SNR calculations.	32
4.4	<i>In situ</i> PXRD and PDF analysis of the reaction to Fe ₃ O ₄	34
4.5	<i>In situ</i> ATR-FTIR analysis of the reaction of Fe(acac) ₃ to Fe ₃ O ₄	35
4.6	<i>In situ</i> Fe K-edge HERFD-XANES analysis of the reaction to Fe ₃ O ₄	36
4.7	Schematic overview of the reaction pathway leading to Fe ₃ O ₄ nanoparticles.	37
S4.1	Cross section of the reactor including the X-ray beam path.	40
S4.2	The rendered image of the Peltier cooling-incorporated reactor.	42
S4.3	Temperature profile of the reactor equipped with Peltier cooling	42
S4.4	Reactor cap pictures.	43
S4.5	Measured temperature profiles of the reactor during heating.	43
S4.6	X-ray transmission of the glass and PEEK inlet.	44
S4.7	Pearson correlation map of the <i>in situ</i> PXRD data.	46
S4.8	Time resolution estimation of PXRD and PDF data.	46
S4.9	<i>in situ</i> ATR-FTIR analysis.	47
S4.10	FEFF simulated XANES spectra and their corresponding density of states.	48
S4.11	Eigenvalue profile of MCR-ALS analysis.	48
S4.12	Schematic of the scanning pattern across the X-ray window.	49
S4.13	Beam damage study on Fe(acac) ₃	49
S4.14	Raw <i>in situ</i> Fe K-edge HERFD-XANES data	50
5.1	Schematic illustration of the present work.	54
5.2	<i>Ex situ</i> characterization of Cu ₃ PdN NPs.	55
5.3	EXAFS fits showing the cation-site disorder.	56
5.4	<i>In situ</i> XANES and PDF analysis of the reaction to Cu ₃ PdN.	58
5.5	Electrocatalytic performance of Cu ₃ PdN NPs for the HER.	61

S5.1	STEM images and size distribution of Cu ₃ PdN NPs.	65
S5.2	TGA performed under a nitrogen atmosphere of Cu ₃ PdN.	66
S5.3	Simulated PXRD pattern of Cu ₃ PdN, Cu ₃ Pd, Cu and Pd.	66
S5.4	Simulated two-phase PXRD pattern of Cu ₃ PdN and Cu ₃ Pd.	67
S5.5	Waterfall plot of EXAFS Cu K-edge, EXAFS Pd K-edge and PXRD of Cu ₃ PdN. . .	67
S5.6	Double-edge Cu K-edge and Pd K-edge EXAFS fit of Cu ₃ PdN.	69
S5.7	Experimental vs. FEFF-simulated EXAFS data of ordered Cu ₃ PdN.	70
S5.8	First derivative XANES spectra of Cu ₃ PdN.	70
S5.9	PXRD simulations of Cu ₃ PdN.	73
S5.10	Rietveld refinements of Cu ₃ PdN.	74
S5.11	Eigen value profile of MCR-ALS analysis.	76
S5.12	MCR-ALS of Cu K-edge HERFED-XANES.	77
S5.13	Cu K-edge EXAFS data of the initial complex.	78
S5.14	Ordered and cation-site disordered 2x2x2 supercell of Cu ₃ PdN.	78
S5.15	Beam damage study on Cu ₃ PdN.	79
S5.16	<i>In situ</i> PDF analysis of the reaction to Cu ₃ PdN.	81
S5.17	PDF simulation comparison of ordered and disordered Cu ₃ PdN.	81
S5.18	Time series of PDFs.	82
S5.19	<i>In situ</i> PDF of the reduction of Cu ₃ PdN to bimetallic Cu ₃ Pd.	83
S5.20	Time series of PDF refinements.	84
S5.21	PDF refinement results.	85
S5.22	Cyclic voltammetry measurement.	85
S5.23	Simple equivalent circle for EIS fitting.	86
S5.24	PXRD of Cu ₃ PdN after being dispersed in 0.5M H ₂ SO ₄ electrolyte.	86
S5.25	XPS core-level spectra of Cu ₃ PdN before and after EC.	87
S5.26	LSV of Cu ₃ Pd compared to Cu ₃ PdN, Pt-C and GC.	87
6.1	Experimental and analytical workflow of single-particle vs. conventional SAXS. . .	92
6.2	Representative diffraction images and corresponding radial integrations. . .	93
6.3	SP-SAXS analysis of the reaction aliquots.	94
6.4	Proposed formation pathway of CoO nanocrystal assemblies.	95
S6.1	Diffraction images of all SP-SAXS classes.	97
S6.2	Radial integration of all SP-SAXS classes.	98
S6.3	Radial integration of SP-SAXS assembly classes.	101
S6.4	Conventional SAXS data of CoO nanocrystal assemblies.	103
S6.5	PDF data of CoO nanocrystal assemblies.	103
S6.6	TEM images of CoO nanocrystal assemblies.	104
S6.7	STEM images of spherical Co(acac) ₂ aggregates.	104
S6.8	SEM image of a rose-like particle.	104
7.1	Formation mechanisms of Fe ₃ O ₄ , Cu ₃ PdN, and CoO nanostructures.	106
A1.1	<i>In situ</i> PXRD of Sn:Fe _x O _y nanoparticle syntheses.	110
A1.2	Comparison of PXRD patterns from different Sn concentrations.	111
A1.3	<i>In situ</i> PDF of Sn:Fe _x O _y nanoparticle syntheses.	112
A1.4	Comparison of PDF patterns from different Sn concentrations.	112
A1.5	Evolution of PDF peak maximum positions and amplitudes.	114
A2.1	PXRD patterns and Rietveld refinements of Cu ₃ N NPs.	117
A2.2	PXRD patterns and Rietveld refinements of phase-pure Cu ₃ N.	118
A3.1	CoO EM images.	122
A3.2	Rietveld refinements of different reaction time points.	123

A3.3 Simulated PXRD patterns of cobalt species.	125
A3.4 CoO SAED analysis.	126
A4.1 PXRD pattern of the nanotextured titania.	128

List of Tables

3.1	Summary of X-ray methods.	9
4.1	Overview of solvothermal reactors for <i>in situ</i> XAS, WAXS and SAXS.	27
S4.1	Comparison of present and previous reactor designs.	40
S4.2	Instrumentally achievable maximum q-values.	41
S4.3	Rietveld refinement results of the final stage of the reaction.	44
S4.4	PDF refinement results.	45
S4.5	Assigned vibrational modes in the ATR-FTIR spectra.	45
S5.1	Review of Cu ₃ PdN solvothermal synthesis routines.	65
S5.2	The scattering paths used to fit the EXAFS.	71
S5.3	EXAFS refined parameters.	72
S5.4	Rietveld Refinement Results	73
S5.5	Summary of the beamlines and synchrotrons utilized for collecting XAS data.	74
S5.6	Values used for processing the PDF.	79
S5.7	Boundaries used for Gaussian fit as shown in Equation 5.	80
S5.8	Initial values and boundaries of PDF refinement parameter.	80
S5.9	PDF refinement algorithm.	80
S5.10	Overview of TMN-based electrocatalysts for HER.	88
S6.1	List of all SP-SAXS classes.	99
A1.1	Atomic correlation of the main PDF contributions.	113
A2.1	Rietveld refinement results.	117
A2.2	Rietveld-refined crystallite sizes of phase-pure Cu ₃ N.	117
A2.3	Cu ₃ N stock solution preparation.	119
A2.4	Fixed parameters for Rietveld refinements.	119
A3.1	Position of Co(OH) ₂ (001) reflection.	124
A3.2	Rietveld refinement results.	125
A3.3	CoO SAED ring positions.	126

List of Publications

- Lukas Grote^{*}, Cecilia A. Zito^{*}, Kilian Frank^{*}, Ann-Christin Dippel, Patrick Reisbeck, Krzysztof Pitala, Kristina O. Kvashnina, Stephen Bauters, Blanka Detlefs, Oleh Ivashko, Pallavi Pandit, Matthias Rebber, **Sani Y. Harouna-Mayer**, Bert Nickel, & Dorota Koziej
X-ray studies bridge the molecular and macro length scales during the emergence of CoO assemblies
Nature Communications 12, 4429 (2021)
<https://doi.org/10.1038/s41467-021-24557-z>
- Lukas Grote, Martin Seyrich, Ralph Döhrmann, **Sani Y. Harouna-Mayer**, Federica Mancini, Emilis Kaziukenas, Irene Fernandez-Cuesta, Cecilia A. Zito, Olga Vasylieva, Felix Wittwer, Michal Odstrčil, Natnael Mogos, Mirko Landmann, Christian G. Schroer, & Dorota Koziej
Imaging Cu₂O nanocube hollowing in solution by quantitative in situ X-ray ptychography
Nature Communications 13, 4971 (2022)
<https://doi.org/10.1038/s41467-022-32373-2>
- **Sani Y. Harouna-Mayer**, Songsheng Tao, ZiZhou Gong, Martin v. Zimmermann, Dorota Koziej, Ann-Christin Dippel, & Simon J. L. Billinge
Real-space texture and pole-figure analysis using the 3D pair distribution function on a platinum thin film
IUCrJ 9, 5 (2022)
<https://doi.org/10.1038/s41467-022-32373-2>
- Francesco Caddeo, Sophie Medicus, Carina Hedrich, Marco Krüger, **Sani Y. Harouna-Mayer**, Robert H. Blick, Robert Zierold, & Dorota Koziej
Enhancing Charge Transport in CuBi₂O₄ Films: The Role of a Protective TiO₂ ALD Coating Probed by Impedance Spectroscopy
Advanced Materials Interfaces 11 (2024)
<https://doi.org/10.1002/admi.202400263>
- Lars Klemeyer, Tjark L. R. Gröne, Cecilia de Almeida Zito, Olga Vasylieva, Melike Gumus Akcaalan, **Sani Y. Harouna-Mayer**, Francesco Caddeo, Torben Steenbock, Sarah-Alexandra Hussak, Jagadesh Kopula Kesavan, Ann-Christin Dippel, Xiao Sun, Andrea Köppen, Viktoriia A. Saveleva, Surender Kumar, Gabriel Bester, Pieter Glatzel, & Dorota Koziej
Utilizing High X-ray Energy Photon-In Photon-Out Spectroscopies and X-ray Scattering to Experimentally Assess the Emergence of Electronic and Atomic Structure of ZnS Nanorods
JACS 146 (2024)
<https://doi.org/10.1021/jacs.4c10257>
- Lars Klemeyer^{*}, Francesco Caddeo^{*}, Tjark L. R. Gröne, **Sani Y. Harouna-Mayer**, Brian Jessen, Cecilia A. Zito, Jagadesh Kopula Kesavan, Ann-Christin Dippel, Fernando Igoa Saldaña, Olivier Mathon, Pieter Glatzel, & Dorota Koziej
Spatially Resolved In Situ X-ray Absorption Spectroscopy Studies of ZnS Nanoparticle Synthesis at the Water - Toluene Interface

ACS Nano 19 (2025)

<https://doi.org/10.1021/acsnano.5c02875>

- **Sani Y. Harouna-Mayer**^{*}, Jagadesh Kopula Kesavan^{*}, Francesco Caddeo^{*}, Lian Belgardt, Chia-Shuo Hsu, Lars Klemeyer Author, Lizzi Kipping, Melike Gumus Akcaalan, Tjark R. L. Groene, Andrea Koeppen, Olivier Mathon, Ann-Christin Dippel, & Dorota Koziej
Cation-site Disordered Cu₃PdN Nanoparticles for Hydrogen Evolution Electrocatalysis
Small 21 (2025)
<https://doi.org/10.1002/smll.202506838>
- Cecilia A. Zito^{*}, Lars Klemeyer^{*}, Brian Jessen, Francesco Caddeo, **Sani Y. Harouna-Mayer**, Tjark L. R. Gröne, Jagadesh Kopula Kesavan, Ann-Christin Dippel, Olivier Mathon, Pieter Glatzel, & Dorota Koziej
In situ X-ray Synchrotron Studies Reveal the Nucleation and Topotactic Transformation of Iron Sulfide Nanosheets
JACS 147 (2025)
<https://doi.org/10.1021/jacs.5c15843>
- **Sani Y. Harouna-Mayer**, Lars Klemeyer, Cecilia A. Zito, Johan Bielecki, Xuemei Cheng, Davide Derelli, Armando D. Estillore, Tjark L.R. Groene, Lukas V. Haas, Romain Letrun, Chan Kim, Jayanath C.P. Koliyadu, Abhishek Mall, Parichita Mazumder, Diogo V.M. Melo, Adam R. Round, Amit K. Samanta, Abhisakh Sarma, Zhou Shen, Xiao Sun, Patrik Vagovic, Tamme Wollweber, Richard Bean, Jochen Küpper, Henry N. Chapman, Dorota Koziej, & Kartik Ayer
Single-Particle X-ray Scattering Reveals a High Local Supersaturation of Precursors as the Origin of CoO Assembly Formation
Manuscript under revision; preprint available on arXiv (2025)
<https://doi.org/10.48550/arXiv.2512.08488>
- **Sani Y. Harouna-Mayer**^{*}, Melike Gumus Akcaalan^{*}, Jagadesh Kopula Kesavan, Tjark R. L. Groene, Lars Klemeyer, Sarah-Alexandra Hussak, Lukas Grote, Davide Derelli, Francesco Caddeo, Cecilia Zito, Paul Stütze, Dorota Speer, Ann-Christin Dippel, Blanka Detlefs, Yannik Apparius, Axel Jacobi von Wangellin, & Dorota Koziej
Modular In Situ Reactor for X-ray Scattering, Spectroscopy, and ATR-IR Studies of Solvothermal Nanoparticle Synthesis
J. Synchrotron Rad. 33 (2026)
<https://doi.org/10.1107/S1600577525009634>

^{*} indicates equal contribution

Curriculum Vitae

Personal information

Name	Sani Yusuf Harouna-Mayer
Date of birth	1 st of July, 1996
Place of birth	Kassel, Germany
Citizenship	Germany

Education

11/2020 – present	Dissertation in Physics Department of Physics University of Hamburg, Germany Thesis: Watching Nanoparticles Form: In Situ and Single-Particle X-ray Studies of Nucleation and Growth
10/2018 – 11/2020	M.Sc. in Nanoscience Department of Physics University of Hamburg, Germany Thesis: Three-Dimensional Atomic Pair Distribution Function of a Textured Platinum Thin Film
10/2015 – 08/2018	B.Sc. in Nanoscience Department of Physics University of Hamburg, Germany Thesis: Electrochromic Effect of Praseodymium Oxide Thin Films Studied by Total X-ray Scattering
08/2006 – 06/2014	Abitur Wilhelmsgymnasium, Kassel, Germany

Acknowledgements

The accomplishment of this Ph.D. work would not have been possible without the support of my colleagues. I am deeply grateful to everyone who contributed to this project, whether through scientific discussions, practical assistance, or by fostering a collaborative and inspiring working environment.

First and foremost, I would like to thank Prof. Dr. Dorota Koziej for giving me the opportunity to work on these exciting projects and for her constant support and trust throughout my Ph.D. journey. Her confidence in me allowed me to work with a high degree of independence and to grow both scientifically and personally. I am deeply grateful for the many inspiring discussions, her constant availability, and her motivating guidance, as well as for the valuable insights and perspectives she shared with me over the years. Further I am very thankful to Dorota for igniting my passion and enthusiasm for X-ray science and for continuously encouraging my curiosity and scientific development.

Furthermore, I am very grateful for the opportunity to work with Dr. Kartik Ayyer, whose insightful discussions and guidance introduced me to the world of XFEL science.

I highly appreciate the pleasant working atmosphere at the CHyN, and would like to thank all present and former members for many interesting discussions, shared moments, and for being such kind and supportive office mates. Especially, I would like to thank my close collaborators Dr. Jagadesh Kopula Kesavan, Dr. Francesco Caddeo, and Melike Gumus Akcaalan for the many productive and open discussions, as well as for the shared enthusiasm that made our joint work both enjoyable and rewarding. I also very much enjoyed working with Dr. Cecilia Zito and Dr. Lukas Grote, and I am thankful for the many insights, ideas, and experiences I gained from them. Many thanks to Tomasz Kacperski and Paul Kühn for their reliable support in the lab and to Dr. Davide Derelli, Tjark Gröhne, Lian Belgardt, and Hauke Damerow for many interesting discussions regarding PDF analysis strategies.

Furthermore, I am truly grateful for the daily support and the countless discussions with Dr. Lars Klemeyer, Sarah-Alexandra Hussak, and Paul Stütze, both on research-related topics and beyond. I also cherished the many productive discussions and refreshing breaks with Sarodi Jonak Dutta, Dr. Marvin Skiba, and Rebeka Reszegi. I feel extremely fortunate to have had you all around during my time at CHyN.

I would like to thank Andrea Köppen, Stefan Werner, and Charlotte Ruhmlieb for electron microscopy measurements and Stefan Fleig and members of the UHH mechanical workshop for the fabrication of the reactors. I am also very grateful to Dr. Ann-Christin Dippel, Dr. Martin v. Zimmermann, Dr. Fernando Igoa, Dr. Jiayu Liu, Dr. Oleh Ivashko, Philipp Glaevecke, Olof Gutowski at beamlines P07 and P21.1, as well as Dr. Xiao Sun and Dr. Sylvio Haas at beamline P62 for their support during various beamtime experiments at DESY. Furthermore, I would like to thank Dr. Blanka Detlefs, Dr. Pieter Glatzel, and Dr. Olivier Mathon for their support during beamtimes at the ESRF beamlines ID24 and ID26.

Finally, I would like to thank my family and friends for their continuous support and encouragement throughout my Ph.D. journey.

Eidesstattliche Versicherung

Hiermit versichere ich an Eides statt, die vorliegende Dissertationsschrift selbst verfasst und keine anderen als die angegebenen Hilfsmittel und Quellen benutzt zu haben.

Sofern im Zuge der Erstellung der vorliegenden Dissertationsschrift generative Künstliche Intelligenz (gKI) basierte elektronische Hilfsmittel verwendet wurden, versichere ich, dass meine eigene Leistung im Vordergrund stand und dass eine vollständige Dokumentation aller verwendeten Hilfsmittel gemäß der Guten wissenschaftlichen Praxis vorliegt. Ich trage die Verantwortung für eventuell durch die gKI generierte fehlerhafte oder verzerrte Inhalte, fehlerhafte Referenzen, Verstöße gegen das Datenschutz- und Urheberrecht oder Plagiate.

Des Weiteren versichere ich, dass dieses gebundene Exemplar der Dissertation und das in elektronischer Form eingereichte Dissertationsexemplar (über den Docata-Upload) und das bei der Fakultät (zuständiges Studienbüro bzw. Promotionsbüro Physik) zur Archivierung eingereichte gedruckte gebundene Exemplar der Dissertationsschrift identisch sind.

Ort, Datum

Unterschrift